DEVELOPMENTS IN PLANE AND CONCAVE GRATINGS: THEORY AND EXPERIMENT

by

Barbara Jean Brown

B.J.Brown, B.Sc.(Hons.), University of Tasmania

A thesis submitted in fulfilment of the requirements

for the degree of

Doctor of Philosophy

in the

UNIVERSITY OF TASMANIA

HOBART

February, 1981

Except as stated herein, this thesis contains no material which has been accepted for the award of any other degree or diploma in any university. To the best of my knowledge and belief, this thesis contains no copy or paraphrase of material previously published or written by another person, except where due reference is made in the text of the thesis.

B. J. Brown.

Barbara J. Brown.

19/2/81

Any part of this thesis may be photocopied.

CONTENTS

ABSTRACT

The developments in grating performance described in this thesis fall naturally into two parts according to whether the grating blank is plane or concave. For plane diffraction gratings, this study utilizes both experimental work and rigorous electromagnetic theories to achieve improved grating and instrument performance. The section concerned with concave gratings is entirely theoretical, drawing on the manipulation of geometric theories to design high quality gratings.

Three types of plane diffraction grating grooves currently generated by holographic techniques are investigated. A discussion of methods for accurately measuring the groove profile is presented with particular reference to quasi-sinusoidal groove profiles. The spectral performance of blazed holographic gratings is shown numerically to be comparable to that of triangular groove gratings. Consideration is then given to simple optical arrangements which permit Fourier synthesis of complex distributions and groove profiles.

Experimental investigations of the behaviour of resonance anomalies exhibited by gratings having surface layers of discontinuous conductivity are presented. It is demonstrated that a coating consisting of a dielectric overlaid with a metal of high conductivity drastically reduces energy absorption.

A theoretical search to determine the optimum groove modulation of both blazed and sinusoidal plane reflection gratings is presented. This will assist with the development of high-gain dye lasers utilizing gratings at grazing incidence.

Aberration coefficients derived using Fermat's principle are used for an examination of aberration-correction for Rowland circle spectrographs. Attention is focussed on the case where the mounting and recording points lie on the Rowland circle. Correction at two wavelengths of primary astigmatism or primary coma under this constraint is demonstrated. Alternatively, primary astigmatism and primary coma can be simultaneously corrected over a restricted wavelength range. Some practical implications are discussed.

The geometric theory of concave gratings is extended to accommodate higher order aberration terms. The magnitude of the individual terms of the light path function, which describes image formation by an aberration-corrected grating, is investigated. Similarly, the behaviour of the image height under these restraints is studied for various values of the relative aperture.

Finally, aberration minimization techniques are employed in the design of a uni-axial, double concave grating monochromator. The performance of this instrument is evaluated for ruled and holographic gratings.

ACKNOWLEDGEMENTS

I sincerely thank everyone who assisted in the formulation of this thesis, whether their contributions were of a practical nature or by way of encouragement. Special thanks are due to the following:

My supervisor, Dr. M.D. Waterworth, whose discussions throughout the years of investigation spanned by this thesis were most appreciated. Dr. I.J. Wilson, CSIRO, who as my collaborator on many of the reported developments aided my insight into the beauty of the world of the diffraction grating. Dr. E.G.Loewen, Bausch and Lamb Inc., for his helpful suggestions.

The companionship and continuing interest of my family and fellow Ph.D. students played a significant role in the completion of this thesis.

Several members of the University staff deserve mention. The staff of the University Computing Centre for the generous provision of computing resources. Barry Wilson and the technical staff, Department of Physics, have assisted in the construction and development of equipment. During the early months of my Ph.D. candidature, experimental work was conducted within the Central Science Laboratory. I thank the staff for making the facilities available. In particular, I am grateful to Dr. A. McKee and Mr. W. Jablonski for the electron-microscope work displayed in Chapter 2.

Mrs. B. Golding and Mrs. J. Scott expertly and patiently typed this manuscript.

Throughout the course of this research, the author was a recipient of an Australian Postgraduate Research Award.

CHAPTER 1

INTRODUCTION AND BASIC THEORIES

> *"... I saw three parallel lines, almost equal in brightbess and on each side four or five other much fainter and growing more faint, coloured and indistinct, the further they were from the middle line ..."* (Rittenhouse 1786 [1.1]).

It is the aim of this chapter to introduce the reader to the world of the diffraction grating. Rittenhouse's description of the first observations of the diffracting properties of a man made grating sets the scene for a brief discussion of the evolution of the contemporary diffraction grating. This historical survey is followed by a comparison of the properties of the two basic types of gratings - the classical, ruled grating and the recently developed holographic grating. Several notable features of the spectrum generated by a diffraction grating are outlined. This description is supplemented by a discussion of the mounting conditions and efficiency measuring techniques which enable the evaluation of the spectral performance of a grating. Electromagnetic theories detailing the distribution of energy into the diffracted orders are used extensively throughout this thesis to aid in the development of gratings exhibiting improved spectral behaviour. A short discussion of the formulation of these theories is presented. Attention is then diverted away from the efficiency of a grating, to a geometric theory of Noda, Namioka and Seya which describes the formation of spectral images by ruled and holographic concave gratings. The introduction is then concluded by a chapter by chapter outline of the contents of this thesis.

1.1 HISTORICAL SURVEY

The diffraction grating in its ideal form, comprises a large number of line slits, parallel and equidistant, located in one plane. However, in the case of Rittenhouse the diffracting elements were parallel hairs laid in a fine screw. Thirty-seven years later Fraunhofer [1.2] produced the first ruled grating by periodically burnishing grooves in flat metallic blanks. Fraunhofer, who displayed an outstanding insight into the behaviour of gratings, not only discovered the principle of plane gratings, but investigated the influence which periodic ruling errors and the groove profile have on the spectra. However, his most notable contribution to the development of the diffraction grating was the formulation of the grating equation, which describes the dispersion of incident light into the diffracted orders

$$\sin\theta_i + \sin\theta_d = \frac{m\lambda}{d} \qquad (1.1)$$

where θ_i and θ_d are the angles formed by the wave propagation vectors of the incident and diffracted waves with the normal to the grating surface. The grating spacing is d, the wavelength of the diffracted radiation λ and the spectral order m. In the notation used here the angle of the diffraction θ_d is positive if the incident and diffracted wavefronts are on the same side of the normal and negative if they are on opposite sides of the normal.

For over one hundred years the grooves of diffraction gratings have been individually imprinted in metal by the diamond of a ruling engine. A series of periodic, mirror-like facets whose angular form is dictated by the shape of the diamond tool is intrinsically generated by such a technique. The father of modern ruled diffraction

gratings was undoubtedly Rowland [1.3] whose sophisticated ruling engine, with minor adjustments, was still operational in the 1950's. Modern spectroscopists owe credit to Rowland [1.3] for uniting the dispersive power of the grating with the imaging properties of a concave mirror to yield the concave grating. The principal innovators contributing to the evolution of the ruled grating include Michelson [1.4], Wood [1.5] and Strong [1.6] who reported the vacuum evaporation of soft metals onto glass flats to form grating blanks. The efforts of these physicists culminated in the introduction of the interferometric servo-control of the diamond carriage and blank movement by Harrison and Stroke [1.7] in 1955. As a consequence, ruling accuracies now approach the optimum, permitting the ruling of large echelle gratings coveted by optical astronomers and high resolution spectroscopists. Today, the art of ruling gratings has achieved the precision whereby optical gratings of ruled areas up to 400 x 600 mm^2 (an increase of about 30 fold in area since Rowland's day) with groove densities ranging from 30 per mm to 3600 per mm are readily available. Resolution has been increased fivefold and the intrinsic dispersion has been increased tenfold. Furthermore, false lines and scattered light have been reduced by more than two orders of magnitude.

In the 1960's the production of high resolution photoresists together with the advent of high powered gas lasers, made holographic recording a viable alternative to the ruling engine. The interference field generated by the intersection of two coherent plane waves causes a variation of solubility throughout the resist. Development yields an undulating surface whose periodicity is related to that of the exposing field. The idea of interference gratings is not new.

Michelson [1.8] in 1927 suggested the production of gratings by photographing stationary waves. However, 40 years elapsed before Rudolph and Schmahl [1.9] and Labeyrie [1.10] generated good optical quality holographic gratings. If the two interfering waves are incident at the same surface of the resist development yields a sinusoidal groove profile. Alternatively, Sheridon [1.11] showed that if the plane waves are incident on opposite sides of the photoresist layer, then a triangular groove profile results.

Experimental configurations representative of both recording arrangements appear in Fig. (1.1). Concerted efforts by several grating groups over the past 10 years have ensured that holographic diffraction gratings compete with classically ruled gratings from the visible to the ultraviolet and soft x-ray regions.

1.2 COMPARISON OF THE PROPERTIES OF HOLOGRAPHIC AND CLASSICAL GRATINGS

Fundamental differences in the properties of holographic and ruled gratings originate from the totally dissimilar production techniques. For the interference grating, the position of the groove is determined by the exposure conditions. Consequently the ruling errors normally associated with mechanical gratings are not introduced. The only spectral impurity that occurs for holographic gratings is diffuse scattered light (less than 1/10 of ruled gratings) caused by surface irregularities. Mechanical restraints are imposed by the ruling engine and eventual wear of the diamond. However, the holographic process is limited only by the optics, permitting the production of large and finer pitched gratings. The diamond usually constrains the groove profile of a ruled grating to linear facets.

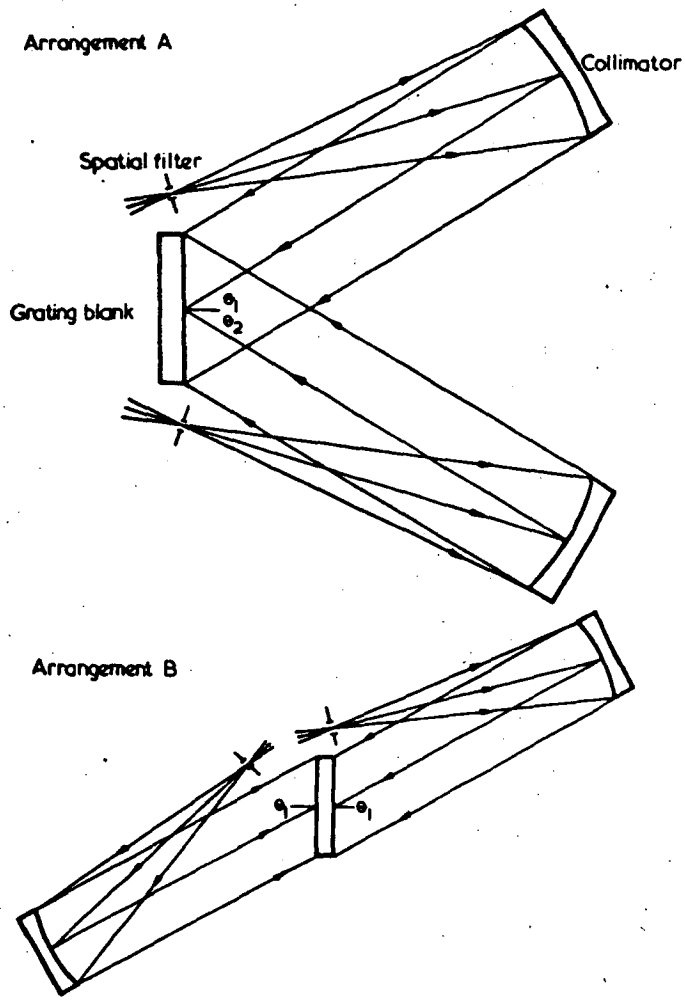

Fig.(1.1) Holographic grating formation : arrangement A - the interfering plane waves are incident on the front surface of the photoresist coated grating blank ; arrangement B - the interfering plane waves are incident on opposite sides of the photoresist coated grating blank (after McPhedran, Wilson and Waterworth, 1973).

No analogous restriction exists for holographic gratings. It is theoretically possible through the Fourier synthesis of the exposing field to generate an unlimited choice of groove profiles. Unfortunately, only minimal control over the holographic groove profile is possible. This is a serious disadvantage, especially as the groove profile governs the distribution of energy into the diffracted orders.

As will be discussed later, the efficiency of a grating is the fraction of the incident radiation diffracted into a particular order. Although holographic gratings lack facets to direct light into a given order, under particular conditions the spectral efficiency of the sinusoidal groove profile is comparable to that of the ruled grating. Petit [1.12, 1.13] demonstrated that in the normalized wavelength range of $0.8 < \lambda/d < 1.7$, efficiencies of holographic gratings are optimal and approach those of ruled gratings.

Significantly, holographic concave gratings can be designed through a judicious choice of recording and mounting parameters to minimize the aberrations of the spectral image introduced by the curved surface of the grating.

1.3 DIFFRACTION GRATING EFFICIENCY

Although the grating equation describes the angular position of the diffracted orders of a grating, a knowledge of the distribution of incident energy amongst these orders is just as significant. The efficiency of a particular diffracted order of a grating is defined by the ratio of the energy propagating in that order to the incident energy. Throughout this thesis, the efficiency is displayed on a scale of 0 to 1.0. The energy distribution is different for each of the two fundamental planes of polarization.

It is appropriate to explain here the S and P polarization terminology employed in this thesis. If the electric vector of the incident wave is aligned parallel to the groove then the radiation is termed P polarized. Alternatively, if it is the magnetic vector that is aligned parallel to the groove, then the incident radiation is said to be S polarized.

Hutley [1.14-1.15] demonstrated that the spectral efficiency of a grating can be fully described only if the efficiency for every wavelength at every angle of incidence is known. This constitutes a grating "efficiency surface". A complete description of the grating efficiency requires one such surface for each of the two fundamental planes of polarization. Each grating mount corresponds to a different cut through the efficiency surface. Of particular interest is the efficiency of a given order as a function of the incident wavelength, when the order under investigation is diffracted back along the incident beam. In practice this Littrow mount is often used with some fixed angle, referred to as the angular deviation, between the incident and diffracted beam. The mount corresponds to practical situations employing fixed entrance and exit slits and a grating on a rotary mount. Other efficiency cross-sections may be measured. One which is particularly convenient is a map of the efficiency for various angles of incidence at a constant wavelength. This approach has been used extensively by the author. The beam of a He-Ne laser is directed at the grating and the power in the incident and diffracted beams is measured using the same detector.

Investigation of the efficiency curves of the diffracted orders of a grating reveals several interesting features. Wood [1.16] in

1902 was the first to observe the rapid variations in the efficiency of a diffracted order which accompany the passing-off of a particular order.

Early electromagnetic theories describing the diffraction from a grating of infinite surface conductivity treated the total dispersed energy as being equal to that incident at the surface. It was assumed that finite conductivity could be accommodated by multiplying the infinite conductivity efficiencies by an appropriate factor to allow for the finite conductivity of the metal coating. Eventually, finite electromagnetic theories confirmed experimental observations that this was not the case. The total diffracted efficiency of metal gratings is not constrained to be 100%. In fact, sharp, absorption peaks, termed resonance anomalies, occur in the total diffracted energy curve near the region of a passing-off of an order. This absorption is due to the "tunnelling" of energy away from the real propagating orders by surface plasmon waves.

Although Fraunhofer knew that the distribution of light among the various grating orders depended on the shape of the individual grooves, it was not until many decades later that Wood concentrated spectral energy into one particular order, thereby creating a "blazed" grating. The principle of "blazing" is to generate the groove profile so that the reflecting elements are tilted with respect to the grating surface. The wavelength of light for which the direction of reflectance from the groove face is the same as the angle of diffraction, for a given angle of incidence, is the blaze wavelength. When a grating is used in the Littrow mount, where $\theta_i = \theta_d$, the blaze condition calls for the groove face to be normal to the ray path, so that the blaze angle is then equal to the diffraction angle of the grating.

1.4 THEORIES OF DIFFRACTION GRATINGS

Although Fraunhofer successfully described the directions of the dispersion of radiation by a grating, his work did not encompass the problem of the distribution of energy into the diffracted orders. However, early investigators were quick to grasp the significance of a thorough understanding of the spectral behaviour of gratings and by the commencement of this century several grating theories had been proposed [1.17-1.20]. Each theory, based on the scalar approach to diffraction, failed to recognize mathematically that gratings act as polarizers, a property known since the time of Fraunhofer. Hence such theories were incapable of adequately describing gratings which display substantial polarization effects.

Following the observation of spectral anomalies for the S plane of polarization by Wood [1.16] in 1902, Rayleigh [1.21] formulated a "dynamical theory of gratings" which predicted some of the features displayed by Wood anomalies. In this theory, the scattered wavefield above the surface of the grating is expanded in terms of outgoing plane waves of constant amplitude. However, there was hesitation in accepting the validity of the Rayleigh expansion within the region enclosed by the grooves [1.22]. Detailed investigations [1.23] have since restricted the validity of this approach to only very shallow grooves.

The first truly rigorous electromagnetic grating theory which did not depend on the Rayleigh expansion was proposed by Petit and Cadilhac [1.24] in 1964. As opposed to the methods based on Rayleigh's assumption, which are all differential in nature, Petit et al developed an integral equation with the induced surface density as the fundamental unknown to describe the diffraction of a plane wave by a perfectly

conducting grating. Unfortunately, the procedure which solves the integral equation limits the application of this theory to grating profiles constructed from a number of linear facets. This infinite conductivity theory has been used in a following chapter to compare the spectral behaviour of blazed holographic gratings and ruled companions of similar blaze angle. Pavageau and Bousquet [1.25] eliminated the profile restriction of the technique of Petit et al by solving the integral equation with a point-matching procedure.

For gratings in the far and extreme ultraviolet, experiment has demonstrated [1.26] that the assumption of a perfectly conducting grating is no longer applicable and consideration must be given to the finite conductivity of the metal coating. The formulation by Van den Berg [1.27] of a numerical solution to a pair of coupled integral equations which describe the diffraction of a plane wave by a finitely conducting structure, is plagued by computational instabilities. Maystre [1.28] succeeded in characterizing the field above the grating surface by a pair of unknowns which may be expressed in terms of a single fictitious variable, analogous to the surface current density of the perfectly conducting theories. Computer programs developed by L.C. Botten in accordance with the theory of Maystre, are used throughout this thesis, particularly to make comparisons between the observed behaviour of a grating and the optimum performance predicted by this theory.

The final electromagnetic theory pertinent to the work treated in this thesis is the formulism derived by Botten [1.29] for diffraction gratings consisting of a single grating surface surrounded by a number of planar films. The technique reduces the diffraction problem to the solution of a Fredholm integral equation of the first kind involving the computation of only one unknown, which is similar to that of Maystre.

This theory has been instrumental in the investigation of the Fourier synthesis of exposure fields for the holographic production of gratings.

1.5 GEOMETRIC THEORY OF THE CONCAVE GRATING

1.5.1 *Introduction*

Concave diffraction gratings can simultaneously disperse and focus radiation incident at their surfaces. This property is highly desirable, especially for instruments designed for applications in the ultra-violet region of the spectrum where the low reflectivity of metalized surfaces can severely limit throughput. The focal characteristics arise through the curved nature of the grating surface and consequently they are accompanied by wavefront aberrations.

Several geometric theories have been developed to illustrate the imaging properties of ruled and holographic concave gratings. The most successful of these theories describe the aberrations by application of Fermat's principle to the light path function. Typical of this type of formulism is that of Noda, Namioka and Seya [1.30] for holographic diffraction gratings where the light path function consists of terms resulting from both the mounting and recording conditions of the grating. This theory is particularly important since it enables the optical designer to take full advantage of the additional freedom introduced by the placement of the recording sources. A knowledge of the correct manipulation of the mounting and recording parameters allows certain aberrations to be reduced or possibly eliminated completely from the final spectral image. Hence, an understanding of the geometric theory of concave gratings can lead to an improvement in the spectral performance of the grating and consequently in spectroscopic instrumentation.

In the following, the derivation of Noda et al's expression for the light path function is outlined. Only a brief description is presented, since several exhaustive accounts of the procedure appear in the literature. The author has extended this theory a further two orders of magnitude to include higher order aberrations. Their contributions become significant at low values of the relative aperture. The expression for each individual aberration term is accompanied by a map displaying contours of the resultant wavefront aberration. Drawing on information gained by personal communication with I.J. Wilson and that published by Welford [1.31] a detailed discussion surrounding the low order aberration terms is presented. These aberration terms play an important role in determining the degree of distortion of the final spectral image.

Although the original work of Noda et al encompassed the more general case of aspheric surfaces, this work considers only diffraction gratings generated on spherical surfaces. Furthermore, interest lies only in the geometric imaging properties of concave gratings and no mention is made of the efficiency of such gratings.

1.5.2 *Derivation of Noda et al's Light Path Function*

Referring now to Fig. (1.2), we show a rectangular co-ordinate system whose origin O is at the vertex of a concave grating having a radius of curvature R. The x-axis is normal to the grating surface at O and the xy plane is defined by the plane of the Rowland-circle passing through object and image points A(x, y, 0), B(x', y', 0) and origin O. $P(\xi, \omega, \ell)$ is a point on the nth groove of the grating giving use to the diffracted ray of PB of wavelength λ and order m. For this ray the expression for the light path function F is composed of the total distance traversed and an additional diffraction phase term.

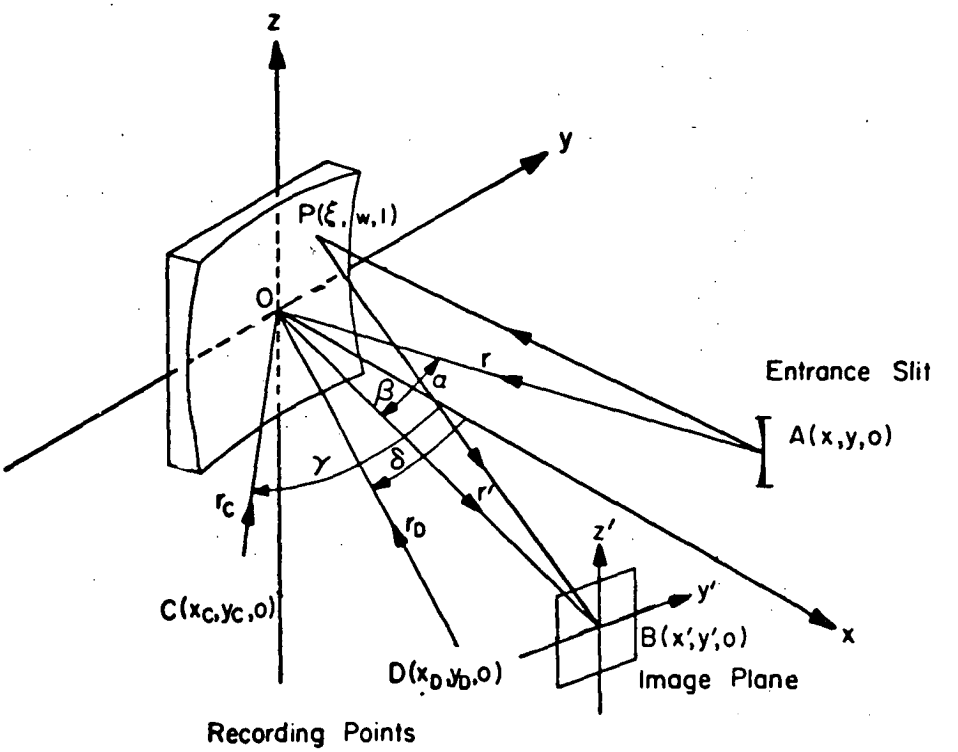

Fig.(1.2) Schematic diagram of the optical system of a holographic concave grating.

Hence

$$F = \langle AP \rangle + \langle PB \rangle + nm\lambda \tag{1.2}$$

where

$$\langle AP \rangle = [(x-\xi)^2 + (y-\omega)^2 + (z-\ell)^2]^{\frac{1}{2}}$$

$$\langle PB \rangle = [(x'-\xi)^2 + (y'-\omega)^2 + (z'-\ell)^2]^{\frac{1}{2}}$$

$$x = r\cos\alpha \qquad y = r\sin\alpha \tag{1.3}$$

$$x' = r'\cos\beta \qquad y' = r'\sin\beta$$

The variables α and β respectively correspond to the angles of incidence and diffraction measured relative to the xy plane.

The grating grooves are formed by the interference of coherent light originating from two recording sources $C(x_C, y_C, z_C)$ and $D(x_D, y_D, z_D)$.

Since Eq. (1.2) assumes that the difference in the distances of C and D from O is an integer multiple of the wavelength of the recording light λ_0, the formation of the grooves is described by

$$n\lambda_0 = [\langle CP \rangle - \langle DP \rangle] - [\langle CO \rangle - \langle DO \rangle] \tag{1.4}$$

where

$$\langle CP \rangle = [(x_C-\xi)^2 + (y_C-\omega)^2 + (z_C-\ell)^2]^{\frac{1}{2}}$$

$$\langle DP \rangle = [(x_D-\xi)^2 + (y_D-\omega)^2 + (z_D-\ell)^2]^{\frac{1}{2}}$$

$$\langle CO \rangle = (r_C^2 + z_C^2)^{\frac{1}{2}} \qquad \langle DO \rangle = (r_D^2 + z_D^2)^{\frac{1}{2}} \tag{1.5}$$

$$x_C = r_C\cos\gamma \qquad y_C = r_C\sin\gamma$$

$$x_D = r_D\cos\delta \qquad y_D = r_D\sin\delta$$

The sign of α and the signs of β, γ or δ are opposite if point A and point B, C or D lie on different sides of the xy plane.

Following the substitution of Eq. (1.4) into Eq. (1.2), Noda et al carried out a series expansion to yield an expression for the light path function of the form.

$$F = F_{000} + \omega F_{100} + \frac{\ell}{R} F_{011} + \left(\frac{\omega^2}{2R}\right) F_{200} + \left(\frac{\ell^2}{2R}\right) F_{020}$$
$$+ \left(\frac{\omega^3}{2R^2}\right) F_{300} + \left(\frac{\omega\ell^2}{2R^2}\right) F_{120} + \left(\frac{\omega\ell}{R^2}\right) F_{111} + \left(\frac{\omega^4}{8R^3}\right) F_{400}$$
$$+ \left(\frac{\omega^2\ell^2}{4R^3}\right) F_{220} + \left(\frac{\ell^4}{8R^3}\right) F_{040} + \left(\frac{\omega^2}{4R^3}\right) + \left(\frac{\ell^2}{4R^3}\right) F_{022}$$
$$+ \left(\frac{\ell^3}{2R^3}\right) F_{031} + \left(\frac{\omega^2\ell}{2R^3}\right) F_{211} + \ldots \qquad (1.6)$$

where the subscripts i j k of F_{ijk} are the exponents of $\omega^i \ell^j z^k$, except for F_{000}. It is the value of these exponents ijk which categorize each aberration type. Therefore, it is possible to express the light path function as the sum of individual terms. Each term consists of a co-ordinate expression $\omega^i \ell^j$ describing the position on the grating surface at which diffraction occurs and a coefficient, F_{ijk} representing the magnitude of the aberration term. These latter components are given by

$$F_{ijk} = M_{ijk} + (m\lambda/\lambda_0) H_{ijk} \qquad (1.7)$$

Since M_{ijk} is a coefficient related to the mounting conditions of the grating, it is present for both grating types. However, the coefficient H_{ijk} specifically arises through the recording parameters and thus contributes to the final light path function only for holographic concave gratings. Expressions for the two components of the aberration coefficient are defined in terms of the mounting parameters $(\rho, \alpha, z, \rho', \beta, z')$ and the recording parameters $(\rho_C, \gamma, z_C, \rho_D, \delta, z_D)$

where

$$M_{ijk} = f_{ijk}(\rho, \alpha, z) + f_{ijk}(\rho', \beta, z')$$
$$H_{ijk} = f_{ijk}(\rho_C, \gamma, z_C) - f_{ijk}(\rho_D, \delta, z_D) \qquad (1.8)$$

and $\rho = r/R, \quad \rho' = r'/R, \quad \rho_C = r_C/R, \quad \rho_D = r_D/R$

It should be noted that for concave gratings with constant spacing and straight grooves, that is to say conventionally ruled gratings, $H_{ijk}(\neq 100) = 0$ and $H_{100} = \lambda_0/\sigma$, where σ is the effective grating constant as defined by Noda et al.

The original light path function treats contributions to the final image arising from at most fourth order aberration terms. However, the author has extended the above procedure to consider aberration terms up to the sixth order such that the exponents obey the relation $i + j + k < 6$, to yield

$$\begin{aligned}
F = {} & F_{000} + \omega F_{100} + \left(\frac{\omega^2}{2R}\right) F_{200} + \left(\frac{\ell^2}{2R}\right) F_{020} + \left(\frac{\ell}{R}\right) F_{011} \\
& + \left(\frac{1}{2R}\right) F_{002} + \left(\frac{\omega^3}{2R^2}\right) F_{300} + \left(\frac{\omega\ell^2}{2R^2}\right) F_{120} + \left(\frac{\omega\ell}{R^2}\right) F_{111} \\
& + \left(\frac{\omega}{2R^2}\right) F_{102} + \left(\frac{\omega^4}{8R^3}\right) F_{400} + \left(\frac{\omega^2\ell^2}{4R^3}\right) F_{220} + \left(\frac{\omega^2\ell}{2R^3}\right) F_{211} \\
& + \left(\frac{\omega^2}{4R^3}\right) F_{202} + \left(\frac{\ell^4}{8R^3}\right) F_{040} + \left(\frac{\ell^2}{4R^3}\right) F_{022} + \left(\frac{1}{8R^3}\right) F_{004} \\
& + \left(\frac{\ell^3}{2R^3}\right) F_{031} + \left(\frac{\ell}{2R^3}\right) F_{013} + \left(\frac{\omega^5}{8R^4}\right) F_{500} + \left(\frac{\omega^3\ell^2}{4R^4}\right) F_{320} \\
& + \left(\frac{\omega^3\ell}{2R^4}\right) F_{311} + \left(\frac{\omega^3}{4R^4}\right) F_{302} + \left(\frac{\omega\ell^4}{8R^4}\right) F_{140} + \left(\frac{\omega\ell^2}{4R^4}\right) F_{122} \\
& + \left(\frac{\omega}{8R^4}\right) F_{104} + \left(\frac{\omega\ell^3}{2R^4}\right) F_{131} + \left(\frac{\omega\ell}{2R^4}\right) F_{113} + \left(\frac{\omega^6}{16R^5}\right) F_{600} \\
& + \left(\frac{\omega^4\ell^2}{16R^5}\right) F_{420} + \left(\frac{\omega^4\ell}{8R^5}\right) F_{411} + \left(\frac{\omega^4}{16R^5}\right) F_{402} + \left(\frac{\omega^2\ell^4}{16R^5}\right) F_{240}
\end{aligned}$$

$$+ \left(\frac{\omega^2 \ell^2}{4R^5}\right) F_{222} + \left(\frac{\omega^2}{16R^5}\right) F_{204} + \left(\frac{\omega^2 \ell^3}{4R^5}\right) F_{231} + \left(\frac{\omega^2 \ell}{R^5}\right) F_{213}$$

$$+ \left(\frac{\ell^6}{16R^5}\right) F_{060} + \left(\frac{\ell^3}{2R^5}\right) F_{033} + \left(\frac{1}{16R^5}\right) + \left(\frac{\ell^4}{16R^5}\right) F_{042}$$

$$+ \left(\frac{\ell^2}{16R^5}\right) F_{024} + \left(\frac{\ell}{8R^5}\right) F_{015} + \left(\frac{\ell^5}{8R^5}\right) F_{051} \qquad (1.9)$$

Detailed mathematical expressions for the aberration terms appearing in the above equation are tabulated on the following pages. Each co-ordinate component is accompanied by an expression for the coefficient f_{ijk}. The displayed form of this coefficient corresponds to the incident ray and consequently is defined in terms of the instrumental parameters (ρ, α, z). Combining Eq. (1.8) for the diffracted ray and the two recording sources, with Eq. (1.7) enables evaluation of the aberration coefficient F_{ijk}. Comprehension of the manner in which each term influences the distortion of the spectral image is aided through the illustration of contours of constant wavefront aberration. For the calculation of these contours not only is it assumed that the recording sources are situated on the xy plane, but similarly it is assumed that the illumination source on the entrance slit occurs in this plane. Contributions are considered only from the co-ordinate component $\omega^i \ell^j$, therefore, for aberration terms having non-zero k, the effect of the height of the diffracted ray is neglected. Finally, employing a similar method to that of Welford [1.32] and ignoring variations with z', it is possible to use a broad analysis to categorize each aberration term. If the wavefront has two planes of symmetry it is defined to be astigmatic. However, if there is only one plane of symmetry, the aberration is coma-like. This latter aberration type can be further classified depending upon

the plane of symmetry. Symmetry in the sagittal plane corresponds to sagittal coma and similarly with tangential coma. Several wavefronts have no planes of symmetry and hence have been categorized as complex.

It is interesting to note that there is no aberration term equivalent to the traditional spherical aberration. In the derivation of this light path function all numerical terms have been expanded to the fullest extent. A term describing primary spherical aberration can be reconstructed, however, little is gained from this exercise since it destroys the simplicity of the light path function and causes the elimination of aberrations to be less successful.

In this section, a light path function for holographic diffraction gratings has been outlined and the format of each aberration term discussed. However, since this function contains a complete mathematical description of the behaviour of the concave grating, it warrants further investigation, as do the properties of several low order aberration terms.

1.5.3 *Discussion of aberration terms*

Application of Fermat's principle

$$\frac{\partial F}{\partial \omega} = 0 \qquad \text{and} \qquad \frac{\partial F}{\partial \ell} = 0 \tag{1.10}$$

to the light path function for the sufficient case where $z = 0$, yields

$$[\lambda_0/(\sin\delta - \sin\gamma)]\,(\sin\alpha + \sin\beta) = m\lambda \tag{1.11}$$

Here, the expression $\lambda_0/(\sin\delta - \sin\gamma)$ describes what Noda et al have called the "effective" grating constant. The period is not constant across the surface of the concave grating since the groove spacing varies with n in accordance with Eq. (1.4). Then, we have

Co-ordinate expression	Coefficient $f_{ijk}(\rho, \alpha, z)$	Contours of wavefront aberration	Aberration type
	$F_{000} = r$		
ω	$F_{100} = -\sin\alpha$	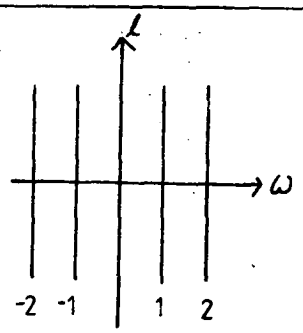	Sagittal coma
$\frac{\omega^2}{2R}$	$f_{200} = \cos\alpha\ (\rho\ \cos\alpha - 1)$	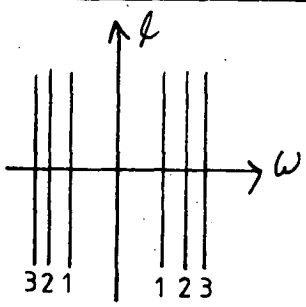	Astigmatism
$\frac{\ell^2}{2R}$	$f_{020} = \rho - \cos\alpha$	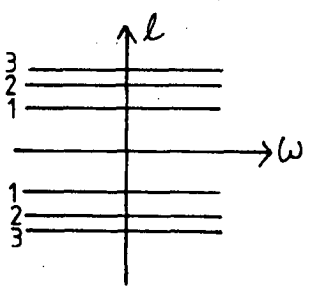	Astigmatism
$\frac{\ell}{R}$	$f_{011} = -\rho z$	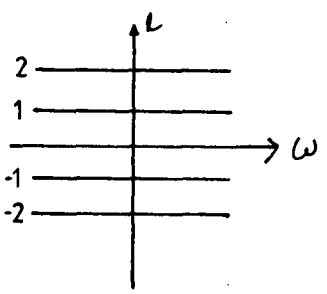	Tangential coma

Co-ordinate expression	Coefficient $f_{ijk}(\rho, \alpha, z)$	Contours of wavefront aberration	Aberration type
$\frac{1}{2R}$	$f_{002} = \rho z^2$		
$\frac{\omega^3}{2R^2}$	$f_{300} = \rho \sin\alpha \; f_{200}(\rho,\alpha,z)$	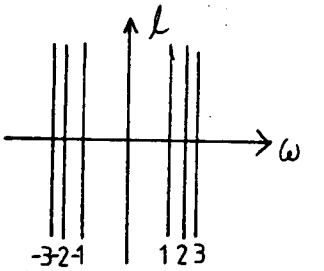	Sagittal coma
$\frac{\omega\ell}{R^2}$	$f_{111} = -\rho^2 \sin\alpha \; z$	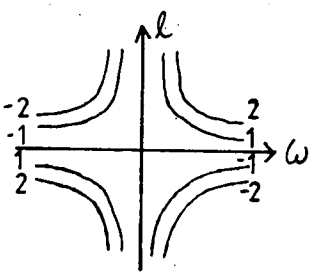	Complex
$\frac{\omega\ell^2}{2R^2}$	$f_{120} = \rho \sin\alpha \; f_{020}(\rho,\alpha,z)$	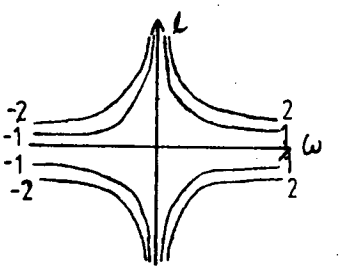	Sagittal coma
$\frac{\omega}{2R^2}$	$f_{102} = \rho^2 \sin\alpha \; z^2$	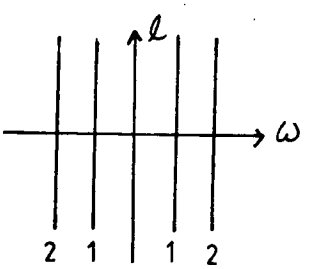	Astigmatism

Co-ordinate expression	Coefficient f_{ijk} (ρ, α, z)	Contours of wavefront aberration	Aberration type
$\frac{\omega^4}{8R^3}$	$f_{400} = f_{020} - \rho f_{200} (f_{200} - 4\rho\sin^2\alpha)$	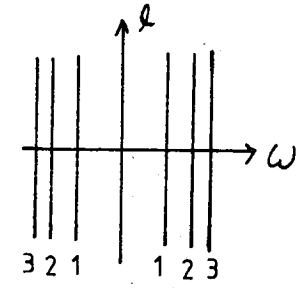	Astigmatism
$\frac{\omega^2\ell^2}{4R^3}$	$f_{220} = f_{020} + \rho f_{020} (2\rho\sin^2\alpha - f_{200})$	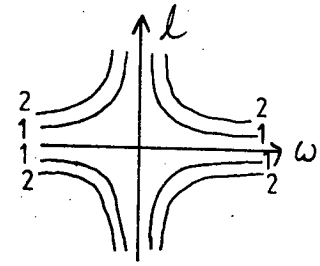	Astigmatism
$\frac{\omega^2\ell}{2R^3}$	$f_{211} = (\rho^2 f_{200} - 2\rho^3\sin^2\alpha)\, z$	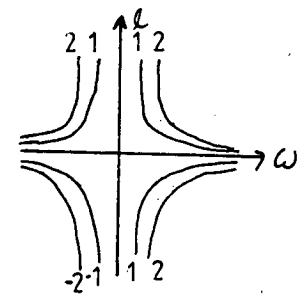	Tangential coma
$\frac{\omega^2}{4R^3}$	$f_{202} = - f_{211}\, z$	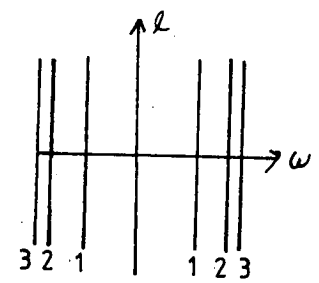	Astigmatism
$\frac{\ell^4}{8R^3}$	$f_{040} = f_{020} - \rho(f_{020})^2$	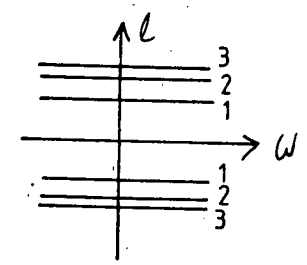	Astigmatism

Co-ordinate expression	Coefficient $f_{ijk}(\rho, \alpha, z)$	Contours of wavefront aberration	Aberration type
$\frac{\ell^2}{4R^3}$	$f_{022} = -\rho^2(2\rho+f_{020})z^2$	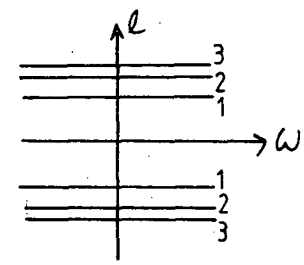	Astigmatism
$\frac{\ell^3}{2R^3}$	$f_{031} = \rho^2 f_{020}\, z$	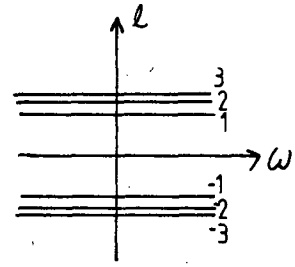	Tangential coma
$\frac{\ell}{2R^3}$	$f_{013} = \rho^3 z^3$	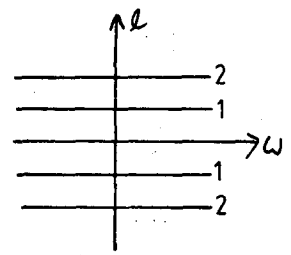	Astigmatism
$\frac{1}{8R^3}$	$f_{004} = -\rho^3 z^4$		
$\frac{\omega^5}{8R^4}$	$f_{500} = \rho\sin\alpha[f_{020}+\rho f_{200}(4\rho\sin^2\alpha-3f_{200})]$	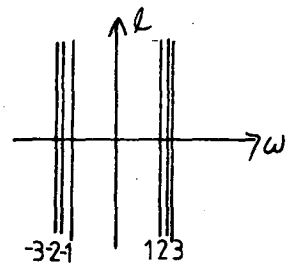	Sagittal coma

Co-ordinate expression	Coefficient f_{ijk} (ρ, α, z)	Contours of wavefront aberration	Aberration type
$\frac{\omega^3 \ell^2}{4R^4}$	$f_{320} = \rho \sin\alpha \, f_{020} (2\rho^2 \sin^2\alpha + 1 - 3\rho f_{200})$	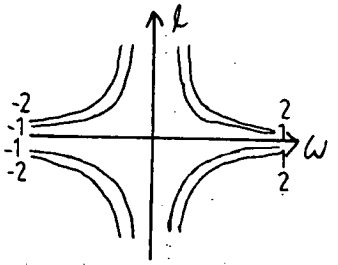	Sagittal coma
$\frac{\omega^3 \ell}{2R^4}$	$f_{311} = \rho^3 \sin\alpha (3f_{200} - 2\rho \sin^2\alpha) z$	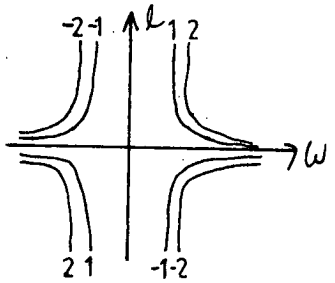	Complex
$\frac{\omega^3}{4R^4}$	$f_{302} = \rho^3 \sin\alpha (2\rho \sin^2\alpha - 3f_{200}) z^2$	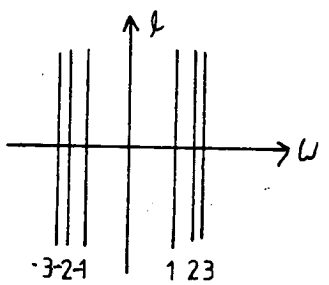	Sagittal coma
$\frac{\omega \ell^4}{8R^4}$	$f_{140} = \rho \sin\alpha \, f_{020} (1 - 3\rho)$	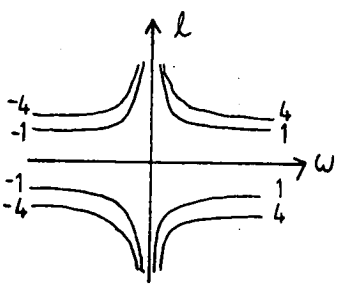	Sagittal coma
$\frac{\omega \ell^2}{4R^4}$	$f_{122} = -3 \sin\alpha \, o^3 (2\rho - f_{020}) z^2$	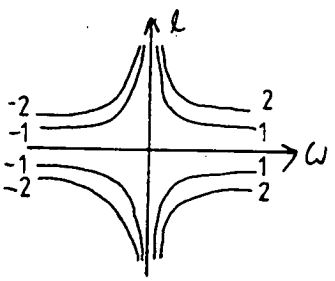	Sagittal coma

Co-ordinate expression	Coefficient f_{ijk} (ρ, α, z)	Contours of wavefront aberration	Aberration type
$\frac{\omega}{8R^4}$	$f_{104} = -3\rho^4 \sin\alpha\ z^4$	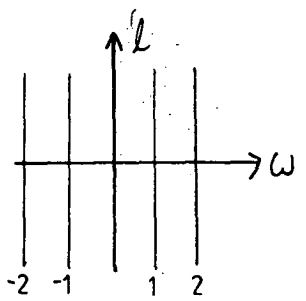	Sagittal coma
$\frac{\omega\ell^3}{2R^4}$	$f_{131} = 3\rho^3 \sin\alpha\ f_{020}\ z$	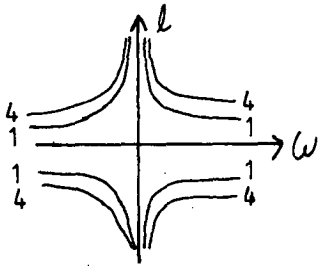	Astigmatism
$\frac{\omega\ell}{2R^4}$	$f_{113} = 3\rho^4 \sin\alpha\ z^3$	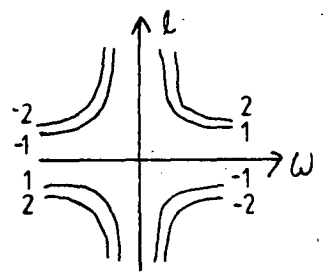	Complex
$\frac{\omega^6}{16R^5}$	$f_{600} = [\rho^2 f_{200} (8\rho^2 \sin^4\alpha - 12\rho \sin^2\alpha\ f_{200} + f_{200}^2) + f_{020}(2\rho^2 \sin^2\alpha + 1 - \rho\ f_{200})]$	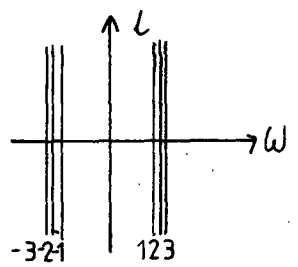	Sagittal coma
$\frac{\ell^6}{16R^5}$	$f_{060} = f_{020}\ (1 - \rho f_{020} + \rho^2 f_{020}^2)$	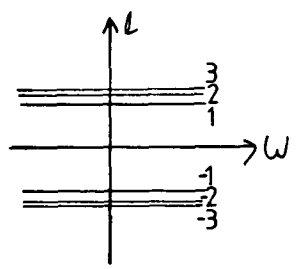	Tangential coma

Co-ordinate expression	Coefficient $f_{ijk}(\rho, \alpha, z)$	Contours of wavefront aberration	Aberration type
$\frac{1}{16R^5}$	$f_{006} = \rho^5 z^6$		
$\frac{\omega^2 \ell^4}{16R^5}$	$f_{240} = f_{020}(2\rho^2\sin^2\alpha + 3 - 12\rho^3\sin^2\alpha\, f_{020} - \rho f_{200} - 2\rho\, f_{020} + 3\rho^2\, f_{020}\, f_{200})$	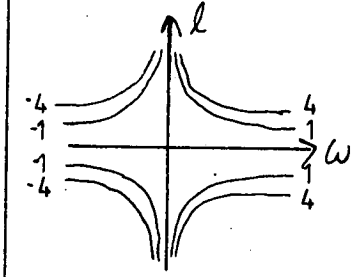	Sagittal coma
$\frac{\omega^4 \ell^2}{16R^5}$	$f_{420} = f_{020}(8\rho^4\sin^4\alpha + 3 + 4\rho^2\sin^2\alpha - 2\rho f_{200} - 24\rho^3\, f_{200}\sin^2\alpha)$	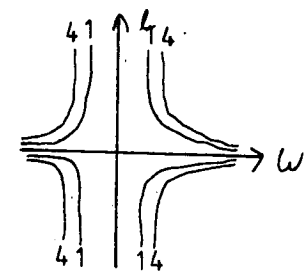	Astigmatism
$\frac{\omega^4}{16R^5}$	$f_{402} = \rho^2(8\rho^3\sin^4\alpha - 24\rho^2\sin^2\alpha\, f_{200} - f_{020} + 3\rho\, f_{200}^2)z^2$	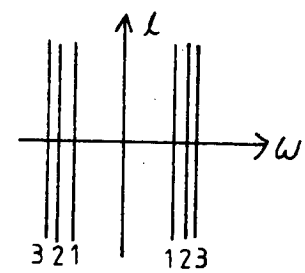	Astigmatism
$\frac{\omega^2}{16R^5}$	$f_{204} = 3\rho^4(-4\rho\sin\rho\alpha + f_{200})\, z^4$	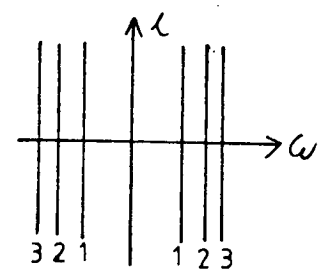	Astigmatism

Co-ordinate expression	Coefficient $f_{ijk}(\rho, \alpha, z)$	Contours of wavefront aberration	Aberration type
$\frac{\omega^2 \ell^2}{8R^5}$	$f_{222} = \rho^2(6\rho^2 f_{200} - 6\rho^3 \sin^2\alpha - 12\rho^2 \sin^2\alpha f_{020} - f_{020}) z^2$	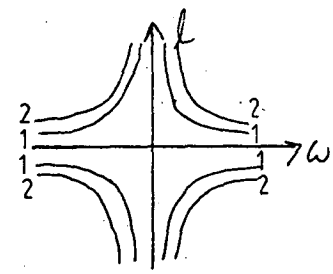	Astigmatism
$\frac{\omega^4 \ell}{8R^5}$	$f_{411} = \rho^2 (f_{020} - 8\rho^3 \sin^4\alpha - 3\rho f_{200}^2 + 24\rho^2 \sin^2\alpha f_{200}) z$	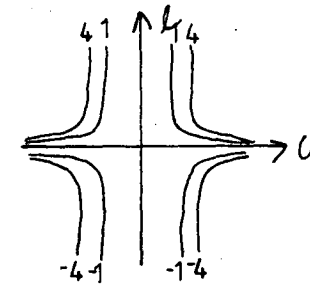	Tangential coma
$\frac{\ell^4}{16R^5}$	$f_{042} = \rho^2 f_{020}(12\rho^2 + 3\rho f_{020} - 1) z^2$	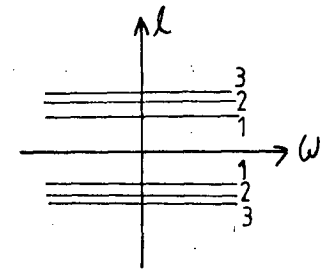	Astigmatism
$\frac{\ell^2}{16R^5}$	$f_{024} = 3\rho^4(f_{020} + 4\rho) z^4$	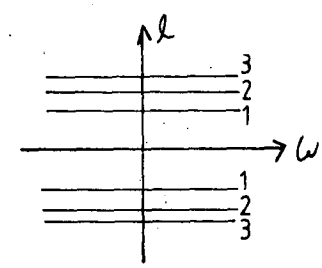	Astigmatism
$\frac{\ell^5}{8R^5}$	$f_{051} = \rho^2 f_{020} (1 - 3\rho f_{020}) z$	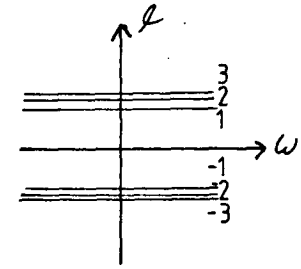	Tangential coma

Co-ordinate expression	Coefficient $f_{ijk}(\rho, \alpha, z)$	Contours of wavefront aberration	Aberration type
$\frac{\ell}{8R^5}$	$f_{015} = -3\rho^5 z^5$	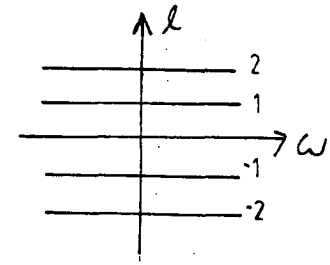	Tangential coma
$\frac{\omega^2\ell}{2R^5}$	$f_{213} = 3\rho^5 \sin\alpha\, z^3$	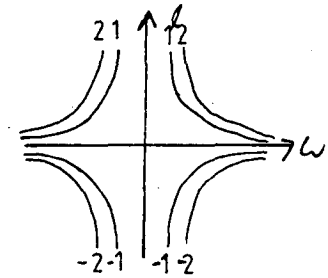	Tangential coma
$\frac{\omega^2\ell^3}{4R^5}$	$f_{231} = \rho^2 f_{020}(12\rho^2\sin^2\alpha + 1)z$	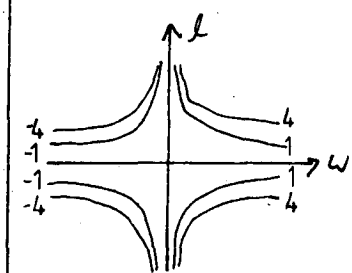	Sagittal coma
$\frac{\ell^3}{2R^5}$	$f_{033} = -\rho^5 z^3$	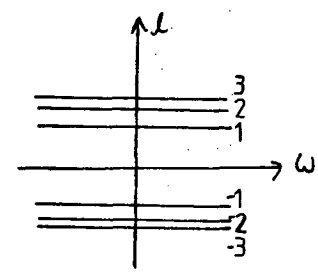	Tangential coma
$\frac{1}{16R^5}$	$f_{006} = \rho^5 z^6$		

$$\sin\delta - \sin\gamma = \lambda_0/\sigma > 0 \tag{1.12}$$

describing the relation between the formation of the grating and the angular placement of the recording sources, and

$$\sin\alpha + \sin\beta = m\lambda/\sigma \tag{1.13}$$

which is the traditional grating equation.

The horizontal focal curve which represents the position of the sagittal focal line is obtained when $F_{200} = 0$, that is

$$\cos\alpha(\rho\cos\alpha-1)+\cos\beta(\rho'\cos\beta-1)+\frac{m\lambda}{\lambda_0}[\cos\gamma(\rho_C\cos\gamma-1)-\cos\delta(\rho_D\cos\delta-1)] = 0 \tag{1.14}$$

Similarly, the vertical focal curve, representing the tangential focal line occurs for $F_{020} = 0$, where

$$(\rho-\cos\alpha) + (\rho'-\cos\beta) + \frac{m\lambda}{\lambda_0}[(\rho_C-\cos\gamma) - (\rho_D-\cos\delta)] = 0 \tag{1.15}$$

To a first approximation, the coefficient F_{200} determines the horizontal width of the final image. Therefore, to achieve maximum resolution for a monochromator, it is extremely important that the contribution from this term be small. In fact the minimization of this term is usually one of the optical instrument designer's initial considerations. The remaining significant second order term $F_{020}\frac{\ell^2}{2R}$ is referred to as second order astigmatism. Just as the value of the coefficient F_{200} governs the width of the image, it will be demonstrated later that this term controls the height of the final image. Since elongation of the image results in loss of intensity, this term should similarly be small for monochromators.

The third order term $F_{300}\frac{\omega^3}{2R^2}$ represents coma in the direction perpendicular to the length of the grooves. For a monochromator corrected for coma or astigmatism it is desired that the contributions to the final image from this term should be small. Similarly, third order z-axis coma is typified by $F_{120}\frac{\omega\ell^2}{2R^2}$. The significance and nature of this aberration term is dependent upon the magnitude of the second order astigmatism. In the presence of reduced astigmatism, this term can be combined with $F_{300}\frac{\omega^3}{2R^2}$, to describe the ordinary Seidel coma. However, Beutler [1.33] illustrated that for an image extended by astigmatism the co-ordinate expression $\omega\ell^2$ produces a curvature of the spectral line.

The two fourth order coefficients, F_{400} and F_{040}, describe the magnitudes of higher order horizontal and vertical focus terms respectively. Finally, in the presence of large astigmatism, the term $F_{220}\frac{\omega^2\ell^2}{4R^3}$, is equivalent to a change of focus along the spectrum line, similar to Seidel field curvature.

Armed with the knowledge of the significance of the low order terms it becomes imperative to control the influence which these terms have on the quality of the final spectral image. It has been known since Rowland first discussed the idea of concave gratings, that aberrations can be eliminated completely from the final image. Inspection of the light path function demonstrates that for this to occur, the corresponding coefficient must be identically zero. Thus

$$F_{ijk} = M_{ijk} + \frac{m\lambda}{\lambda_0} \cdot H_{ijk} = 0 \qquad (1.16)$$

For a mechanically ruled concave grating this relation can only be achieved by manipulation of the instrument parameters to give

$$f_{ijk}(\rho, \alpha, z) + f_{ijk}(\rho', \beta', z') = 0 \qquad (1.17)$$

In contrast, for holographic gratings there is the additional degree of freedom introduced by the placement of the recording sources. The correct mounting of an appropriately designed concave grating results in the elimination of several aberrations for all scanning wavelengths. This is particularly apparent for the Rowland circle mount to be discussed in Chapter 5, where three magnitude coefficients vanish for all wavelengths.

Of course not all important aberration terms disappear from the light path function. However, a grating instrument can be mathematically designed to minimize the influence of a given aberration term over the required wavelength range. This is equivalent to imposing on $F_{ijk's}$ the condition

$$I_{ijk} = \int_{\theta_1}^{\theta_2} F_{ijk^2}(\rho, \rho', \alpha, \beta, \rho_C, \gamma, \rho_D, \delta)d\theta = \text{minimum} \quad (1.18)$$

where θ_1 and θ_2 are the angles of grating rotation corresponding to the scanning wavelength.

1.5.4 *Application of the geometric theory*

Now that a solution of the problem of describing the geometric imaging properties of the concave gratings has been presented, it becomes possible to extract maximum advantage from the additional freedom introduced to grating design by holographic techniques. In the subsequent chapters the light path function will be used to examine the influence which individual aberration terms have on the form of the final image. In particular, the magnitude of the second order astigmatism and third order coma, present for a Rowland circle mount is thoroughly investigated. An examination of image behaviour

with variations in the relative aperture of the optical systems, illustrates the control which these two low order aberration terms have over the image height. Hence, the fact that the light path function enables the design of instruments containing holographic concave gratings capable of the simultaneous elimination of both astigmatism and coma from the final image, clearly displays the significance of this theory.

Furthermore, by applying the aberration-minimizing procedure to the light path function, two new uni-axial monochromators are proposed. The design of both monochromators is beautifully simple. Scanning of the diffracted wavelengths is achieved through simultaneous rotation of the two optical elements - no translantion is necessary.

1.6 INTRODUCTION TO THESIS

The developments reported in this thesis fall naturally into two distinct categories. Chapters 2-4 are concerned primarily with plane gratings, while the work described in Chapters 5-7 concentrates on gratings generated on concave surfaces.

Chapter 2 describes the formation of the groove profiles of holographic diffraction gratings. Techniques for determining the profiles of such gratings are outlined, with reference to a set of four quasi-sinusoidal gratings generated by the author. A numerical study [1.34] of the spectral performance of blazed holographic gratings using the rigorous electromagnetic theories of Petit [1.35] and Bolomey [1.36] is presented. Several innovative Fourier synthesis procedures are evaluated, extending the work previously reported by I.J. Wilson and the author [1.37].

Part of the investigations of blazed gratings and Fourier synthesis of the exposing interference field is contained in the author's Honours' thesis [1.38].

An experimental study of the influence of a discontinuous surface conductivity on the energy absorbed by resonance anomalies is presented in Chapter 3. The efficiencies of ruled gratings are observed for coatings whose conductivity varies either along the groove profile (bi-metallic gratings) or perpendicular to the surface (conformally coated gratings).

The finite electromagnetic theory of Maystre [1.28] is employed in Chapter 4 to improve the performance of a dye laser through a knowledge of grazing incidence grating efficiencies. This study which was conducted in collaboration with I.J. Wilson and E.G. Loewen, was reported in a paper published in Applied Optics [1.39].

In Chapters 5-7 the geometric theory of Noda et al [1.30] has been used in the design of aberration-corrected gratings. Elimination of either primary astigmatism or primary coma or a combination of both from the final spectral image at two wavelengths is demonstrated for a Rowland circle mount. The solution to a set of simultaneous equations yields the appropriate mounting and recording parameters. The behaviour of the image height and magnitude of the individual light path terms, with relative aperture for aberration-corrected gratings under these conditions is investigated. Similarly, techniques for the minimization of the horizontal focus term, F_{200}, over a given wavelength range, are applied to the design of a new uni-axial, double concave grating monochromator.

Progress in the formulation of these design procedures has been guided by I.J. Wilson who initiated the study. Papers based on the work presented in Chapters 5 and 7 have been submitted to Optica Octa for publication.

REFERENCES

[1.1] Rittenhouse D. (1786) Trans. Amer. Phil. Soc., 2, 201.

[1.2] Fraunhofer J. von (1821/22) Denschr. Kgl. Akad. Wiss. München, 8, 1.

[1.3] Rowland H.A. (1882) Phil. Mag., 13, 469.

[1.4] Richelson A.A. (1912) Nature, 88, 362.

[1.5] Wood R.W. (1924) Phil. Mag., 48, 497.

[1.6] Strong J. (1936) Phys. Rev., 49, 296.

[1.7] Harrison G.R. and Stroke G.G. (1955) J. Opt. Soc. Amer., 45, 112.

[1.8] Michelson A.A. (1927) Studies in Optics 3rd edn. (Chicago: Chicago UP), 104.

[1.9] Schmahl G. and Rudolph D. (1968) Mitt. Astr. Ges., 24, 41.

[1.10] Labeyrie A. and Flamand J. (1969) Pitics Communications, 1, 5.

[1.11] Sheridon N.K. (1968) Appl. Phys. Letters, 12, 316.

[1.12] Petit R. and Maystre D. (1972) Rev. Phys. Appl., 1, 427.

[1.13] Maystre D. and Petit R. (1971) Optics Commun., 4, 25.

[1.14] Hutley M.C. (1973) Optica Acta, 20, 607.

[1.15] Hutley M.C. and Bird V.M. (1973) Optica Acta, 20, 771.

[1.16] Wood R.W. (1902) Phil. Mag., 4, 396.

[1.17] Rowland H.A. (1893) Phil. Mag., 35, 397.

[1.18] Hatcher R.D. and Rohrbaugh J.H. (1956) J. Opt. Soc. Amer., 46, 104.

[1.19] Madden R.P. and Strong J. (1958) in "Concepts of Classical Optics", 597 (San Francisco: W.H. Freeman and Company).

[1.20] Janot C. and Hadni A. (1962) J. Physique Rad., 23, 152.

[1.21] Rayleigh Lord, (1907) Proc. Roy. Soc. A, 79, 399.

[1.22] Lippman B.A. (1953) J. Opt. Soc. Amer., 43, 408.

[1.23] Petit R. and Cadilhac M. (1966) C.R. Acad. Sci. Paris, 262, 468.

[1.24] Petit R. and Cadilhac M. (1967) C.R. Acad. Sci. Paris, 264, 1441.

[1.25] Pavageau J. and Bousquet J. (1970) Optica Acta, 17, 469.

[1.26] Hutley M.C. and Maystre D. (1976) Opt. Commun., 19, 431.

[1.27] Vanden Berg P.M. (1971) Thesis, Delft, Report No. 1971-16.

[1.28] Maystre D. (1972) Opt. Commun., 6, 50.

[1.29] Botten L.C. (1978) Optica Acta, 25, 481.

[1.30] Noda H., Namioka T. and Seya M. (1974) J. Opt. Soc. Amer., 64, 1031.

[1.31] Welford W.T. (1965) Progress in Optics IV (North-Holland Publishing Co., Amsterdam), p.241.

[1.32] Welford W.T. (1974) "Aberrations of the Symmetrical Optical System" (Academic Press), p.109.

[1.33] Beutler H.G. (1945) J. Opt. Soc. Amer., 35, 311.

[1.34] Wilson I.J. and Brown B.J. (1977) Optics Communications, 20, 418.

[1.35] Petit R. (1966) Rev. Opt., 45, 249.

[1.36] Bolomey J.C. (1971) Thèse No. A05604.

[1.37] Wilson I.J. and Brown B.J. (1976) University of Tasmania Research Report OGRG 76/2.

[1.38] Brown B.J. (1976) University of Tasmania Honours Thesis (unpublished).

[1.39] Wilson I.J., Brown B.J. and Loewen E.G. (1979) Appl. Optics, 18, 426.

CHAPTER 2

PLANE HOLOGRAPHIC DIFFRACTION GRATING GROOVE PROFILES

2.1 PRELIMINARY COMMENTS

Since the groove profile dictates the distribution of incident light amongst the various diffracted orders, achievement of the high spectral performances predicted by rigorous electromagnetic theories require accurate recognition of the correct groove shape. Several techniques for the investigation of groove profiles have been suggested in the past [2.1-2.13]. Basically, the methods fall into three distinct categories.

(i) theoretical models of groove profile formation,

(ii) comparison of observed efficiencies with those predicted by theory,

(iii) actual physical inspection of the groove profile.

In this chapter, sinusoidal groove profile gratings manufactured in our laboratory at the University of Tasmania, are used to examine the effectiveness of the last two methods.

Application of a theoretical groove profile formation model to the production of blazed holographic gratings allows the evaluation of the spectral performance of such gratings. Furthermore, this groove formation model is used as an aid in the study of Fourier synthesis. The exposure of a photoresist layer to more than one set of interference beams represents an alternate avenue whereby the library of groove profiles may be extended.

2.2 SINUSOIDAL GROOVE PROFILE GRATINGS

2.2.1 *Experimental production of holographic gratings*

Displayed in Fig. (2.1) is a photograph of the experimental arrangement used by the author to generate holographic gratings from a sinusoidal intensity distribution. Basically, the interferometer is constructed from a beam splitter, two beam expanders and two collimating mirrors. Coherent light from the laser travels through a variable density beam splitter and is expanded by high quality microscope objectives. Any local irregularities in the beam intensity are effectively eliminated by a 5 μm pin-hole acting as a spatial frequency filter. Two 5^{o} off-axis parabolic mirrors of focal length 0.9 m collimate the expanded beams. The two resulting plane waves intersect in the vicinity of the grating blank. Temperature fluctuations and air movements along the interferometer arms are avoided by using a large insulating enclosure placed over all but the laser light source.

Following a thorough cleansing of an optically flat substrate, a 1 μm thick coating of Shipley AZ1350J photoresist is deposited by spinning it at 3,000 r.p.m. for 60 seconds. For the holographic gratings discussed here, the illuminating source was a Spectra Physics Model 164/03 Argon Ion laser, which has an output power of 200 mW at the exposing wavelength of 458 nm. Following exposure, the resist is developed by submergence in diluted Shipley AZ Developer Solution. The substrate is subsequently baked at a temperature of 95^{o}C. In order to obtain a reflection grating, a 1000 Å film of aluminium is evaporated onto the photoresist surface at a pressure of 5×10^{-6} TORR.

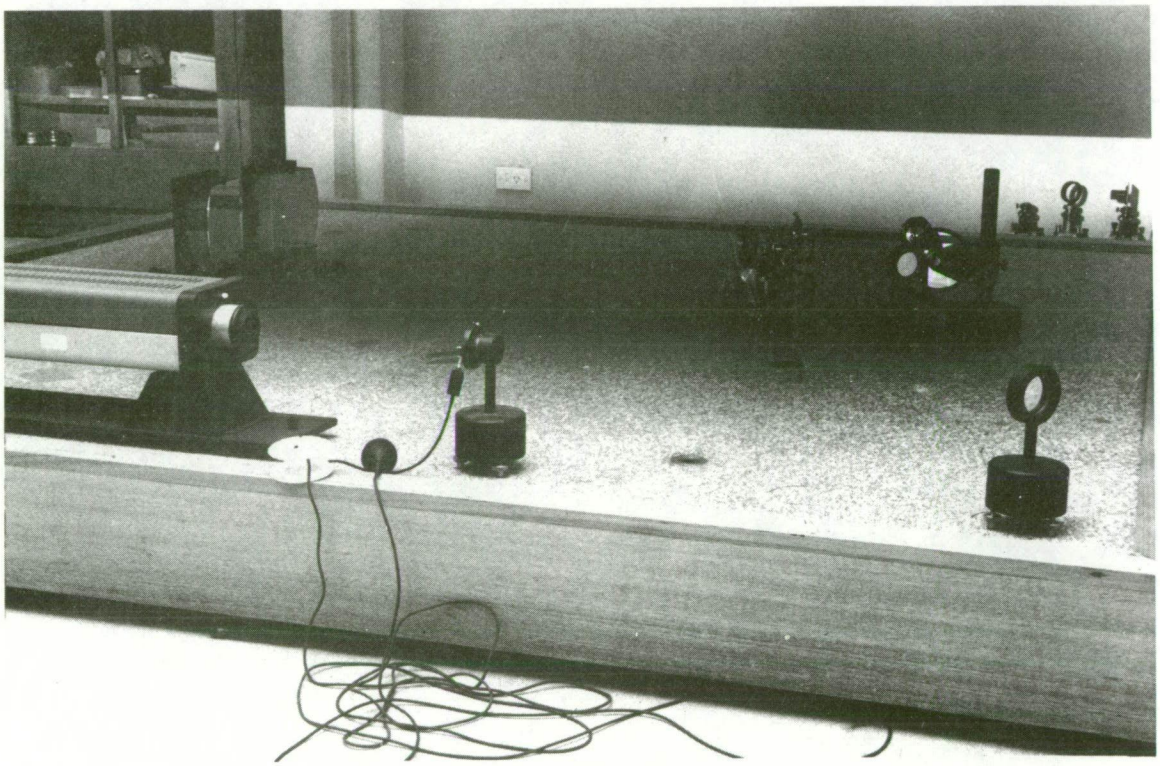

Fig.(2.1) Experimental arrangement for the production of holographic diffraction gratings having sinusoidal groove profiles.

To facilitate an investigation of the groove profiles generated by a sinusoidal intensity distribution, two groove profile determination techniques were applied to a set of holographic gratings manufactured in AZ13505J resist. Four gratings of groove frequency 1180 gr/mm, were produced by immersion in developer solution for 18 seconds following an exposure of 3-6 minutes duration. The observed efficiencies of the 1th diffracted order as a function of incidence angle for a constant wavelength of 633 nm are displayed in Fig. (2.2).

2.2.2 *Inspection of groove profile*

Verrill [2.14] and Palmer et al [2.15] have demonstrated the ease with which a Rank Precision Industries Talystep measures directly the surface profile of a grating. A diamond stylus is drawn across the surface of the groove and its vertical movement is converted to an electrical signal which can be displayed as a pen recorder trace. An example of this technique is shown in Fig. (2.3), reproduced from Verrill's paper. This method has the disadvantage of uncertainty in resolving the groove apex due to the finite tip.

An alternative instrument, which is used by the author, is the electron-microscope which has both the resolution and depth of focus required to evaluate groove profiles. However, its usefulness is governed by the proper presentation of specimens. Early work by Anderson et al [2.2] involved the evaporation of platinum past an asbestos whisker lying across the groove. The resulting shadow cast by the whisker is then used to determine the groove shape. An example is shown in Fig. (2.4).

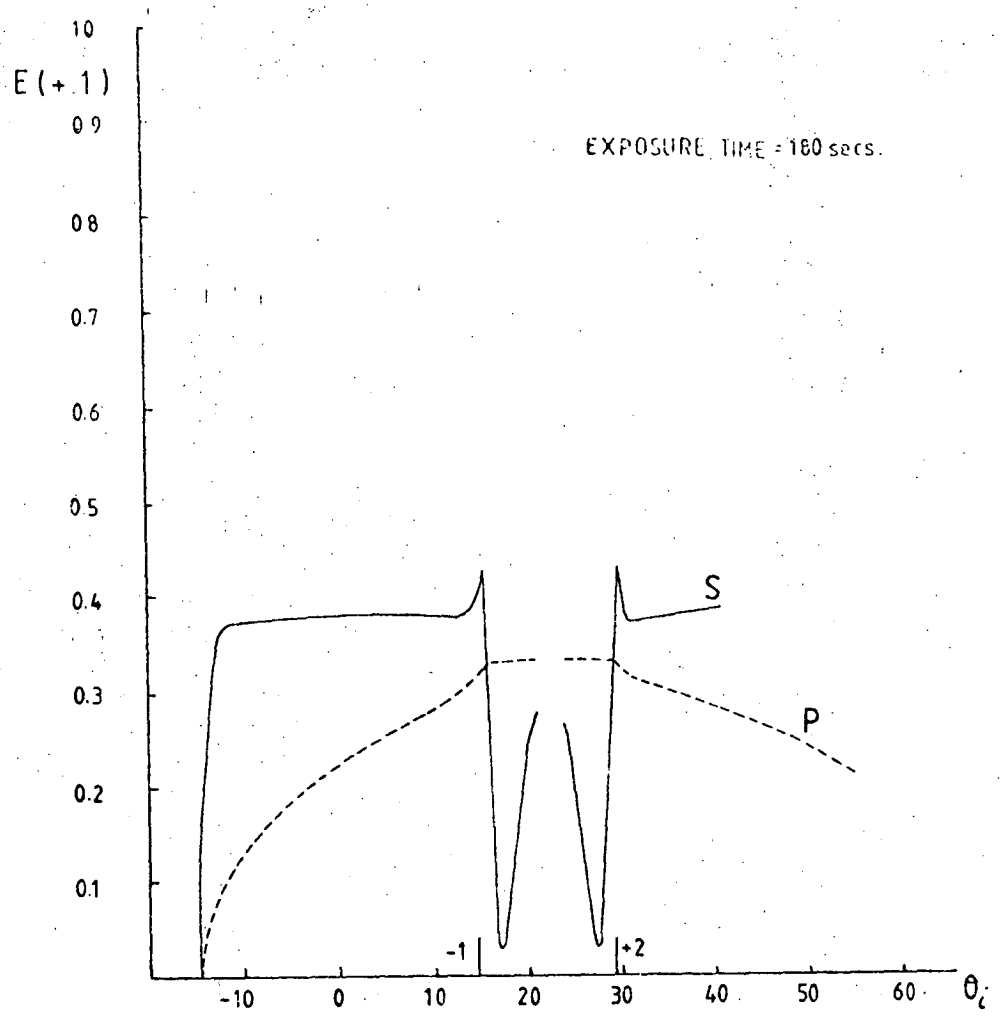

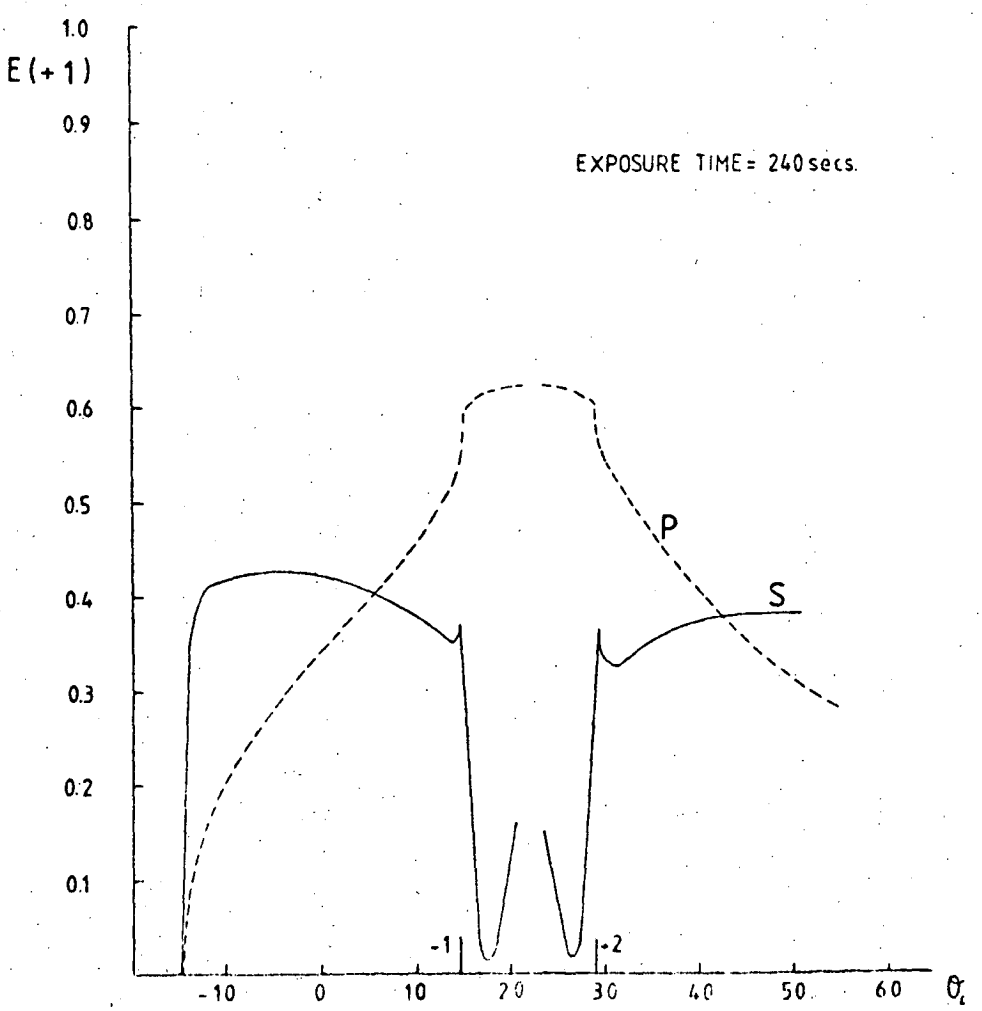

Fig.(2.2) Observed first order efficiencies corresponding to the gratings generated by the author.

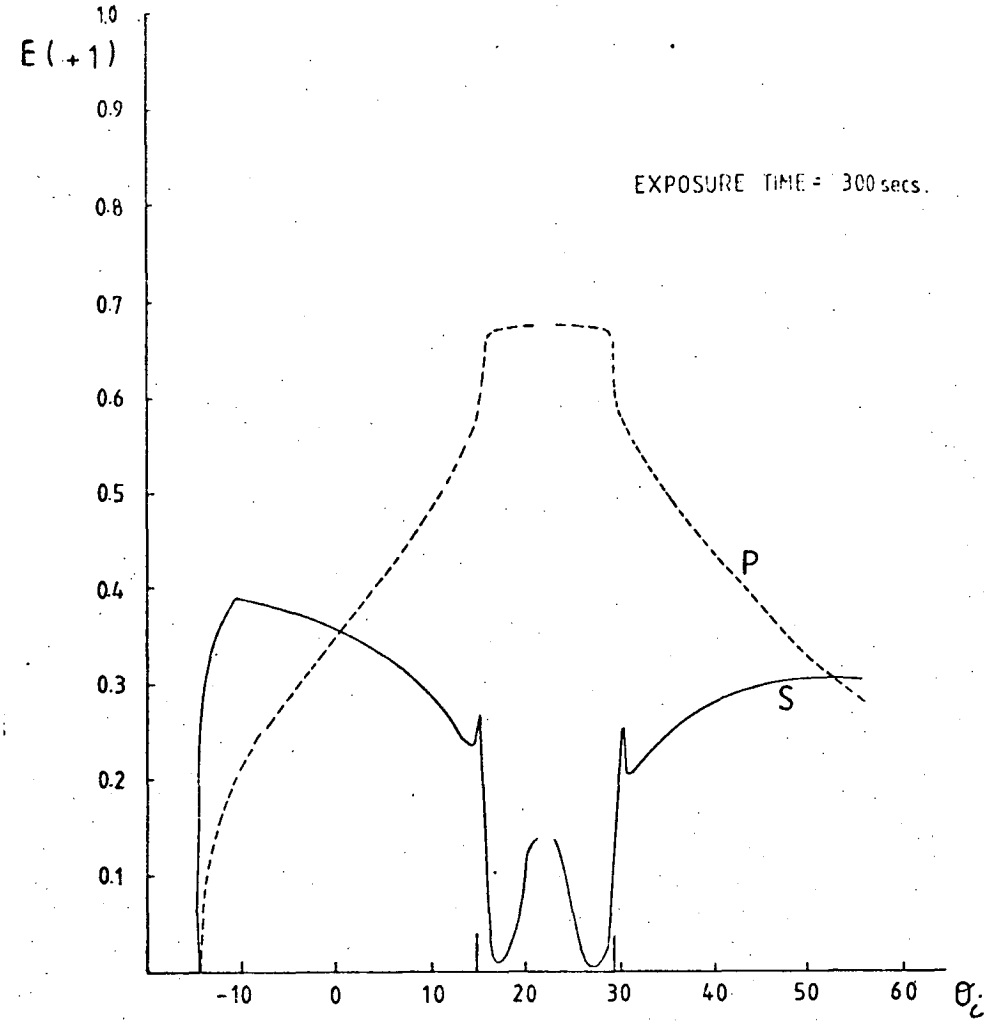

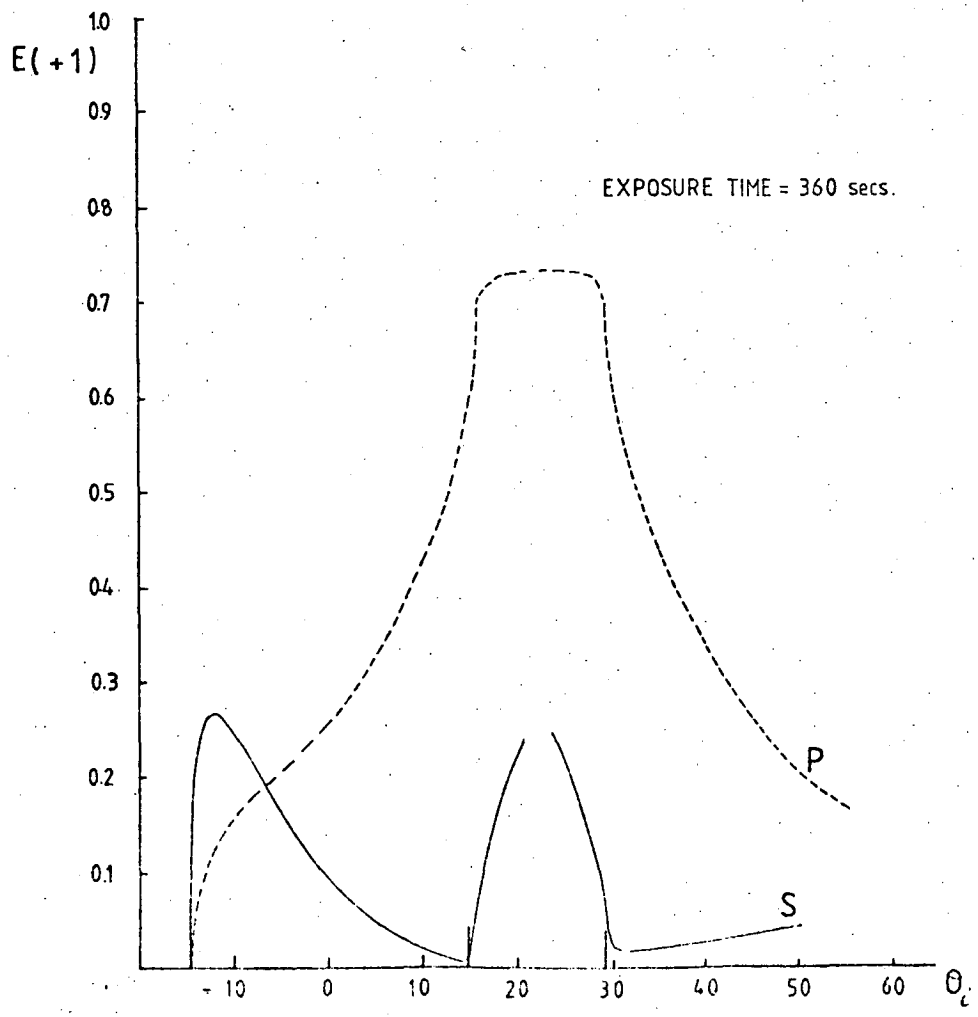

Fig. (2.2) - continued.

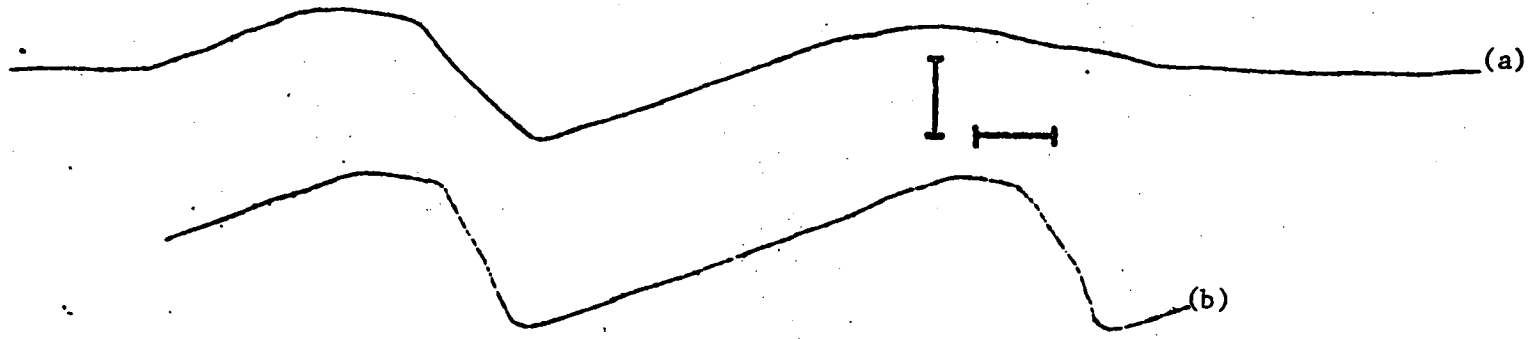

Fig.(2.3) Talystep traces of single (a) and consecutively ruled grooves (b) formed with ruling angles of 48·5° and 21·5°. The vertical and horizontal scales are 100 nm. (after Verrill, 1975).

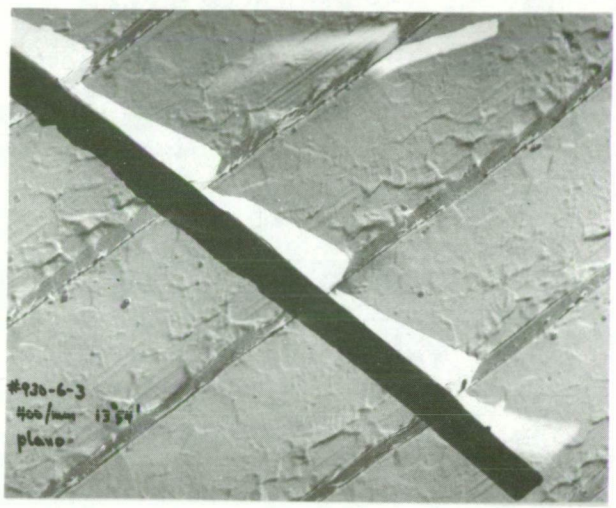

Fig.(2.4) An example of an electron-micrograph of a grating using asbestos whisker. Bausch and Lomb grating, blaze angle $13^{o}54'$, $400mm^{-1}$.

Although this process gives an indication of the surface quality of the grating, it can present a distorted view of the groove profile. A superior method is the inspection of a thin fragment of aluminium foil embossed with the surface relief of the grating. The technique of sample preparation followed by the author for the four holographic gratings mentioned previously, is described below. With a few minor variations it is that outlined by Bennett [2.3].

Several additional layers of aluminium are evaporated onto the grating surface. Then a piece of bare foil imprinted with the surface profile is created by peeling off the aluminium layer with scotch tape. This foil is carefully wrapped over a thin U-shaped slab of brass and attached by a few drops of a silver electroconductor cement. The grating foil acts as a shadow mask when inserted into the beam of the electron-microscope.

The electron-microscope allows an overall inspection of the grating surface as revealed by Fig. (2.5) which displays the surface irregularities of a holographic diffraction grating of groove frequency 1180 gr/mm, at 25,000X magnification. Electronmicrographs of the groove profiles corresponding to the four sinusoidal gratings appear in Fig. (2.6). Table (2.1) details the grating number, exposure time and the H/D value determined from repeated measurements of the groove depth. Here, the term H/D refers to the ratio of the peak-to-peak depth to the period of the grating.

Examination of the grating silhouettes indicates that not only do the size and shape of the consecutive grooves vary, but they deviate from the true sinusoidal form. This profile deformation is magnified in Fig. (2.7) through a comparison with sinusoidal curves of similar period and H/D ratio.

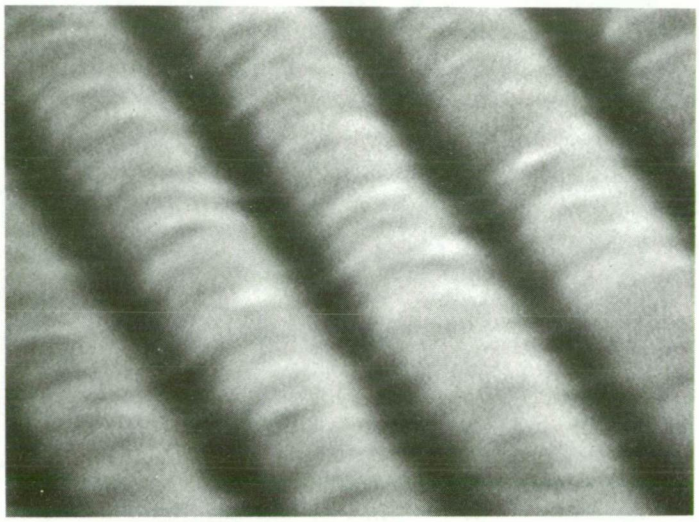

Fig. (2.5) Electron-micrograph illustrating surface irregularities of a sinusoidal groove surface, magnified 25,600x.

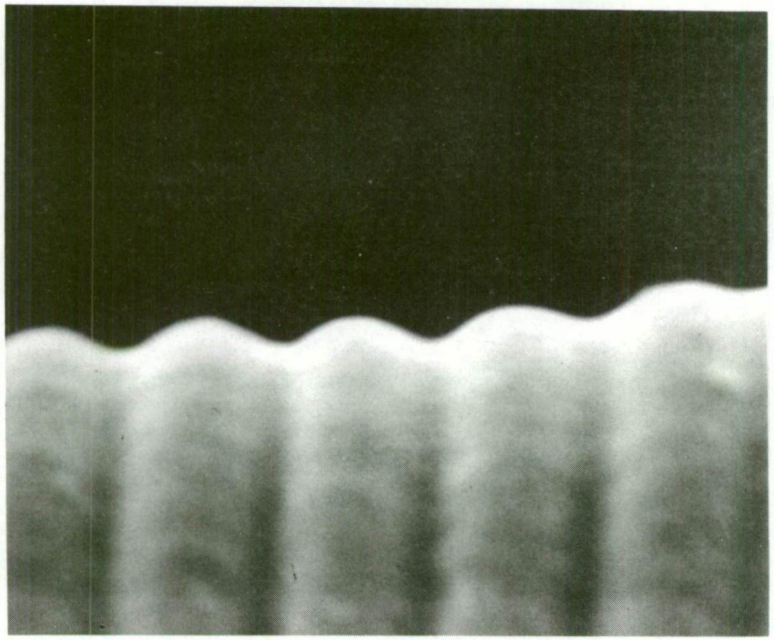

Grating No. 1.
Exposure Time = 180 secs.

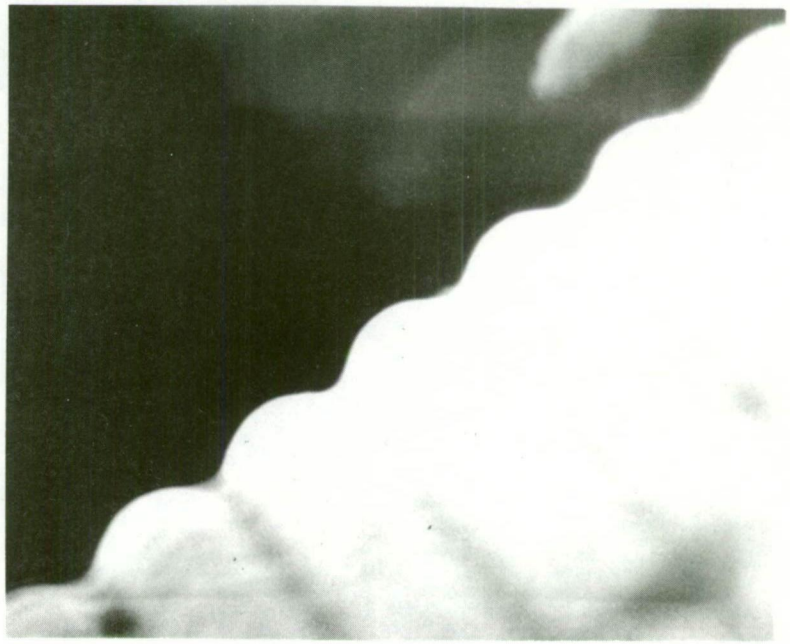

Grating No. 2.
Exposure Time = 240 secs.

Fig. (2.6a) Electron-micrographs at a magnification of 25,600x of groove profiles resulting from the exposure of photoresist to a sinusoidal intensity distribution.

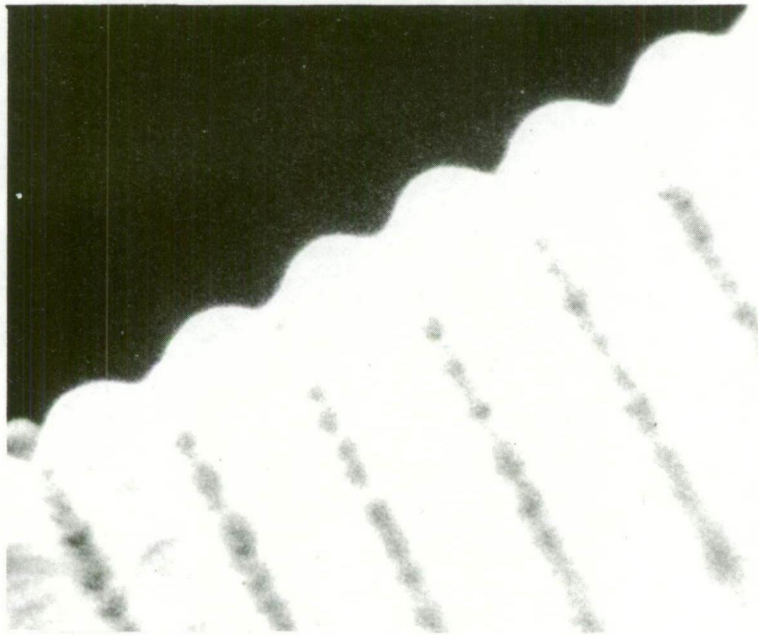

Grating No. 3.
Exposure Time = 300 secs.

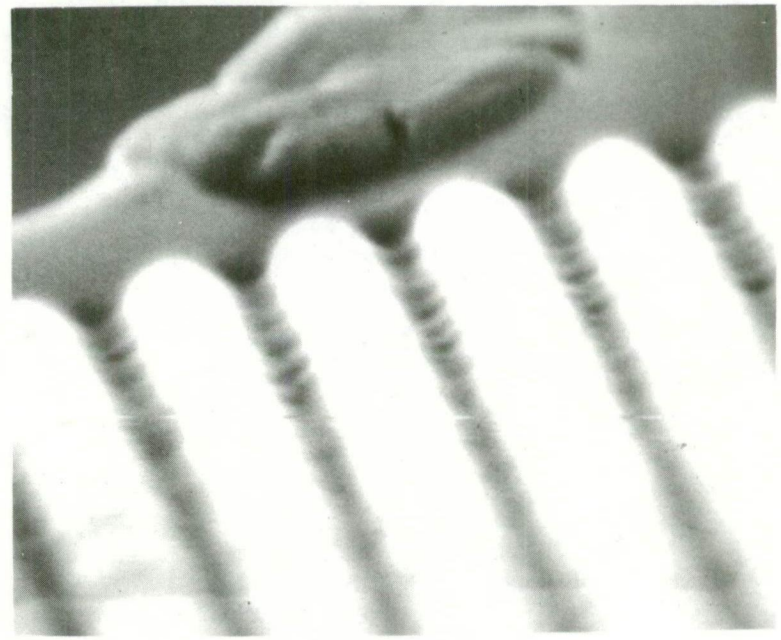

Grating No. 4.
Exposure Time = 360 secs.

Fig. (2.6b) Electron-micrographs at a magnification of 25,600x of groove profiles resulting from the exposure of photoresist to a sinusoidal intensity distribution.

Grating number	Exposure time (secs)	H/D from E.M.
1	180	0.154 ± 0.01
2	240	0.235 ± 0.01
3	300	0.247 ± 0.01
4	360	0.338 ± 0.01

TABLE (2.1) Details of the H/D values determined from the electronmicrographs for each of the four sinusoidal gratings.

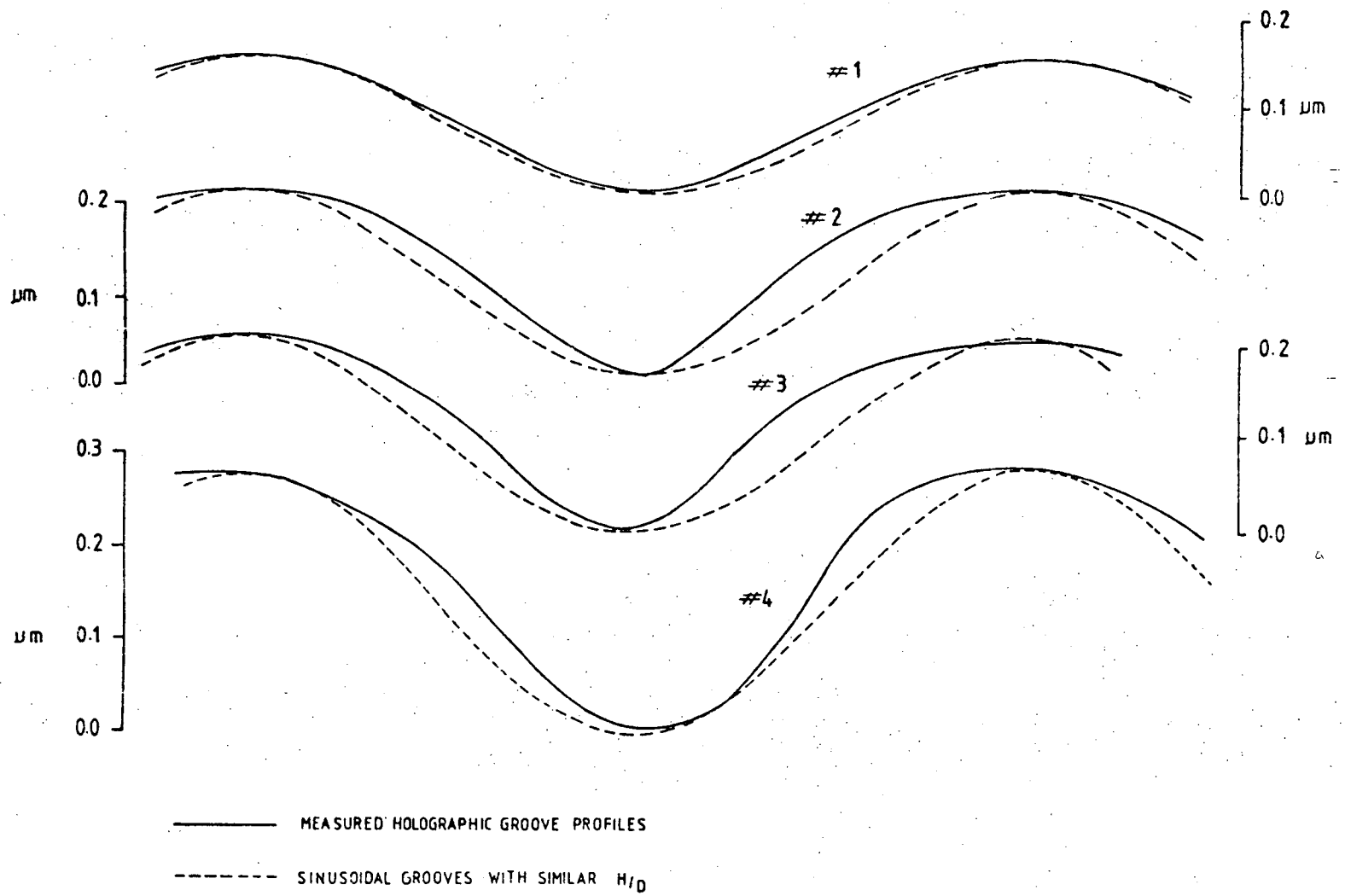

Fig. (2.7) Distorted groove profiles obtained from electron-micrographs of gratings generated by the author (————) compared to sinusoidal curves of similar H/D ratio (------).

The non-linearity of the exposure-development process for the photoresist, which is typified by rounded crests and steepened troughs, is clearly demonstrated by each groove profile. Furthermore, an asymmetric exposure field has produced non-symmetric groove profiles with the degree of distortion governed by the duration of the exposure.

The electron-microscope not only displays surface irregularities, but enables direct measurements of the depth and degree of distortion of the groove profile of a holographic grating to be made. Both features significantly control the production of high quality holographic gratings necessary to achieve the spectral performance predicted by theory. Clearly, successful manipulation of electron-microscope techniques represents a powerful tool in acquiring improved holographic gratings. A second, theoretical approach will now be employed to gather information on the groove profiles of the four sample gratings.

2.2.3 *Theoretical determination of groove depth*

In 1977 Wilson and Botten [2.16] described a technique for determining the groove depth of gratings having sinusoidal grooves, whereby absolute efficiencies measured using a laser are compared with numerical results. This method accurately determines the groove depth provided the efficiencies are observed under conditions where the spectral behaviour is most sensitive to variations in groove depth. Wilson et al chose two mounts: the Littrow +1, where the 0^{th} order efficiency is examined and the normal incidence mount where a first order beam is investigated. Measurements are determined for both planes of polarization.

The theoretical behaviour of the efficiency as a function of groove depth at the two important sampling angles is conveniently summarized in Fig. (2.8). The displayed curves correspond to sinusoidal gratings of groove frequency 1200 mm^{-1} and a testing wavelength of 633 nm.

Table (2.2) outlines the grating number and the corresponding ratio of H/D calculated from a comparison of the observed results with those displayed in Fig. (2.8). Appearing in Fig. (2.9) are the four observed efficiency curves and those numerically calculated for gratings having H/D values given in the above table. Agreement between the observed efficiency of grating #1 and the theoretical counterpart is excellent. The only discrepancy occuring for the S polarized light in the region of the +1 Littrow angle. As the duration of exposure lengthens to 4 minutes the equivalent theoretical groove depth approaches H/D = 0.25. The previous degree of agreement is not maintained, since the observed efficiency falls below its theoretical companion, particularly near the -1 and +2 Wood anomalies. Although minimal, this disparity signifies the commencement of a trend in which the spectral performance of the observed S polarized light deteriorates with increased exposure. For the extreme case of grating #4, correlation between theory and observation is very poor. Obviously, the increase in groove depth with duration of exposure is accompanied by a departure of the spectral performance away from that exhibited by a perfect sinusoidal groove grating. Similarly the unsymmetrical nature of the observed efficiencies indicate asymmetric groove profiles.

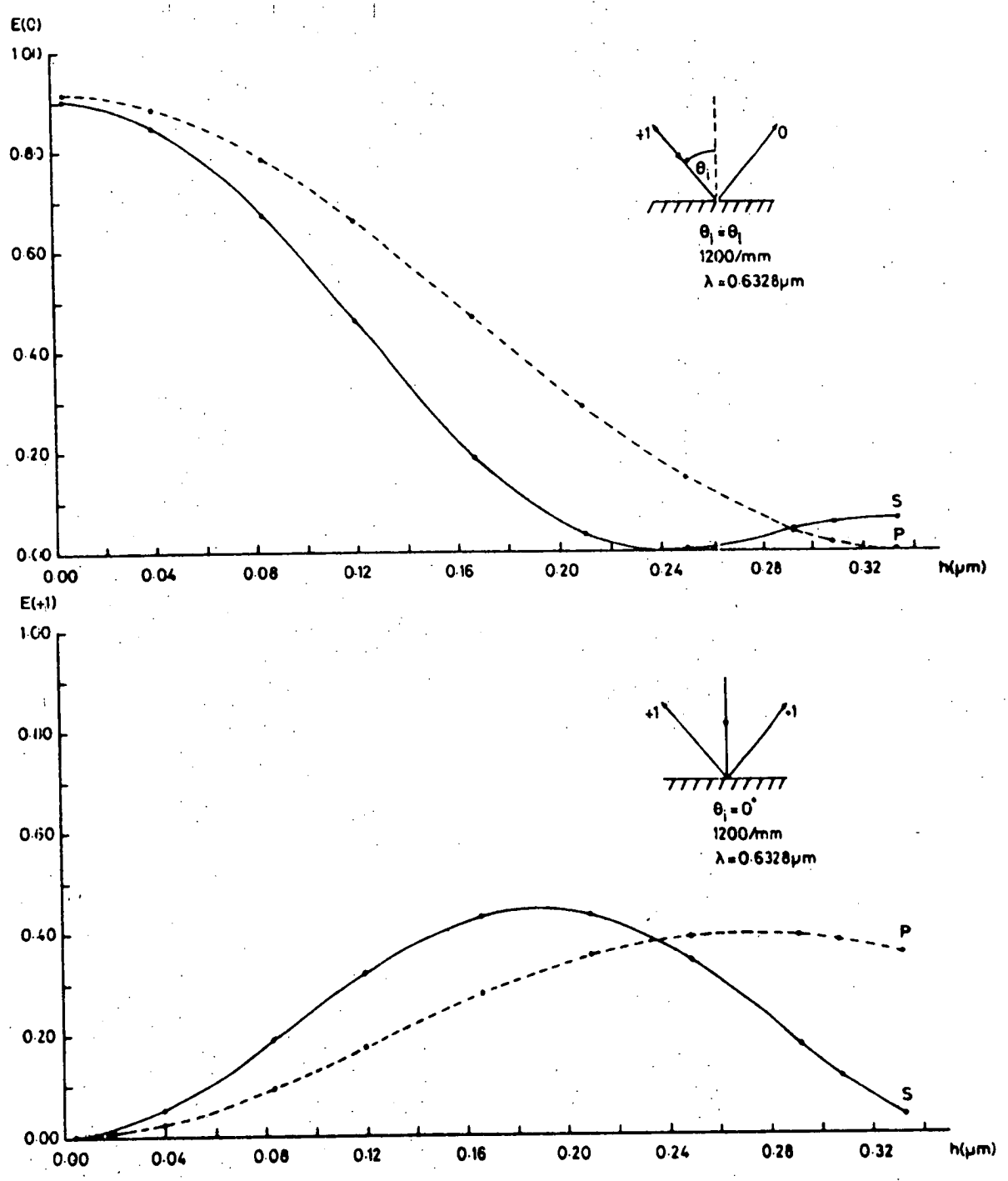

Fig.(2.8) Zero and first order efficiencies for the Littrow and normal incidence mounts as a function of groove depth, h. The gratings have evaporated aluminium surfaces, 1200 grooves/mm and the wavelength is 0.6328 μm. (After Wilson, 1977).

Grating number	Exposure time (secs.)	H/D (Wilson et al)
1	180	0.17 ± 0.01
2	244	0.25 ± 0.01
3	300	0.28 ± 0.01
4	360	0.30 ± 0.01

TABLE (2.2) Details of the H/D values determined from comparison with the theoretical efficiency curves of Wilson et al.

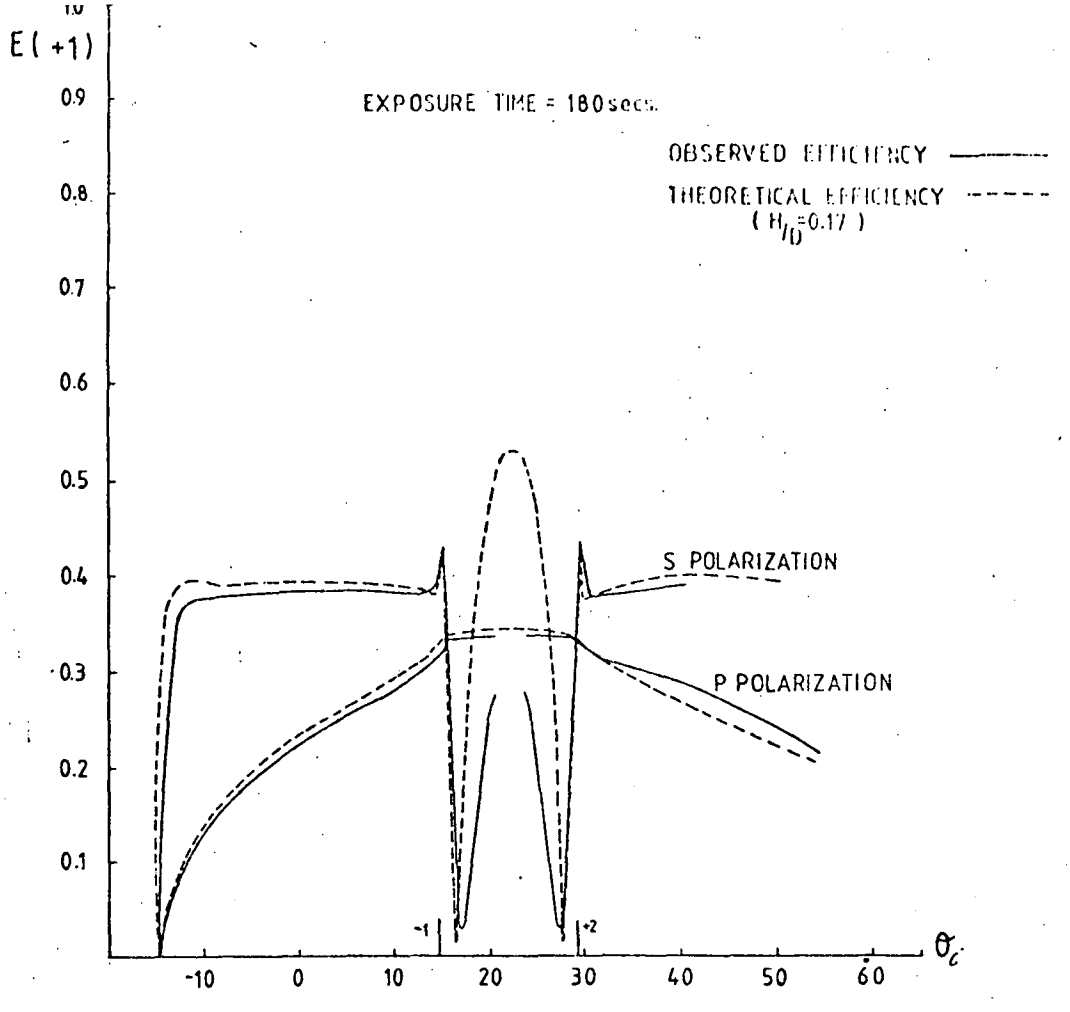

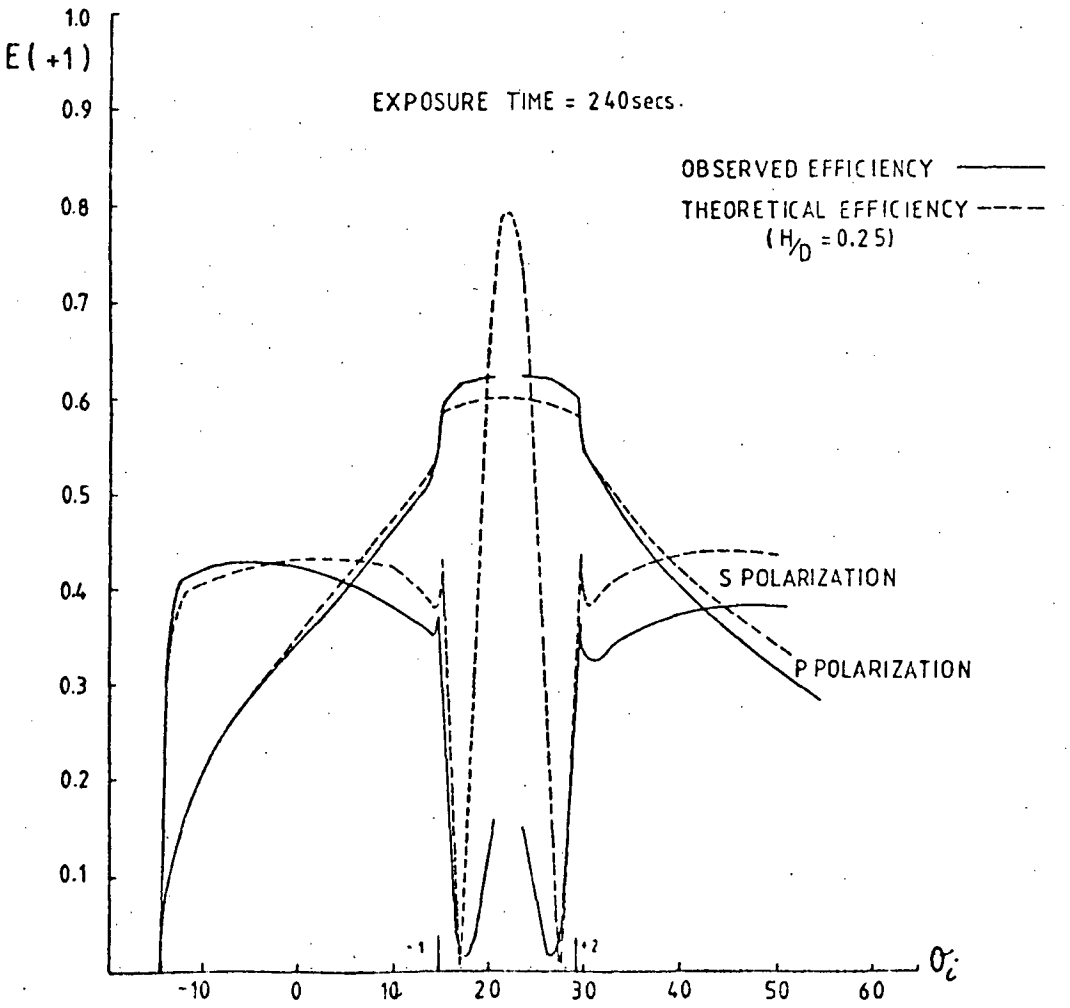

Fig.(2.9) Comparison of observed first order efficiencies (———) with those computed for grooves having sinusoidal profiles of similar H/D ratio (------).

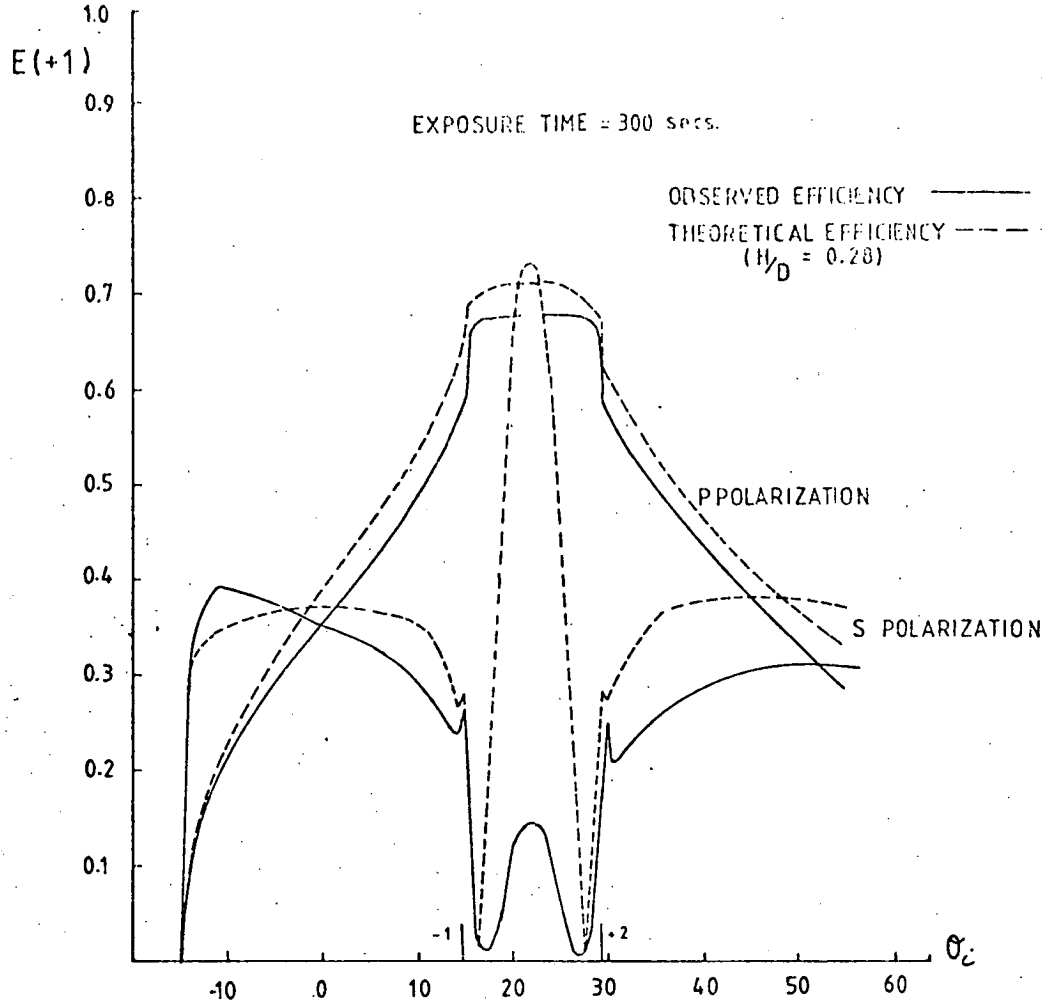

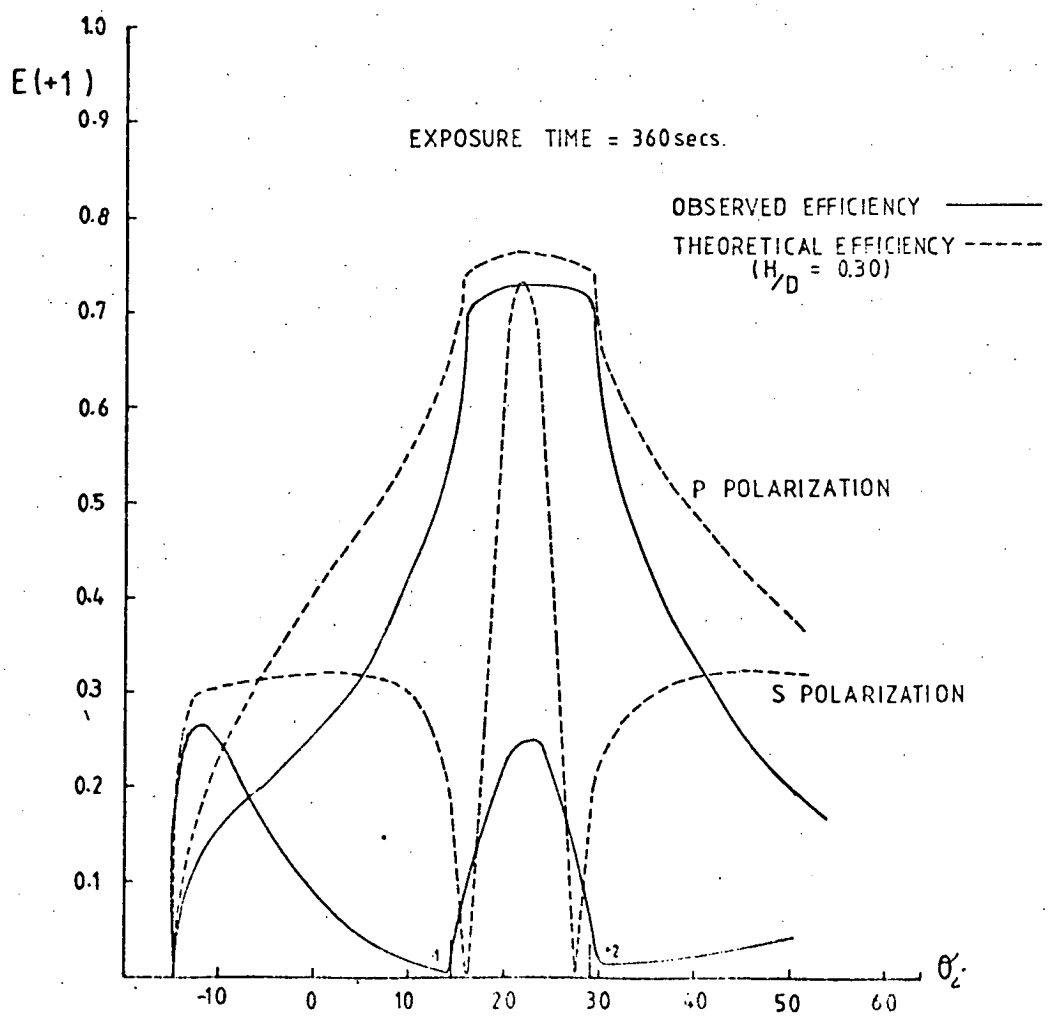

Fig. (2.9) - continued.

2.2.4 *Distorted quasi-sinusoidal gratings*

Both techniques indicate the groove depth of the grating profile, however the distorted grooves complicate the theory comparison process. Although the electron-microscope reveals the nature of the distortion of the groove profile, the latter theoretical treatment merely indicates its presence. The groove deformation is a consequence of the non-linearity of the exposure-development process for resist layers. Exposure of photoresist to a sinusoidal intensity field typically generates a grating having a quasi-sinusoidal groove profile. Extensive investigations show that groove distortion may be minimized either by a pre- or post exposure of the resist, or by varying the developer concentration. However, non-linearity need not be detrimental. Combining the finite conductivity theory of Maystre with a groove profile formation model, Wilson [2.17] demonstrated that groove distortion can be exploited by the production of a first generation replica grating exhibiting an improved spectral performance over that of a sinusoidal groove grating.

It is pertinent to enquire if the spectral efficiencies of the replicas of the four sample gratings achieve the larger bandwidth suggested by Wilson. Information gleaned from the electronmicrographs enables the numerical efficiency of the replica of grating #3 to be calculated from the finite conductivity theory of Maystre.
Shown in Fig. (2.10) is the Littrow +1 efficiency wavelength scan for both planes of polarization. Appearing are the behaviour of the master, replica and true sinusoidal profile grating of $H/D \simeq 0.25$.
The performance of the replica grating is disappointing.
Obviously, although the distortion of the master groove profile is large, it is not significant, nor of the correct type to achieve the

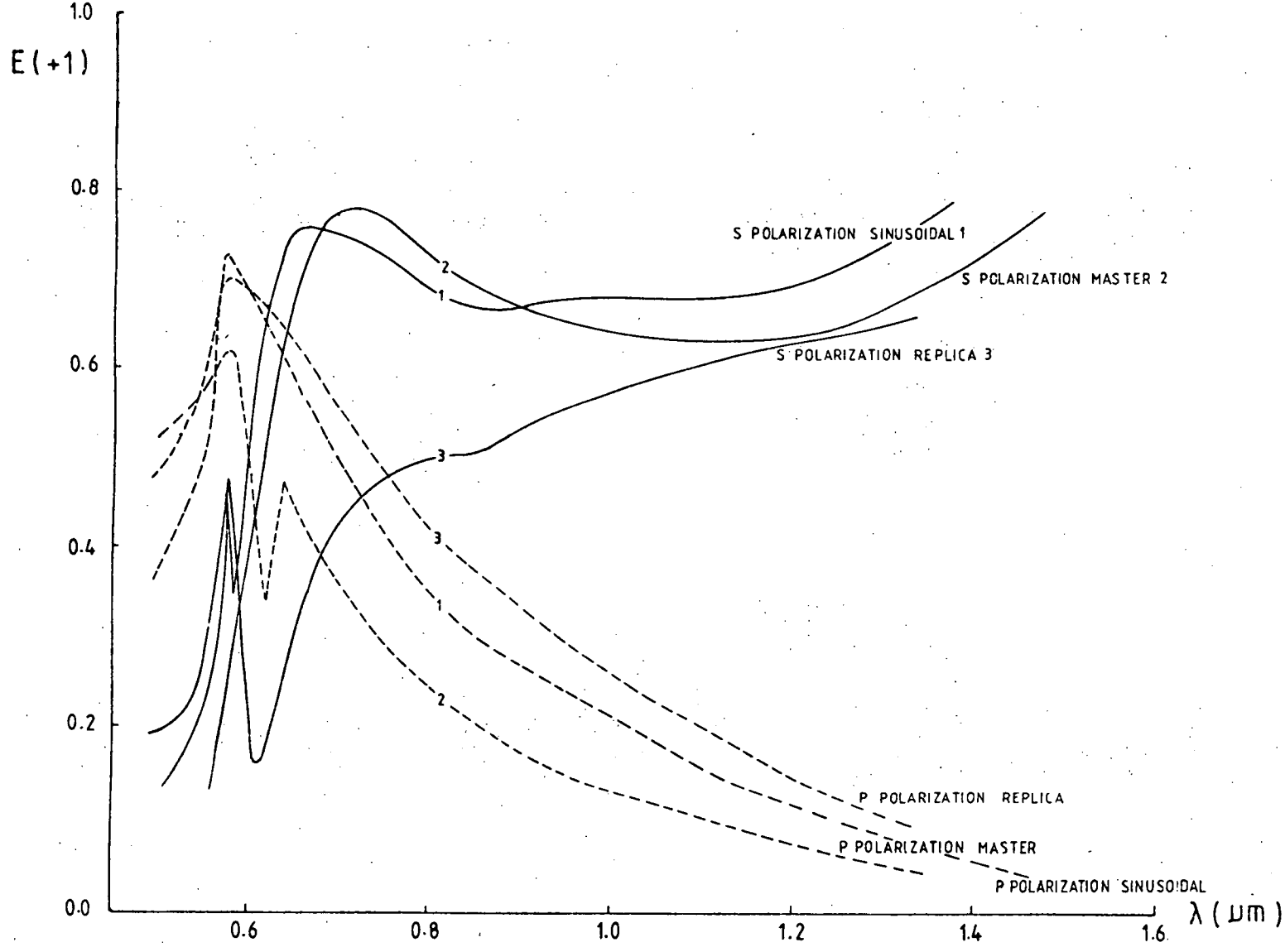

Fig.(2.10) First order Littrow efficiencies for the master grating manufactured by the author, the first generation replica and a grating having a sinusoidal groove profile of H/D=0.25.

theoretically predicted amelioration in spectral behaviour. Perhaps, as reasoned by Wilson and supported by the work of Bovin [2.18] an index mismatch between the photoresist and the grating substrate may be necessary to achieve the required degree of distortion.

Since the sinusoidal groove profile does not have a flat groove facet to specularly reflect incident light into a diffracted order, it normally does not exhibit high diffraction efficiencies over a wide wavelength range. The next section is devoted to the spectral behaviour of blazed holographic gratings and how it compares to that of ruled gratings.

2.3 BLAZED HOLOGRAPHIC GRATINGS

In recent years the possibility that blazed holographic diffraction gratings represent a viable alternative to ruled gratings has received careful consideration. Although the interference technique has the advantages of both time and cost over the traditional ruling engine, the limited groove profile control is a serious handicap. Several experimental studies of the efficiency of blazed gratings produced by the Sheridon technique [2.19] have been made. However, it is only with the formulation of integral and differential electromagnetic theories that rigorous theoretical efficiency calculations have become possible.

This section discusses the absolute efficiencies of four blazed holographic gratings having groove profiles predicted from the groove profile formation model of Dill et al.

2.3.1 *Groove profile formation model of Neureuther and Dill*

Before describing the numerical results of the survey into blazed holographic gratings, it is appropriate to present a brief outline of the groove formation model of Neureuther et al [2.13]. Since this model considers the photo-chemistry of the resist and developer, it is ideally suited to modelling processes involving the popular resist Shipley AZ1350.

Typically a positive photoresist consists of three components, a base resin which gives the resist its film making properties, a photoactive compound and finally a volatile solvent to aid application. In the presence of the photoactive compound, the dissolution rate in aqueous alkaline developer is in the range 0.1-0.2 nm/s. Hence the term "inhibitor" has been introduced by the authors to emphasize the functional role of the photoresist component inhibiting dissolution. Radiant energy in a wavelength range of 300-450 nm destroys the inhibitor component, resulting in an increased film dissolution rate up to 100-200 nm/s in the developer solution.

The model is considered as two distinct processes: exposure involving the destruction of the inhibitor concentration by photon absorption and the development which is a surface-limited etching reaction. Following exposure to a known intensity distribution, a map of the inhibitor concentration throughout the resist is calculated. This map is then transformed by a rate function to yield the rate of development. The surface profile is then traced through successive, small time increments.

2.3.2 *Spectral performance of blazed holographic gratings*

For a Sheridon-type grating the theoretical blaze wavelength is equal to twice the separation of the fringes inside the resist and furthermore, is independent of the angle between the fringes and the substrate. This angle will of course determine the blaze angle and the pitch, however these vary in such a way as to keep the blaze wavelength constant. Since the minimum value of the fringe separation is $\lambda_0/2n$ (where λ_0 is the recording wavelength an n is the refractive index of the resist) the minimum value for the blaze wavelength is theoretically λ_0/n. Therefore the experimental conditions (with λ_0 = 458 nm) considered by the inhibitor model should generate diffraction gratings all with identical blaze wavelengths of 273 nm.

Using the inhibitor model, the exposure of a photoresist film to a Sheridon-type interference field was simulated for blazed gratings having groove frequencies of 1200, 1800, 2400 and 3600 gr/mm. Shown in Fig. (2.11a) are the predicted groove profiles. The most significant feature of the convex grooves is the occurrence of "land" where little if any of the photoresist is removed by the development process. Fig. (2.12) illustrates the alteration in groove profile as development proceeds for the grating of period 1/2400 mm. Although the effective apex angle decreases as the development time progresses, undercutting of the surface occurs before the optinum value of 90^{o} is attained. Apparent in Fig.(2.12) is a similar change in effective blaze angle with development time, which suggests that the blaze wavelength displayed by the efficiency curves for each groove will be shorter than the predicted value of 273 nm.

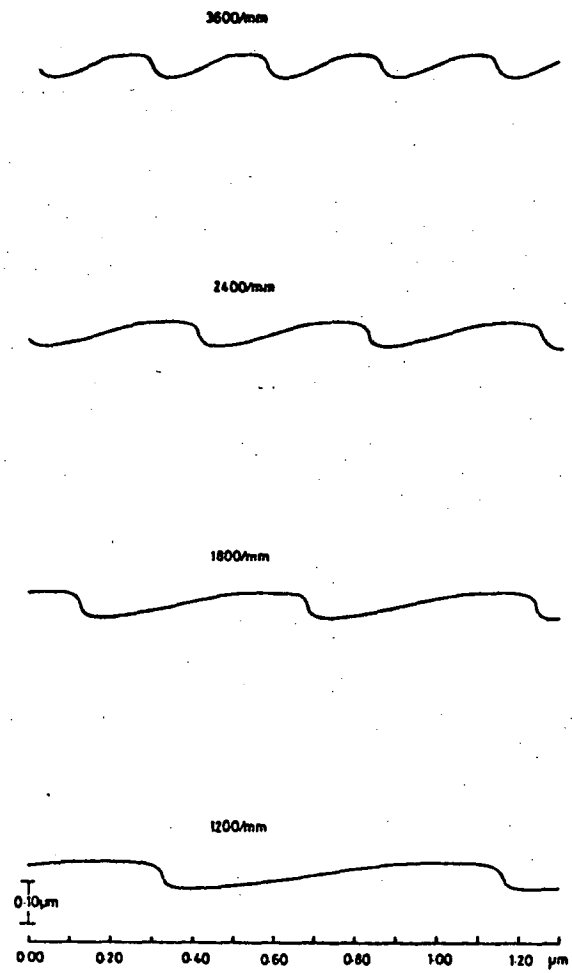

Fig.(2.11a) Groove Profiles corresponding to exposure distribution of arrangement type B.

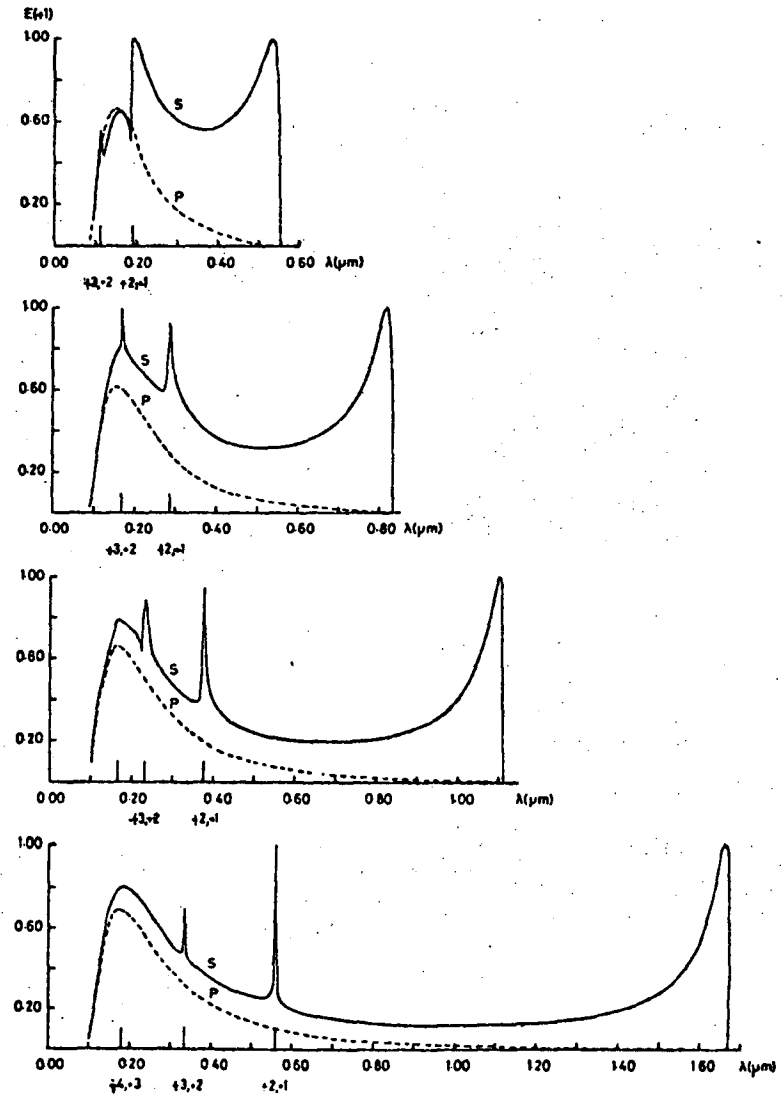

Fig.(2.11b) Theoretical efficiency curves for the Sheridon-type gratings.

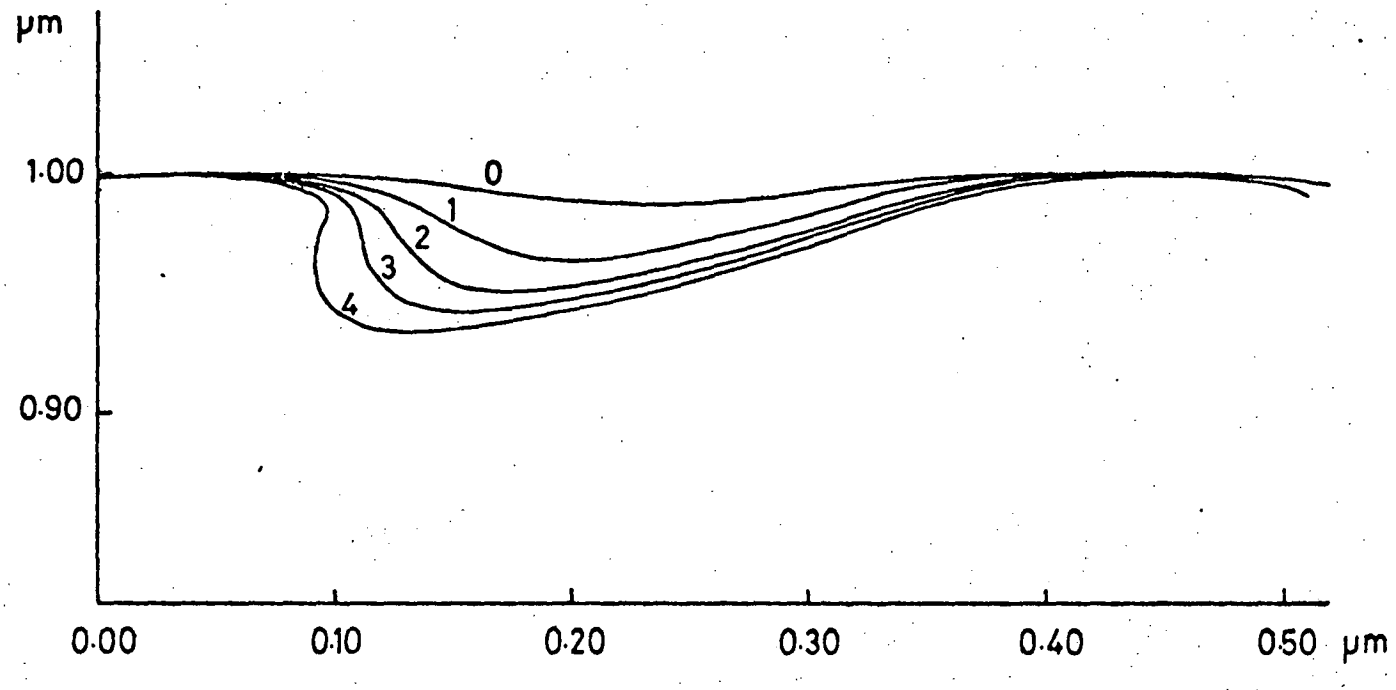

Fig.(2 12) Alteration in groove profile as development proceeds for the grating of period 0.4167μm.

Table (2.3) illustrates the comparison between the predicted blaze wavelengths and corresponding effective blaze angles and those determined from the elementary theory. All blaze wavelengths and the corresponding effective blaze angles are lower than predicted by the simple theory. Hutley [2.19] attributed this phenomenon to either an unexpectedly small blaze angle due to premature completion of development or shrinkage of the resist. The infinite conductivity theories of Petit [2.20] and Bolomey [2.21] were used to calculate the efficiency curves for each of the four holographic gratings and for triangular groove gratings with 90^{o} apex angles having blaze angles corresponding to the effective blaze angle of each modelled groove. Order +1 Littrow efficiencies for both planes of polarization are summarized in Fig. (2.11b) together with efficiencies computed for the triangular groove gratings.

The comparison between the theoretical efficiency of the triangular profile and holographic gratings is interesting. Noticeable for all four interference gratings is a lowering in blaze efficiency relative to the triangular groove gratings. For S polarization this reduction generally manifests itself as a drop in efficiency from 100% to 80%. Although the value of the efficiency peak varies with the grating period, the reduction in efficiency for P polarization is of the order of 20%. Accompanying the reduction in the blaze efficiency of the Sheridon-type gratings, is a corresponding reduction in the efficiency blazewidth for both polarizations. For the holographic grating of period 1/1200 mm the 50% efficiency blazewidth for P polarization is 125 nm as compared to 150 nm for the ruled grating.

Groove freq. ($gr\ mm^{-1}$)	Period (μm)	Elementary theory λ_B (μm)	Elementary theory θ_B (^{o})	Infinite conductivity theory λ_B (μm)	Infinite conductivity theory θ_B (^{o})
1200	0.8333	0.2726	9.412	0.1800	6.200
1800	0.5555	0.2726	14.20	0.1650	8.541
2400	0.4167	0.2726	19.09	0.1675	11.59
3600	0.2778	0.2726	29.28	0.1600	16.74

TABLE (2.3) S polarization blaze angles and blaze wavelengths derived from elementary theory and the infinite conductivity theory.

There is a definite trend for the holographic gratings to approach their ruled counterparts in spectral performance at longer incident wavelengths. This is to be expected since the longer the wavelength of the incident radiation, the less able it is to distinguish imperfections in the groove profile.

The wavelength corresponding to the P polarization efficiency peak varies for each grating period. However the efficiency peaks for the ruled gratings always occur at values which are less than or equal to that of the corresponding interference grating. This discrepancy is as large as 25 nm in the case of the grating of period 1/3600 mm.

In general the resonance peaks corresponding to the Rayleigh wavelengths for the holographic gratings are sharper than those for ruled gratings. For the triangular grating the leading edge of the peak has a gentler slope. This is particularly evident when comparing the $\lambda_R(+3, -2)$ resonance peaks. Special comment is required for the efficiency curves corresponding to the gratings of period 1/3600 mm and 1/2400 mm. The triangular groove grating having the latter period shows no sign of the otherwise dominant (+3, -2) Wood anomaly. The reason for this is that for blaze angles near 11.5^{o}, the blaze wavelength λ_B is close to the Rayleigh wavelength $\lambda_R(+3, -2)$. In the order +1, the S polarization efficiency for the triangular groove grating has to be 100% at λ_B, a constraint which prevents the formation of an anomaly. However, if the apex angle differs substantially from 90^{o}, the constraint is removed and a strong anomaly is free to develop within the blaze region. For the interference grating of period 1/3600 mm the reduction in the peak efficiency has allowed the (+2, -1) resonance anomaly to develop into a dominant feature of the efficiency curve, more marked than for the ruled grating of similar period.

Evidence indicates that the transition from triangular groove gratings to blazed holographic gratings is accompanied by a dramatic change in spectral efficiency. This transition is characterized by a significant reduction in blaze efficiencies for both planes of polarization. It has been observed that the blaze wavelengths of the holographic gratings are considerably shorter than that predicted by the elimentary $\lambda_B = \lambda_0/n$ formula.

McPhedran [2.22] has presented a detailed discussion of the influence of land on the efficiency of triangular groove gratings. In relation to P polarization the introduction of land no only results in a general lowering of the first order diffraction efficiencies, but also causes a bodily shift of the efficiency curve towards shorter wavelengths. However, the land does not initiate a decrease away from 100% of the S polarization blaze efficiency, although the drop away from the blaze peak on its long wavelength side increases with land length. Consequently, it appears that the lower blaze wavelength can be attributed to several influences including the presence of land on the groove profile, incomplete development and non-linear profile facets.

Stroke and Marèchal [2.23] demonstrated that for S polarization and grooves of apex angle 90^o, the blaze wavelength must correspond to an efficiency of 100% in order m for a grating of infinite conductivity. Thus blaze efficiencies less than this optimum are indicative of a departure away from 90^o apex angles to larger apex angles. For the grooves discussed here the effective apex angle is probably about 103^o for the 1200 gr/mm grating and 110^o for the 3600 gr/mm grating.

Although these results indicate that blazed holographic gratings may not be capable of exhibiting high blaze efficiencies, the other spectroscopic properties of holographic gratings such as the absence of ghosts and low scattered light compare more than favourably with the best ruled gratings. It is interesting to note that the reduced blaze wavelengths reported here for blazed holographic gratings have been observed experimentally by E.G. Loewen [2.24].

Now that the two elementary holographic groove profiles have been investigated, attention is directed towards the techniques of Fourier synthesis which theoretically has the potential to mass produce an extensive range of groove profiles. Mention is made of various experimental approaches, in particular the scheme employing a transmission grating for the Fourier synthesis of groove profiles suggested by Wilson and Brown [2.25].

2.4 FOURIER SYNTHESIS OF GROOVE PROFILES

McPhedran et al [2.8] demonstrated in 1973 that it is theoretically possible, although practically difficult to form a Fourier synthesis of any desired interference field. Subsequently, the feasibility of this holographic technique was experimentally confirmed by Hutley. The high design tolerances inherent in McPhedran et al's method were overcome by Schmahl [2.26] who suggested interference between the diffracted orders from a single grating as the source of the required intensity field. A significant disadvantage of Schmahl's method is that the size of the reference grating must be several times that of the final grating.

Simplifications proposed by Wilson have removed the size restrictions of Schmahl's technique. Fig. (2.13) shows amendments to the above arrangement which enable the exposing radiation to pass through the substrate and resist layer before being incident on the reference grating. The prescribed asymmetric intensity distribution for the manufacture of gratings exhibiting good blazing properties, is achieved by illuminating a blazed reference grating at normal incidence. For a reference grating blazed in the first order, interference between the incident beam and the diffracted first order will generate an intensity distribution of periodicity equal to that of the reference grating. The groove profile produced following exposure of the resist to the interference field generated by Fourier synthesis of the diffracted orders is determined from the groove formation model of Dill et al. An example of the relative intensity, relative inhibitor concentration on a scale of 1-10 (ie. between 0 and *), and the resulting groove profile obtained for a reference grating of period 1/1200 mm, blaze angle $21^{o}06'$ and exposing wavelength 458 nm appears in Fig. (2.14). It should be noted that no account has been taken of the multiple reflections between the reference grating and the resist film. Initially it was hoped that this technique would supersede the Sheridon configuration for the production of quasi-triangular grooves. However, since the resist is exposed to a sum of standing waves the restriction on the blaze wavelength still applies.

This method is further simplified by the use of a transmission rather than a reflection reference grating. The proposed arrangement is represented schematically in Fig.(2.15).

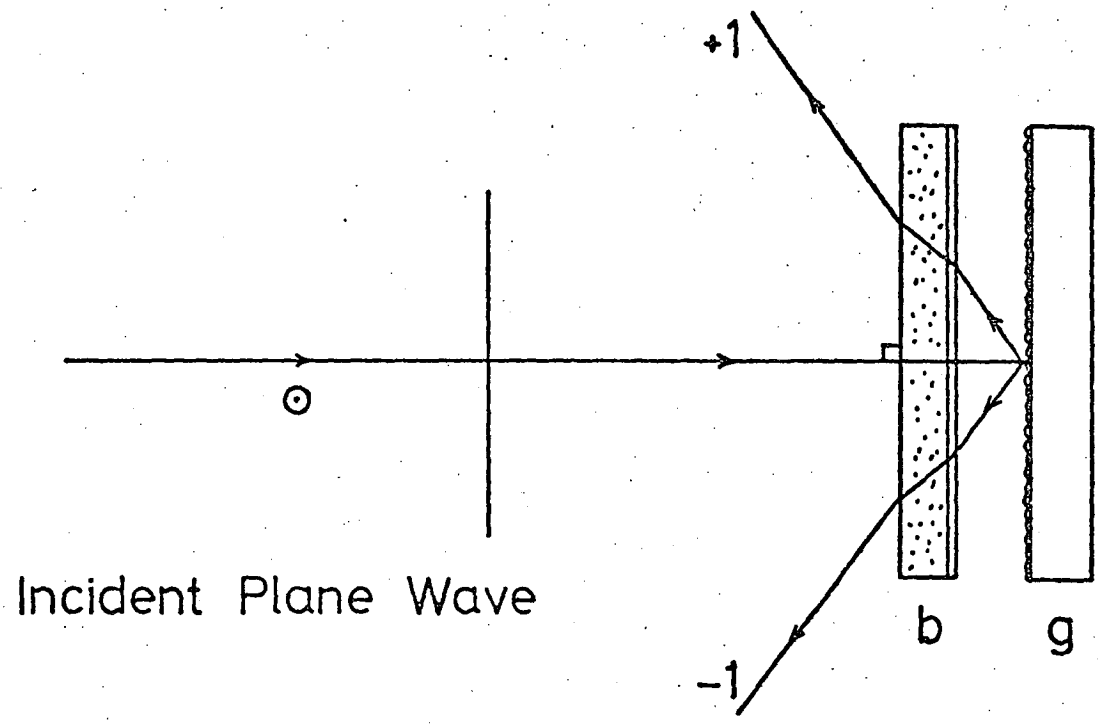

Fig. (2.13) A modification of Schmahl's technique for Fourier Synthesis of groove profiles.

(a)

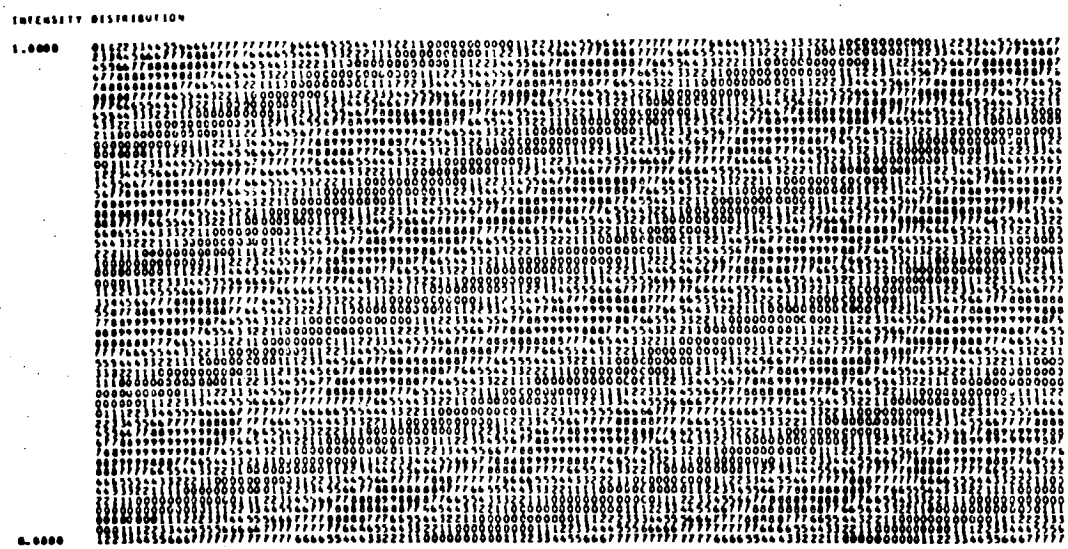

(b)

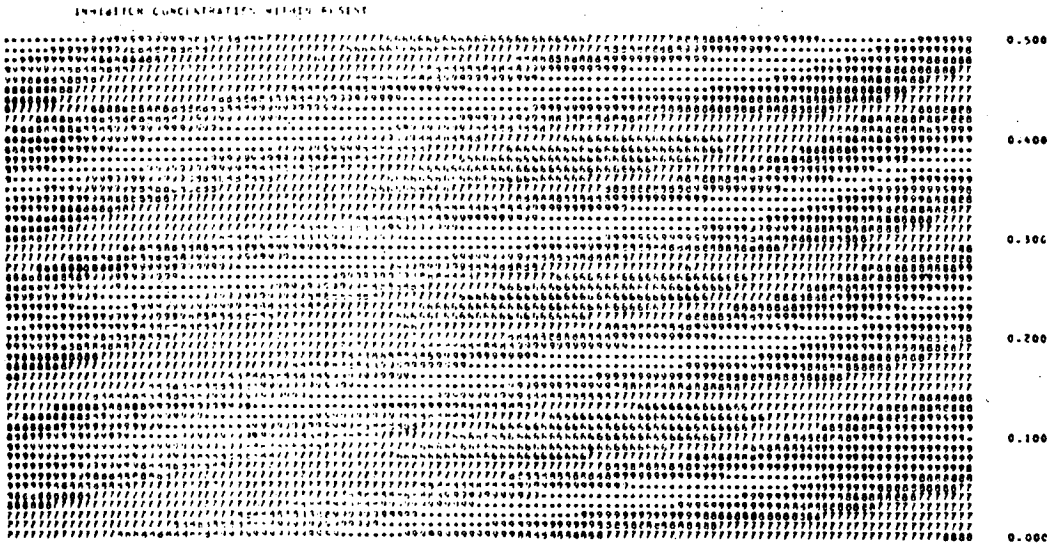

(c)

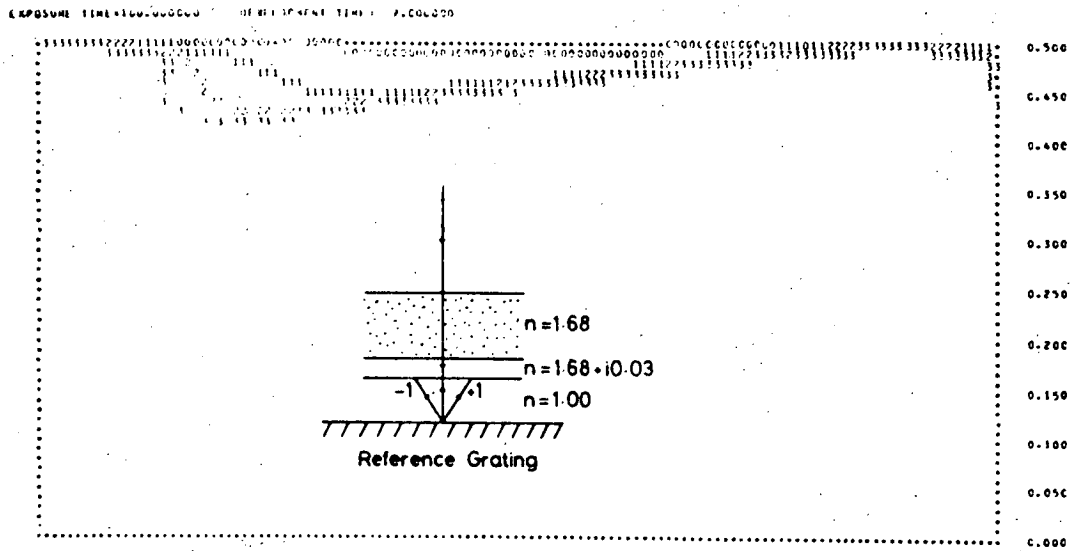

Fig.(2.14) Formation of a blazed grating using a modification of Schmahl's technique for Fourier Synthesis of groove profiles.

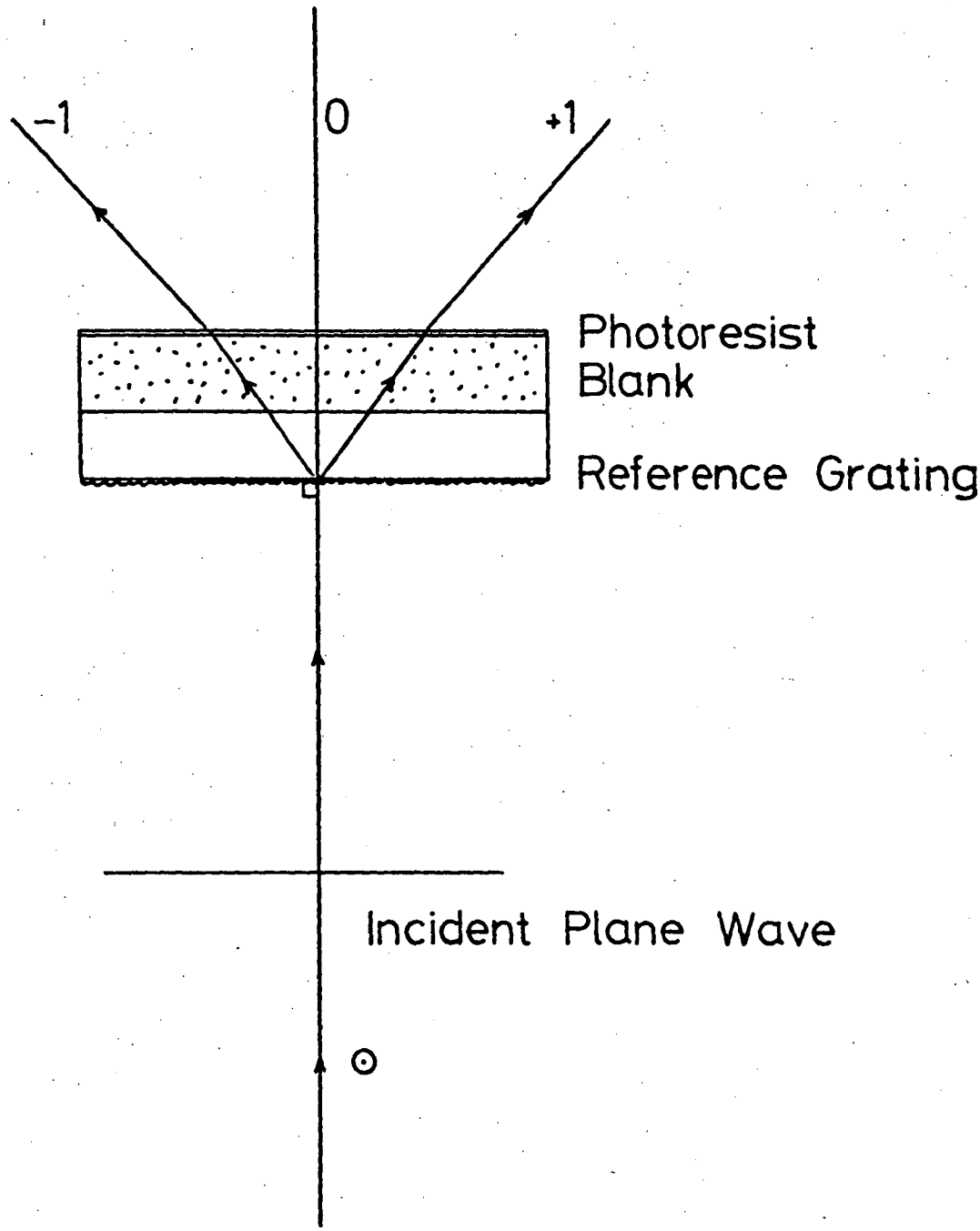

Fig.(2.15) A scheme employing a transmission grating for Fourier Synthesis of groove profiles.

A simple experimental procedure would be to make a sinusoidal or asymmetric groove reference grating on a parallel optical flat. Then bring this transmission grating into contact with the back surface of a parallel blank coated with photoresist. Illumination of the reference grating will generate an interference field having the same period and with the potential for the mass production of holographic gratings. However, the simplicity of this method is of little consequence, if the generated groove profiles do not exhibit a satisfactory spectral performance. Reverting yet again to the model of Dill et al it is possible to predict the form of these groove profiles.

Displayed in Fig. (2.16) is the optical configuration modelled by the application of the theory of Dill et al. The amplitudes and phases of the transmitted orders within the resist are calculated from the integral formalism of Botten [2.27]. By altering the groove depth of the reference grating, the amplitudes and phases of the transmitted orders can be varied relative to each other in much the same way as for the reflection grating. The interference field within the resist is constructed not only from downward travelling waves but also from waves reflected at the resist-air boundary. The heavy attenuation of the waves and the refractive index mismatch combine to limit the energy associated with the reflected waves. However, an exception occurs for the total internal reflection of an order which is a large propagator of energy. Numerical studies for a reference grating having a sinusoidal depth of H/D = 0.30 and period 1/1200 mm illuminated at angles of incidence ranging from 0^{o} to 33.33^{o} have been carried out.

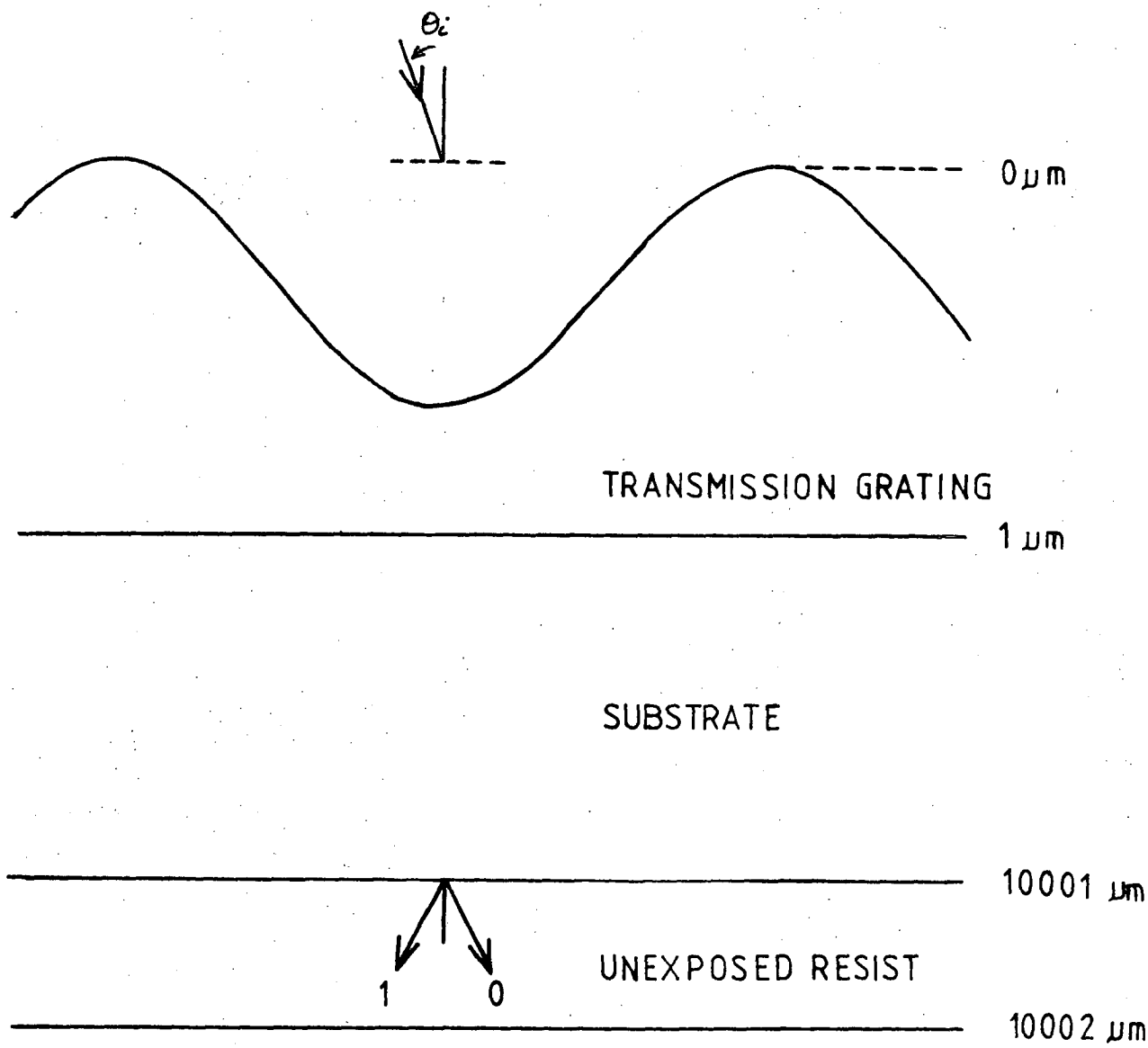

Fig.(2.16) The geometrical arrangement employing the rigorous electromagnetic theory of Botten to determine the amplitudes and phases of the transmitted orders within the resist.

Examples of the inhibitor concentration within the resist resulting from incidence angles of 12^{o}, 15.95^{o} and 33.33^{o} are displayed in Fig. (2.17). It is important to note that development commences at the lower air boundary and proceeds up into the resist.

For low angles of incidence the interference field consists of two fringe patterns, varying little in strength. Consequently, development yields a groove profile consisting of a large region of land between shallow grooves. The study of blazed holographic gratings in the previous section indicates that such a groove profile is unlikely to exhibit a high spectral efficiency. For the Littrow +1 angle of incidence (15.95^{o}) the contrast within the two fringe patterns of the concentration has improved. Fig. (2.18) depicts the changes in groove profile as development proceeds for a sinusoidal reference grating following an exposure time of 200 seconds. The groove profile consists of two grooves of unequal depth per period. As development proceeds, the surface retreats horizontally rather than vertically into the resist layer. At an incidence angle of 33.33^{o}, the energy transported by the reflected waves increases dramatically due to total internal reflection of the first diffracted order. Interference between the upward and downward travelling first order waves, produces strong interference planes inclined at a shallow angle to the resist surface. Recalling that development travels upwards from the lower resist surface, these planes are clearly displayed in the inhibitor concentration map. Once the etched surface of the resist encounters the "horizontal" interference planes, development continues horizontally. Consequently very shallow, unblazed grooves are generated.

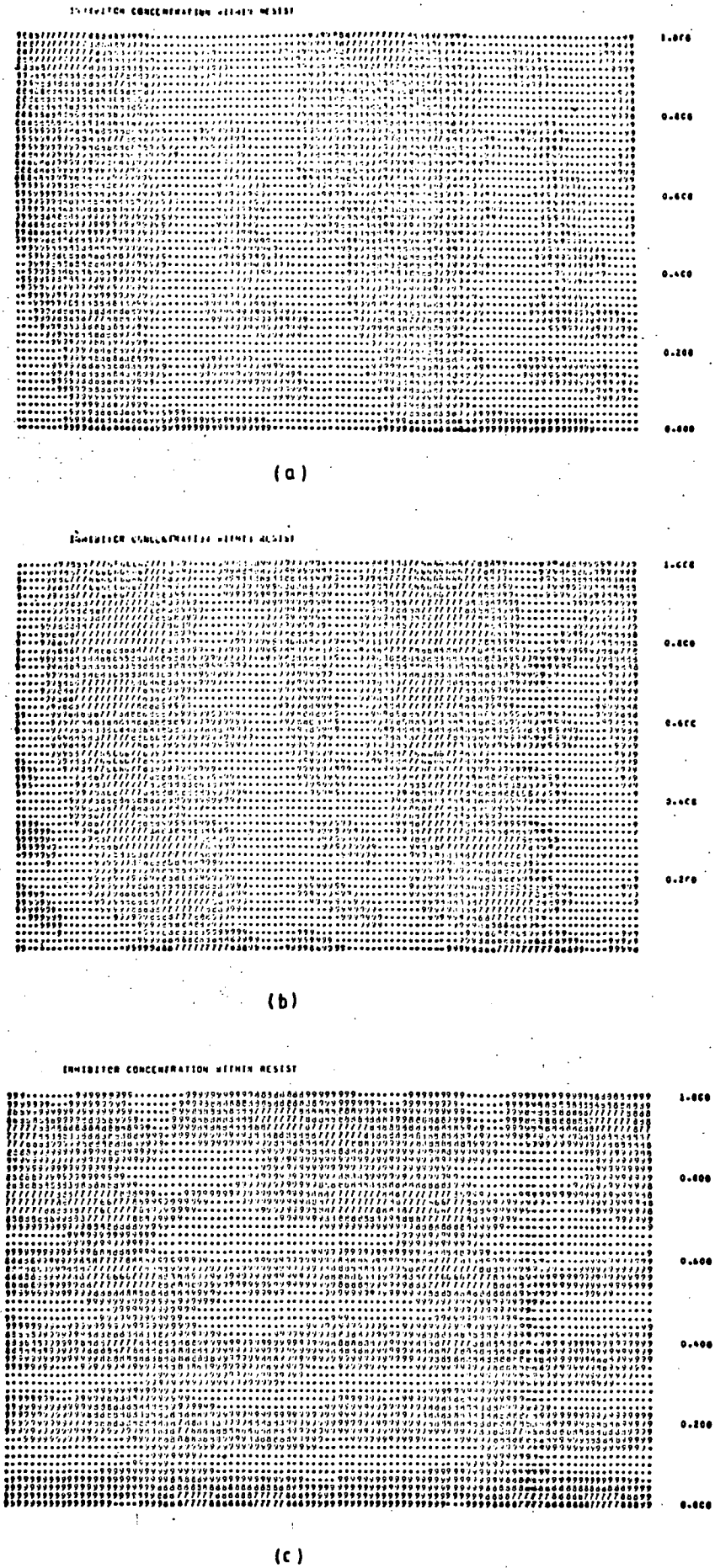

Fig.(2.17) Examples of the inhibitor concentration within the resist resulting from the illumination of the transmission grating at (a) 12^{o}, (b) 15.95^{o} and (c) 33.33^{o} at a wavelength of 458nm.

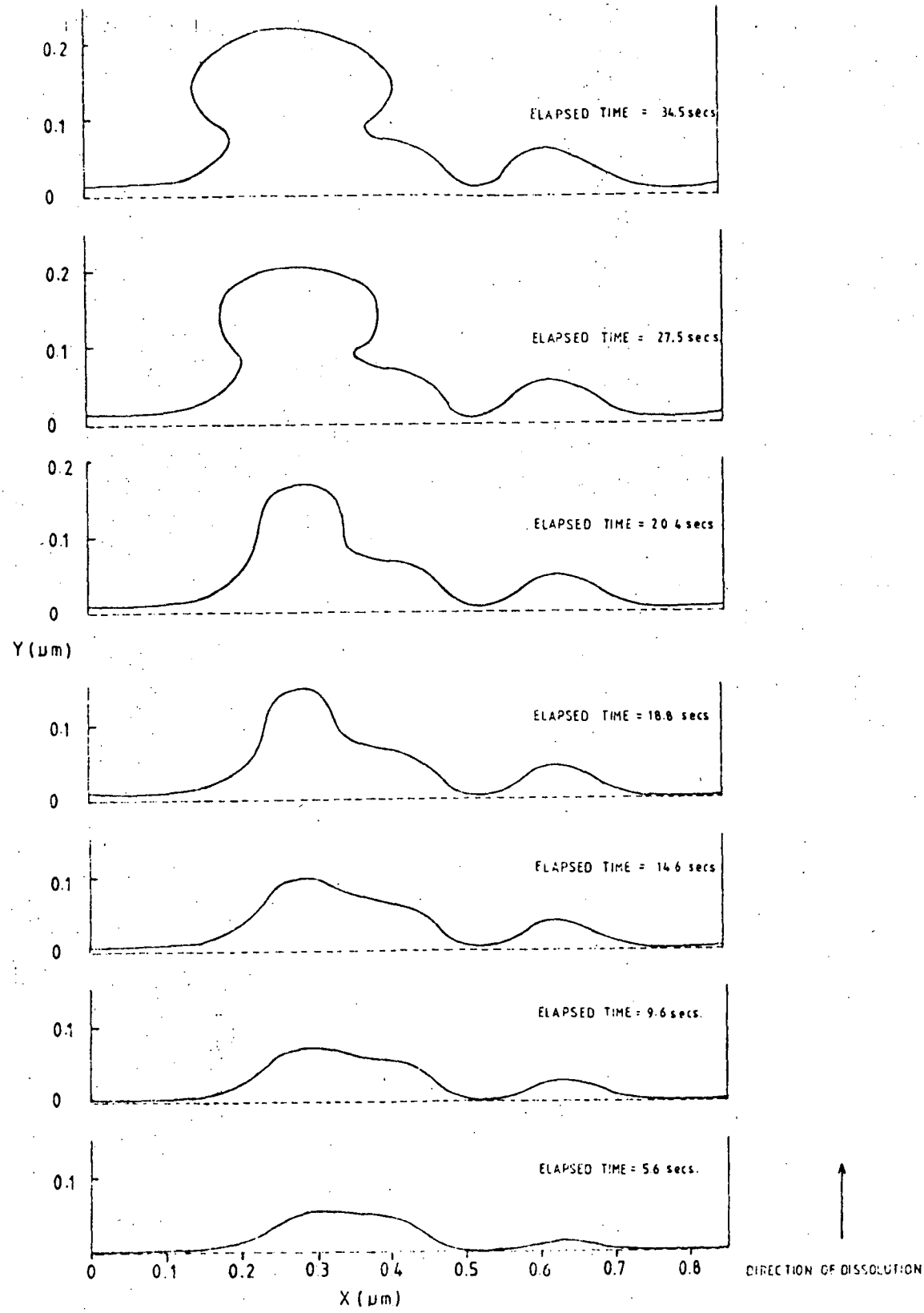

Fig. (2.18) Changes in groove profile as development proceeds following the exposure of a sinusoidal transmission grating at an angle of 15.95° for 200 seconds.

Obviously, the success of this process for a sinusoidal reference grating lies with angles of incidence near the Littrow +1 angle. However, it is anticipated that the high percentage of land and shallow grooves will give rise to a grating exhibiting a low spectral efficiency.

A further technique has been suggested by the Swedes [2.28], whereby many of the practical difficulties are circumvented by choosing to operate with a fixed standing wave field and rotate only the work-piece in this field. The experimental procedure envisaged is as follows. Set up a sinusoidal intensity distribution with, for example, a spatial frequency of 600 gr/mm. Expose an annulus 10 mm wide at the edge, masking-off the central disk. Development will produce a grating only around the exposed annulus, and the developer will have minimal action on the unexposed region. After drying, the substrate can be returned to the exact recording position by observing the Moire fringes due to the interactions between the transmission grating annulus and the standing wave field. The central disk is then exposed as normal - this will be the fundamental component determining the groove frequency of the end product. An exact harmonic relationship between the spatial frequency of the first recording and the second order can be established by rotating the work and studying the Moire frings. A relative phase shift can be introduced at this stage by changing the path length in one beam using a piezo-electric pusher on a folding mirror.

An investigation of this technique by the author, although only cursory, has indicated that the potential of this procedure is destroyed by the shallow secondary interference planes which were formed in the resist by the previous transmission grating procedure. It appears that success can only be achieved by an extensive survey of the amplitudes and phases of several gratings of varying depths.

The preceding discussion has thrown some light onto the problems of the Fourier synthesis of interference fields generated for the production of holographic gratings. There are numerous, basic problems inherent in the technique. Any method which reduces the high design tolerances required, must eliminate the shallow secondary interference planes before the production of deep, blazed gratings can be achieved. Initially it was thought that the method of Fourier synthesis would revolutionize holographic groove profiles, however it appears that in practice this potential may not be realized.

In this chapter we have discussed the groove profiles formed by holographic processes and mentioned procedures which lead to the recognition of the correct groove profile to achieve the optimum spectral performance predicted by theory. In the next chapter attention is directed towards improving the spectral efficiency of all types of diffraction gratings by the elimination of resonance anomalies with appropriate surface layers.

REFERENCES

[2.1] Pröger H.J. (1961) Exp. Tech. Phys., 9, 236.

[2.2] Anderson W.A., Griffin G.L., Mooney C.F. and Wiley R.S. (1965) Appl. Optics, 4, 99.

[2.3] Bennett J.M. (1969) J. Phys. E.: Sci. Instrum., 2, 816.

[2.4] Brandes R.G. and Curran R.K. (1971) Appl. Optics, 10, 2101.

[2.5] Maystre D. and Petit R. (1970) Opt. Commun., 2, 309.

[2.6] Hutley M.C. (1974b) Sci. Prog. Oxford, 61, 301.

[2.7] Sheridon N.K. (1968) Appl. Phys. Lett., 12, 316.

[2.8] McPhedran R.C., Wilson I.J. and Waterworth M.D. (1973b) Opt. Laser Technol., 5, 16.

[2.9] Wilson I.J. McPhedran R.C. and Waterworth M.D. (1973) Ninth Aust. Spec. Conf. Canberra.

[2.10] Wilson I.J., McPhedran R.C. and Waterworth M.D. (1973) Opt. Commun., 9, 263.

[2.11] Austin S. and Stone F.T. (1976) Appl. Optics, 15, 1071.

[2.12] Dill F.H., Neureuther A.R., Tuttle J.A. and Walker E.J. (1975) IEEE Trans. Electron Devices, 22, 456.

[2.13] Neureuther A.R. and Dill F.H. (1974) Proc. Sym. on Optical and Acoustical Micro-Electronics, Polytechnic Institute, New York, 233.

[2.14] Verrill J.F. (1976) Opt. Acta. 23, 425.

[2.15] Palmer E.W., Hutley M.C., Franks A., Verrill J.F. and Gale B. (1975) Rep. Prog. Phys., 38, 975.

[2.16] Wilson I.J. and Botten L.C. (1977) Appl. Optics., 16, 2086.

[2.17] Wilson I.J. (1977) Ph.D. Thesis, University of Tasmania.

[2.18] Bovin L.P. (1973) Opt. Commun., 9, 206.

[2.19] Hutley M.C. (1975) Aptica Acta, 22, 1.

[2.20] Bolomey J.C. (1971) Thèse No. A05604.

[2.22] McPhedran R.C. (1974) Ph.D. Thesis, University of Tasmania.

[2.23] Marèchal A. and Stroke G. (1959) CR Acad. Sci. (Paris) 249, 2042.

[2.24] Loewen E.G. (1980) Private communication.

[2.25] Wilson I.J. and Brown B.J. (1976) University of Tasmania Research Report DGRG 76/2.

[2.26] Schmahl G. (1974) Proc. Sym. on Diffraction Gratings and Grating Instruments, Spec. Soc. Japan, Tokyo, 10.

[2.27] Botten L.C. (1978) Optica Acta, 25, 6, 481.

[2.28] Johansson S., Nilsson LE., Biederman K. and Leveby K. (1977) Applications of Holography and Optical Data Processing, Jerusalem, Israel, Aug. 1976. (Oxford, England: Pergamon) p.521-30.

CHAPTER 3

INFLUENCE OF SURFACE COATINGS ON GRATING RESONANCE ANOMALIES

3.1 PRELIMINARY COMMENTS

In 1902 Wood [3.1] observed that very small shifts in wavelength initiated rapid variations in the spectral intensity of some orders diffracted from a grating. Furthermore, he observed that this behaviour only occurred for light having the magnetic field vector, H, aligned with the grooves (S polarization). It was Rayleigh [3.2] who first suggested a theoretical explanation of these anomalies. He attributed their origin to a re-distribution of energy which must accompany the "passing-off" of an order. A real diffracted order ceases to propagate when the sine of the angle of diffraction exceeds ±1. From the grating equation, we see that this condition can be expressed mathematically by

$$\sin \theta_d = \frac{m\lambda}{d} - \sin \theta_i = \pm 1 \qquad (3.1)$$

Therefore, for a particular angle of incidence, the wavelength (termed the Rayleigh wavelength, λ_R) at which a given order "passes-off" can readily be calculated.

In 1965 Hessel and Oliner [3.3] recognized the existence of two very distinct types of anomalies, one related to the Rayleigh wavelength, the other to surface waves. Whereas the position of the Rayleigh anomaly is determined from the grating equation, the resonance type anomaly appears at slightly longer wavelengths than λ_R. This latter anomaly usually takes the form of a narrow, sharp minimum in the total diffracted energy curve which has the appearance of an absorption band in any spectrum generated by a spectrophotometer.

Experimental observations illustrating grating absorption and re-emission of light due to surface plasmon resonances were reported by Hutley and Bird [3.4]. Their study of grating anomalies for various metal coatings revealed that a definite relationship existed between the presence and form of the resonance anomaly and the conductivity of the coating. Utilization of this knowledge led to some success in predicting the location of plasmon resonances.

During the past decade many experimental and theoretical studies of plasmon resonances have been carried out. In particular Cowan and Arakawa [3.5] gave a theoretical explanation of the anomalies and absorption peaks in terms of surface plasmon oscillations. The correlation between the bandwidths of the resonances and the ratio $Im(r)/Re(r)$ (where r is the refractive index of the surface material) were observed and investigated by Wheeler et al [3.6] and Botten [3.7].

Resonance anomalies reduce the effective wavelength range of a particular grating and lead to complications in spectral analysis. Although, Cowan and Arakawa succeeded in describing the formation of resonance anomalies, little has been done to minimize their influence or to eliminate them altogether from grating efficiency curves. Since it is evident that the position and form of these anomalies are due, mainly to the conductivity of the metal coating, it appears that any success in resonance reduction lies in the choice of the surface material.

The experimental investigations reported in this chapter represent an attempt to reduce the influence of resonance anomalies

by manipulation of additional coatings applied to the surface of a grating. The grating configurations studied fall into two categories:

(i) bi-metallic gratings, which can be defined as a structure composed of two species of metals arranged so that both the profile and the conductivity of the structures are periodically modulated.

(ii) "conformally coated gratings" generated by the application of over-coatings of dielectric and highly conducting layers.

3.2 BI-METALLIC GRATINGS

The initial investigation of bi-metallic gratings appears to have been an experimental study conducted by Sugahara, Kita and Shimotakahara [3.8], who reported successful suppression of grating anomalies using a replication process involving the deposition of aluminium on the off-blaze facet of a silver-aluminium master grating. Motivated by the Japanese results Botten [3.9] presented an integral formalism describing the diffraction properties of bi-metallic gratings and achieved suppression by overcoating the off-blaze facet of a triangular profile grating with a metal of weak conductivity. The study considered a coating of infinite conductivity applied to the blaze facet with a low conductivity plug. Botten attributed the anomaly reduction to the excitation of lossy (or inelastic scattered) plasmons.

Since Botten treated the ideal, theoretical configuration of an infinite conductivity coating applied to the blaze facet, the

author has conducted an experimental investigation into the practical case of bi-metallic gratings constructed with two finitely conducting coatings. Additional metal coatings were applied by slant evaporation to the triangular surfaces of two ruled gratings of period 1/1200 mm and respective blaze angles $\theta_B = 9^0$ and $\theta_B = 26.75^0$. The initial aluminium surface coating was that provided by the manufacturers. A film of silver with a thickness in excess of 4 times the skin depth was evaporated onto the off-blaze facet of the aluminium grating, generating the Al-Ag configuration, A further complete overcoating of silver yielded the continuous silver layer, while an additional coating of aluminium evaporated onto the blaze facet of this grating gave use to the Ag-Al grating. All coatings were of sufficient thickness to shield underlying layers from the incident electromagnetic field. Appearing in Fig. (3.1) is a schematic diagram of the cross-section of the bi-metallic grating designated by Al-Ag.

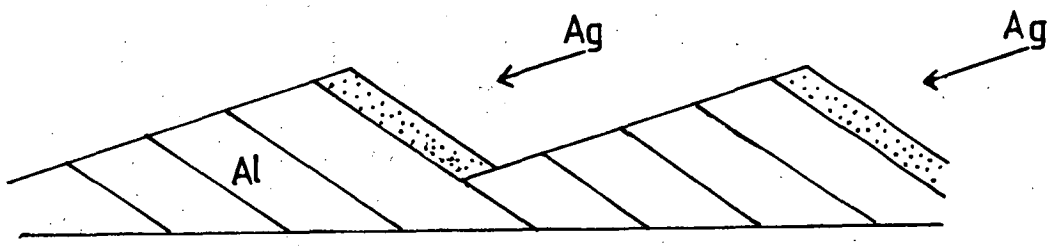

Fig. (3.1) Schematic diagram of the cross-section of the bi-metallic grating designated by Al-Ag.

The efficiency for S polarized light was measured at a constant wavelength of 632.8 mm for various angles of incidence for each coating combination.

3.2.1 *The 9° blaze angle grating*

Fig. (3.2) displays the experimental curves illustrating the marked effects of the bi-metallic coatings on the S polarization anomalies for a grating of blaze angle 9°. The total diffracted energy curve for the initial Al-Al coating is distorted by four resonance anomalies occurring at incidence angles subsequent to the passing-off of the 1st and 2nd orders. This anomalous behaviour manifests itself as very narrow, sharp absorption peaks, which would lead to complications in any spectroscopic analysis. A reduction in the total diffracted efficiency of 87% to 18%, corresponding to a rotation of the grating through 2.5° causes the +1 anomaly to be particularly significant. This dramatic decrease in efficiency reinforces the necessity to eliminate or lessen the energy absorbed by the surface plasmons.

As can be seen from the curves of Fig. (3.2), the application of the higher conductivity metal to the off-blaze facet of the grating has shifted the positions of the weakened absorption away from the Rayleigh angles. Although the silver coating has broadened the minima, the total energy diffracted by the grating in the region of the ±1 Littrow angles has been reduced.

For a grating having a continuous layer of silver, the total efficiency in the region of 0° differs little from that for the initial aluminium grating. However, it is again the regions of the ±1 Littrow angles where the change in metal coating is not evident.

Fig. (3.2)

Observed diffracted energy spectra for a triangular profile grating having a blaze angle of 9^{o} and a right-angled apex. Each graph displays the S polarized diffracted energy as a function of the incidence angle for a constant wavelength of 632.8 mm. The efficiency for the 3 diffracted orders ±1, 0 together with the total diffracted energy efficiency are illustrated. The symbols for the curves appearing in the graphs represent the following configurations:

(i) Al-Al ————————

(ii) Al-Ag — — — — -

(iii) Ag-Ag .....

(iv) Ag-Al — —— —

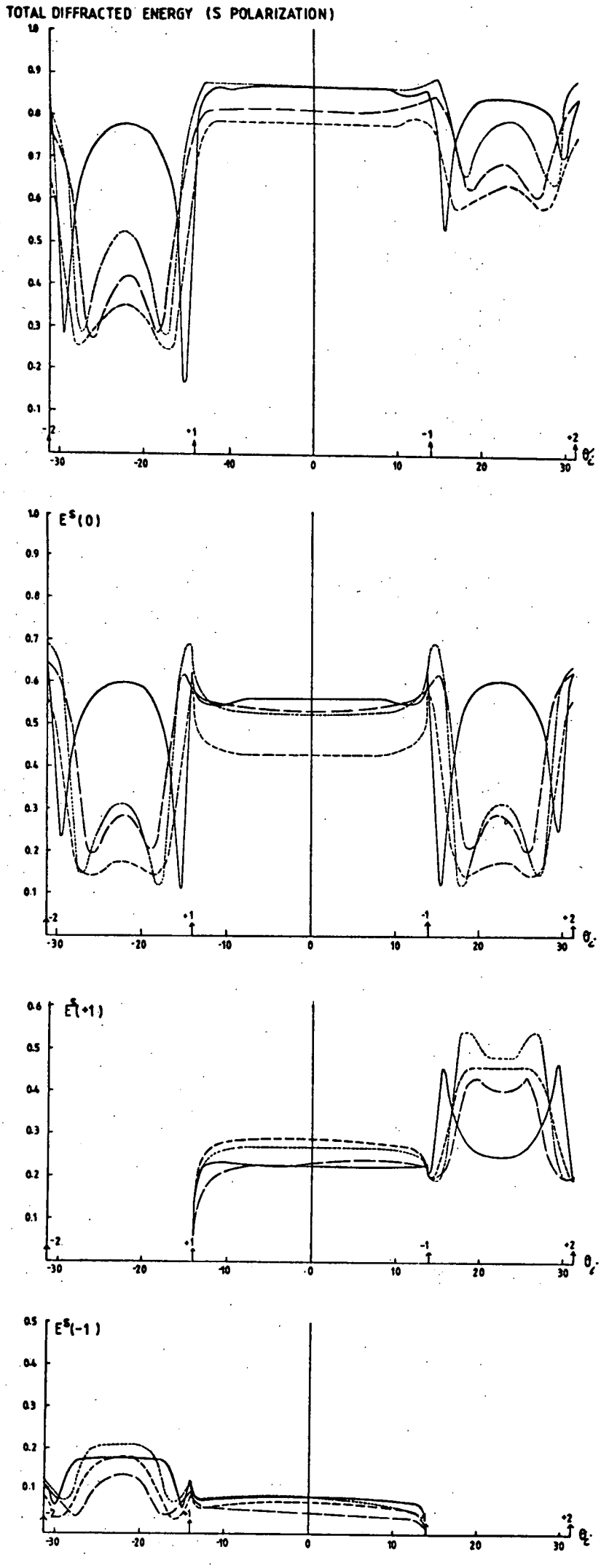
TOTAL DIFFRACTED ENERGY (S POLARIZATION)
$E^S(0)$
$E^S(+1)$
$E^S(-1)$
θ_i

Subsequent to the diffracted energy minima, the efficiency for this grating fails to achieve the level displayed by the Al-Al grating. In a manner similar to the Al-Ag bi-metallic grating, the positions of the absorption minima for the Ag-Ag grating have shifted further away from the Rayleigh angles and their bandwidths increased.

The final bi-metallic grating tested by the author was generated by the evaporation of silver onto the blaze facet of the aluminium grating. Although the overall form of the diffracted energy curve for this grating is similar to that of the Al-Ag and Ag-Ag gratings, two important features should be noted. Firstly, the magnitude of the total diffracted energy for this bi-metallic grating is an average of that for the other two gratings. Secondly, the broadening of the absorption maximum is not as great as that for the Al-Ag grating, but it is better than that achieved by the Ag-Ag grating.

The performance of the +1 efficiency curve is particularly important for gaining information concerning the behaviour of the grating operated in the +1 Littrow mount. Success in this experimental study cannot solely be judged from the constant wavelength efficiency curves. Consideration must be given to the behaviour of the grating in the +1 Littrow mount. Fig. (3.3) displays the +1 Littrow efficiency curve for a 9^{o}, 90^{o} apex angle triangular groove grating having an infinite surface conductivity. The testing wavelength of 632.8 mm occurs within the region of the very strong S polarization resonance anomaly present on the long wavelength side of the (+2, -1) Wood anomaly. Hence the performance of the +1 efficiency curve for incidence angles near the +1 Littrow angle is very pertinent to this investigation, as it gives an indication of the shape and form of the (+2, -1) resonance anomaly.

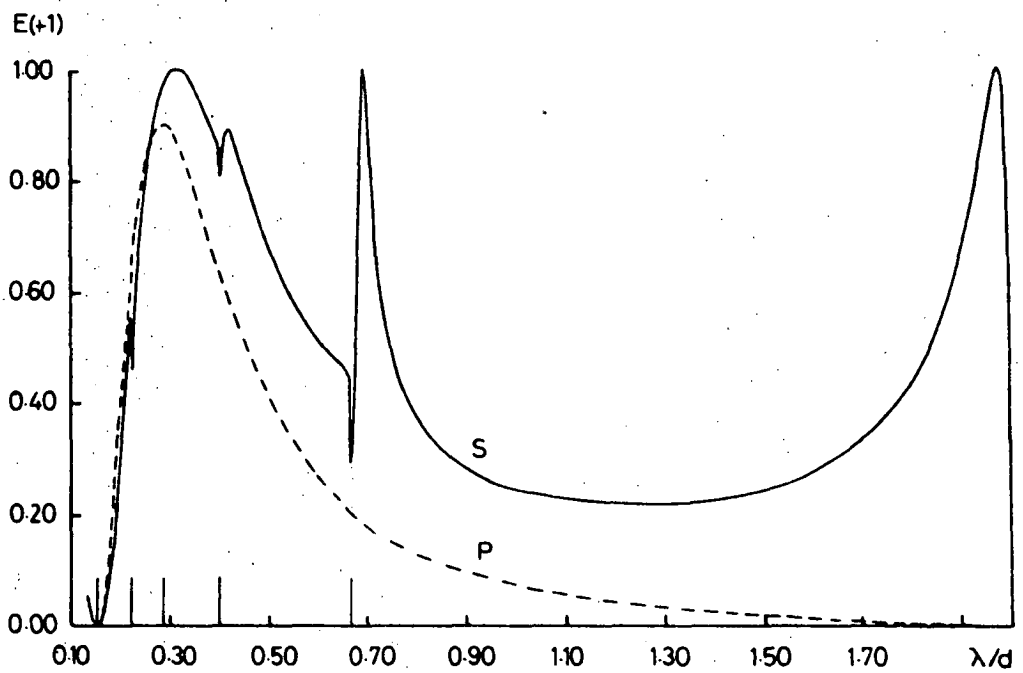

Fig.(3.3) Order +1 Littrow efficiency curves for a 9^{o}, 90^{o} apex angle triangular groove grating having infinite surface conductivity. The S polarization efficiency is unity for angles of incidence of 9^{o} and 81^{o} (after Wilson, 1977).

For all but a very restricted range of incidence angles, the +1 efficiency curve for the Al-Ag bi-metalic grating is an improvement upon that for the grating having a continuous aluminium surface. In the region of the +1 Littrow angle, the Ag-Ag grating has the highest efficiency followed by the two bi-metallic gratings Al-Ag and Ag-Al in that order. It is interesting that the form of the efficiency curves for both the bi-metallic gratings follows closely that for the silver grating as opposed to the initial aluminium grating.

3.2.2 *The $26^{o}45'$ blaze angle grating*

Fig. (3.4) displays the experimental curves demonstrating the changes that occur in the S polarization anomalies for a grating of blaze $26^{o}45'$ for various metallic coatings. Certainly the total diffracted energy curves observed for this grating do not exhibit the dramatic effects of resonance anomalies displayed by the 9^{o} blaze grating. There are no sharp absorption maximum which affected the efficiency of the previous grating. However, the efficiency in the +1 Littrow regions has been reduced. Although there are no diffracted energy curves presented for the Ag-Al bi-metallic grating, it is interesting to note that for all but one of the sets of efficiency curves, the behaviour of the Al-Ag grating closely imitates that of the silver rather than the aluminium grating. The only exception is the +1 diffracted order where the similarity in efficiency curves between the bi-metallic grating and the Al-Al grating is startling. Introducing the different conductivity coating to the off-blaze facet has been successful in reducing the influence of the resonance anomalies occurring in the ±1 efficiency curves, however, it has not lead to a dramatic improvement in the overall effective efficiency.

Fig. (3.4)

Observed diffracted energy spectra for a triangular profile grating having a blaze angle of $26^{o}45'$ and a right-angle apex. Each graph displays the S polarized diffracted energy as a function of the incidence angle for a constant wavelength of 632.8 mm. The efficiency for the 3 diffracted orders ±1, 0, together with the total diffracted energy efficiency are illustrated. The symbols for the curves appearing in the graphs represent the following configurations:

(i) Al-Al ————————

(ii) Al-Ag – – – – – – –

(iii) Ag-Ag .....

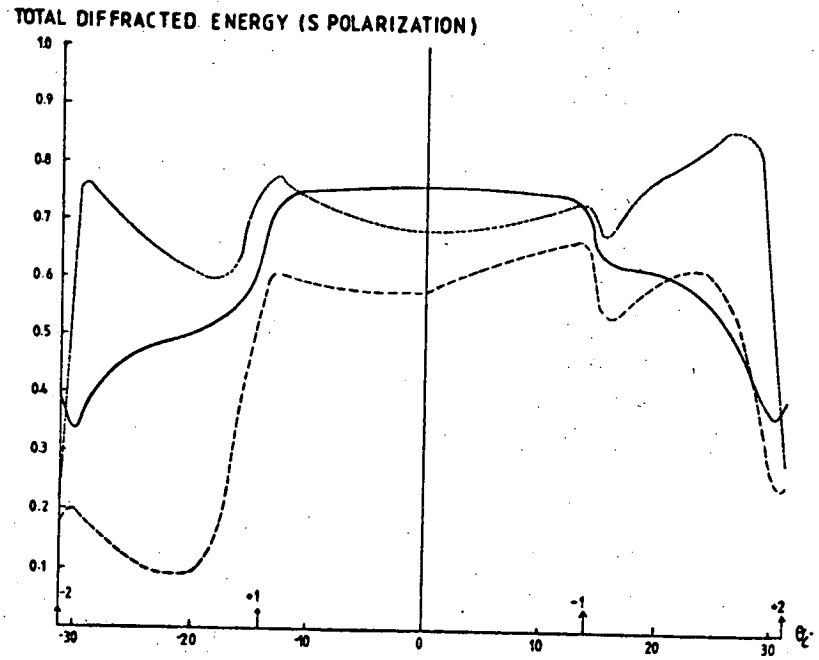
TOTAL DIFFRACTED ENERGY (S POLARIZATION)
1.0
0.9
0.8
0.7
0.6
0.5
0.4
0.3
0.2
0.1
-2
+1
-1
+2
-30
-20
-10
0
10
20
30
θi

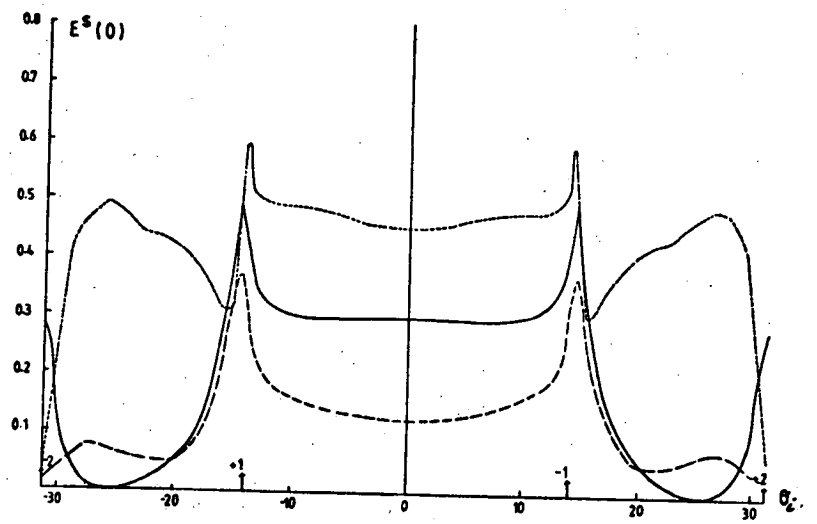
E^S(0)
0.8
0.7
0.6
0.5
0.4
0.3
0.2
0.1
-2
+1
-1
+2
-30
-20
-10
0
10
20
30
θi

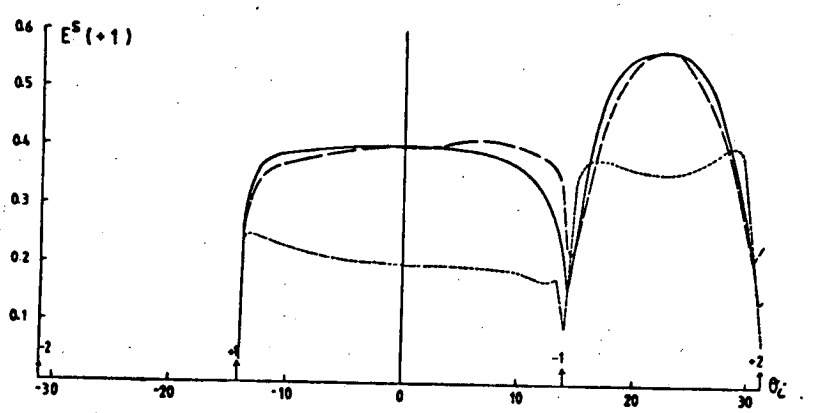
E^S(+1)
0.6
0.5
0.4
0.3
0.2
0.1
-2
+1
-1
+2
-30
-20
-10
0
10
20
30
θi

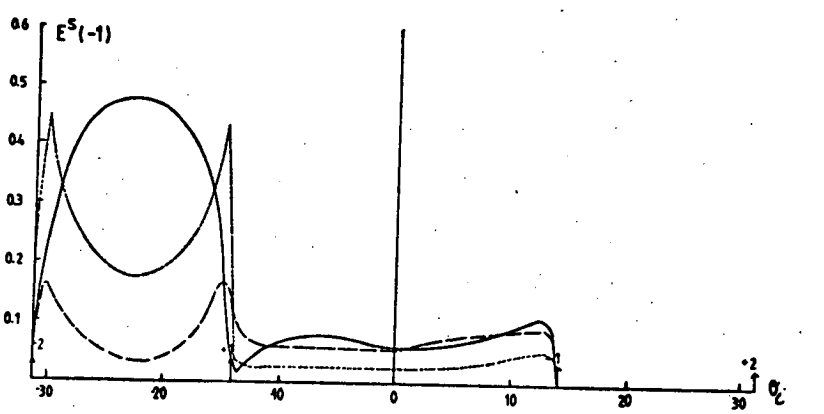
E^S(-1)
0.6
0.5
0.4
0.3
0.2
0.1
-2
+1
+2
-30
-20
40
0
10
20
30
θi

3.2.3 *Concluding remarks*

The diffracted energy and efficiency curves measured in the course of this study certainly confirm the existence of a strong relationship between the form and position of the resonance anomalies and the conductivity of the grating surface. Without doubt a bi-metallic surface alters the energy absorbed by surface waves. This phenomenon is clearly demonstrated by the 0^{o} blaze grating where the minima for both bi-metallic gratings are broader than for the single metal coatings. However, the lessening of the resonance influence occurs at the sacrifice of the total diffracted energy in the region of the +1 Littrow angle.

In terms of the form of the spectral behaviour, bi-metallic gratings appear to resemble the single coated grating having the surface layer of higher conductivity. This effect is apparent irrespective of where the higher conductivity coating is situated on the grating surface. Consideration of the magnitude of the total energy diffracted by the 9^{o} blaze grating reveals that of the two bi-metallic gratings, the efficiency corresponding to the Ag-Al configuration is the higher, while the ±1 efficiency curves exhibit little difference between the coatings. Obviously this can be attributed to the presence of the higher conductivity layer of silver on the longer blaze facet of the grating. However, the discontinuity in conductivity across the grating surface reduces the overall efficiency of the two bi-metallic gratings to below that of either single-coated gratings.

In his numerical study of bi-metallic gratings Botten considered a metal of low-conductivity as the off-blaze plug. The results

indicated that the additional metal coating needs to have a relatively low conductivity in order to create lossy plasmon resonances of a sufficiently broad nature to mask any sharp spectral features. This does not appear to be the case in practice, since plugs of high conductivity have been observed to obliterate the resonance anomalies. However, it is possible that we are falsely attributing the observed variations in spectral behaviour of the bi-metallic gratings to the formation of lossy plasmons. The observed reduction in the diffracted efficiency subsequent to the resonance anomaly may be a consequence of a property of the refractive index of the surface material unrelated to the creation of lossy plasmons.

Although the success of this investigation has been limited, it represents an insight into the experimental behaviour of bi-metallic gratings. Since resonance anomalies destroy the effective spectral range of a diffraction grating, all avenues leading to their elimination must be thoroughly explored.

3.3 "CONFORMALLY COATED" GRATINGS

To ensure that the alterations of the spectra observed following the application of the additional coatings to the surface of the gratings in the previous section were not initiated by variations in groove profile, several further coatings of aluminium were applied to the total grating surface. The energy diffracted into the 0th order for S polarized light was monitored between repeated evaporations. As the efficiency curves were plotted a a curious phenomenon was revealed. Further evaporation of aluminium onto the grating surface was producing a pronounced reduction in the

-2 resonance anomaly. A rough sketch of these initial promising results is depicted in Fig. (3.5). This behaviour is attributed to the formation of a dielectric layer of Al_2O_3 formed during evaporation. This was due to the actual coating pressure being too high due to the lack of a suitable diffusion pump of large enough capacity. A detailed investigation was then commenced.

3.3.1 *Dielectric coatings on grating*

The serious loss of efficiency resulting from the formation of an oxide layer on aluminium gratings can be prevented by an appropriate dielectric coating. A recent resurgence of interest in the properties of gratings having a dielectric surface has led to a comprehensive understanding of the manner in which these gratings alter the spectral performance of a grating.

Wood observed anomalies only for S polarized light, however in 1952 Palmer [3.10] demonstrated that diffraction anomalies did occur for the orthogonal (P) polarization and that these were enhanced by an overcoating of a dielectric film. Further experimental work by Cowan and Arakawa [3.11] has shown that quite thin dielectric layers, such as the usual oxide layer that forms an aluminium, markedly affect the spectral performance of the grating.

Nevière et al [3.12] produced the first theoretical results illustrating the effect of dielectric layers on gratings of infinite conductivity used in the Littrow mount. Their study predicted that for dielectric coatings, S polarization anomalies split in two, while very strong P polarization anomalies are introduced. These theoretical assertions were confirmed by a detailed experimental investigation into the effect of overcoating a metal grating with a

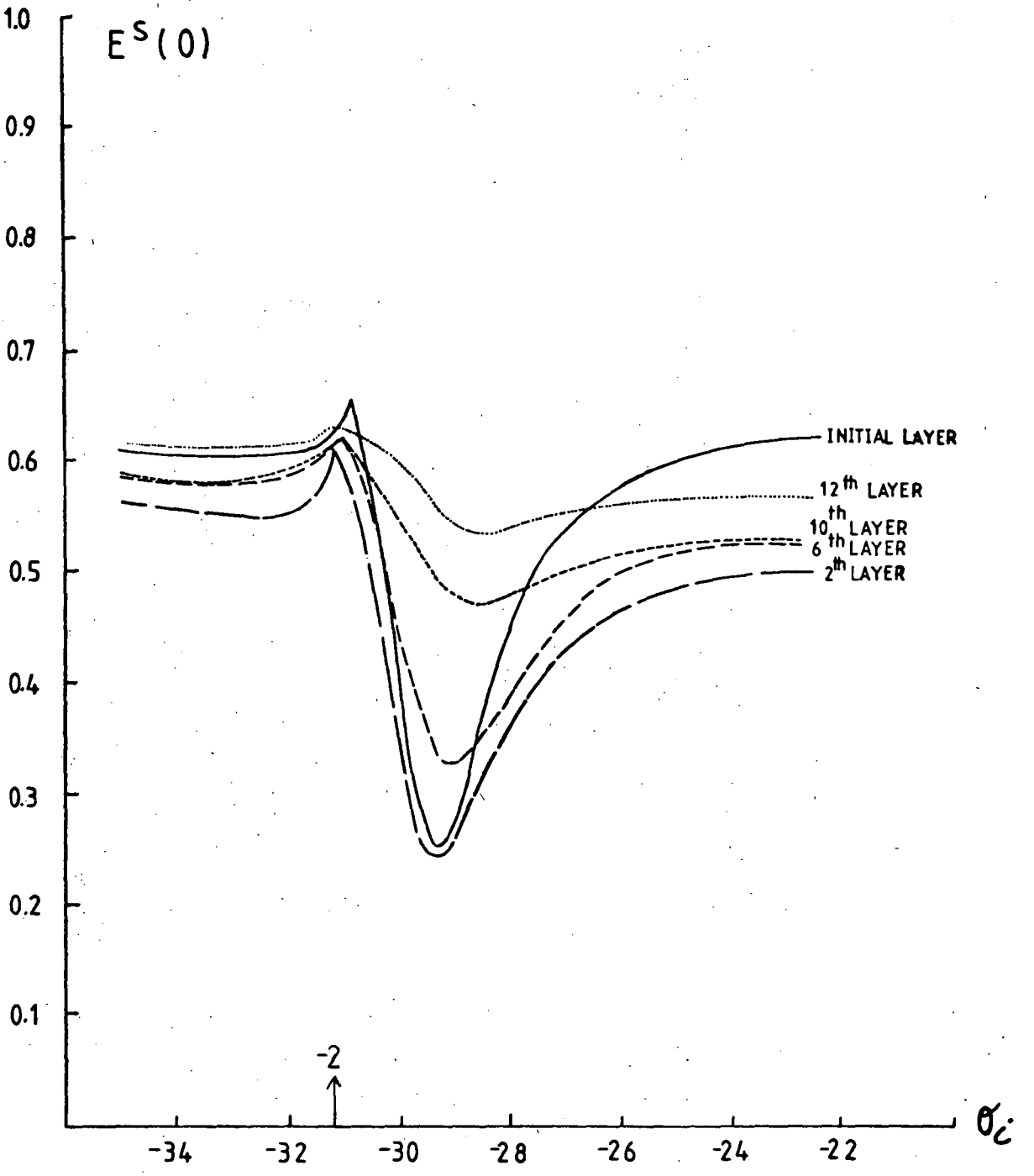

Fig.(3.5) Variations in the 0^{th} order efficiency curve in the region of the -2 resonance anomaly with additional Al layers.

dielectric carried out in 1974 by Hutley et al [3.13]. It has been demonstrated by theory and corroborated by experiment that metallic gratings cannot adequately be described by infinite conductivity formalisms. Consequently in 1975 Hutley et al [3.14] derived a rigorous formulism for the study of diffraction by a grating of finite conductivity covered with a thin film of dielectric. The results were in excellent agreement with those observed by previous experimental investigations. The most recent developments in dielectric grating theories were achieved by Maystre [3.15], who presented a rigorous integral formalism for the theoretical study of dielectric coated gratings which predicts, in the entire range of wavelengths and for any polarization, the behaviour of metallic, dielectric, or infinitely conducting gratings coated with any number of dielectric or metallic films.

3.3.2 *Experimental method*

Measurements were taken for two 1200g/mm, 9^{o} blaze gratings, studied in the previous bi-metallic investigation. This grating is ideal for resonance evaluation due to the very strong anomalies occurring in the 0th order and consequently in the total diffracted efficiency curves corresponding to the -2 and +1 anomalies. One grating was repeatedly coated with additional aluminium layers at a pressure of 5×10^{-6} TORR, while a layer of Al_2O_3 was allowed to form on the surface of an equivalent grating by the evaporation of aluminium at the high pressure of 10^{-4} TORR. This latter grating was then treated in a similar manner to the first, with additional coats of aluminium being evaporated onto the surface over the dielectric film. The thickness of each layer was determined from

the theoretical considerations of Holland [3.16], who demonstrated that the thickness of the deposit on a receiver at a hight h, above a point source of total mass m and density ρ, is given by

$$t_o = \frac{m}{4\pi\rho} \cdot \frac{1}{h^2} \tag{3.2}$$

Following each evaporation, the efficiencies were measured as a function of angle of indence for the constant wavelength of 632.8 nm for all diffracted orders propagating in the angular range -31.25^o to -12^o.

3.3.3 *Resulting experimental efficiencies*

Displayed in Tables (3.1) and (3.2) are the thicknesses of the total additional aluminium layers evaporated onto each of the two gratings. The observed constant wavelength efficiency curves for the total diffracted energy and the 0th order for the finitely conducting and dielectric gratings are shown in Figs. (3.6) and (3.7) respectively. Consider initially the efficiency measurements corresponding to the all aluminium grating. Since the first additional layer exhibited no noticeable variation in spectral performance from that of the initial grating, it is not displayed. However, all subsequent coatings initiate perturbations in the efficiency curves. The position of the resonance minima continually shift away from the Wood anomalies, while the magnitude of the energy absorbed is reduced. Furthermore, the efficiency in the region of the +1 Littrow angle is lessened. According to the numerical results of Botten [3.7], the movement and reduction of the resonance minima are indicative of a change in conductivity of the surface layer. Clearly, even at a pressure of 5×10^{-6} TORR, a thin film of contaminants has formed on the grating, altering the conductivity of the diffracting layer.

Coating Number	Total Thickness (nm)
1	146
2	292
3	584
5	1022

TABLE(3.1) Total calculated thickness of additional aluminium layers following a given number of evaporations.

Coating Number	Total Thickness (nm)
Dielectric	292
1	487
5	1071
8	1509
12	2093

TABLE(3.2) Total calculated thickness of additional aluminium layers following a given number of evaporations.

Fig. (3.6)

Observed diffracted energy spectra for a triangular profile grating having a blaze angle of 9^{o} and a right-angled apex. Each graph displays the S polarized diffracted energy as a function of the incidence angle for a constant wavelength of 632.8 mm. The symbols for the curves appearing in the graphs represent the following coatings:

———— Initial Al surface

--------- 3rd Additional Al coating

..... 5th Additional Al coating

Fig. (3.6(a)) Total diffracted energy in region of -2 Wood anomaly.

(3.6(b)) Oth order efficiency in region of -2 Wood anomaly.

(3.6(c)) Total diffracted energy in region of +1 Wood anomaly.

(3.6(d)) Oth order efficiency in region of +1 Wood anomaly.

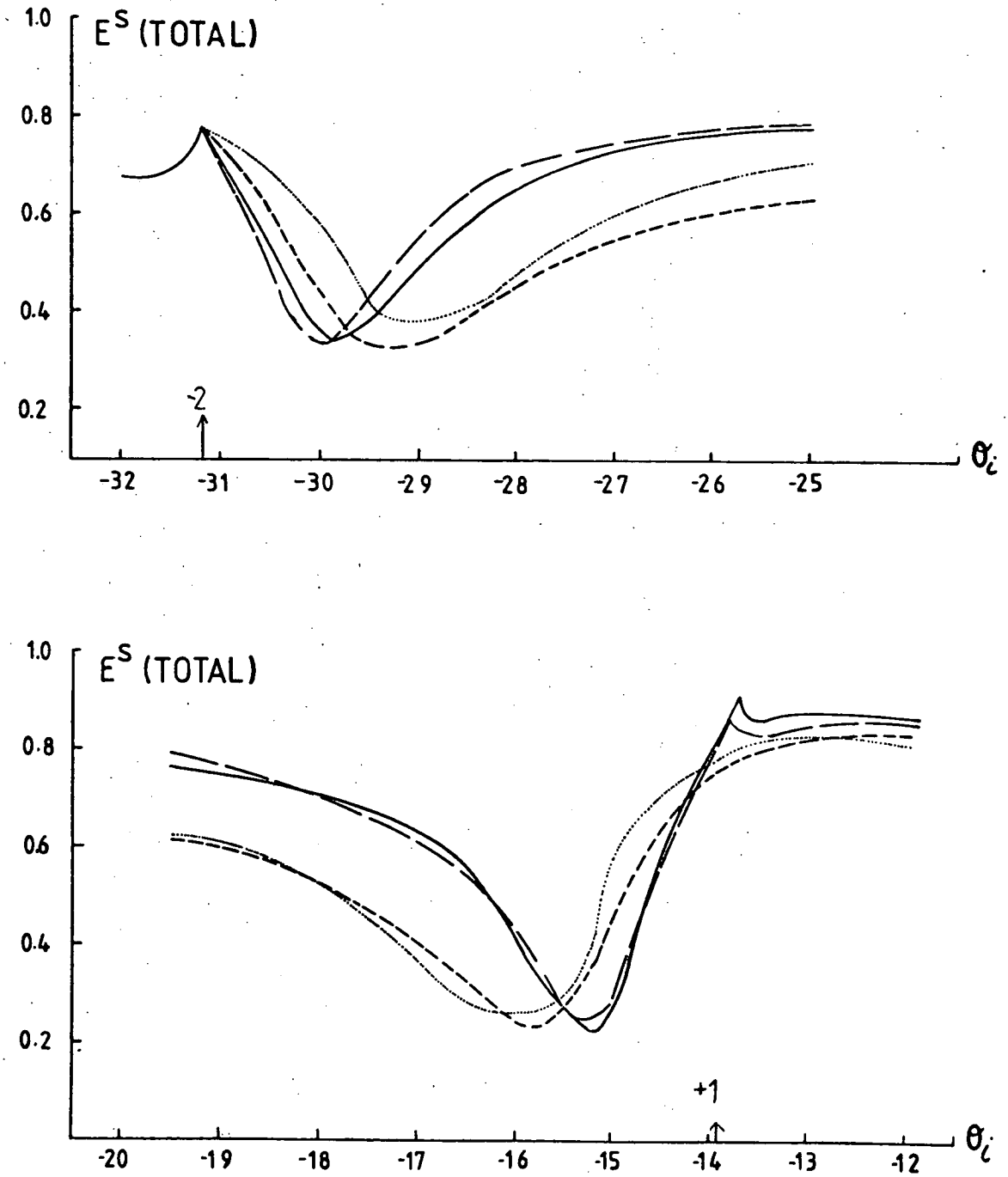

Fig. (3.6(a)) and Fig. (3.6(c))

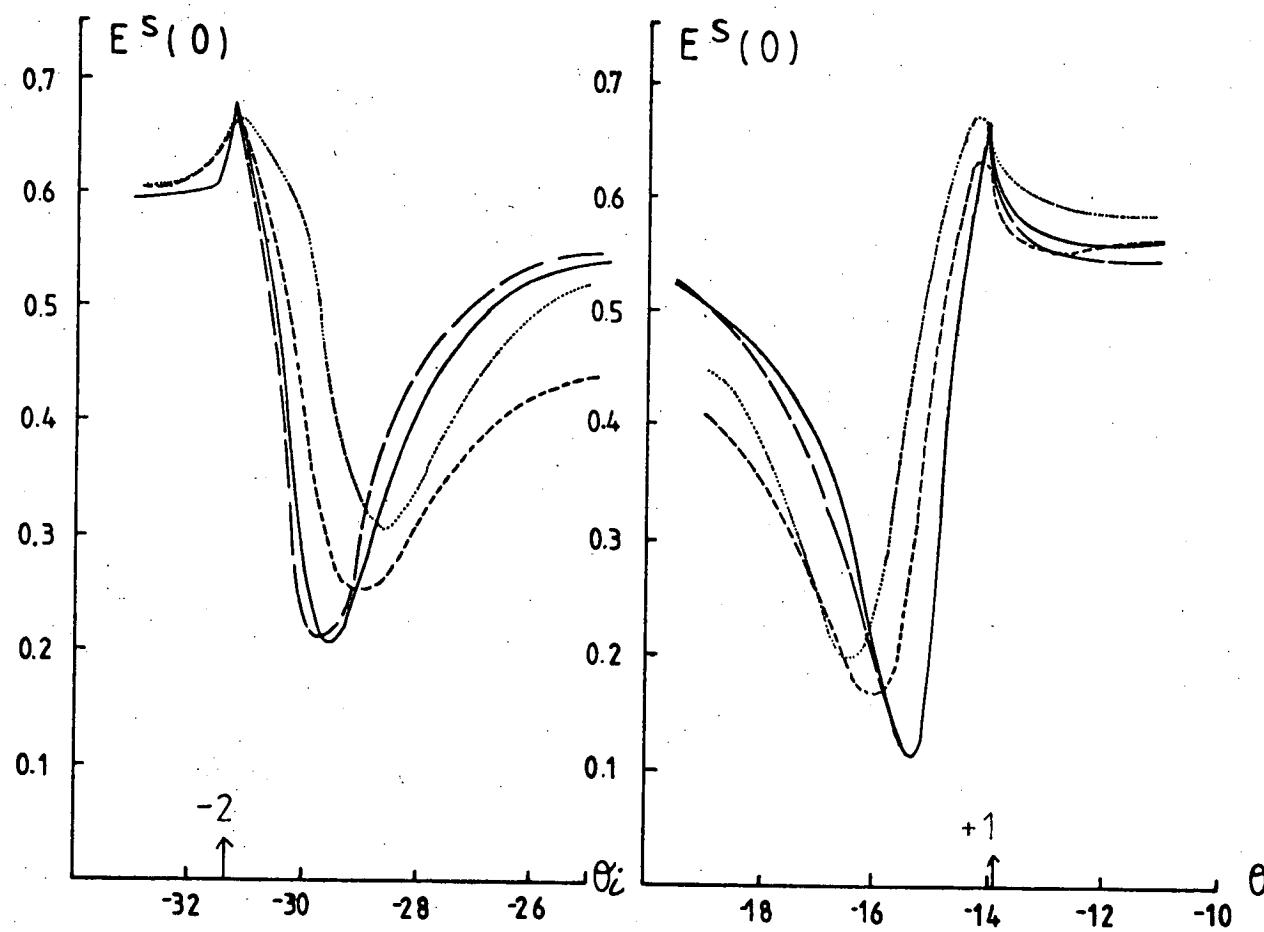

Fig.(3.6(b)) and Fig.(3.6(d))

Fig. (3.7)

Observed diffracted energy spectra for a triangular profile grating having a blaze angle of 9^{o} and a right-angled apex. Each graph displays the S polarized diffracted energy as a function of the incidence angle for a constant wavelength of 632.8 mm. The symbols for the curves appearing in the graphs represent the following coatings:

———— Initial Al surface

—— —— Dielectric Al_2O_3 layer

– – – – – 5th Additional Al coating

---------- 8th Additional Al coating

..... 12th Additional Al coating

Fig. (3.7(a)) Total diffracted energy in region of -2 Wood anomaly.

(3.7(b)) 0th order efficiency in region of -2 Wood anomaly.

(3.7(c)) Total diffracted energy in region of +1 Wood anomaly.

(3.7(d)) 0th order efficiency in region of +1 Wood anomaly.

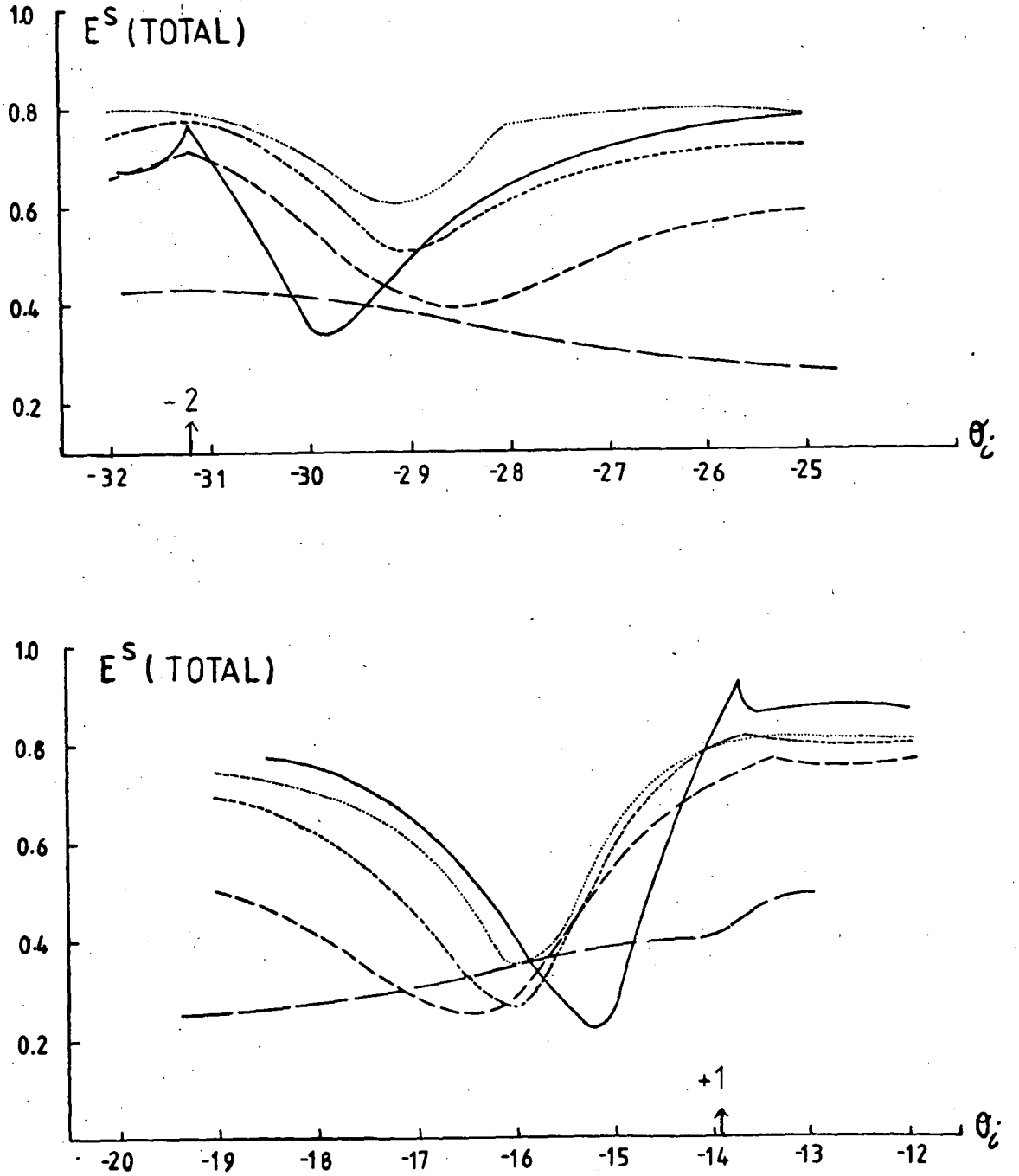

Fig. (3.7(a)) and Fig. (3.7(c))

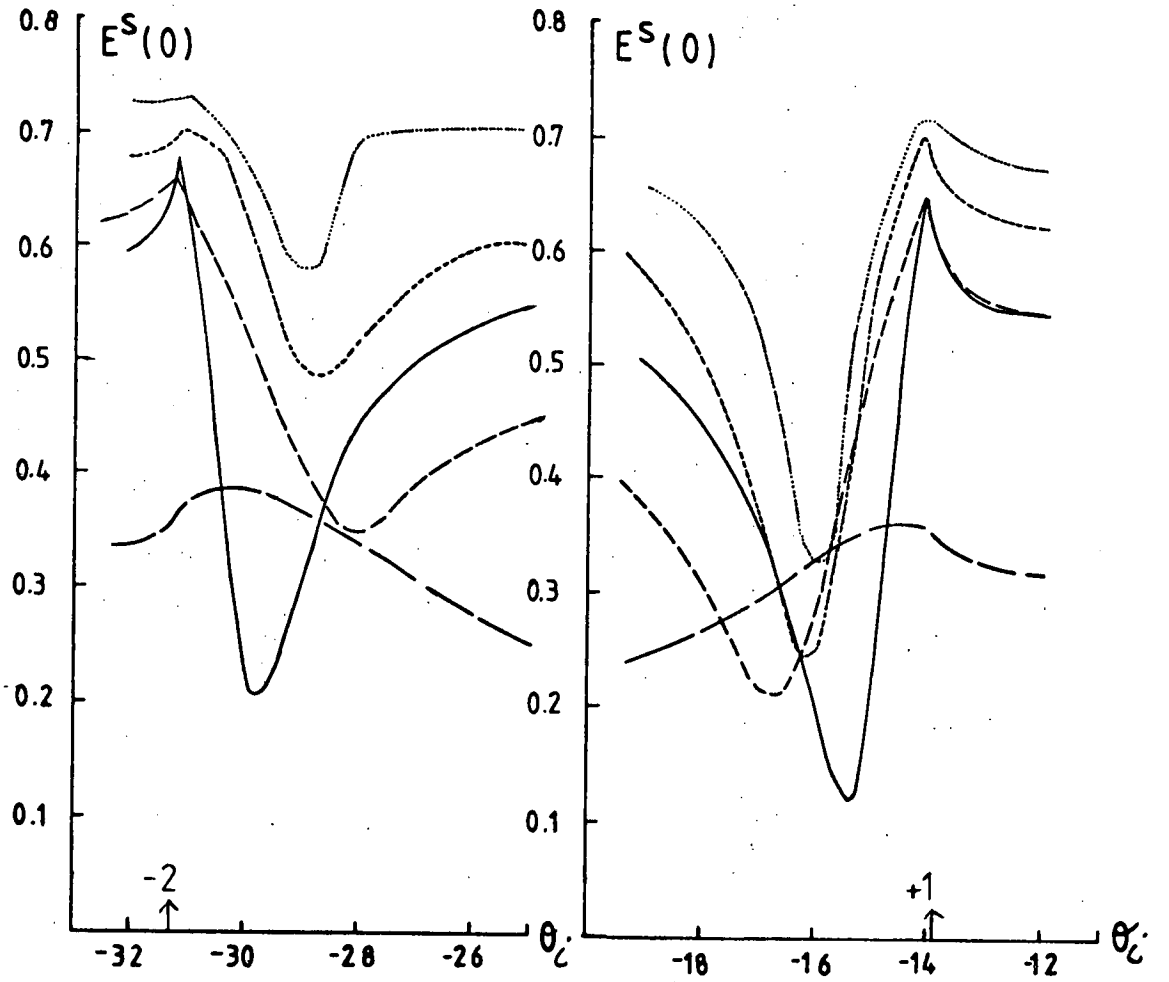

Fig.(3.7(b)) and Fig.(3.7(d))

As predicted by Hutley et al [3.13], Fig. (3.7) shows that the dielectric layer has both drastically reduced the spectral performance of the grating and smoothed out the anomalies. However, following the evaporation of a single layer of aluminium over this dielectric, the form of the spectral efficiency immediately reverts to that of the finitely conducting surface. In a manner similar to that observed previously in Fig. (3.6) the diffracted energy minima has moved further away from the Wood anomalies and the post-anomaly efficiency has failed to achieve a level comparable to that observed for the initial grating. By the fifth overcoating, the resonance absorption peaks are noticeably diminishing, particularly for the -2 anomaly. As further coatings are applied general trends in changes to the spectral behaviour manifest themselves.

The incidence angles corresponding to the maximum absorption of energy follow trajectories back towards the position of the initial grating anomalies. With each additional evaporated layer, the magnitude of the absorbed energy decreases and the overall efficiency of the grating increases so that for the -2 resonance anomaly it exceeds that displayed by the bare grating. It would be expected that an overcoating of 2 μm thickness, would be sufficient to mask the underlying dielectric layer. This is certainly indicated by the return of the absorption peak to that prior to the application of the dielectric film. However, the diminishing resonances imply the opposite. It was demonstrated earlier that each aluminium layer is contaminated during deposition, while exposure to air must produce further films of Al_2O_3. Cowan et al [3.5] showed that very thin layers of dielectric influence the spectral behaviour. Thus the

diminishing resonances suggest that an interaction occurs between the finitely conducting layers and thin oxide layers of the grating surface. Strangely, the reduction for the -2 anomaly is more diamatic than that occurring for the +1 anomaly. However, it is anticipated that the energy absorbed by this latter resonance anomaly would decrease with further coatings.

3.4 CONCLUDING REMARKS

The bi-metallic results, although not notably successful, are interesting in that they give an indication of the practical behaviour exhibited by gratings of discontinuous surface conductivity.

The second investigation has been more fruitful with the observations being very promising for resonance reduction. The observed efficiencies certainly suggest success in diminishing the energy absorbed by surface plasmons. An interaction between layers of finitely conducting and dielectric materials must account for this phenomenon, but an explanation for this interaction has not been discussed. However, the rigorous formalism of Maystre [3.15] describing the behaviour of a multi-layered, discontinuous conductivity surface, should be ideal for a theoretical investigation of resonance reduction by conformally coated gratings.

In the following chapter, developments in the operation of dye lasers are achieved through a numerical study of grazing incidence grating efficiencies.

REFERENCES

[3.1] Wood R.W. (1902) Phil. Mag., 4, 396.

[3.2] Rayleigh Lord (1907) Phil. Mag., 14, 60.

[3.3] Hessel A. and Oliner A.A. (1965) Appl. Optics, 4, 1275.

[3.4] Hutley M.C. and Bird V.M. (1973) Optica Acta, 20, 607 and 771.

[3.5] Cowan J.J. and Arakawa E.T. (1977) Opt. Commun., 21, 428.

[3.6] Wheeler C.E., Arakawa E.T. and Ritchie R.H. (1976) Phys. Rev. B, 13, 237.

[3.7] Botten L.C. (1978) Ph.D. Thesis, University of Tasmania.

[3.8] Sugahara K., Kita T. and Shimotakahara T. (1974) Proc. Sym. on Diffraction Gratings and Grating Instruments. Spec. Soc. Japan, 21.

[3.9] Botten L.C. (1980) J. Optics, 11, 161.

[3.10] Palmer C.H. (1952) J. Opt. Soc. Amer., 42, 269.

[3.11] Cowan J.J. and Arakawa E.T. (1970) Z. Physik, 97, 235.

[3.12] Nevière M., Cadilhac M. and Petit R. (1972) Optics Commun., 6, 34.

[3.13] Hutley M.C., Verrill J.F. and McPhedran R.C. (1974) Optics Commun., 11, 207.

[3.14] Hutley M.C., Verrill J.F., McPhedran R.C., Nevière M. and Vincent P. (1975) Nouv. Rev. Optique, 6, 87.

[3.15] Maystre D. (1978) J. Opt. Soc. Amer., 68, 490.

[3.16] Holland L. (1958) Vacuum Deposition of Thin Films (London: Chapman and Hall Ltd.).

CHAPTER 4

TUNING DYE LASERS AT GRAZING INCIDENCE

4.1 PRELIMINARY COMMENTS

This brief chapter describes the first efforts towards choosing suitable grating groove frequencies and geometry, both blazed and sinusoidal for operation at grazing incidence as an example of the use of electromagnetic theories to improve the performance of grating instruments. Previous publication of theoretical grating efficiencies [4.1] has not included the grazing incidence region. Use of the increasingly popular nitrogen - laser - pumped dye laser functioning at grazing incidence is investigated, and the dependence of the efficiency upon the angle of incidence is also discussed.

4.2 DYE LASERS

Since Hänsch [4.2] reported the first successful cavity design for pulsed tunable dye lasers, the instrument has had a profound impact upon optical spectroscopy. Initially, the spectral narrowing and tuning were achieved by a diffraction grating in a Littrow mounting near grazing incidence. Wavelength selectivity was improved by using an intracavity beam expander such as a lens telescope or a prism. Unfortunately, such designs have several serious disadvantages. Diffraction gratings blazed for such unusual angles of incidence are not readily available. Similarly the linewidth and direction of the output is strongly dependent upon the rotation angle.

Shoshan et al [4.3] suggested that these design faults could be overcome by utilizing the diffraction grating in a non-Littrow mounting, with a retro-reflecting mirror to tune the dye laser.

Such an arrangement generates an angular dispersion twice as large as that obtained in the usual Littrow configuration under the same conditions. However, in order for this method to be competitive with other techniques, the grazing incidence grating needs to have a high efficiency. This problem lends itself to an extensive numerical study utilizing a rigorous electromagnetic theory.

4.3 GRAZING INCIDENCE GRATING EFFICIENCIES

A search for optimal groove modulation, blazed and sinusoidal, is conducted using Maystre's finite conductivity formalism for plane reflection gratings. Equally important is a search to locate optimal groove frequencies. Since P- plane efficiencies are always low at large angles of incidence, only light polarized with the electric vector perpendicular to the grooves (S- plane) is considered.

When the illumination is near grazing incidence, the whole width of the grating may be illuminated. In this way the highest resolution obtainable with the grating is achieved. Consequently, the search is commenced by choosing a fixed angle of incidence of 89^{o} at a single wavelength of 632.8 nm. The groove depth is varied for several groove frequencies. Once the optimum ranges for both were found, an investigation of the effect of varying the angle of incidence is conducted. Following this procedure, all the necessary information proved obtainable.

Standard groove frequencies of 600 gr/mm, 1200 gr/mm, 1800 gr/mm and 2400 gr/mm were studied. The first two groove frequencies turned out to have lower efficiency values than the finer pitch gratings. This is a fortuitous circumstance, since the latter also have the necessary high dispersion. The most interesting of these

sets of results are displayed in Figs. (4.1)and (4.2). For ruled gratings, only the 1800 gr/mm grating shows real promise (Fig.(4.1)), and then only if the blaze angle exceeds 30^{o}. Such gratings are notoriously difficult to produce. Fig. (4.2) shows the behaviour of the equivalent sinusoidal gratings. Higher efficiencies appear to be obtainable with sinusoidal gratings, however, only at depth modulations so high that they have not yet been reported for 1800 gr/mm gratings. It is of interest to discover that infinite conductivity surfaces have remarkably high efficiencies at low modulation depths. No equivalent phenomenon occurs for triangular groove profiles. The 2400 gr/mm results turn out to be particularly important, because while they show similar efficiency in the 20% (h/d = 0.2) modulation range which is readily achievable, this is accompanied by 33% increased dispersion, compared with 1800 gr/mm. One can see from the previously published theoretical calculations of Loewen et al [4.1] that this must be due to the difficulty of obtaining sufficiently deep sinusoidal modulation at 1800 gr/mm.

The second part of this chapter illustrates how efficiency depends on the angle of incidence. Fig. (4.3) shows 1800 gr/mm blazed gratings with $26^{o}45'$ and 37^{o} blaze angles. The advantage of the latter, if it can be produced, is evident. The sharp drop in efficiency with incidence angle is only too obvious. Fig. (4.4) is for fairly deeply modulated (30%) sinusoidal gratings with 1800 and 2400 gr/mm groove frequencies, respectively. There is a slight efficiency advantage for 1800 gr/mm, which in practice is more than counterbalanced by the increased dispersion of the 2400 gr/mm.

Since for the angles described here one always works with a wavelength-to-groove spacing ration λ/d near 1, the grazing incidence

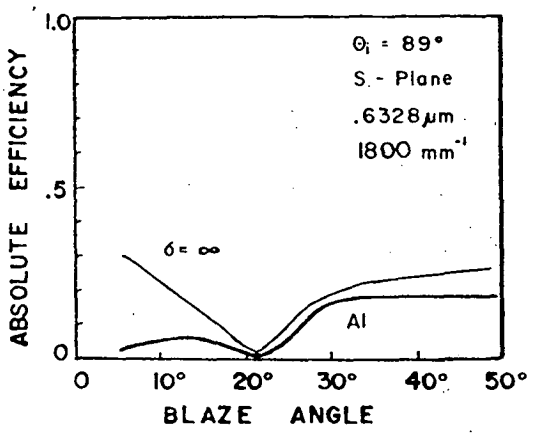

Fig.(4.1) Theoretical absolute first order efficiency in S-plane polarization as a function of blaze angle θ_B. Wavelength 632.8nm. Groove frequency 1800mm^{-1}. Angle of incidence 89°. Infinite conductivity (fine line), aluminium surface (heavy lines).

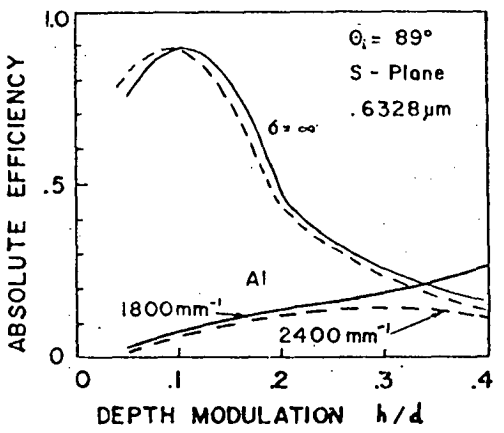

Fig.(4.2) Similar to Fig.(4.1) except groove shape is sinusoidal with its height ratio H/D as the variable. 1800mm^{-1} groove frequency (solid lines), 2400mm^{-1} (dashed lines).

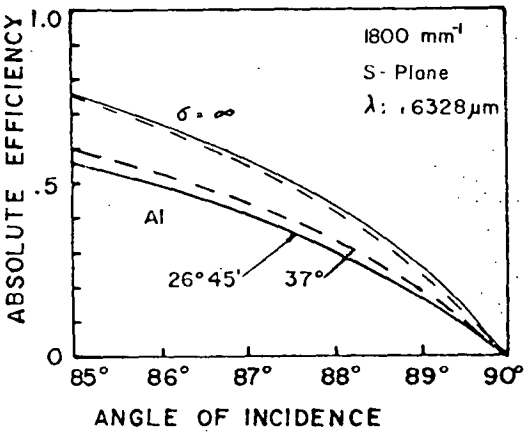

Fig.(4.4) Similar to Fig.(4.3), except for sinusoidal grooves with 30% depth modulation. 1800mm^{-1} groove frequency (solid lines), 2400mm^{-1} (dashed lines).

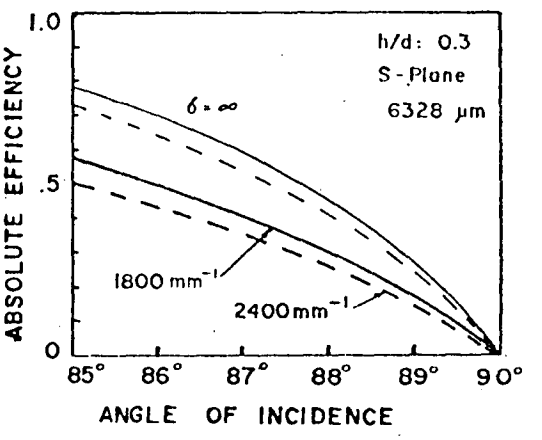

Fig.(4.3) Theoretical S-plane first order efficiency for 1800mm^{-1} blazed grating as a function of angle of incidence. 26°45' blaze angle (solid curves), 37° blaze angle (dashed curves). Infinite conductivity surface (fine lines); aluminium (heavy lines). Wavelength 632.8nm.

tuning concept can be transposed to other wavelengths by simply decreasing groove frequency in proportion to wavelength increase. Performance will improve with increasing wavelength because metal reflection behaviour approaches that of infinite conductivity.

4.4 CONCLUDING REMARKS

By investigating grating efficiencies at grazing incidence, gratings of suitable groove modulation, blazed and sinusoidal have been determined which ensure the design of high gain dye lasers. Such lasers represent viable alternatives to the configuration of Hänsch which depends upon an intracavity beam expanding telescope together with a diffraction grating in Littrow mount for wavelength tuning.

This chapter completes the discussion of plane diffraction gratings in this thesis. Attention is now directed towards diffraction gratings generated on non-planar surfaces. In particular the geometric theories of Noda et al are applied to spherical concave gratings in the construction of aberration-corrected grating instruments. Initially the aberration coefficients derived in Chapter 1 using Fermat's principle, are used to design aberration reduced Rowland circle spectrographs. Aberration minimizing techniques are then employed in the development of a very simple, uni-axial monochromator containing two concave gratings.

REFERENCES

[4.1] Loewen E., Neviere M. and Maystre D. (1977) Appl. Opt., 16, 2711.

[4.2] Hänsch (1972) Appl. Opt., 11, 895.

[4.3] Shoshan I., Danon N. and Oppenheim U. (1977) J. Appl. Phys., 48, 4495.

CHAPTER 5

ROWLAND CIRCLE MOUNT ABERRATION CORRECTION

5.1 PRELIMINARY COMMENTS

In the following chapter the aberration coefficients derived using Fermat's principle are used to examine the state of correction of Rowland circle spectrographs when the mounting and recording points lie on the Rowland circle. Initially the correction at two wavelengths of primary astigmatism or primary coma under this constraint is demonstrated. This treatment is then generalized to show how to correct primary astigmatism or primary coma at two wavelengths in two orders. A further state of correction that permits the simultaneous correction of primary astigmatism and primary coma for a given value of $1 < m\lambda/\lambda_0 < 2$ is introduced.

5.2 ROWLAND CIRCLE MOUNT

Most spectrographs using a concave grating utilize a configuration known as the Rowland circle mount. In 1881 H.A. Rowland [5.1] drew attention to the properties of this circle by the following words.

> *"In thinking over what would happen were the grating ruled on a surface not flat I thought of a new method of attacking the problem, and soon found that if the lines were ruled on a spherical surface the spectrum would be brought to a focus...*
>
> *"The laws of the concave grating are very beautiful on account of their simplicity. Draw the radius of curvature of the grating to the centre of the mirror and from its central point with a radius equal to half*

the radius of curvature draw a circle; this cirle passes through the centre of curvature of the grating and touches the grating at its centre. Now if the source of light is anywhere in this circle, the image of this source and the different orders of the spectra are all brought to focus on this circle. The word focus is hardly applicable to the case, however, for if the source of light is a point the light is not brought to a single point on the circle, but is drawn out into a straight line with its length parallel to the axis of the circle."

Rowland's observation of the light forming a straight line in the image plane rather than the anticipated spot, is a good example of one of the major faults of any Rowland circle mount, the aberrations, especially the large astigmatism inherent in the system. Thus it is clear that if one wishes to take full advantage of the elegant simplicity of the Rowland circle mount, a method for reducing these aberrations must be found.

Typically a Rowland circle mount has three elements - an entrance slit through which the light passes before being incident at the surface of the second element - a concave grating, from which the desired wavelength is diffracted through the remaining element - the exit slit situated on the focal curve. One such mounting was devised by Paschen and Runge and is often referred to as the Paschen-Runge Mount. Both the entrance slit and the grating are fixed on on the Rowland circle giving a chosen angle of incidence, usually in the neighborhood of 45^{o} and the angle of diffraction covers a very extensive range of the focal circle, perhaps from -40^{o} to $+ 70^{o}$. The Paschen-Runge mounting and recording geometry is illustrated in Fig. (5.1). The approximate angular range covered by this and

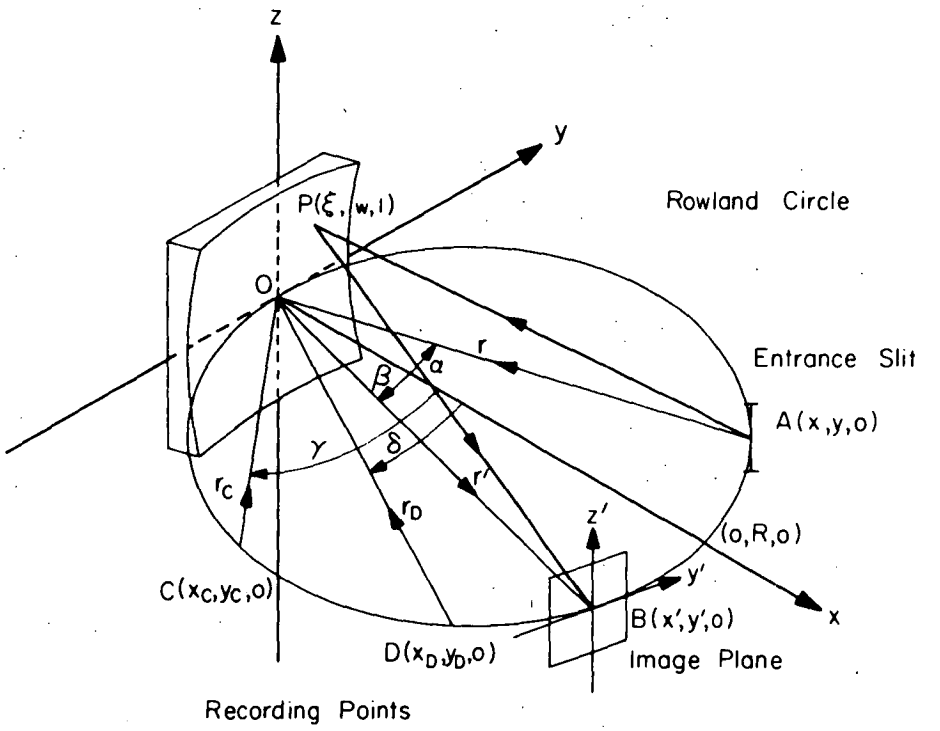

Fig.(5.1) Rowland circle mounting and recording geometry.

similar mounts were conveniently summarized in diagramatic form by Zernike [5.2] and later by Beutler [5.3] and Welford [5.4]. Welford improved the method of data presentation developed by the previous authors and it is his representation which is utilized in Fig. (5.2) where the sines of the angles of incidence and diffraction are plotted linearly.

5.3 ABERRATION CORRECTION PROPERTIES OF THE ROWLAND CIRCLE

This treatment of the imaging properties of the Rowland circle mount follows closely the theoretical approach of previous authors (see, for example, [5.5-5.9]) who have used Fermat's principle to derive a power series expansion for the light path function F in terms of the aberration coefficients F_{ijk} which in turn depend on the mounting configuration and additionally in the case of holographic gratings on the recording parameters. The method follows as closely as possible the notation used by Noda et al [5.5, 5.6] and their theory forms the basis of the present work.

It was demonstrated in a previous chapter that to eliminate any aberration term from the final spectral image for a particular wavelength and diffracted order, the corresponding aberration coefficient, F_{ijk} must be identically equal to zero. For a mechanically ruled diffraction grating where the coefficient, F_{ijk}, is dependent only on the instrument parameters, the absence of any aberration term from the final image is a consequence of the manipulation of the mounting conditions. Here lies the beauty of a Rowland circle mount - at least three aberration terms can be eliminated from the spectral image for all wavelengths.

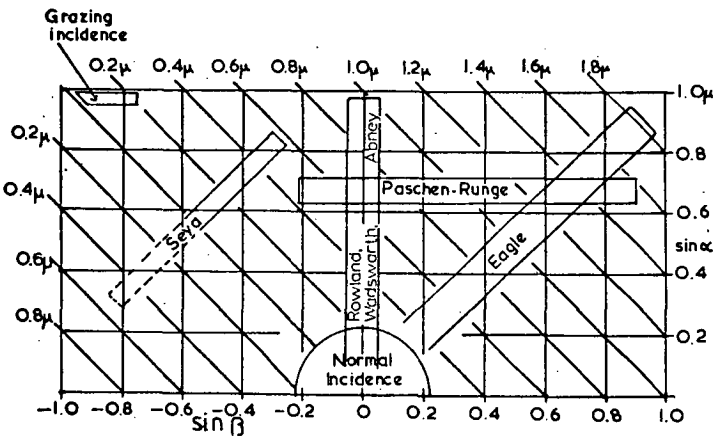

Fig.(5.2) Concave grating mountings. The diagonal lines correspond to wavelengths according to the grating equation

$$\sin\alpha+\sin\beta=m\lambda/\sigma$$

with σ/m equal to one micron. [After W.T.Welford, Progress In Optics IV (North-Holland Publishing Co., Amsterdam, 1965), p241].

Numerous authors have discussed this property showing that for a ruled concave grating mounted on the Rowland circle, where the position of the entrance slit and focal point are restricted by the relations

$$R = r\cos\alpha \qquad \text{or} \qquad \rho = \frac{1}{\cos\alpha}$$

and (5.1)

$$R = r'\cos\beta \qquad \text{or} \qquad \rho' = \frac{1}{\cos\beta}$$

the coefficients F_{200}, F_{300} and F_{400} are identical to zero for all wavelengths. Recalling that the coefficient, F_{200}, for a ruled grating is described by

$$F_{200} = (\rho\cos\alpha - 1)\cos\alpha + (\rho'\cos\beta - 1)\cos\beta \tag{5.2}$$

it becomes evident upon substitution of Eqn. (5.1) that the term $F_{200}\left(\frac{\omega^2}{2R}\right)$ disappears from the light path function. Therefore, Eqn. (5.2) describes the horizontal focal curve. Similarly, the coma-like coefficient F_{300} and the higher order term F_{400} are expressed by

$$F_{300} = \rho\sin\alpha\,[(\rho\cos\alpha-1)\cos\alpha] + \rho'\sin\beta\,[(\rho'\sin\beta-1)\cos\beta]$$

and

$$\begin{aligned} F_{400} = {} & \rho(\rho\cos\alpha-1)\cos\alpha\,[\rho(\rho\cos\alpha-1)\cos\alpha-4\rho\sin\alpha] \\ & + \rho'(\rho'\cos\beta-1)\cos\beta\,[\rho'(\rho'\cos\beta-1)\cos\beta-4\rho'\sin\beta] \end{aligned} \tag{5.3}$$

can be easily shown to be indentically zero under the conditions described by Eqn. (5.1)

With holographic concave gratings the aberration coefficients F_{ijk} are governed not only by the mounting conditions, but also by the recording conditions as indicated in the following equation

$$F_{ijk} = M_{ijk} + \frac{m\lambda}{\lambda_0} H_{ijk} \tag{5.4}$$

If this equation is to be identically zero at all wavelengths then both the mounting dependent term M_{ijk} and the recording dependent term H_{ijk} must vanish. It is clear that this may be achieved if the recording positions C and D are constrained to lie on the Rowland circle in a manner similar to that imposed on object and image points A and B. Then the positions of the recording sources are defined by

$$R = r_C \cos_\gamma \qquad \text{or} \qquad \rho_C = 1/\cos_\gamma$$

and (5.5)

$$R = r_D \cos\delta \qquad \text{or} \qquad \rho_D = 1/\cos\delta$$

The horizontal focus coefficient F_{200} then becomes

$$F_{200} = f_{200}(\rho, \alpha) + f_{200}(\rho'\beta)$$

$$+ m \frac{\lambda}{\lambda_0} [(\rho_C \cos\gamma - 1)\cos\gamma - (\rho_D \cos\delta - 1)\cos\delta] \tag{5.6}$$

and is identically zero for all wavelengths under condition (5.5). Similarly the coefficients F_{300} and F_{400} also vanish.

If the contribution due to several aberration coefficients is removed from the image by carefully selecting the mounting and recording conditions, those remaining can still play an important role in hampering the formation of an ideal image. In the present

case it is well known that instead of an ideal image a curved line in the vertical plane is observed. This is due mainly to the large amount of residual astigmatism characteristic of the mount.

5.4 IMAGE HEIGHT AND RESIDUAL SECOND ORDER ASTIGMATISM

It is possible to gain an impression of the effect of residual second order astigmatism on the image height using the method of Beutler [5.3].

Following Noda et al [5.6], the residual second order astigmatism is characterized by the aberration coefficient F_{020} where for a concave grating with the mounting and recording elements all situated on the Rowland circle

$$F_{020} = \left(\frac{1}{\cos\alpha} - \cos\alpha\right) + \left(\frac{1}{\cos\beta} - \cos\beta\right) + m\frac{\lambda}{\lambda_0}\left[\left(\frac{1}{\cos\gamma} - \cos\gamma\right) - \left(\frac{1}{\cos\delta} - \cos\delta\right)\right] \qquad (5.7)$$

The height of the extended image due to astigmatism can be calculated by applying Fermat's principle of the shortest path length to the light path function F. The directions of the light paths in the vertical planes that include z, z' and l are governed to a first approximation by the terms $l^2F_{020}/2R$, lF_{011}/R and $F_{002}/2R$. Application of Fermat's principle to these terms yields the following

$$\frac{\partial F}{\partial l} = \frac{l}{R}F_{020} + \frac{1}{R}F_{011} = 0 \qquad (5.8)$$

or

$$lF_{020} + F_{011} = 0 \qquad (5.9)$$

Now for a point source A(x,y,o) situated on the xy plane giving rise to a diffracted ray which intersects the image plane at B with co-ordinates (r', β, z'), the coefficient F_{011} is

$$F_{011} = -z'/\cos\beta \tag{5.10}$$

Then equation (5.9) becomes

$$lF_{020} - z'/\cos\beta = 0 \tag{5.11}$$

The height of the image above the x-y plane is given by the co-ordinate of the image in the z direction, namely z', where

$$z' = l\cos\beta F_{020} \tag{5.12}$$

Therefore the total height of the image in the absence of a contribution from any other aberration terms is $L\cos\beta F_{020}$ where L is the length of the grating grooves. The value of this oversimplification is in emphasising the importance of grating size and the proportionality of the image elongation to the astigmatism coefficient. In order to improve the image intensity one must attempt to approach more closely the ideal imaging conditions by reducing the magnitude of F_{020} since L and cosβ are considered fixed for the purposes of this discussion.

5.5 SINGLE WAVELENGTH CORRECTION OF SECOND ORDER ASTIGMATISM

For a concave grating with all of the mounting and recording elements, located on the Rowland circle, the residual second order astigmatism coefficient is given by Eq.(5.7). It has been demonstrated [5.10, 5.11] that this expression can have a zero for certain values of the mounting and recording parameters and a

particular value of the incident wavelength $\lambda = \lambda_1$. Given the angle of incidence α_0 of the principal ray and the wavelength λ_1, we determine the principal angles γ and δ of the recording pencils as follows.

The effective grating constant generated by the interference of the two waves originating from point sources C and D is fixed so that

$$\sin\delta - \sin\gamma = \lambda_0/\sigma \tag{5.13}$$

Then the angle of diffraction β_0 of the principal ray obeys the grating equation

$$\sin\alpha_0 + \sin\beta_0 = m\lambda_1/\sigma \tag{5.14}$$

Under these conditions $F_{020} = 0$ so that

$$\left(\frac{1}{\cos\alpha_0} - \cos\alpha_0\right) + \left(\frac{1}{\cos\beta_0} - \cos\beta_0\right)$$

$$+ m\,\frac{\lambda_1}{\lambda_0}\left[\left(\frac{1}{\cos\gamma} - \cos\gamma\right) - \left(\frac{1}{\cos\delta} - \cos\delta\right)\right] = 0 \tag{5.15}$$

An iterative technique can now be used to solve the simultaneous Eqs. (5.13, 5.14, 5.15) for α_0, γ and δ while r_C and r_D are found using condition (5.5).

Following extensive use of this aberration correction procedure the authors have noted certain conditions which ensure the existence of real solutions and make possible the accurate prediction of initial values. Two cases arise corresponding to positive and negative diffracted orders. For the case of a positive

order it was discovered that if satisfactory solutions for the recording angles existed, then the maximum value of γ was always such that

$$\frac{1}{\cos\gamma} - \cos\gamma << \frac{1}{\cos\delta} - \cos\delta \tag{5.16}$$

We now use this inequality as the justification for neglecting the term $1/\cos\gamma - \cos\gamma$ in Eq.(5.15) so that now

$$\left(\frac{1}{\cos\alpha_0} - \cos\alpha_0\right) + \left(\frac{1}{\cos\beta_0} - \cos\beta_0\right) + m\frac{\lambda_1}{\lambda_0}\left(\cos\delta - \frac{1}{\cos\delta}\right) \sim 0 \tag{5.17}$$

Upon rearranging this equation we arrive at the following quadratic equation in $\cos\delta$

$$m\frac{\lambda_1}{\lambda_0}\cos^2\delta + \left[\left(\frac{1}{\cos\alpha_0} - \cos\alpha_0\right) + \left(\frac{1}{\cos\beta_0} - \cos\beta_0\right)\right]\cos\delta$$

$$- m\frac{\lambda_1}{\lambda_0} \sim 0 \tag{5.18}$$

In the solution of Eq.(5.18) we require $-\pi/2 < \delta < \pi/2$ so that only the positive square root need be considered. For the case where the diffracted order is negative the maximum value of δ has been observed to satisfy

$$\frac{1}{\cos\delta} - \cos\delta << \frac{1}{\cos\gamma} - \cos\gamma \tag{5.19}$$

Proceeding as before we arrive at a similar quadratic equation for $\cos\gamma$

$$m\frac{\lambda_1}{\lambda_0}\cos^2\gamma - \left[\left(\frac{1}{\cos\alpha_0} - \cos\alpha_0\right) + \left(\frac{1}{\cos\beta_0} - \cos\beta_0\right)\right]\cos\gamma$$

$$- m\frac{\lambda_1}{\lambda_0} \sim 0 \qquad (5.20)$$

In this case $-\pi/2 < \gamma < \pi/2$ and the negative square root solution is appropriate.

In Table (5.1) we demonstrate the utility of the approximate solutions for the recording angles γ and δ by making a comparison with the exact solutions obtained using Eqs.(5.13, 5.14, 5.15). The results are for a concave grating with effective grating constant σ = 1/1200 mm, recording wavelength 442 nm and second order astigmatism corrected at a wavelength λ_1 = 250 nm. It is clear that for most applications the approximate solutions are sufficiently accurate as they stand.

5.6 DOUBLE WAVELENGTH CORRECTION OF SECOND ORDER ASTIGMATISM

During our study of the single wavelength correction of second order astigmatism it was discovered that for certain angles of incidence the aberration coefficient F_{020} can be zero for two wavelengths. It is considered that an understanding of the conditions under which this double wavelength correction of astigmatism occurs would be extremely useful to grating instrument designers. Not only would there be the freedom to eliminate astigmatism at two wavelengths, but presumably a reduction in image height for intermediate wavelengths would result. We will now discuss the restrictions on the angle of incidence required to ensure double wavelength correction.

	Approximate Solution		Exact Solution		
α_0^o	γ^o	δ^o	γ^o	δ^o	$\frac{1/\cos\delta - \cos\delta}{1/\cos\gamma - \cos\gamma}$
-40	27.054	80.153	27.124	80.511	25.3
-20	16.791	55.023	17.743	56.632	13.0
0	-7.970	23.068	-7.051	24.057	12.0
20	-4.792	26.547	-4.481	26.889	37.5
40	16.834	56.094	17.785	56.705	13.0
60	25.506	73.958	25.757	74.788	16.9
80	27.745	84.848	27.756	84.943	46.0
σ = 1/1200 mm, m = +1, λ_0 = 442 nm, λ_1 = 250 nm					

Table (5.1)

Let λ_1 and λ_2 be the two diffracted wavelengths of order m for which the astigmatism coefficient F_{020} is to be identically zero. The mounting parameters α_0, β_1 and β_2 must satisfy the grating equation at the correction wavelengths so that

$$\sin\alpha_0 + \sin\beta_1 = m\lambda_1/\sigma \tag{5.21}$$

and

$$\sin\alpha_0 + \sin\beta_2 = m\lambda_2/\sigma \tag{5.22}$$

As before the effective grating constant σ is defined in terms of the recording conditions

$$\sin\delta - \sin\gamma = \lambda_0/\sigma \tag{5.23}$$

The expressions for F_{020} under these conditions are

$$\left(\frac{1}{\cos\alpha_0} - \cos\alpha_0\right) + \left(\frac{1}{\cos\beta_1} - \cos\beta_1\right)$$

$$+ \frac{\lambda_1}{m_{\lambda_0}}\left[\left(\frac{1}{\cos\gamma} - \cos\gamma\right) - \left(\frac{1}{\cos\delta} - \cos\delta\right)\right] = 0 \tag{5.24}$$

and

$$\left(\frac{1}{\cos\alpha_0} - \cos\alpha_0\right) + \left(\frac{1}{\cos\beta_2}\right)$$

$$+ \frac{\lambda_2}{m_{\lambda_0}}\left[\left(\frac{1}{\cos\gamma} - \cos\gamma\right) - \left(\frac{1}{\cos\delta} - \cos\delta\right)\right] = 0 \tag{5.25}$$

The five Eqs.(5.21-5.25) form a set of simultaneous equations which may be solved numerically for α_0, β_1, β_2, γ and δ once the correction wavelengths λ_1, λ_2 and grating constant σ have been selected.

An approximate solution for the recording angle γ and δ may be found as in Section (5.4) if an approximate choice for the angle of incidence α_0 is made. To find suitable values for α_0 which result in real solutions for β_1, β_2, γ and δ we proceed as follows. Using Eq. (5.25) we find

$$\left(\frac{1}{\cos\gamma} - \cos\gamma\right) - \left(\frac{1}{\cos\delta} - \cos\delta\right)$$

$$= -\frac{\lambda_0}{m\lambda_2}\left[\left(\frac{1}{\cos\alpha_0} - \cos\alpha_0\right) + \left(\frac{1}{\cos\beta_2} - \cos\beta_2\right)\right] \tag{5.26}$$

Substitution into Eq. (5.24) eliminates γ and δ resulting in an equation in terms of the mounting parameters only. This expression may be simplified to yield a quadratic equation in $\cos\alpha$.

$$\left(\frac{\lambda_1}{\lambda_2} - 1\right)\cos^2\alpha_0 + \left[\left(\frac{1}{\cos\beta_1} - \cos\beta_1\right) - \frac{\lambda_1}{\lambda_2}\left(\frac{1}{\cos\beta_2} - \cos\beta_2\right)\right]\cos\alpha_0$$

$$+ \left(1 - \frac{\lambda_1}{\lambda_2}\right) = 0 \tag{5.27}$$

We now use the grating Eqs.(5.21, 5.22) to derive expressions for $\cos\beta_1$ and $\cos\beta_2$ in terms of α_0 so that

$$\cos\ _1 = \left[1 - (m\lambda_1/\sigma - \sin\alpha_0)^2\right]^{\frac{1}{2}} \tag{5.28}$$

and

$$\cos\beta_2 = \left[1 - (m\lambda_2/\sigma - \sin\alpha_0)^2\right]^{\frac{1}{2}} \tag{5.29}$$

Substitution of these relations into Eq.(5.27) generates an equation in terms of the unknown α_0 which can be solved numerically.

Having found a value for the angle of incidence we are now free to find approximate solutions for the recording angles γ and δ. Using inequality (5.16) to eliminate γ from Eqs. (5.14, 5.25) establishes an approximate quadratic equation for $\cos\delta$

$$\frac{m}{\lambda_0}(\lambda_2 - \lambda_1)\cos^2\delta - [(\frac{1}{\cos\beta_1} - \cos\beta_1) - (\frac{1}{\cos\beta_2} - \cos\beta_2)]\cos\delta$$

$$- \frac{m}{\lambda_0}(\lambda_2 - \lambda_1) \sim 0 \qquad (5.30)$$

In common with Eq. (5.18) the positive square root solution is appropriate for positive orders. For negative orders a similar treatment results in a quadratic equation for $\cos\gamma$

$$\frac{m}{\lambda_0}(\lambda_2 - \lambda_1)\cos^2\gamma + [(\frac{1}{\cos\beta_1} - \cos\beta_1) - (\frac{1}{\cos\beta_2} - \cos\beta_2)]\cos\gamma$$

$$- \frac{m}{\lambda_0}(\lambda_2 - \lambda_1) \sim 0 \qquad (5.31)$$

where the negative square root solution is appropriate. Thus the computation of a value for the angle of incidence α_0 using Eq. (5.27) specifies the position of the entrance slit on the Rowland circle which in turn predetermines the existence of suitable recording angles γ and δ. Eqs. (5.30, 5.31) are then used to find approximate values for γ and δ corresponding to the correction of second order astigmatism for wavelengths λ_1 and λ_2. The value of α_0 and approximate solutions for γ and δ are then used as initial values in the numerical solution of simultaneous Eqs. (5.21-5.25).

We demonstrate the success of the technique by applying the theory to the design of a Rowland circle spectrograph using a concave grating having an effective grating constant σ 1/1200 mm and recording wavelength λ = 442 nm.Table (5.2)shows a list of values of α_o calculated from Eq. (5.27) and the corresponding solutions for recording angles γ and δ. Correction wavelength λ_2 = 250 nm is held constant while λ_1 varies from 50 nm to 700 nm. It is pleasing to note the reasonable range of values of α_0, γ and δ under this state of correction.

To conclude this section we will attempt to give a qualitative impression of the spectral image using spot diagrams. The example we have chosen is a concave grating of effective grating constant σ = 1/1800 mm, radius of curvature R = 500 mm and ruled area 100 x 100 mm. The grating is recorded with light of wavelength λ_0 = 442 nm and the primary astigmatism in the first order is corrected at wavelengths λ_1 = 200 nm and λ_2 = 300 nm. Table (5.3) contains the relevant mounting and recording parameters. The spot diagrams were generated by a ray tracing procedure following the guidelines of Noda et al [5.12]. The ray trace considers rays originating from a point A(R$\cos\alpha_0$, R$\sin\alpha_0$, 0) on the entrance slit and diffracted from a grid of 77 points P(ξ,w,1) on the grating surface. The image plane y'z' was taken to be perpendicular to the principal diffracted ray at B(R$\cos\beta_0$, R$\sin\beta_0$, 0). Fig.(5.3)shows the results of this calculation for the first order image at wavelengths λ = 150, 200, 250, 300 and 350 nm. Contributions from the uncorrected higher order aberration terms prevent the attainment of zero image height at λ_1 and λ_2 although a significant reduction is demonstrated. The equivalent conventionally ruled grating has gross image elongation by comparison.

α_0^o	λ_1(nm)	γ^o	δ^o
5.473	50	-10.687	20.180
7.722	100	-11.207	19.636
9.450	150	-11.215	19.628
10.911	200	-10.960	19.894
13.384	300	-9.996	20.905
14.481	350	-9.362	21.575
15.515	400	-8,654	22.330
16.504	450	-7.880	23.160
17.461	500	-7.048	24.060
18.395	550	-6.161	25.029
19.316	600	-5.219	26.068
20.237	650	-4.224	27.178
21.154	700	-3.171	28.365
σ = 1/1200 mm, m = +1, λ_0 = 442 nm, λ_2 = 250 nm			

Table (5.2)

σ = 1/1800 mm	m = +1
R = 500 mm	100 x 100 mm
α_0 = 18.065^o	r = 475.35 mm
λ_0 = 442 nm	λ_1 = 200 nm, λ_2 = 300 nm
γ = -16.247^o	r_C = 480.03 mm
δ = 31.052^o	r_D = 428.44 mm

Table (5.3)

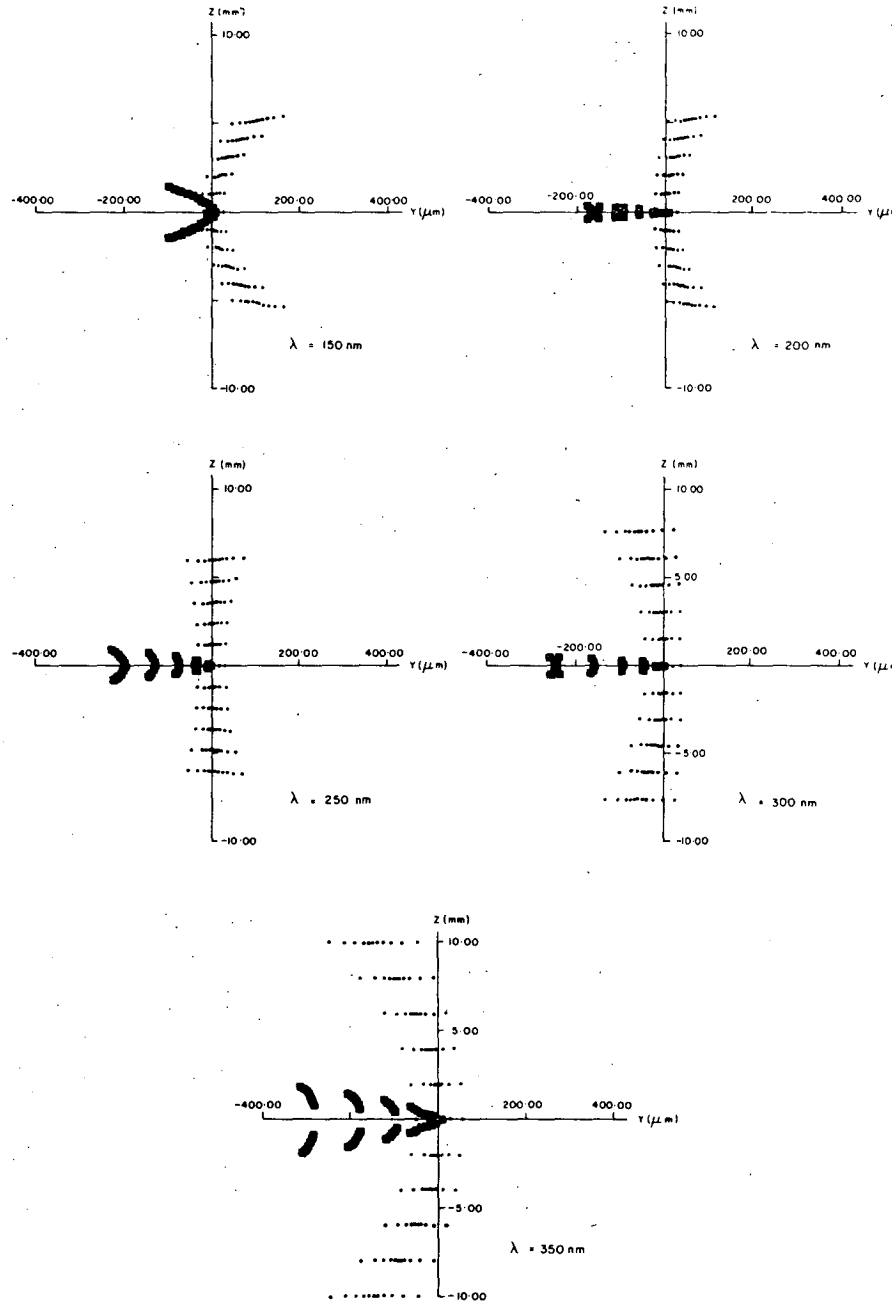

Fig. (5.3) Double wavelength correction of primary astigmatism at wavelengths λ_1 = 200nm and λ_2 = 300nm for an 1800mm^{-1} grating used in first order. Holographic grating □ , ruled +.

It is interesting to note the effect of the remaining coma-like aberration terms which cause the image to flare in the horizontal plane and thereby degrade resolution.

5.7 DOUBLE WAVELENGTH CORRECTION OF THIRD ORDER COMA

Another aberration type which can influence the quality of the image and resolution of the grating is coma. In the preceding example we have seen a graphic illustration of its effect in the absence of second order astigmatism. Thus the coma term $wl^2F_{120}/2R^2$ should be corrected for monochromators and spectrographs if the opportunity arises. In the case of the Rowland circle mount where the y axis coma coefficient F_{300} is already zero for all wavelengths, the advantages of correcting F_{120} can be considerable. We will now indicate how the remaining third order coma coefficient may be corrected.

The general expression for coefficient F_{120} is

$$F_{120} = \rho\sin\alpha f_{020}(\rho,\alpha) + \rho'\sin\beta f_{020}(\rho',\beta)$$
$$+m\frac{\lambda}{\lambda_0}\left[\rho_C\sin\gamma f_{020}(\rho_C,\gamma) - \rho_D\sin\delta f_{020}(\rho_D,\delta)\right] \qquad (5.32)$$

where

$$f_{020}(\rho,\alpha) = \rho - \cos\alpha \qquad (5.33)$$

and similarly for the other combinations, (ρ',β), (ρ_C,γ) and (σ_D,δ). For a concave grating with all the mounting and recording elements situated on the Rowland circle the expression for F_{120} becomes

$$F_{120} = \frac{\sin^3\alpha}{(1 - \sin^2\alpha)} + \frac{\sin^3\beta}{(1 - \sin^2\beta)} + \frac{m\lambda}{\lambda_0}\left[\frac{\sin^3\gamma}{(1 - \sin^2\gamma)}\right.$$

$$\left. - \frac{\sin^3\delta}{(1 - \sin^2\delta)}\right] \qquad (5.34)$$

To achieve single wavelength correction of third order coma at wavelength $\lambda = \lambda_1$ and angle of incidence α_0, we proceed exactly as in Section (5.4) solving simultaneous Eqs. (5.13, 5.14, 5.15) for the recording angles γ and δ. Solution of this set of equations indicates for each angle of incidence and correction wavelength that there are two possible sets of recording angles (γ_1,δ_1) and (γ_2,δ_2). These angles are related as follows

$$\delta_1 = -\gamma_2 \qquad \text{and} \qquad \gamma_1 = -\delta_2 \qquad (5.35)$$

and lead to two choices for an approximate solution. Firstly it is found that

$$\left|\frac{\sin^3\gamma}{1 - \sin^2\gamma}\right| >> \left|\frac{\sin\delta}{1 - \sin^2\delta}\right| \qquad (5.36)$$

when the solution (γ_1,δ_1) is used while the alternative inequality

$$\left|\frac{^3\gamma}{1 - \sin^2\gamma}\right| >> \left|\frac{^3\delta}{1 - \sin^2\delta}\right|$$

arises when (γ_2,δ_2) is the solution. The inequalities (5.36, 5.37) are then used in Eq. (5.34) with $F_{120} = 0$ to find approximate values for recording angles γ and δ.

The coma coefficient F_{120} can also be corrected at two wavelengths λ_1 and λ_2 in a manner analogous to that used in section 5. In the present case when $F_{120} = 0$ we have

$$\frac{\sin^3\alpha_0}{(1-\sin^2\alpha_0)} + \frac{\sin^3\beta_1}{(1-\sin^2\beta_1)} + \frac{m\lambda_1}{\lambda_0}\left[\frac{\sin^3\gamma}{(1-\sin^2\gamma)} - \frac{\sin^3\delta}{(1-\sin^2\delta)}\right] = 0 \tag{5.38}$$

and

$$\frac{\sin^3\alpha_0}{(1-\sin^2\alpha_0)} + \frac{\sin^3\beta_2}{(1-\sin^2\beta_2)} + \frac{m\lambda_2}{\lambda_0}\left[\frac{\sin^3\gamma}{(1-\sin^2\gamma)} - \frac{\sin^3\delta}{(1-\sin^2\delta)}\right] = 0 \tag{5.39}$$

Then solution of simultaneous Eqs. (5.21, 5.22, 5.23, 5.38, 5.39) yields the required mounting and recording parameters. To find initial values for the solution of this set of equations we eliminate γ and δ from Eqs. (5.38, 5.39) which leads to the following equation for α_0

$$\left(1 - \frac{\lambda_1}{\lambda_2}\right)\frac{\sin^3\alpha_0}{(1-\sin^2\alpha_0)} + \frac{(m\lambda_1/\sigma - \sin\alpha_0)^3}{[1-(m\lambda_1/\sigma - \sin\alpha_0)^2]}$$

$$- \frac{\lambda_1(m\lambda_2/\sigma - \sin\alpha_0)^3}{\lambda_2[1-(m\lambda_2/\sigma - \sin\alpha_0)^2]} = 0 \tag{5.40}$$

Similarly an approximation for $\sin\gamma$ can be found using inequality (5.36) and Eqs. (5.38, 5.39).

$$\frac{m}{\lambda_0}(\lambda_1 - \lambda_2)\frac{\sin^3\gamma}{(1-\sin^2\gamma)} + \frac{(m\lambda_1/\sigma - \sin\alpha_0)^3}{[1-(m\lambda_1/\sigma - \sin\alpha_0)^2]}$$

$$- \frac{(m\lambda_2/\sigma - \sin\alpha_0)^3}{[1-(m\lambda_2/\sigma - \sin\alpha_0)^2]} = 0 \tag{5.41}$$

Having found a value for γ from this equation, δ may be determined using Eq. (5.23). All that remains to be done is to use the value of α_0 determined from Eq. (5.40) and the approximate values of γ and δ to solve the set of simultaneous equations for exact values of the recording parameters.

An example of results obtained using the above procedure for the double wavelength correction of third order coma is shown in the spot diagrams of Fig. (5.4). The effective grating constant σ = 1/1200 mm, radius of curvature R = 500 nm and ruled area 100 x 100 mm. The recording wavelength λ_0 = 458 nm while first order correction wavelengths are λ_1 = 250 nm and λ_2 = 550 nm. The spot diagrams were computed by tracing similar pencils to those used in Fig. (5.3) for wavelengths λ = 200, 250, 400, 550 and 600 nm. In Fig.(5.4) we can see some improvement in resolution, particularly near $\lambda = \lambda_1$, as well as a reduction in image height. This result is expected since the coefficient F_{120} appears in the power series expansion (1.6) for the light path function in the term $wl^2F_{120}/2R^2$ which influences the spot diagrams in both the y and z directions. Table (5.4) summarizes the mounting and recording parameters.

In the next sections the basic ideas employed in the earlier part of this chapter are extended to consider two further states of correction having important practical implications. The first case relates to concave gratings used in spectrographs where two orders, usually first and second order, cover the spectral range. It will be shown how primary astigmatism or primary coma may be corrected at wavelength λ_1 in order m_1 and at wavelength λ_2 in order m_2. For example it may be desired to correct astigmatism at wavelength λ_1 = 300 nm in order m_1 = +1 and for wavelength λ_2 = 220 nm in

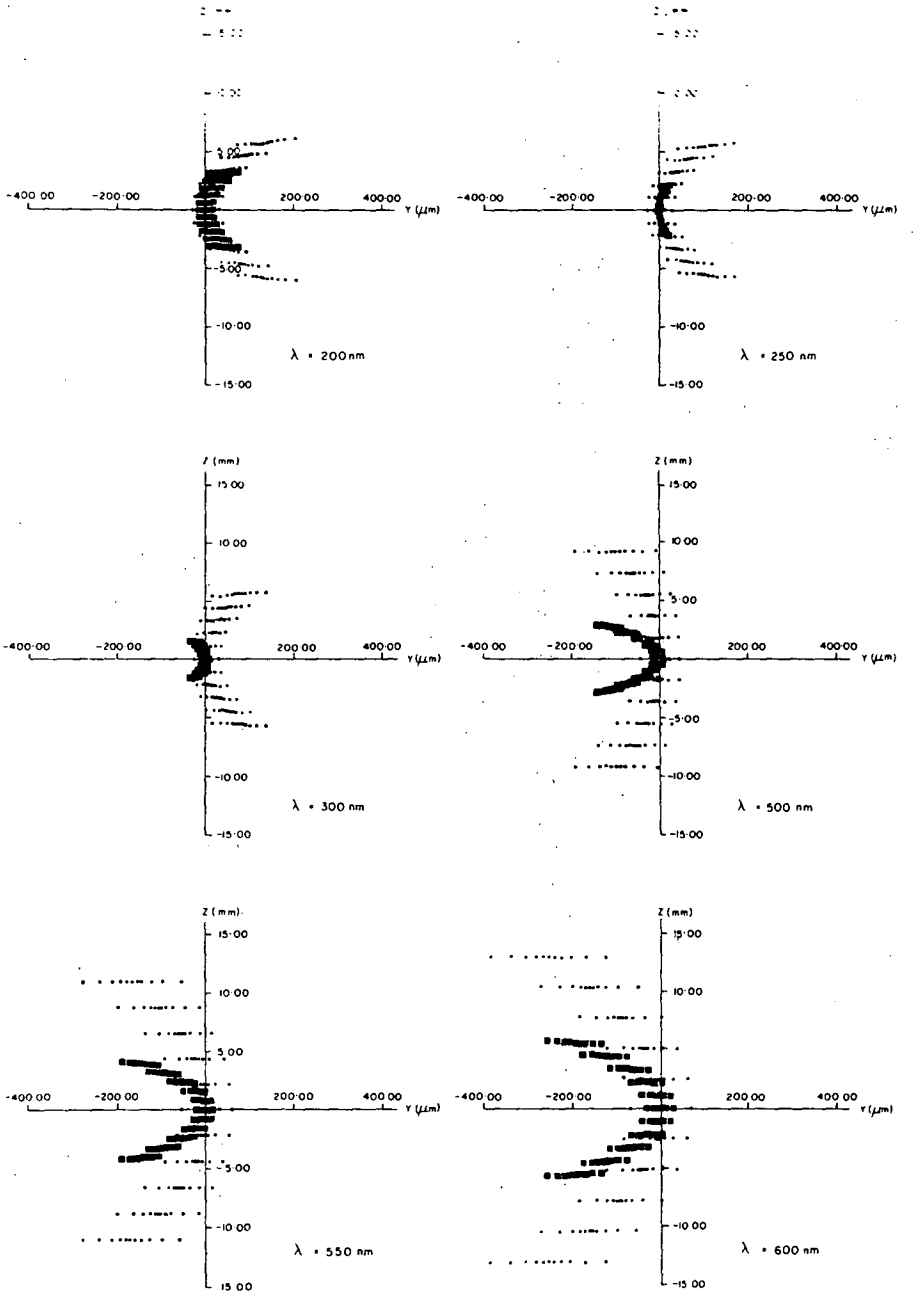

Fig.(5.4) Double wavelength correction of primary coma at wavelengths λ_1=250nm and λ_2=550nm for a 1200mm^{-1} grating used in first order. Holographic grating □, ruled grating +.

σ = 1/1200 mm	m = +1
R = 500 mm	100 x 100 mm
$\alpha_0 = 18.712^o$	r = 473.57 mm
λ_0 = 458 nm	λ_1 = 250 nm, λ_2 = 550 nm
$\gamma = -9.983^o$	r_C = 492.43 mm
$\delta = 22.101^o$	r_D = 463.26 mm

Table (5.4)

order $m_2 = +2$. In this instrument first order might cover the spectral range 200-400 nm while second order covers 180-250 nm. The second case involves the simultaneous correction of primary astigmatism and primary coma at a chosen value of $m\lambda/\lambda_0$. This state of correction can approach the ideal image at least for pencils originating near the meridional plane.

5.8 CORRECTION OF ASTIGMATISM OR COMA IN TWO ORDERS AT TWO WAVELENGTHS

A close inspection of the work reported in Sections (5.6) and (5.7) on the double wavelength correction of astigmatism and coma shows that this is a special solution of a more general case. If instead of nominating correction wavelengths for a given order we choose to select two different orders, then we define a more general problem. Again five non-linear simultaneous equations require solution. Following the notation used previously we have

$$\sin\delta - \sin\gamma = \frac{\lambda_0}{\sigma} \tag{5.42}$$

$$\sin\alpha_0 + \sin\beta_1 = \frac{m_1\lambda_1}{\sigma} \tag{5.43}$$

$$\sin\alpha_0 + \sin\beta_2 = \frac{m_2\lambda_2}{\sigma} \tag{5.44}$$

$$F_{020}(\alpha_0,\beta_1,m_1,\lambda_0,\lambda_1,\gamma,\delta) = 0 \tag{5.45}$$

$$F_{020}(\alpha_0,\beta_2,m_2,\lambda_0,\lambda_2,\gamma,\delta) = 0 \tag{5.46}$$

or

$$F_{120}(\alpha_0,\beta_1,m_1,\lambda_0,\lambda_1,\gamma,\delta) = 0 \tag{5.47}$$

$$F_{120}(\alpha_0,\beta_2,m_2,\lambda_0,\lambda_2,\gamma,\delta) = 0 \tag{5.48}$$

Solutions to Eqs. (5.42-5.46) correspond to second order astigmatism correction while Eqs. (5.42, 5.44, 5.47, 5.48) may yield the mounting and recording parameters for third order coma correction. Initial values for solution of these sets of equations are found as in the earlier sections of this chapter. For example in the case of astigmatism correction we find the following quadratic equation for $\cos\alpha_0$

$$\cos^2\alpha_0 + [(\frac{m_1\lambda_1}{m_1\lambda_1 - m_2\lambda_2} - 1)\ (\frac{1}{\cos\beta_1} - \cos\beta_1)$$

$$-(\frac{m_1\lambda_1}{m_1\lambda_1 - m_2\lambda_2})(\frac{1}{\cos\beta_2} - \cos\beta_2)]\ \cos\alpha_0 - 1 = 0 \tag{5.49}$$

Then we numerically solve a quadratic equation for $\cos\gamma$ which for negative orders is given by

$$\frac{(m_1\lambda_1 - m_2\lambda_2)}{\lambda_0}\cos^2\gamma - [(\frac{1}{\cos\beta_1} - \cos\beta_1) - (\frac{1}{\cos\beta_2} - \cos\beta_2)]\cos\gamma$$

$$-(\frac{m_1\lambda_1 - m_2\lambda_2}{\lambda_0}) \sim 0 \tag{5.50}$$

Using these initial values we attempt to solve the set of simultaneous equations for exact values of the mounting and recording perameters. It should be stressed that it is not always possible to find useful solutions particularly in the case of coma correction where the residual astigmatism tends to be dominant.

To demonstrate the success of the technique we show in Figs. (5.5) and (5.6) sets of spot diagrams corresponding to orders $m_1 = +1$ and $m_2 = +2$ corrected for second order astigmatism at wavelengths $\lambda_1 = 350$ nm and $\lambda_2 = 200$ nm. The effective grating constant is $\sigma = 1/2400$ mm, radius of curvature R = 1000 mm and grating size 75 x 75 mm. The mounting and recording parameters are shown in Table (5.5). The reduction in image height at the correction wavelengths is considerable however, the effect of the remaining coma type aberrations causes a gross flare of the image in the meridional plane. Nevertheless when one considers the high angular dispersion available using a 2400 mm^{-1} groove frequency, the resolution with a 250 μm exit slit width is still respectable, about 0.1 nm in first order and 0.05 nm is second order at the correction wavelengths.

A further consideration of practical importance is the behaviour of the image for finite entrance slit heights. We have attempted to illustrate this behaviour by tracing pencils of rays originating at distance 5 mm above and below the meridional plane, that is for slits of length 10 mm. Fig.(5.7) shows the results of this ray trace for the two correction wavelengths and orders corresponding to the Table (5.5) data. It is pleasing to note that there is minimal effect due to astigmatism although that image is broadened with a consequent reduction in available resolution. Nevertheless it must be agreed that the performance of this type of grating, particularly when handling weak signals, represents a significant improvement compared with currently available ruled gratings.

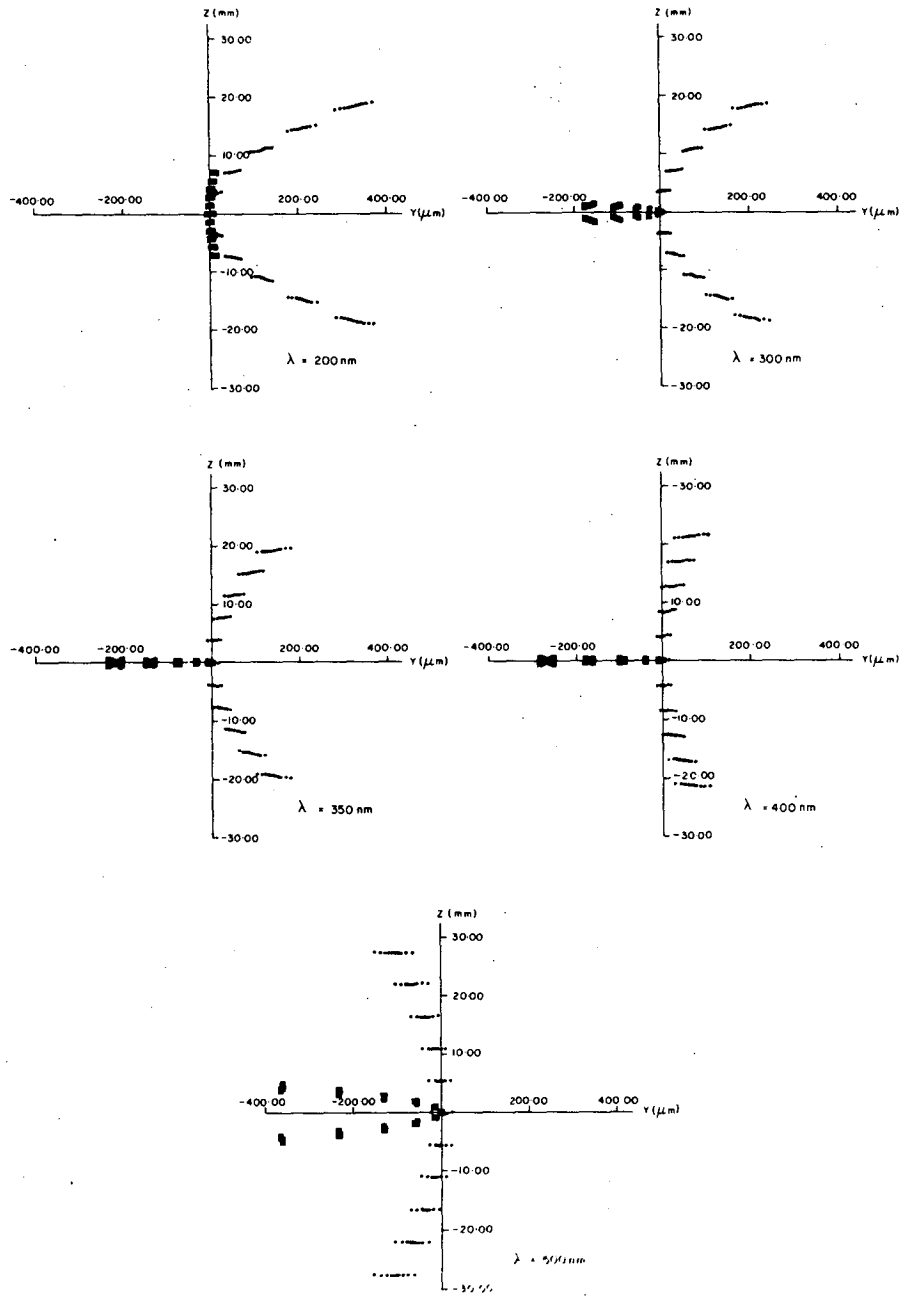

Fig.(5.5) Correction of primary astigmatism at wavelength λ_1= 350nm in order m_1= +1 for a 2400mm^{-1} grating. Holographic grating □ , ruled grating +.

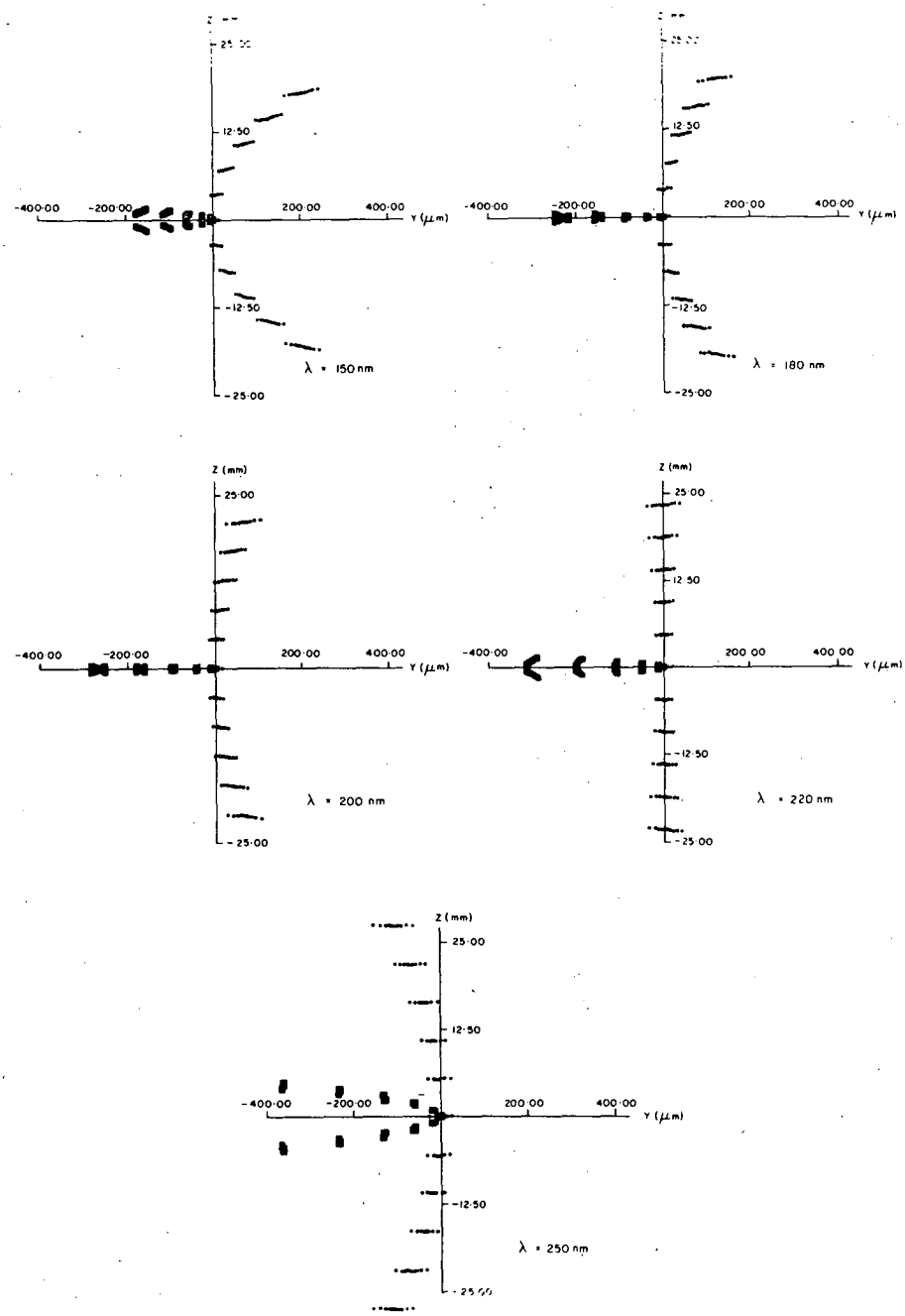

Fig.(5.6) Correction of primary astigmatism at wavelength λ_2= 200nm in order m_2= +2 for the Fig.(5.5) grating. Holographic grating □ , ruled grating +.

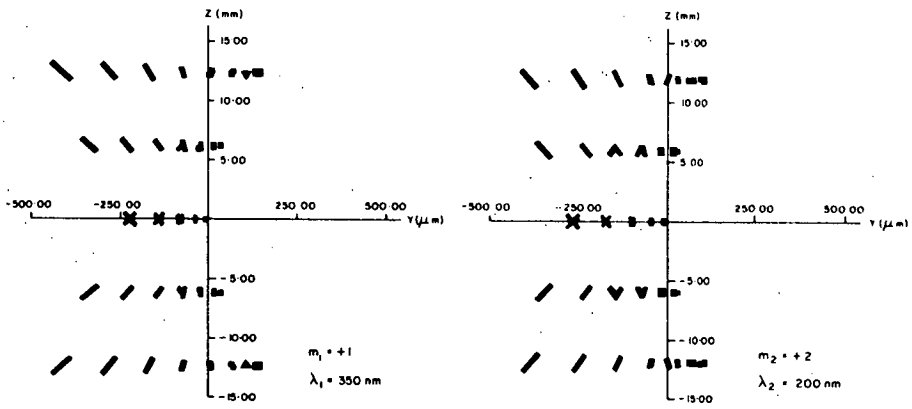

Fig.(5.7) Spot diagrams for the Fig.(5.5) aberration reduced grating computed at the correction wavelengths for an entrance slit of 10mm length.

σ = 1/2400 mm	m = +1, + 2
R = 1000 mm	75 x 75 mm
α_0 = 37.803°	r = 790.120 mm
λ_0 = 442 nm	λ_1 = 350 nm, λ_2 = 200 nm
γ = -19.264°	r_C = 944.002 mm
δ = 46.959°	r_D = 682.515 mm

TABLE (5.5)

5.9 SIMULTANEOUS CORRECTION OF ASTIGMATISM AND COMA

Following our previous design strategy we now treat the case of simultaneously correcting second order astigmatism and third order coma at a given value of $m\lambda/\lambda_0$. The relevant nonlinear equations that require simultaneous solution are

$$\sin\delta - \sin\gamma = \frac{\lambda_0}{\sigma} \tag{5.51}$$

$$\sin\alpha + \sin\beta = \frac{m\lambda}{\sigma} \tag{5.52}$$

$$F_{020}(\alpha_0,\beta_0,m,\lambda_0,\lambda,\gamma,\delta) = 0 \tag{5.53}$$

$$F_{120}(\alpha_0,\beta_0,m,\lambda_0,\lambda,\gamma,\delta) = 0 \tag{5.54}$$

Having specified σ, λ_0, m and λ it is necessary to solve Eqs. (5.52-5.54) for the mounting angles α_0, β_0 and recording angles γ, δ. Some idea of the spectral performance to be expected from this type of aberration correction may be gained from Fig.(5.8). Here we show spot diagrams for a 1200 mm^{-1} grating corrected in second order at a wavelength λ = 300 nm. The radius of curvature is R = 500 mm and grating size 100 x 100 mm. A full description of the mounting and recording conditions is given in Table (5.6).

We have studied the solution set [α_0, β_0, γ, δ] for a wide range of values of the groove spacing σ and a number of recording wavelengths λ_0 available using ion lasers and the He-Cd laser. Fig. (5.9) shows typical results where we have plotted graphs of the solution values against $m\lambda/\lambda_0$. The groove frequencies chosen are 1800 mm^{-1} and 2400 mm^{-1}. A number of interesting features of these results should be mentioned. Firstly we identify the well known stigmatic solutions where γ = 0 and $m\lambda/\lambda_0$ = 1 or 2.

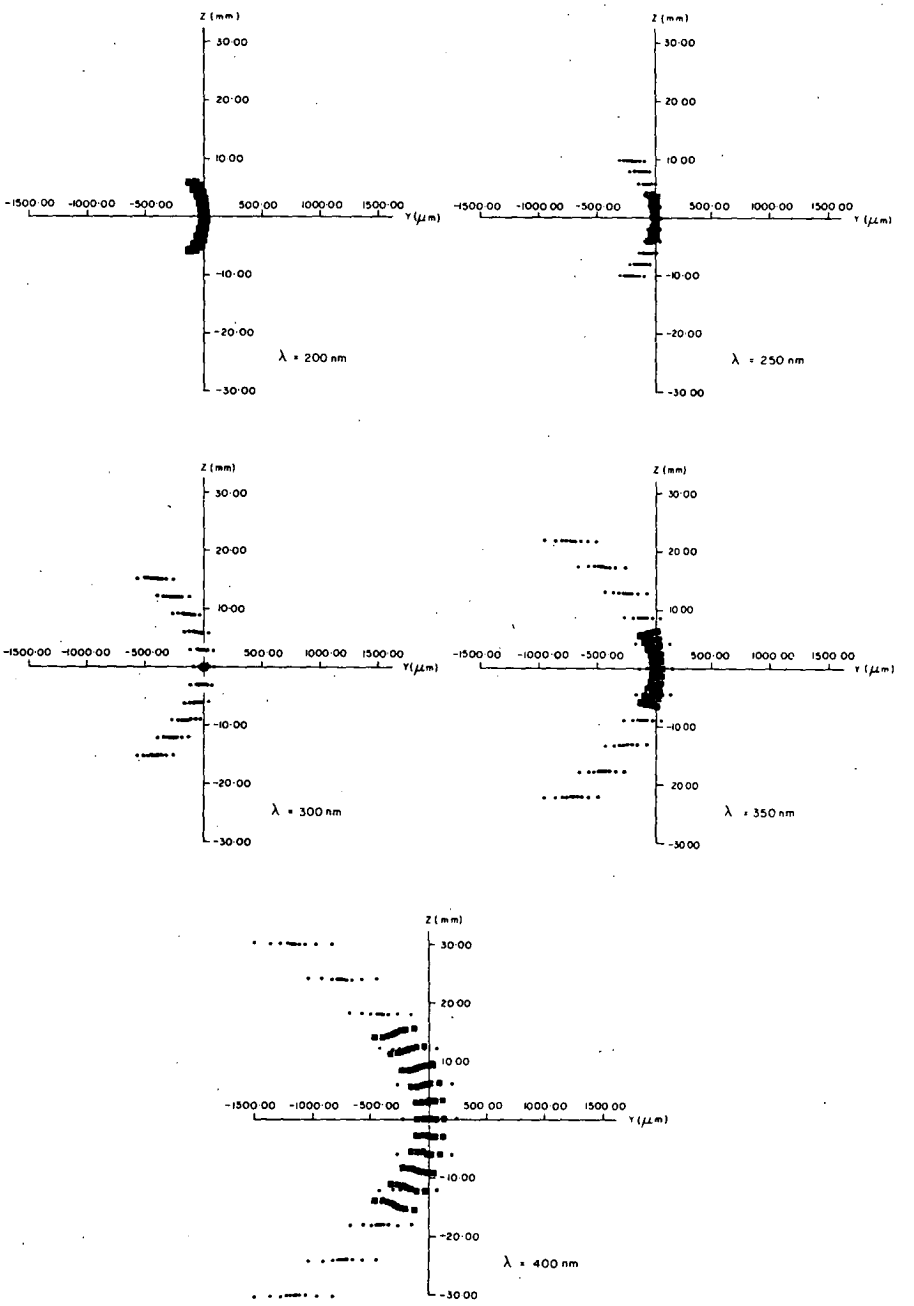

Fig. (5.8) Simultaneous correction of primary astigmatism and primary coma at a wavelength λ= 300nm in order m= +2 for a 1200mm^{-1} grating. Holographic grating □ , ruled grating +.

σ = 1/1200 mm	m = +2
R = 500 mm	100 x 100 mm
α_0 = 11.858°	r = 489.333 mm
λ_0 = 442 nm	λ_{COR} = 300 nm
γ = -2.926°	r_C = 499.346 mm
δ = 28.643°	r_D = 438.816 mm

TABLE (5.6)

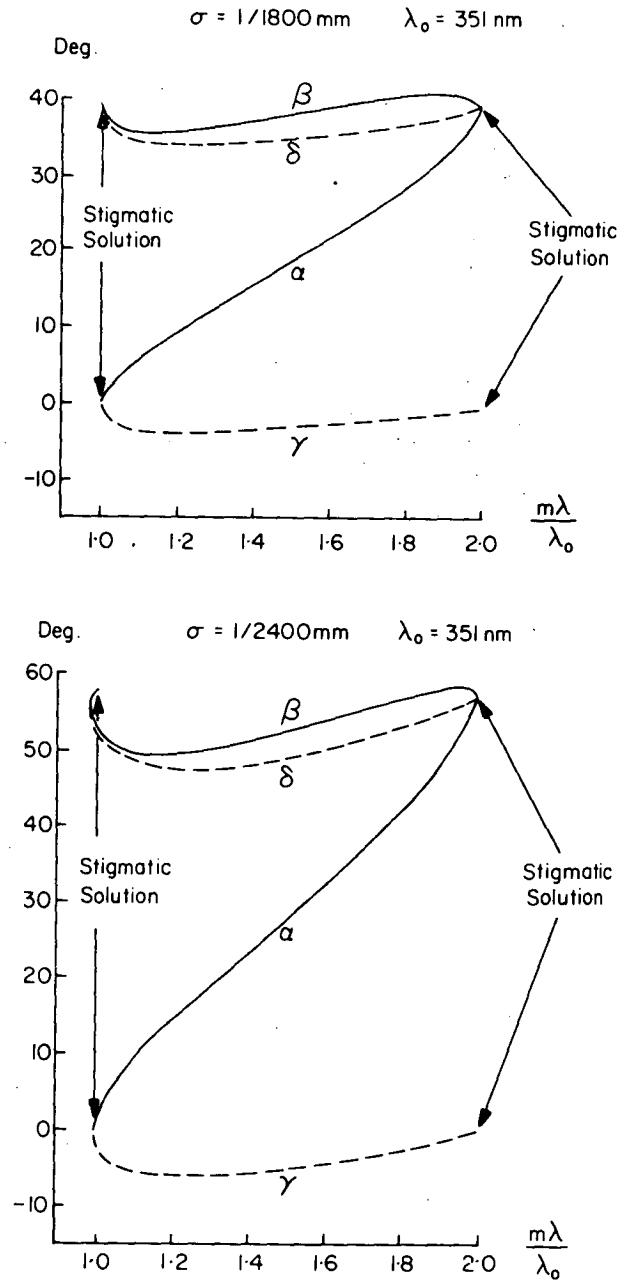

Fig.(5.9) Mounting and recording angles as a function of $m\lambda/\lambda_o$ corresponding to the simultaneous correction of primary astigmatism and primary coma.

These two solutions have been discussed extensively in the literature [5.5, 5.6, 5.7] and correspond to the formation of a stigmatic image, that is one free from aberrations. When $m\lambda/\lambda_0 = 1$ we have a grating that is useful in high resolution direct reading spectrographs. The other stigmatic image formed when $m\lambda/\lambda_0 = 2$ is also of interest since it corresponds to the Littrow configuration for concave gratings with $\alpha_0 = \beta_0$. This configuration is more commonly called the Eagle mount.

The second interesting feature of Fig. (5.9) is that the recording angles γ and δ are roughly constant. We have found that this observation is more nearly satisfied for larger groove spacings and for shorter recording wavelengths. The implications of this are that if a grating is corrected for astigmatism and coma at one wavelength in the range $1 < m\lambda/\lambda_0 < 2$ then we should expect the image quality to be comparable at other wavelengths in the range. Indeed this is what we find from our numerical studies. Rather than the need to use a different grating to cater for each correction wavelength one might choose, it is possible to use just one grating with suitable adjustments to the angle of incidence α_0.
To illustrate this point we present Fig. (5.10) which shows the behaviour of a grating of groove space σ = 1/2400 mm, radius of curvature R = 1000 mm and size 75 x 75 mm. The recording solution corresponds to $m\lambda/\lambda_0 = 1.5$ in Fig.(5.9) while the angle of incidence is changed such that $m\lambda/\lambda_0 = 1.25$, 1.5 and 1.75. Details of the mounting and recording conditions are given in Table (5.7).

The dependence of the solution for the mounting and recording parameters on $m\lambda/\lambda_0$ should be stressed since it implies that the spot diagrams will be the same for all real orders and a given value of

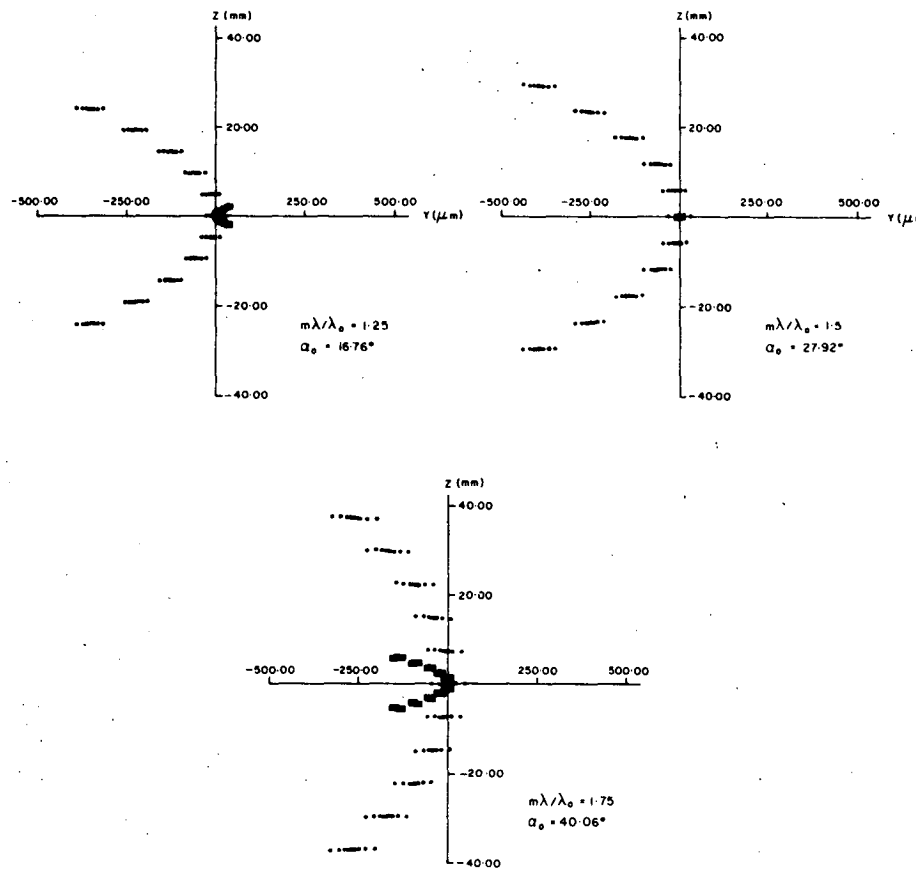

Fig. (5.10) Spot diagrams showing the effect of changing the angle of incidence for a 2400mm^{-1} grating corrected for $m\lambda/\lambda_0 = 1.5$. Holographic grating □ , ruled grating +.

σ = 1/2400 mm	γ = -5.018^{o}
R = 1000 mm	δ = 49.019^{o}
$\alpha_0(m\lambda/\lambda_0 = 1.25) = 16.76^{o}$	r_C = 996.165 mm
$\alpha_0(m\lambda/\lambda_0 = 1.5) = 27.92^{o}$	r_D = 655.815 mm
$\alpha_0(m\lambda/\lambda_0 = 1.75) = 40.06^{o}$	75 x 75 mm
λ_0 = 351 mm	

TABLE (5.7)

$m\lambda/\lambda_0$. This has far reaching practical implications since for example the Fig. (5.10) results with $m\lambda/\lambda_0 = 1.5$ could represent first or second order behaviour, each order having an identical spot diagram. The high angular dispersion in second order, equivalent to a 4800 mm-1 grating in first order, would be usefully accessible in view of the high resolution indicated by the spot diagrams. There is however one important practical disadvantage with this state of correction. By making $m\lambda/\lambda_0$ one of the design variables we have lost some flexibility which causes the aberration reduction to occur around only one angle of diffraction. Ideally we desire the aberration reduction in say first and second order on different arcs of the Rowland circle as in Section (5.8).

A close inspection of the magnitude of the aberration coefficients arising from the solution of Eqs. (5.52-5.54) is fruitful. It shows that the fourth order coefficients F_{220} and F_{040}, which are components of spherical aberration, are very nearly zero at the correction wavelength when $1 < m\lambda/\lambda_0 < 2$. F_{400} is already zero for all wavelengths by virture of the Rowland circle constraint. Thus the solution set for $1 < m\lambda/\lambda_0 < 2$ is very close to that required for stigmatic imaging. In many cases it is the diffraction limit that determines the ultimate resolution and not the residual spherical aberration.

5.10 CONCLUDING REMARKS

A simple scheme which improves the imaging properties of Rowland circle spectrographs by choosing suitable holographic recording conditions has been formulated. In particular, aberrations due to primary astigmatism and coma have been treated in terms of aberration coefficients derived from an application of Fermat's principle of the shortest light path. The work leads to the identification of mounting and recording points, which are constrained to lie on the Rowland circle, enabling primary astigmatism or primary coma to be corrected at two wavelengths. Certain restrictions on the existence of real solutions have been discovered, and it should be noted that not all real solutions provide for better imaging across the spectral range than that attainable with a conventionally ruled grating. The astigmatism correction procedure seems to always yield solutions which effectively reduce image height however the efficiency of the coma correction varies.

Using a simple design approach it is possible to reduce Rowland circle mount aberrations for a number of important practical cases. Constraining the mounting and recording elements to be situated on the Rowland circle, real solutions exist which permit astigmatism or coma to be corrected at two wavelengths in two orders. Gratings designed with this state of correction will lend themselves admirably to use in inductively coupled plasma emission spectrographs. In this application it should be possible to select the grating size to give high resolution while maintaining high signal levels.

Another state of correction discussed may be used to simultaneously correct astigmatism and coma for a given value of $1 < m\lambda/\lambda_0 < 2$. Such solutions for many applications are very nearly stigmatic and for pencils originating close to the meridional plane diffraction limited resolution is approached. Gratings of this type could be used in high resolution direct reading spectrographs in a multitude of applications.

There are other options available for aberration reduction which have not been discussed. For example it is possible to deviate from the Rowland circle or use toroidal blanks, thereby increasing the number of degrees of freedom available. A different aberration minimization procedure could have been used instead of simply finding the zeros of the aberration coefficients. There is also important work to be done in the study of the solution domain for problems of this type. No attempt has been made to treat in any detail the effect on the image of a large deviation of the incident pencil from the meridional plane. Although this study has been restricted to the Rowland circle mount and to gratings having a spherical substrate, it does serve to illustrate some new possibilities for this classical configuration.

A discussion of image formation on the Rowland circle is not complete without consideration of changes which occur for variations in the relative aperture of the grating instrument. The following chapter concentrates on the behaviour of the image height for several aberration-corrected gratings as a function of the grating size. Mention is also made of the numerical magnitude of individual terms of the light path function as the relative aperture changes.

REFERENCES

[5.1] Rowland H.A. (1882) Phil. Mag., 4, 469.

[5.2] Zernike F. (1935) in Festschrift "Pieter Zeeman" (Martinus the Hague) p. 323.

[5.3] Beutler H.G. (1945) J.Opt. Soc. Amer., 35, 311.

[5.4] Welford W.T. (1965) Progress in Optics IV (North-Holland Publishing Co., Amsterdam) p.241.

[5.5] Noda H., Namioka T. and Seya M. (1974) J.Opt. Soc. Amer., 64, 1031.

[5.6] Namioka T., Seya M. and Noda H. (1976) Japan J. Appl. Phys., 15, 1181.

[5.7] Pouey M. (1974) J. Spec. Soc. Japan, 23, Suppl. 1, 67.

[5.8] Velzel C.H.F. (1976) J. Opt. Soc. Amer., 66, 346.

[5.9] Morozumi S. (1979) Optik, 53, 75.

[5.10] Pieuchard G. and Flamand J. (1972) Final Report of Jobin Yuon to Goddard Space Flight Center, NASA Contract No. NASW-2146.

[5.11] Namioka T., Noda H. andSeya M. (1973) Sci. Light, 22, 77.

[5.12] Noda H., Namioka T. and Seya M. (1974) J.Opt. Soc. Amer., 64, 1037.

[5.13] Cordell J., Flamand G., Piechard G. and Labeyrie A. (1970) Optical Instruments and Techniques, edited by Home Dickson (Newcastle-Upon_Tyne: Oriel Press), p.117.

[5.14] Velzel C.H.F. (1977) J.Opt. Soc. Amer., 67, 1021.

CHAPTER 6

IMAGE VARIATION WITH RELATIVE APERTURE FOR THE ROWLAND CIRCLE MOUNT

6.1 PRELIMINARY COMMENTS

Design techniques for the minimization of aberrations present in the spectral image generated by a Rowland circle mount have been described in the previous chapter. Attention is now directed towards the utilization of the geometric theory of Noda, Namioka and Seya to explore the influence which the relative aperture of the grating system has on image formation. Initially the variation with grating size of the height of an image free from given aberrations is surveyed. Secondly the dependence of the numerical size of individual terms of the light path function on the relative aperture is discussed.

6.2 VARIATION OF IMAGE HEIGHT WITH RELATIVE APERTURE

It has been previously demonstrated that to a first approximation the height of the final spectral image is governed by the length of the grooved surface and the value of the second order astigmation coefficient F020. This relation is described by the following expression:

$$Z' = L \cos\beta \, F020 \qquad (6.1)$$

where L is the total length of the illuminated grooved surface. For a grating of constant size, the only avenue to reducing the value of the image height in the above equation is through the coefficient F020. The contribution from this aberration term can be eliminated completely from the spectral image for at least two wavelengths.

However, the higher order terms of the light path function still remain to influence the performance of the grating. As a consequence Eq. (6.1), an increase in the size of a grating generating an image distorted by the presence of second order astigmatism, results in an elongation of this image. However, the relation gives no indication of the behaviour of the higher order terms when astigmatism is absent. Nor does it describe the change in the height of an image free from astigmatism as the size of the grooved surface is altered.

In the following section the performance of a grating under these conditions will be investigated.

6.2.1 *Design of Paschen circle spectrograph*

A Paschen circle spectrograph with a radius of curvature of R = 500 mm was considered for this study. Using the guidelines discussed earlier, the mount has been designed to eliminate the second order astigmatism coefficient at a correction wavelength of 589 nm. The corresponding instrumental and recording parameters are displayed in Table (6.1). Both the recording light sources are situated on the xy plane.

Varying the size of a grating of constant radius of curvature is equivalent to altering the relative aperture of the spectrograph. For any Rowland circle mount, the relative aperture of the optical system is given by

$$\text{relative aperture (R.A.)} = \frac{R}{\text{diagonal length of grating}} \qquad (6.2)$$

During the course of this investigation, convenience of calculation dictates the consideration of a square concave grating.

Recording Parameters	Mounting Parameters
r_C = 496.72 nm	r = 353.55 nm
γ = 6.545°	α = 45.0°
	σ = 1/1200 nm
r_D = 382.21 nm	
δ = 40.145°	
λ_0 = 442 nm	

TABLE (6.1) Recording and mounting parameters calculated for astigmatism elimination at LCOR = 589 nm.

Under this condition, the expression for the relative aperture of the spectrograph becomes

$$\text{relative aperture} = \frac{R}{2\sqrt{2}\ \omega_{MAX}} \tag{6.3}$$

where WIDTH = $2 * \omega_{MAX} = 2 * \ell_{MAX}$ = LENGTH

Hence an increase in the value of the relative aperture accompanies any reduction in the dimension of the illuminated area of the grating.

Utilizing a ray-tracing procedure developed according to the method of Noda, Namioka and Seya [6.1] it is possible to determine the maximum height of the final spectral image. This value, which will be referred to as Z'_{MAX}, represents the maximum value of the Z co-ordinate of the image. Therefore, it is equal to half the total image length.

A computer program traces a pencil of incident light from a point A $(x_A, y_A, 0)$ on the entrance slit till it is diffracted by an array of 121 points on the grating surface and finally focussed at the image plane. It is assumed that the spectral image is observed in a plane perpendicular to the diffracted principal ray and passes through a point B_0 $(x_0', y_0', 0)$ on the diffracted principal ray. The rays were traced for a total of eight different values of the relative aperture of the spectrograph. Table (6.2) depicts the relative aperture for each spectrograph, as well as the corresponding dimensions of the illuminated area and values for the array of diffraction points on the grating surface.

Relative aperture	Width (mm)	ω, ℓ (mm)
2	176.78	0, ±17.68, ±35.36, ±53.04, ±70.72, ±88.40
4	88.39	0, ±8.84, ±17.68, ±26.52, ±35.36, ±44.20
6	58.92	0, ±5.89, ±11.78, ±17.68, ±23.57, ±29.46
8	44.19	0, ±4.42, ±8.84, ±13.26, ±17.68, ±22.10
10	35.36	0, ±3.45, ±7.07, ±10.61, ±14.14, ±17.68
20	17.68	0, ±1.77, ±3.54, ±5.30, ±7.07, ±8.84
33	10.71	0, ±1.07, ±2.14, ±3.22, ±4.29, ±5.36
67	5.25	0, ±0.525, ±1.05, ±1.57, ±2.10, ±2.63

TABLE (6.2) Values for the relative aperture, together with the width of the illuminated area and the values for the array of diffraction points on the grating surface.

6.2.2 *Results*

The relationship between the image height and the relative aperture for various wavelengths is displayed schematically in Fig. (6.1). All graphs have been plotted on a logarithmic scale. As expected, the image height is a minimum at the correction wavelength of 589 nm, irrespective of the grating dimensions. Clearly, the behaviour of Z'_{MAX} falls into two distinct categories which are governed by the values of the test wavelengths. At the correction wavelength the gradient of the graph indicates that the image height is proportional to the inverse square of the relative aperture. Hence, if the length of the grating is doubled for this wavelength, the image height is quadrupled. In comparison, for wavelengths other than that corresponding to astigmatism correction, the image height varies as the inverse of the relative aperture. In this instance, halving the relative aperture, will increase the image height twofold. There is a region, near the correction wavelength, where the behaviour of Z'_{MAX} undergoes a transition from one category to the other. At these wavelengths, the image height obeys the relation

$$Z'_{MAX} \propto \frac{1}{\text{relative aperture}} \qquad (6.4)$$

for the higher values of the relative aperture. Conversely, for large gratings, the behaviour of the image height resembles that for the correction wavelength.

The relationship which obviously exists between the image height and the size of the concave grating can be explained mathematically by returning to the expression for the light path function.

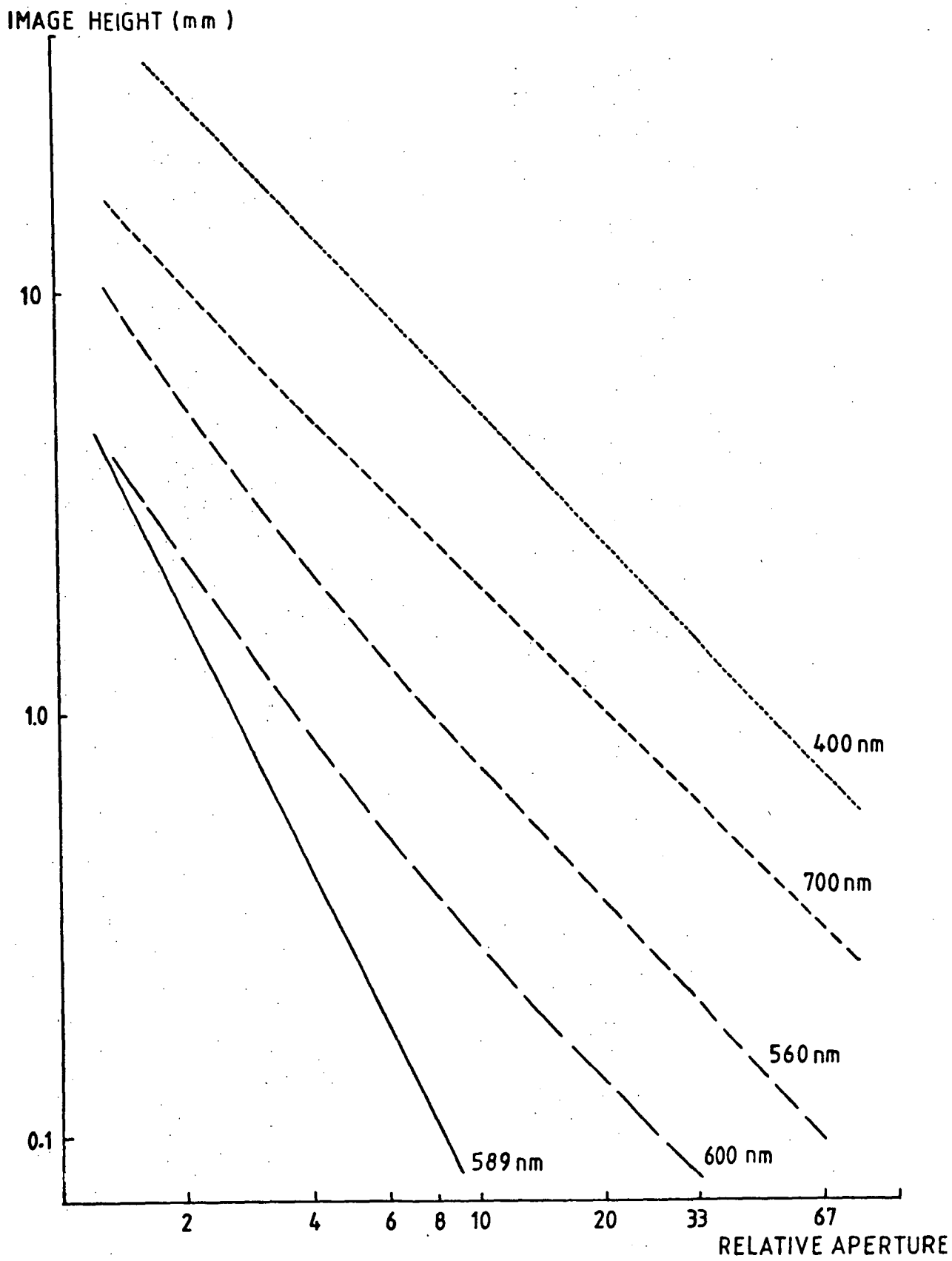

Fig.(6.1) Variation of image height with relative aperture for various wavelenths plotted on a logarithmic scale. The spectrograph was designed according to the parameters appearing in Table(6.1) to enable the elimination of astigmatism from the final image at λ=589nm. The gradient of the line corresponding to λ=589nm is -2, while that for λ=400nm is -1.

6.2.3 *Mathematical justification*

To a second approximation, considering aberration terms whose coefficients Fijk are such that i + j + k <3, the optical light path function is expressed as

$$F = F_{000} + F_{100}\omega + F_{200}\left(\frac{\omega^2}{2R}\right) + F_{020}\left(\frac{\ell^2}{2R}\right) + F_{011}\left(\frac{\ell}{R}\right) + F_{002}\left(\frac{1}{2R}\right) + F_{300}\left(\frac{\omega^3}{2R^2}\right) + F_{120}\left(\frac{\omega\ell^2}{2R^2}\right) + F_{111}\left(\frac{\omega\ell}{R^2}\right) + F_{102}\left(\frac{\omega}{2R^2}\right) \tag{6.5}$$

Applying Fermat's Principle of the shortest path length to this expression generates the following equation

$$\frac{\partial F}{\partial \ell} = 0 = F_{020}\left(\frac{\ell}{R}\right) + F_{011}\left(\frac{1}{R}\right) + F_{120}\left(\frac{\omega\ell}{R^2}\right) + F_{111}\left(\frac{\omega}{R^2}\right) \tag{6.6}$$

For the spectrograph mount under investigation, it should be remembered that both recording sources are situated on the xy plane, as is the entrance slit illumination point. Hence, use of the following equations

$$F_{011} = \frac{-Z'}{\cos\beta} \qquad F_{111} = \frac{-\sin\beta}{\cos^2\beta} \tag{6.7}$$

causes the expression for the optical light path function to become

$$\frac{\ell}{R}\left(F_{020} + \frac{\omega}{R}F_{120}\right) - Z'\left(\frac{1}{R\cos\beta} + \frac{\omega}{R^2}\frac{\sin\beta}{\cos^2\beta}\right) = 0 \tag{6.8}$$

This can be simplified in the manner presented below

$$Z' = \frac{\frac{\ell}{R}\left(F_{020} + \frac{\omega}{R^2}F_{120}\right)}{\left(\frac{1}{R\cos\beta} + \frac{\omega}{R^2}\frac{\sin\beta}{\cos^2\beta}\right)} \tag{6.9}$$

$$\frac{Z'}{R} = \frac{\frac{\ell}{R}\left(F_{020} + \frac{\omega}{R}F_{120}\right)\cos\beta}{\left(1 + \frac{\omega}{R}\tan\beta\right)} \tag{6.10}$$

The limitations imposed on the mounting conditions for this Paschen circle spectrograph give use to the following inequalities

$$\frac{\omega}{R}\tan < \frac{\omega_{MAX}}{R}\tan\beta = \frac{\tan\beta}{2\sqrt{2}(R.A.)} < \frac{\tan\beta}{4\sqrt{2}} \simeq 0.03 \qquad (6.11)$$

Consequently, the term $\frac{\omega}{R}\tan\beta$ can be neglected. From Eq. (6.10) it is clear that Z'_{MAX} is the image height corresponding to ω_{MAX} and ℓ_{MAX} and is described by

$$\frac{Z'_{MAX}}{R} \simeq \frac{\ell_{MAX}}{R}\left(F_{020} + \frac{\omega_{MAX}}{R} F_{120}\right)\cos\beta \qquad (6.12)$$

Upon substitution of the expressions for the relative aperture of the spectrograph, this equation has the final form

$$\frac{Z'_{MAX}}{R} \simeq \frac{1}{2\sqrt{2}\,(R.A.)}\left(F_{020} + \frac{F_{120}}{2\sqrt{2}\,(R.A.)}\right)\cos\beta \qquad (6.13)$$

The behaviour of the image height with variations in the relative aperture of the spectrograph can readily be explained with the aid of the above expression. At the correction wavelength, the second order astigmatism coefficient F_{020} disappears, consequently Z'_{MAX} obeys the equation

$$Z'_{MAX} = \frac{R}{8(R.A.)^2} F_{120}\cos\beta \qquad (6.14)$$

which accounts for the inverse square relation existing between Z'_{MAX} and the relative aperture. It is interesting to note that in the absence of second order astigmatism, the image height is directly proportional to the coefficient of third order coma F_{120}. When astigmatism is present, the expression for the image height reverts at large relative apertures to the first approximation presented previously, where

$$Z'_{MAX} = \frac{R}{2\sqrt{2}\,(R.A.)}\, F_{020} \cos\beta \qquad (6.15)$$

Here, Z'_{MAX} is directly proportional to the value of the astigmatism coefficient F_{020}, but inversely proportional to the relative aperture which is in agreement with the results depicted in Fig. (6.1).

The preceding discussion has been devoted to a Paschen circle spectrograph designed to eliminate second order astigmatism from the final image. However, instrument requirements often dictate the removal of third order coma from the spectral image. Inspection of Eq. (6.13) under this design condition reveals that the behaviour of the image height with relative aperture should not alter with wavelength. In order to confirm this statement, a study was conducted into the performance of a Paschen circle mount. Although this spectrograph is similar to that discussed above, it was designed to eliminate not astigmatism, but third order coma from the final image. The resultant instrument and recording parameters are displayed in Table (6.3). Fig. (6.2) illustrates that the relationship between image height and grating size is independent of the wavelength. As anticipated the gradient of each plot indicates that Z'_{MAX} is inversely proportional to the relative aperture. These logarithmic graphs also show that the minimum image height does not coincide with the correction wavelength. Rather it occurs at a slightly shorter wavelength.

6.2.4 *Height of image free from astigmatism and coma*

We have seen that to a first approximation, the image height is dependent upon second order astigmatism. Furthermore, in the absence of this aberration, it is the value of the third order coma coefficient F_{120}, which governs the height of the image. Since the simultaneous elimination of coma and astigmatism can be achieved, it is of interest to discover the behaviour of the height of a spectral image free from both

Recording parameters	Mounting parameters
r_C = 495.34 mm	r = 353.55 mm
γ = 7.830^o	α = 45.0^o
	σ = 1/1200 mm
r_D = 372.69 mm	
δ = 41.808^o	
λ_0 = 442 nm	

TABLE (6.3) Recording and mounting parameters calculated for coma elimination at LCOR = 589 nm.

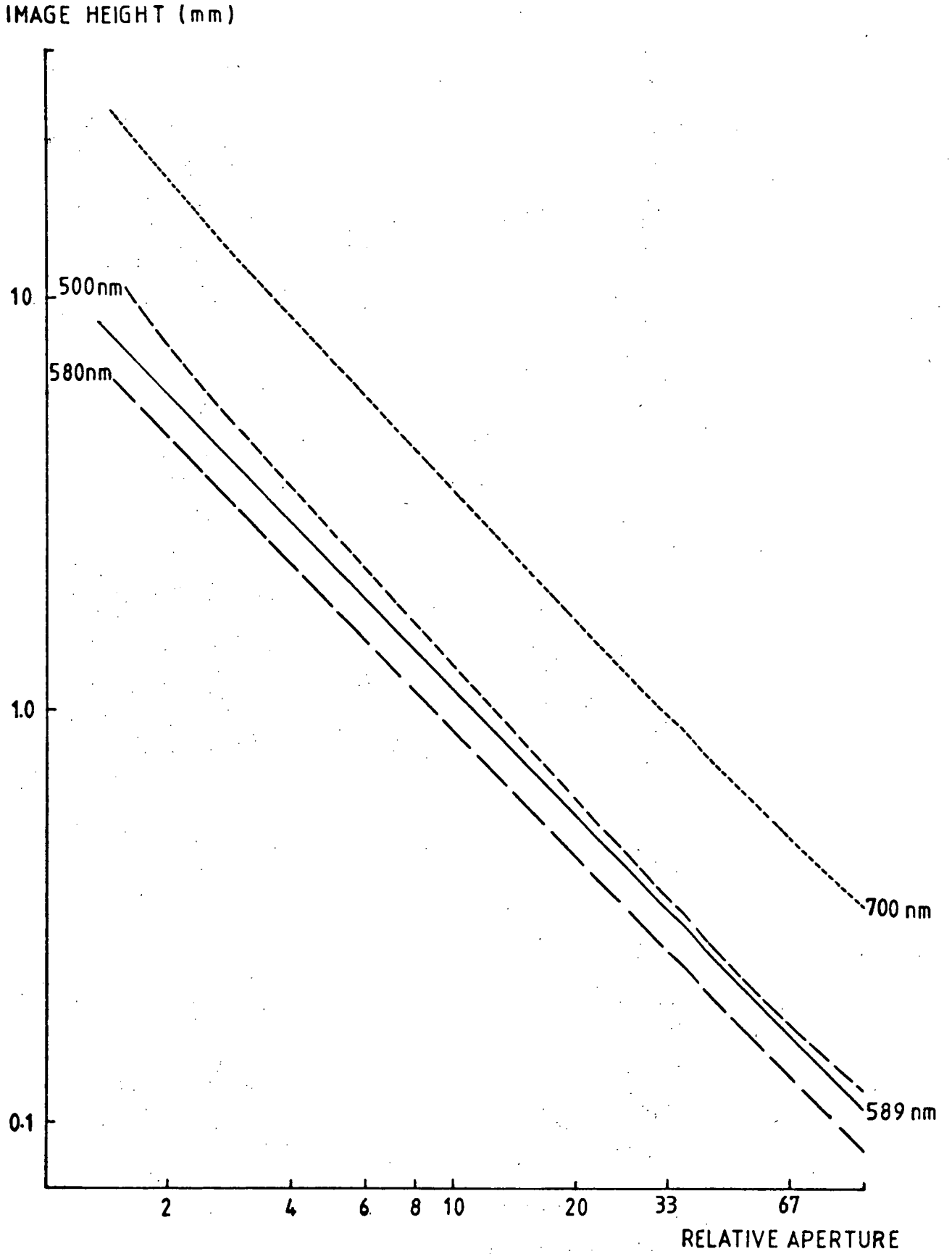

Fig.(6.2) Variation of image height with relative aperture for various wavelengths plotted on a logarithmic scale. The spectrograph was designed according to the parameters appearing in Table(6.3) to enable the elimination of coma from the final image at λ=589nm. The gradient of each line is -1.

Recording parameters	Mounting parameters
r_C = 499.32 mm	r = 490.408 mm
γ = -2.9797°	α = 11.242°
	σ = 111200 mm
r_D = 439.066	
δ = 28.582°	
λ_0 = 442 nm	
M = +1	

TABLE (6.4) Recording and mounting parameters calculated for the elimination of both astigmatism and coma at LCOR = 589 nm.

aberrations. In a manner similar to that outlined previously, a Paschen circle mount was designed to remove both astigmatism and coma from the final image for the 1st order diffracted ray at a wavelength of 589 nm. The relevant instrument and recording parameters appear in Table (6.4). It should be noted that the simultaneous removal of astigmatism and coma requires that the angle of incidence is no longer 45^{o}. Displayed in Fig. (6.3) is the behaviour of the image height with relative aperture for several diffracted wavelengths.

A simple relation no longer exists between the image height and the grating size for the corrected wavelength. This is to be expected from a consideration of the 4th order light path function, where application of Fermat's principle to diffracted rays in the Z direction yields

$$\frac{\partial F}{\partial \alpha} = \left(\frac{\ell}{R}\right) F_{020} + \frac{1}{R} F_{011} + \frac{\omega \ell}{R^2} F_{120} + \frac{\omega}{R^2} F_{111} + \frac{\omega^2 \ell}{2R^3} F_{220} + \frac{\omega^2}{2R^3} F_{211} + \frac{\ell^3}{2R^3} F_{040} + \frac{\ell}{2R^3} F_{022} + \frac{3\ell^2}{2R^3} F_{031} + \frac{1}{2R^3} F_{013} = 0 \qquad (6.16)$$

Substitution of expressions for the aberration coefficients under the conditions of the Paschen mount, generates a cubic equation in the image height Z', which is given by

$$\frac{Z'^3}{2R^3\cos^3\beta} - Z'^2 \left| \frac{\ell}{2R^3} \left(\frac{3-\cos^2\beta}{\cos^3\beta}\right) \right| + Z' \left| \frac{3\ell^2}{2R^3} \left(\frac{1-\cos^2\beta}{\cos^3\beta}\right) - \frac{\omega^2}{R^3} \frac{\sin^2\beta}{\cos^3\beta} - \frac{\omega}{R^2} \frac{\sin\beta}{\cos^2\beta} - \frac{1}{R\cos\beta} \right| + \left| \left(\frac{\ell}{R}\right) F_{020} + \left(\frac{\omega\ell}{R^2}\right) F_{120} + \left(\frac{\omega^2\ell}{2R^3}\right) F_{220} + \frac{\ell^3}{2R^3} F_{040} \right| = 0 \qquad (6.17)$$

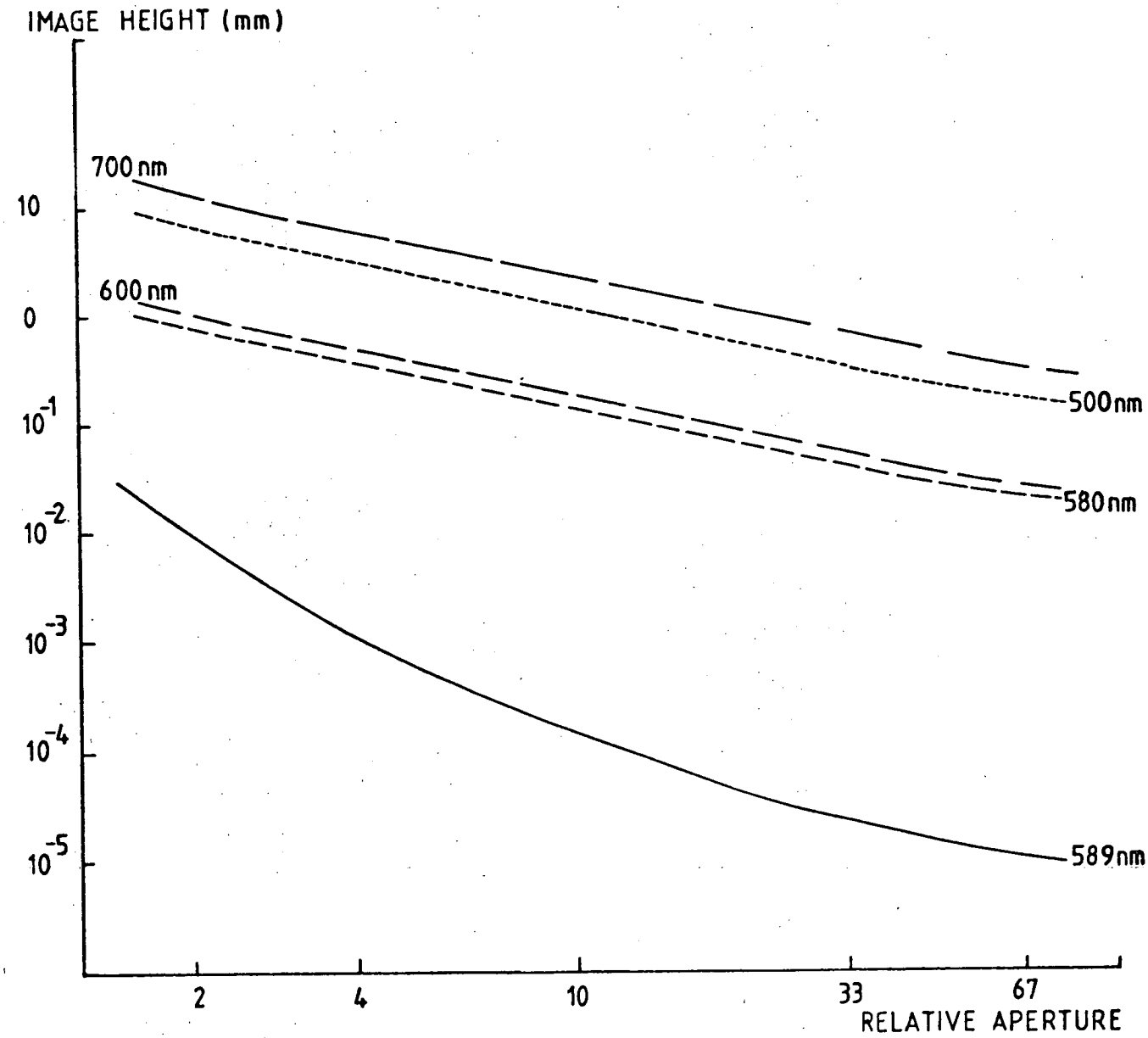

Fig.(6.3) Variation of image height with relative aperture for various wavelengths plotted on a logarithmic scale. The spectrograph was designed according to the parameters appearing in Table(6.4) to enable the elimination of both astigmatism and coma from the final image at λ=589nm.

Clearly, this equation is far more complex than that depicted in Eq. (6.8) which was derived for the third order light path function. Consequently, the disappearance of the coefficients F_{024} and F_{120} from this expression at the correction wavelength, will not lead to a simple linear relationship.

However, the dominant aspect of the behaviour of the double aberration eliminated grating is the superiority of the image produced at the correction wavelength. The image height has been reduced by at least two orders of magnitude. Unfortunately, this startling decrease does not occur at wavelengths other than the correction wavelength. In fact, for a small departure from this wavelength, the image height reverts to being governed by Eq. (6.10) and is of similar magnitude to the previous design gratings. The transition period which was evidence for the single aberration corrected gratings, is not apparent. Therefore, for any wavelength other than the correction wavelength, the values of the two coefficients F_{020} and F_{120} become significant compared to the higher order terms. Under these conditions, the image height behaves in a manner expected of a grating distorted by both astigmatism and coma, where the image height is inversely proportional to the relative aperture.

6.3 VARIATION IN NUMERICAL SIZE OF THE ABERRATION TERMS OF THE LIGHT PATH FUNCTION.

The dependence of the image height upon the magnitude of the second order astigmatism coefficient and in its absence, upon the third order coma coefficient, has been illustrated. However, little has been written of the behaviour of the remaining aberration terms with variations in the relative aperture. To investigate the contributions from these terms, alterations in the magnitude of the

individual terms of the light path functions which describe image formation by the two astigmatism-corrected gratings designed in the previous section were monitored. Tables (6.1) and (6.4) display the suitable recording and instrument parameters for the two Paschen circle mounts, calculated to eliminate second order astigmatism and second order astigmatism combined with third order coma respectively, from the final spectral image. Estimates of the size of all components of the function F, (Eq. (1.9)) were determined at the three wavelengths λ = 500 nm, 589 nm and 700 nm. Each term was considered to be composed of the product of the aberration coefficient and the corresponding co-ordinate expression. Logarithmic graphs of the modulus of the values of the significant aberration terms for various wavelengths and illuminated grating areas appear in Figs. (6.4)- (6.5). The importance of each aberration term is gauged by its value computed at low relative apertures, which must differ by less than 2 orders of magnitude from the largest numerically sized aberration term.

Inspection of Fig. (6.4) for the astigmatism-corrected grating mounted in accordance with Table (6.1), indicates that no particular term is outstanding, either at low or high relative apertures. The term having the largest numerical value at each of the three wavelengths and for all grating sizes is $F_{011}\,\frac{\ell}{R}$. At wavelengths other than the correction wavelength the magnitude of this term varies in inverse proportion to the square of the relative aperture. It is interesting to note that under these conditions the value of the second order astigmatism term is always half that of $F_{011}\,\frac{\ell}{R}$. Justification for this behaviour can readily be shown by considering two mathematical expressions from the previous section of this chapter, where

$$F_{011} = \frac{Z'}{\cos\beta} \qquad \text{and} \qquad Z' = \ell \cos\beta\, F_{020}.$$

Fig. (6.4)

The logarithmic behaviour of the magnitude of the significant aberration terms with changing relative aperture for the diffracted wavelengths 500, 589 and 700 nm. The grating is designed according to the specifications appearing in Table (6.1) for the elimination of astigmatism at the diffracted wavelength of 589 nm. The graphical symbols displayed for each wavelength represent the following aberration terms.

$\left| F_{020} \cdot \frac{\ell^2}{2R} \right|$ ---------

$\left| F_{120} \cdot \frac{\omega \ell^2}{2R^2} \right|$ ----------

$\left| F_{011} \cdot \frac{\ell}{R} \right|$ ——————

$\left| F_{031} \cdot \frac{\ell^3}{2R^2} \right|$ ——·——·——

$\left| F_{002} \cdot \frac{1}{2R} \right|$ ——x——x——

$\left| F_{044} \cdot \frac{\ell^4}{8R^3} \right|$ ——□——□——

$\left| F_{220} \cdot \frac{\omega^2 \ell^2}{4R^3} \right|$ ——o——o——

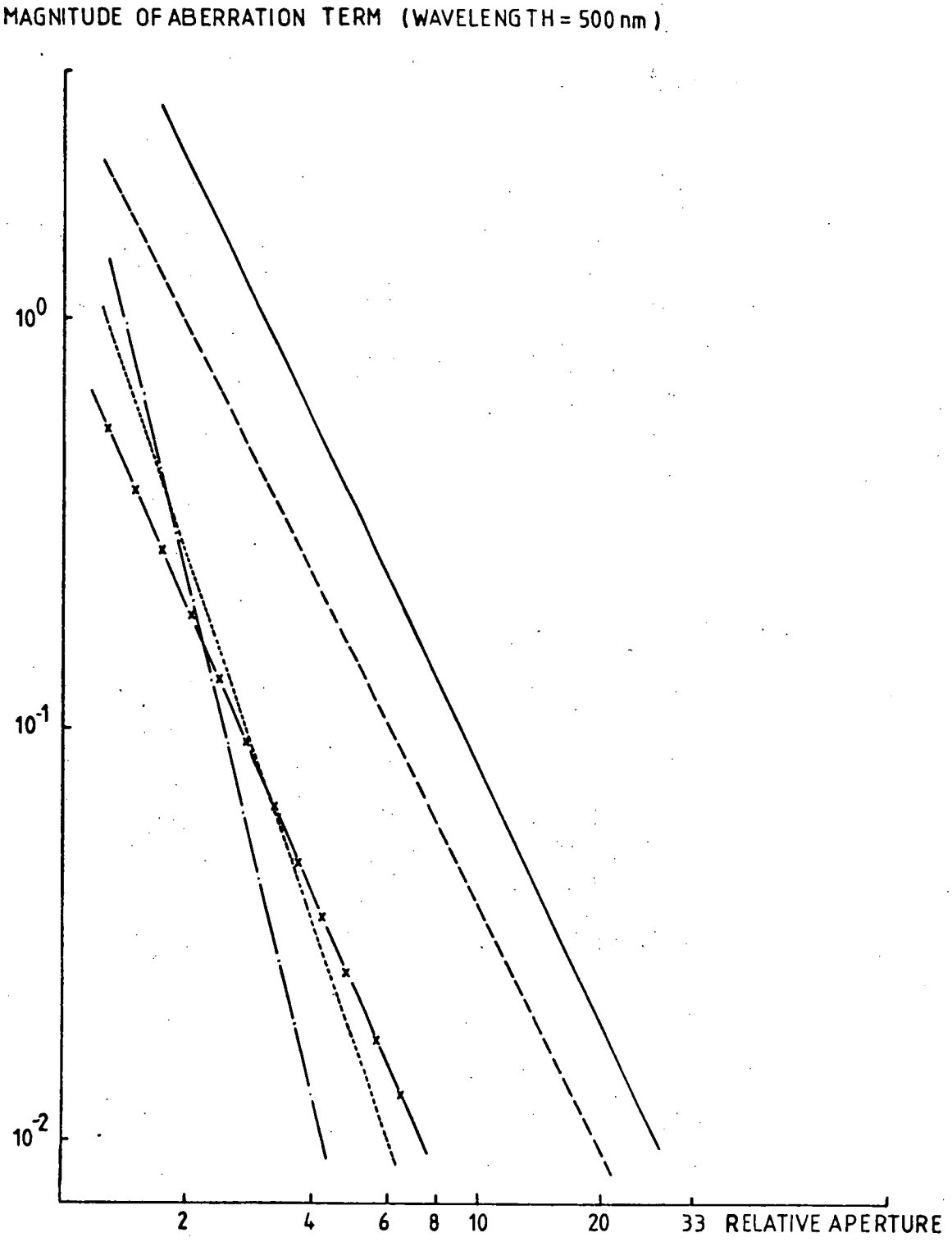
MAGNITUDE OF ABERRATION TERM (WAVELENGTH = 500 nm)
10^0
10^{-1}
10^{-2}
2
4
6
8
10
20
33
RELATIVE APERTURE

Fig. (6.4)

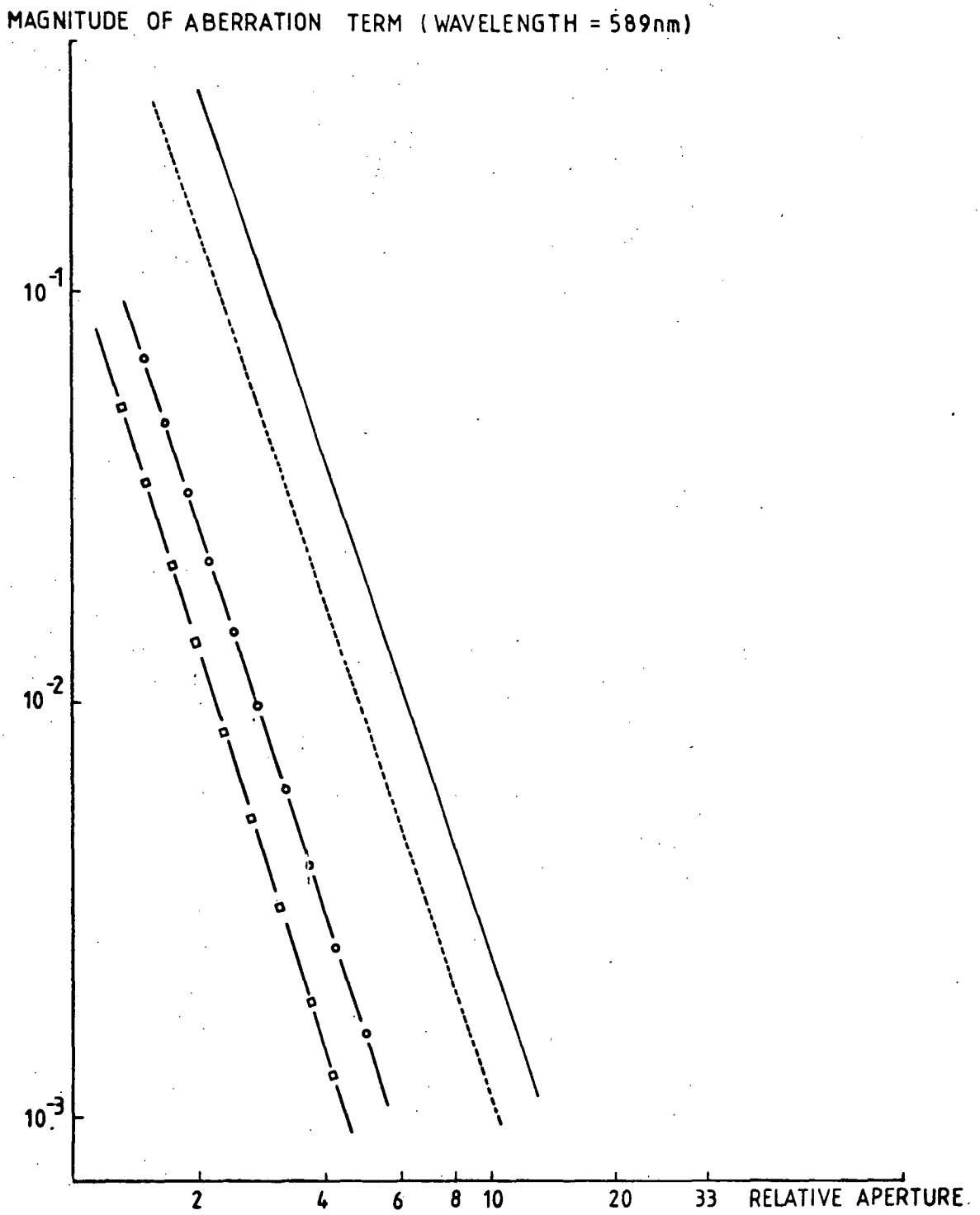

Fig.(6.4) - continued.

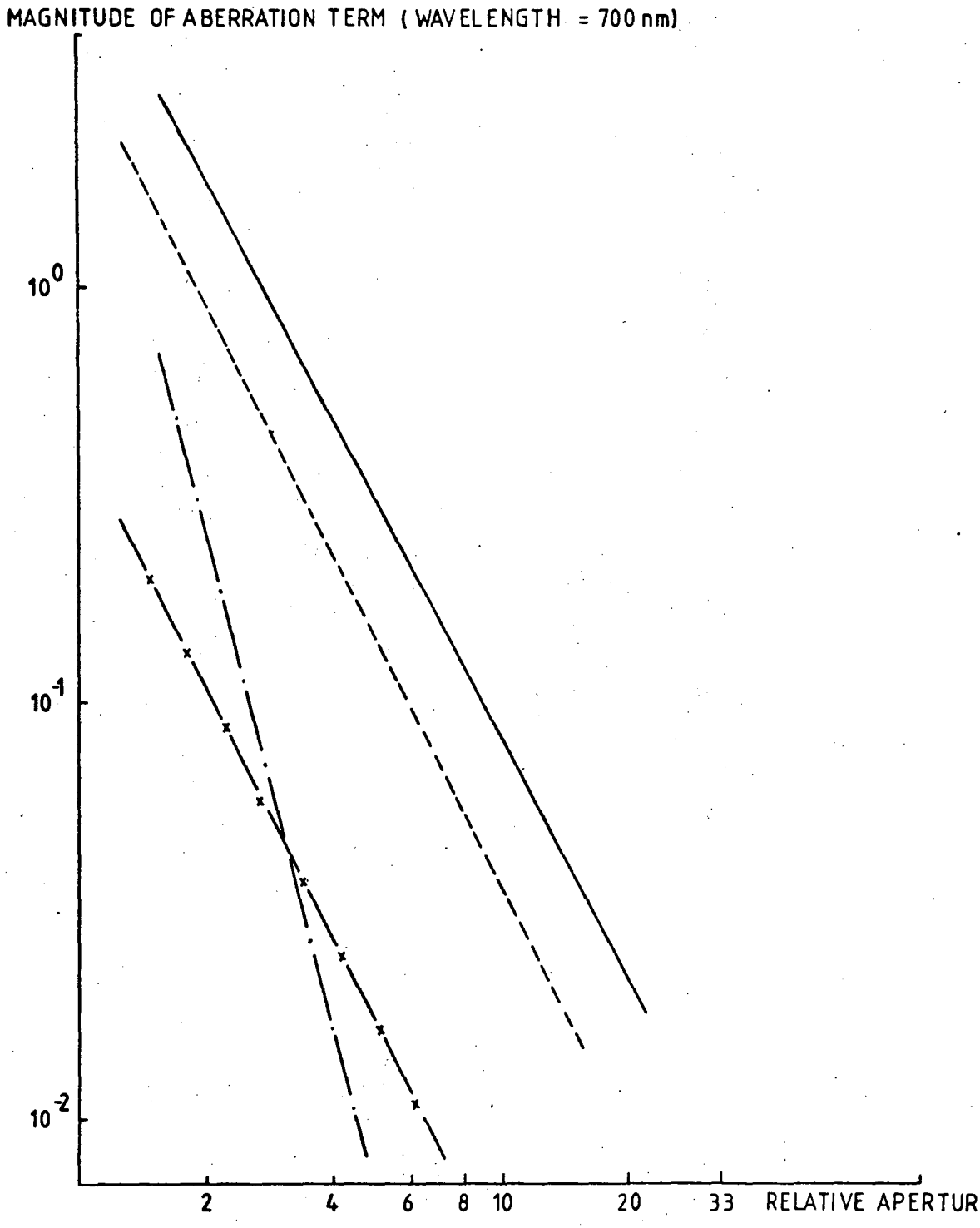

Fig. (6.4) - continued.

Fig. (6.5)

The logarithmic behaviour of the magnitude of the significant aberration terms with changing relative aperture for the diffracted wavelengths 500, 589 and 700 nm. The grating is designed according to the specifications appearing in Table (6.4) for the simultaneous elimination of astigmatism and coma at the diffracted wavelength of 589 nm. The graphical symbols displayed for each wavelength represent the following aberration terms.

$\left| F_{011} \cdot \frac{\ell}{R} \right|$ ——————

$\left| F_{031} \cdot \frac{\ell^3}{2R^2} \right|$ —— · —— · ——

$\left| F_{024} \cdot \frac{\ell^2}{2R} \right|$ — — — —

$\left| F_{220} \cdot \frac{\omega^2 \ell^2}{4R^3} \right|$ ——o——o——

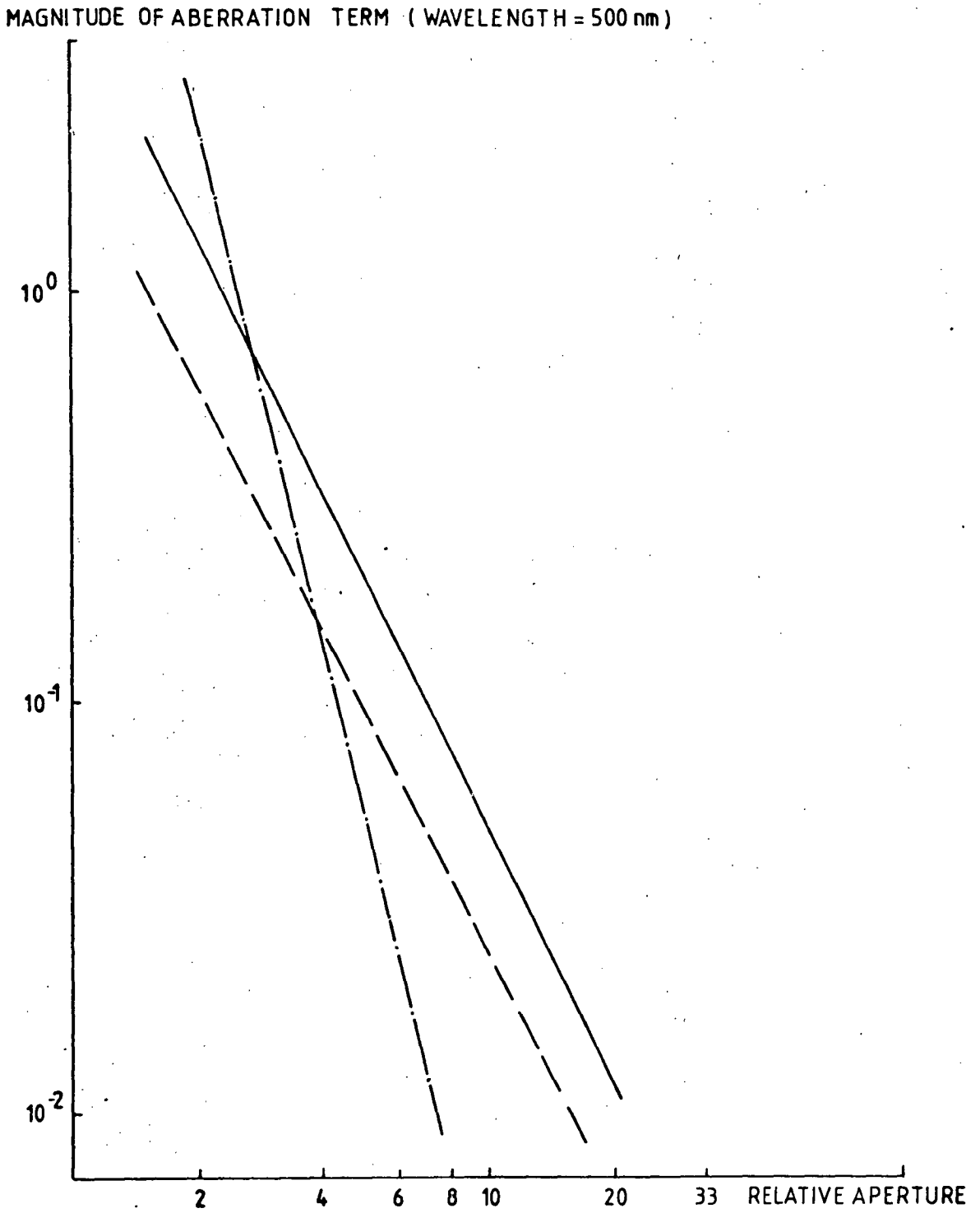
MAGNITUDE OF ABERRATION TERM (WAVELENGTH = 500 nm)
10^0
10^{-1}
10^{-2}
2
4
6
8
10
20
33
RELATIVE APERTURE

Fig.(6.5)

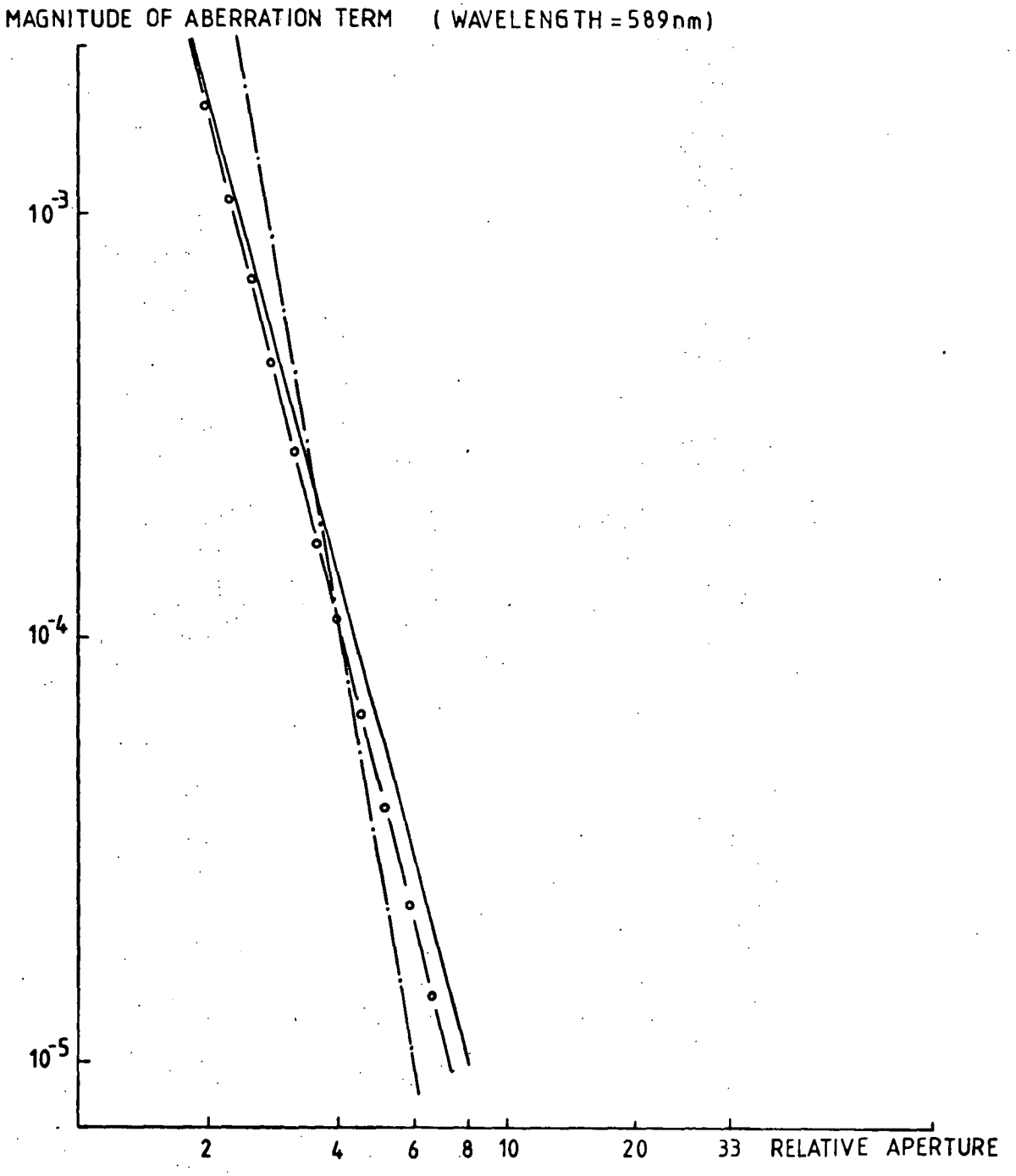

Fig.(6.5) - continued.

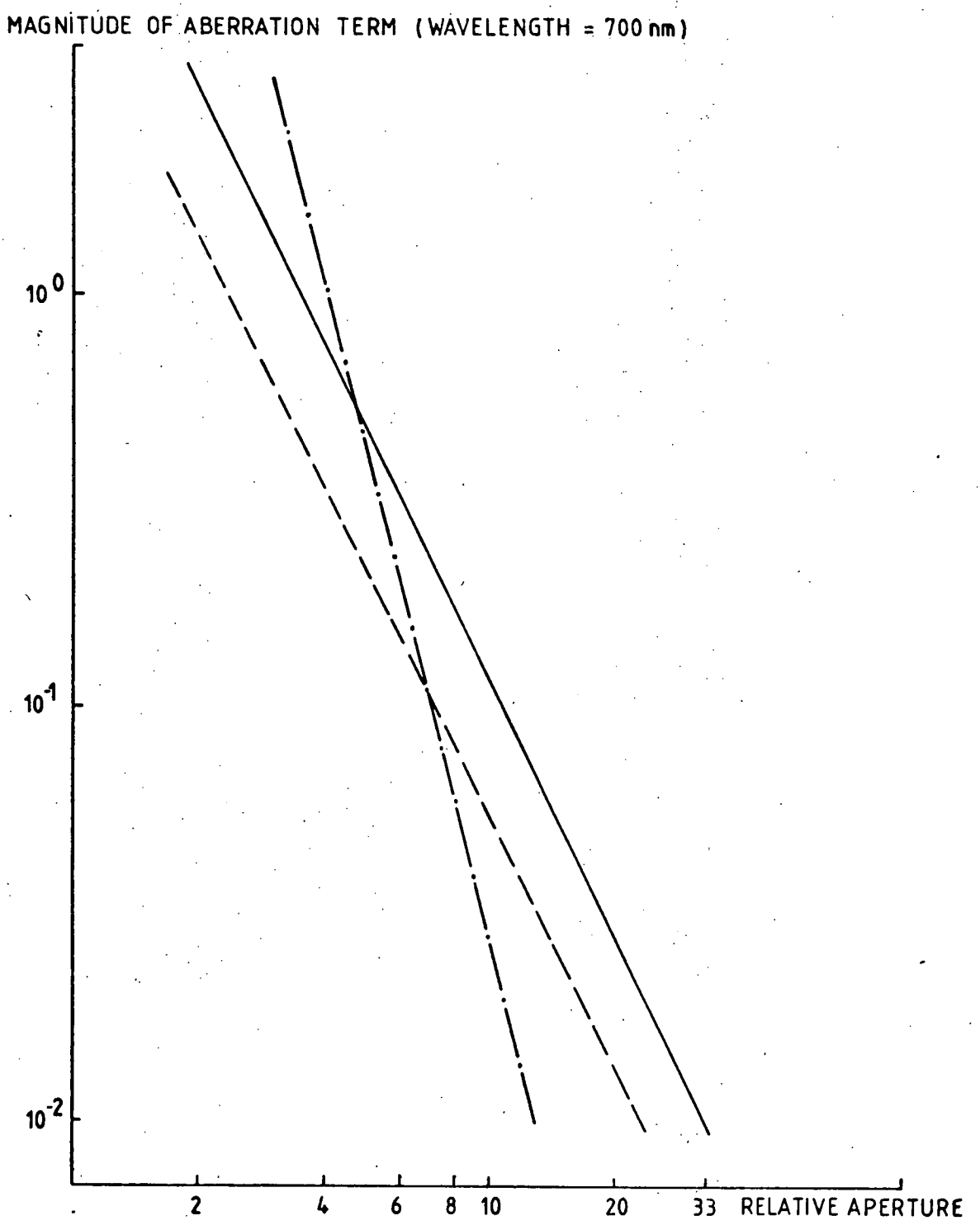

Fig.(6.5) - continued.

These equations can be combined to yield

$$F_{011}\frac{\ell}{R} = \frac{Z'}{\cos\beta}\cdot\frac{\ell}{R} = F_{020}\frac{\ell^2}{R} = 2\left(F_{020}\frac{\ell^2}{2R}\right) \qquad (6.18)$$

The term $F_{031}\frac{\ell^3}{2R^3}$, in the presence of second order astigmatism, becomes significant for very small illumination areas on the grating surface, when its magnitude is proportional to the inverse of high powers of the relative aperture.

At the correction wavelength, the astigmatism coefficient vanishes and the value of the term $F_{011}\frac{\ell}{R}$ is twice that of $F_{120}\frac{\omega\ell^2}{2R^2}$ for all grating sizes. This phenomenon is a consequence of the image height behaviour mentioned earlier. In the absence of the astigmatism coefficient, we have

$$Z'_{MAX} = \frac{R}{8(R.A.)^2}F_{120}\cdot\cos\beta \qquad (6.14)$$

where

$$R.A. = \frac{R}{2\sqrt{2}\ \omega_{MAX}} \quad \text{and} \quad R.A. = \frac{R}{2\sqrt{2}\,\ell_{MAX}}$$

which can be re-written to give

$$Z' = \frac{\omega\ell}{R}F_{120}\cos\beta \qquad (6.19)$$

Therefore, the expression for the term $F_{011}\frac{\ell}{R}$ becomes

$$F_{011}\frac{\ell}{R} = \frac{Z'}{\cos\beta}\ \frac{\ell}{R} = \frac{\omega\ell}{R}F_{124}\cos\beta\ \frac{1}{\cos\beta}\ \frac{\ell}{R}$$

$$= F_{120}\frac{\omega\ell^2}{R^2}$$

$$= 2\left(F_{120}\frac{\omega\ell^2}{2R^2}\right) \qquad (6.20)$$

It is also at the correction wavelength that two of the terms constituting primary spherical aberration become significant.

However, it is probably more the case of the remaining aberration terms being reduced down in magnitude to that of the terms $F_{220}\frac{\omega^2\ell^2}{4R^3}$ and $F_{040}\frac{\ell^4}{8R^3}$ rather than the converse.

Fig. (6.5) which corresponds to the grating mounted to cause the simultaneous disappearance of the aberration coefficients F_{020} and F_{120} at λ = 589 nm, illustrates that $F_{011}\frac{\ell}{R}$ has the largest magnitude of the aberration terms for all relative apertures greater than 4. For very fast optical systems the term $F_{031}\frac{\ell^3}{2R^3}$ dominants at all wavelengths. In a manner similar to the single elimination of second order astigmatism, the term $F_{220}\frac{\omega^2\ell^2}{4R^3}$ becomes significant at the correction wavelength.

In conclusion it can be stated that although the magnitudes of the higher order terms typically vary inversely with high powers of the relative aperture, their values even for fast optical systems are not large enough to be significant when compared to the low order terms of $F_{011}\frac{\ell}{R}$, $F_{020}\frac{\ell^2}{2R^2}$ and $F_{120}\frac{\omega\ell^2}{2R^2}$. It is only in the absence of second order astigmatism that the spherical aberration components, $F_{040}\frac{\ell^4}{8R^3}$ and $F_{220}\frac{\omega^2\ell^2}{4R^3}$ become comparable with $F_{011}\frac{\ell}{R}$.

In the following, final chapter, the performance of several uni-axial concave grating monochromators is evaluated for both mechanical and holographic aberration corrected gratings.

REFERENCES

[6.1] Noda H., Namioka T. and Seya M. (1974) J. Opt. Soc. Am., 64, 8, 1037.

CHAPTER 7

DEVELOPMENT OF A UNI-AXIAL DOUBLE CONCAVE GRATING MONOCHROMATOR

7.1 PRELIMINARY COMMENTS

A number of contemporary monochromators utilize concave diffraction gratings as the dispersing element. Traditionally, these gratings are generated by mechanical ruling engines. However, the recent introduction of holographic recording procedures into the production of concave gratings has created greater flexibility in grating design. Noda, Namioka and Seya [7.1] demonstrated that the aberrations present in the final spectral image of a monochromator can be minimized through the appropriate choice of recording and mounting parameters. Although the attention of these authors was focussed on the Seya-Namioka monochromator, the underlying principles of their geometric theory will now be applied to the development of a uni-axial double concave grating monochromator.

Initially, the aberration-minimization procedure is utilized in the design of a single concave grating mounted in an auto-collimation configuration. This configuration may have applications in low to medium resolution stellar spectroscopy since the grating can be used as a Newtonian telescope.

Addition of a spherical concave mirror mounted axially with the single grating following the entrance slit generates a monochromator similar to the commercially available P.R.A. MONOCHROMATOR 030. Ultimately the replacement of the spherical

mirror by a second concave grating, identical to the first, forms the proposed double grating monochromator.

Through an inspection of spot diagrams, the spectral performance of all three configurations are evaluated for both mechanically ruled and holographic aberration-minimized gratings. It will be shown that the size of the spectral image generated by a double concave grating monochromator with two gratings of effective period 1/600 mm is superior to that produced by a similar instrument containing a spherical mirror and a 1200 gr/mm grating. No loss in resolution accompanies this improved behaviour.

7.2 MINIMIZATION TECHNIQUES

Within this section the mathematical details of the minimization technique of Noda et al are discussed. With aberration-correction for Rowland circle spectrographs a particular aberration term is eliminated from the final spectral image for a given diffracted wavelength. In contrast, the method reported in this chapter minimizes the aberration coefficient over a pre-determined wavelength range.

Displayed in Fig. (7.1) is a schematic representation of the recording configuration for a holographic concave grating where the recording sources C and D are constrained to lie on the xy plane. Appearing also is the principal ray, which is defined to be the ray originating from the centre of the entrance slit, $A_0(x_0,y_0,0)$ and diffracted from O at an angle of β_0. The grating equation for this ray is given by

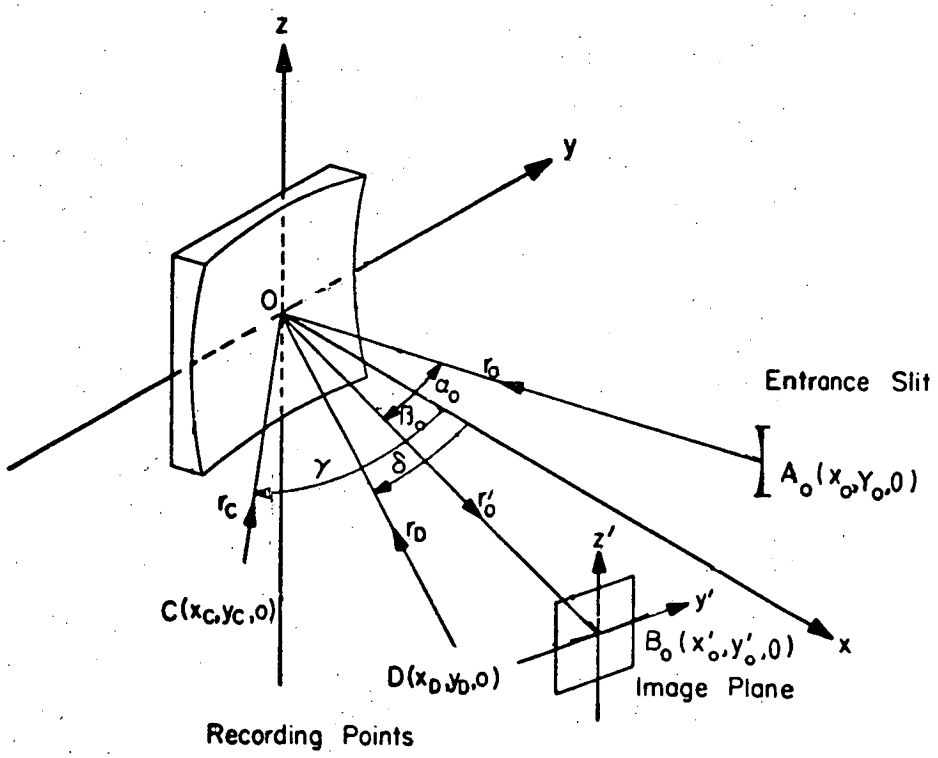

Fig.(7.1) Schematic representation of the recording configuration for a holographic concave grating where the recording sources C and D are constrained to lie on the xy plane.

$$\sin \alpha_o + \sin \beta_o = \frac{m\lambda}{\sigma} \tag{7.1}$$

where σ is the effective grating constant defined by

$$\sigma = \lambda_o/(\sin \delta - \sin \gamma), \quad \delta > \gamma \tag{7.2}$$

Recalling that each aberration coefficient derived using Fermat's principle is composed of a mechanical and holographic compoment such that

$$F_{ijk} = M_{ijk} + (m\lambda/\lambda_o)H_{ijk} \tag{7.3}$$

a further holographic term, A_{ijk}, can be defined by

$$A_{ijk} = H_{ijk}/(\sin \delta - \sin \gamma) \tag{7.4}$$

Combining Eqs.(7.4) and (7.2) yields

$$A_{ijk} = (\sigma/\lambda_o)H_{ijk} \tag{7.5}$$

which enables Eq.(7.3) describing the aberration coefficient to be re-written as

$$F_{ijk} = M_{ijk} + A_{ijk}(\sin \alpha_o + \sin \beta_o) \tag{7.6}$$

If the aberration coefficient for the principal ray is denoted by $\bar{F}_{ijk}$, then each coefficient can be expressed in terms of the mounting parameters $(\bar{\rho},\bar{\rho}')$, the angle of rotation of the grating (θ) and the holographic term A_{ijk}, that is,

$$\bar{F}_{ijk} = \bar{F}_{ijk}(\bar{\rho},\bar{\rho}',\theta,A_{ijk}) \tag{7.7}$$

where $\bar{\rho} = R/r_o \qquad \bar{\rho}' = R/r_o'$ (7.8)

The minimization process is achieved by imposing the condition

$$I_{ijk} = \int_{\theta_1}^{\theta_2} \bar{F}_{ijk}^{\,2}\, d\theta = \text{minimum} \qquad (7.9)$$

where θ_1 and θ_2 are the respective lower and upper limits placed on the angle of rotation of the grating.

Although any aberration coefficient can be reduced by this technique, it is extremely important for monochromators to fulfil the criterion of horizontal focus, $F_{200} \approx 0$, over the scanning wavelength range. Under this restraint, Eq.(7.9) becomes

$$I_{200} = \int_{\theta_1}^{\theta_2} \bar{F}_{200}^{\,2} d\theta = \text{minimum} \qquad (7.10)$$

This minimizing condition is satisfied by choosing values of $\bar{\rho}, \bar{\rho}'$ and A_{200} such that the following expressions hold,

$$\frac{\partial I_{200}}{\partial \bar{\rho}} = 0 \qquad \frac{\partial I_{200}}{\partial \bar{\rho}'} = 0 \qquad \frac{\partial I_{200}}{\partial A_{200}} = 0 \qquad (7.11)$$

Solution of Eq.(7.11) determines the mounting parameters of the monochromator which describes the distance of the first optical element from the entrance slit and that of the grating from the exit slit. Once values for $\bar{\rho}, \bar{\rho}'$ and A_{200} are known, each of the remaining integrals $I_{ijk}, i+j+k \geq 2$ becomes a function of A_{ijk} only. Consequently, the remaining values of A_{ijk}'s satisfying Eq.(7.10) are given by

$$\frac{\partial I_{ijk}}{\partial A_{ijk}} = 0 \qquad (7.12)$$

Re-arrangement of Eq.(7.5) makes it possible to determine suitable positions for the recording sources from a knowledge of the mounting parameters and the holographic terms A_{ijk}. For each grating, the recording parameters ρ_C, ρ_D, γ and δ are calculated such that either primary astigmatism [(ijk) = (020)] and the coma-type aberration [(ijk) = (300)] or the two coma-type aberrations [(ijk) = (300) and (120)] are minimized. Therefore, the correction of primary astigmatism and third order y-axis coma is achieved by the simultaneous solution of the following equations,

$$\begin{aligned} \sin\delta - \sin\gamma &= \lambda_o/\sigma \\ f_{200}(\rho_C,\gamma) - f_{200}(\rho_D,\delta) &= (\lambda_o/\sigma)A_{200} \\ f_{020}(\rho_C,\gamma) - f_{020}(\rho_D,\delta) &= (\lambda_o/\sigma)A_{020} \\ f_{300}(\rho_C,\gamma) - f_{300}(\rho_D,\delta) &= (\lambda_o/\sigma)A_{300} \end{aligned} \tag{7.13}$$

Similarly, for the correction of the two coma-type aberrations, the equations,

$$\begin{aligned} \sin\delta - \sin\gamma &= \lambda_o/\sigma \\ f_{200}(\rho_C,\gamma) - f_{200}(\rho_D,\delta) &= (\lambda_o/\sigma)A_{200} \\ f_{300}(\rho_C,\gamma) - f_{300}(\rho_D,\delta) &= (\lambda_o/\sigma)A_{300} \\ f_{120}(\rho_C,\gamma) - f_{120}(\rho_D,\delta) &= (\lambda_o/\sigma)A_{120} \end{aligned} \tag{7.14}$$

are solved.

It is convenient if the aberration-minimized holographic concave gratings are interchangeable with mechanically ruled concave gratings of the same radius of curvature. This versatility is possible if the instrumental constants $\bar{\rho}$ and $\bar{\rho}'$

calculated for mechanically ruled concave gratings are considered in the design of holographic concave gratings. Appropriate mounting parameters for mechanically ruled concave gratings are determined from

$$I_{200}' = \int_{\theta_1}^{\theta_2} \bar{M}_{200}^2 \, d\theta = \text{minimum} \qquad (7.15)$$

or

$$\frac{\partial I_{200}'}{\partial \bar{\rho}} = 0 \qquad \frac{\partial I_{200}'}{\partial \bar{\rho}'} = 0 \qquad (7.16)$$

The holographic equivalent of the ruled grating is described by the parameters $\bar{\rho}$ and $\bar{\rho}'$ calculated from Eq.(7.16) and the holographic term A_{200} determined from Eq.(7.12). This design approach is referred to as the modified method.

Therefore, three grating design procedures are employed in the development of the monochromators under study. These methods are summarized in Table (7.1). The performance of each monochromator is evaluated using a ray-tracing procedure formulated by the author from that presented by Noda et al [7.2]. Spot diagrams are constructed for diffracted wavelengths of λ = 200, 400 and 700 mm in the plane y'z' of the exit slit, considered to be perpendicular to the principal ray OB_o.

7.3 CONCAVE GRATING IN AN AUTO-COLLIMATION CONFIGURATION

The development of the proposed double grating monochromator is commenced with an investigation of the spectral performance of a single concave grating used in an auto-collimation configuration as shown in Fig.(7.2). For this grating the following identities hold

Design Method	Grating Type	Parameters
General method	Purely holographic	$\bar{\rho}$, $\bar{\rho}'$, A_{200}
Modified method	Holographic, interchangeable with mechanically ruled concave grating of the same radius of curvature	$\bar{\rho}$, $\bar{\rho}'$, A_{200}
Mechanical	Purely mechanical, mounting parameters equal to those calculated for modified method	$\bar{\rho}$, $\bar{\rho}'$

TABLE (7.1) Outline of the three grating design procedures employed in the development of the monochromator under study.

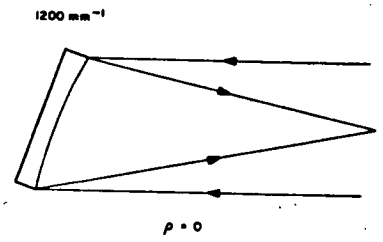

Fig.(7.2) Schematic representation of concave grating mounted in an auto-collimation configuration.

$$\alpha_o = \beta_o = \theta \quad \text{where} \quad \sin \alpha_o = \frac{m\lambda}{2\sigma} \tag{7.17}$$

and $\bar{\rho} = 0$

Under conditions (7.17) the relation between the angle of rotation of the grating and the diffracted wavelength is given by

$$\lambda = \frac{2\sigma}{m} \sin \theta \tag{7.18}$$

The coefficient of the horizontal focus term associated with the principal ray of a concave spherical grating in auto-collimation has the form

$$\begin{aligned} \bar{F}_{200} &= \bar{M}_{200} + 2A_{200}\sin \theta \\ &= \bar{\rho}'\cos^2\theta - 2 \cos \theta + 2A_{200}\sin \theta \end{aligned} \tag{7.19}$$

The mechanical components of the coefficients of the remaining significant low order aberration terms are given by

$$\begin{aligned} \bar{M}_{020} &= \bar{\rho}' - 2 \cos \theta \\ \bar{M}_{300} &= \bar{\rho}'^2\cos^2\theta.\sin \theta - \bar{\rho}' \cos \theta.\sin \theta \\ \bar{M}_{120} &= \bar{\rho}'^2\sin \theta - \bar{\rho}' \sin \theta.\cos \theta \\ \bar{M}_{400} &= \bar{\rho}'(\bar{\rho}' - \cos \theta)[2\bar{\rho}' \sin^2\theta - (\bar{\rho}' \cos \theta - 1)\cos \theta] \\ \bar{M}_{040} &= \bar{\rho}'(\bar{\rho}' - \cos \theta)^2 \end{aligned} \tag{7.20}$$

The holographic term H_{ijk} is described by

$$H_{ijk} = f_{ijk}(\rho_C,\gamma) - f_{ijk}(\rho_D,\delta)$$

$$\text{for } (ijk) = (200),(020),(300),(120)$$

$$H_{ijk} = H_{020} - (-1)^{\frac{1}{2}i}[f_{ijk}(\rho_C,\gamma) - f_{ijk}(\rho_D,\delta)] \tag{7.21}$$

$$\text{for } (ijk) = (400),(220),(040)$$

where

$$f_{200}(\rho_C,\gamma) = (\rho_C\cos\gamma - 1)\cos\gamma$$

$$f_{020}(\rho_C,\gamma) = \rho_C - \cos\gamma$$

$$f_{300}(\rho_C,\gamma) = \rho_C\sin\gamma\, f_{200}(\rho_C,\gamma)$$

$$f_{120}(\rho_C,\gamma) = \rho_C\sin\gamma\, f_{020}(\rho_C,\gamma)$$

$$f_{400}(\rho_C,\gamma) = \rho_C f_{200}(\rho_C,\gamma)[f_{200}(\rho_C,\gamma) - 4\rho_C\sin^2\gamma]$$

$$f_{220}(\rho_C,\gamma) = \rho_C f_{020}(\rho_C,\gamma)[2\rho_C\sin^2\gamma - f_{200}(\rho_C,\gamma)]$$

$$f_{040}(\rho_C,\gamma) = \rho_C[f_{020}(\rho_C,\gamma)]^2 \tag{7.22}$$

Hence, the expression for I_{200} generated by applying the general minimization method as Eq.(7.19) is given by

$$I_{200} = \frac{\bar{\rho}'^2}{32}(12\theta + 8\sin 2\theta + \sin 4\theta)$$

$$- \frac{\bar{\rho}'}{3}[A_{200}(3\cos\theta + \cos 3\theta) + (9\sin\theta + \sin 3\theta)]$$

$$+ (2\theta + \sin 2\theta) + A_{200}^2(2\theta - \sin 2\theta) + 2A_{200}\cos 2\theta \Big|_{\theta_1}^{\theta_2} \tag{7.23}$$

and the corresponding equation for the modified method is

$$I_{200}' = \frac{\bar{\rho}'^2}{32}(12\theta + 8\sin 2\theta + \sin 4\theta) - \frac{\bar{\rho}'}{3}(9\sin\theta + \sin 3\theta) + (2\theta + \sin 2\theta)\Big|_{\theta_1}^{\theta_2} \tag{7.24}$$

Following the computation of the instrumental parameters from Eq.(7.23), the values of A_{ijk}'s which satisfy Eq.(7.21) are determined from the relation $\partial I_{200}/\partial A_{ijk} = 0$:

where

$$A_{ijk} = [B_{ijk}(\theta_2) - B_{ijk}(\theta_1)]/[2(\theta_2-\theta_1)-(\sin 2\theta_2-\sin 2\theta_1)] \tag{7.25}$$

and

$$B_{200}(\theta) = \frac{\bar{\rho}'}{3}\cos\theta(1 + \cos 2\theta) - \cos 2\theta$$

$$B_{020}(\theta) = 2\bar{\rho}'\cos\theta - \cos 2\theta$$

$$B_{300}(\theta) = \frac{\bar{\rho}'^2}{16}(\sin 4\theta-2\theta) + \frac{\bar{\rho}'}{6}(3\sin\theta - \sin 3\theta)$$

$$B_{120}(\theta) = \frac{\bar{\rho}'}{6}(3\sin\theta - \sin 3\theta) + \frac{\bar{\rho}'^2}{2}(\sin 2\theta-2\theta) \tag{7.26}$$

All three procedures described in the previous section are applied to the design of aberration-corrected gratings suitable for use in the auto-collimation configuration. For this single concave grating mount it is assumed that the required wavelength range is 0 - 700 nm in the first order, the effective grating constant is σ = 1/1200 mm and the recording wavelength is λ_o = 442 nm.

The instrumental constants determined are

$$\bar{\rho}' = 1.972090 \qquad \bar{\rho} = 0 \qquad A_{200} = 0.1984176 \tag{7.27}$$

for the general method;

$$\bar{\rho}' = 2.09532 \qquad \bar{\rho} = 0 \qquad A_{200} = -3.91787\times10^{-6} \tag{7.28}$$

for the modified method; and

$$\bar{\rho}' = 2.09532 \qquad \bar{\rho} = 0 \tag{7.29}$$

for the mechanical concave grating.

Demonstrated by Fig.(7.3) is the behaviour of the horizontal focus coefficient $\bar{F}_{200}$, resulting from the use of the general and modified methods. Since the value of A_{200} calculated for the modified method is low, there is no discernable difference between the curves describing $\bar{F}_{200}$ for this method (indicated in the figure by the dashed line) and for the ruled grating. It is seen from the figure that a grating mounted in accordance with the parameters of the general method exhibits superior horizontal focussing over all but a narrow band of the wavelength range.

Eqs.(7.13) and (7.14) are sensitive to the values of the holographic term A_{ijk}. Therefore, the existence of suitable aberration-reducing recording parameters is ultimately governed by the maximum angle of grating rotation used in Eq.(7.25) for the determination of A_{ijk}. If a value for θ_2 of 24.83° (λ_2 = 700 nm) is considered in the computation of A_{300},

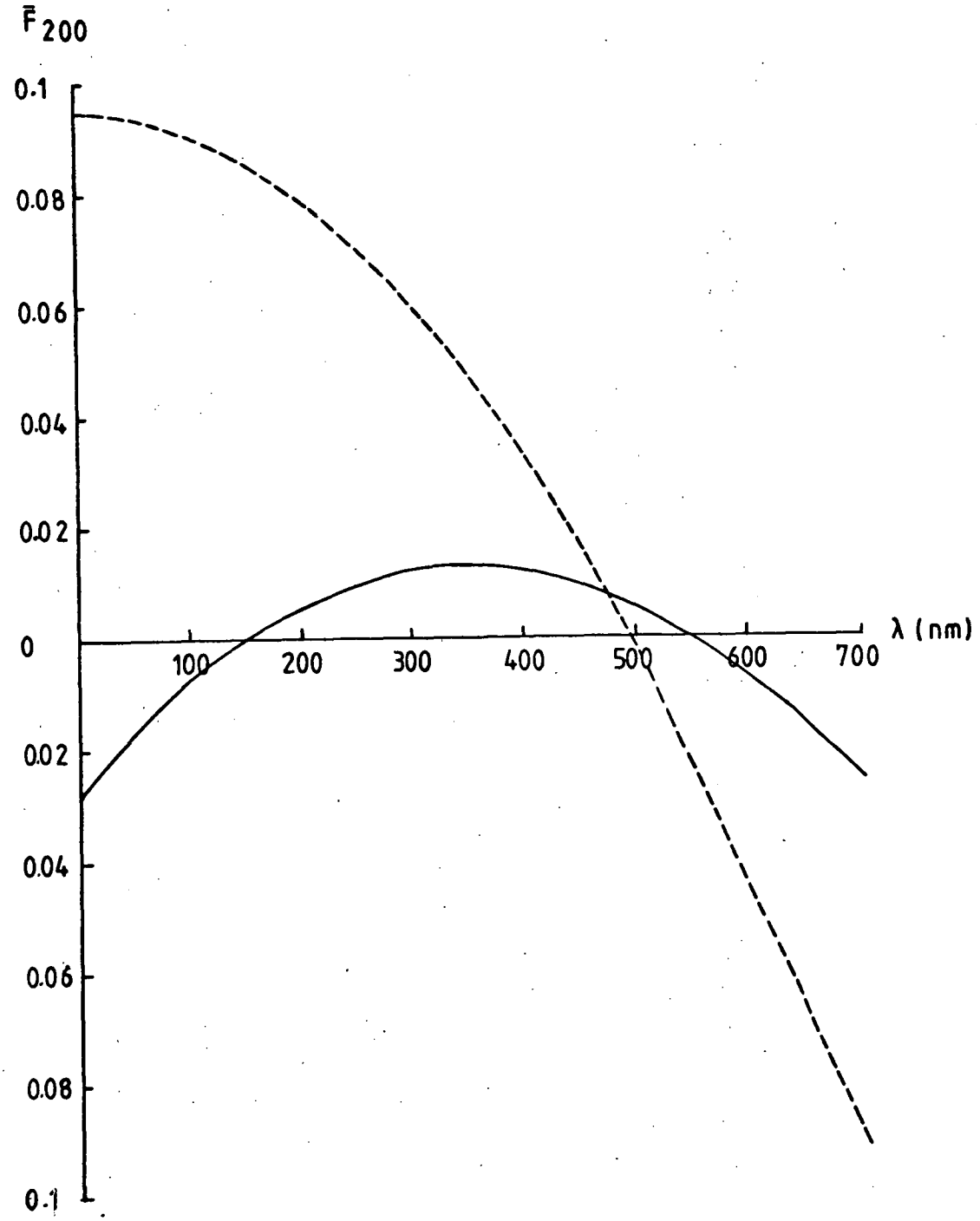

Fig.(7.3) Magnitude of $\bar{F}_{200}$ as as function of the diffracted wavelength. The dashed curve and the solid curve are calculated by the use of the modified method and the general method respectively.

disappointingly large recording angles result. However, increasing θ_2 to 36.87° (λ_2 = 1000 nm) produces a far more satisfactory set of recording parameters. Therefore, the following values of θ_1 and θ_2 are adopted in the computation of A_{ijk}'s

$$\begin{aligned} \theta_1 &= 0° \qquad (\lambda_1 = 0 \text{ nm}) \\ &\qquad\quad \text{for } (ijk) = (200),(020),(300),(120) \\ \theta_2 &= 24.83° \quad (\lambda_2 = 700 \text{ nm}) \\ &\qquad\quad \text{for } (ijk) = (200),(020),(120) \\ &= 36.87° \quad (\lambda_2 = 1000 \text{ nm}) \\ &\qquad\quad \text{for } (ijk) = (300) \end{aligned} \tag{7.30}$$

Using the values appearing in Eqs. (7.27),(7.28),(7.29) and (7.30), the recording parameters are determined from Eqs. (7.13) and (7.14). Shown in Table (7.2) are the recording parameters calculated from both the general and modified design procedures for correcting astigmatism and coma for the single grating mount. It is interesting to note that the two methods yield practically the same recording parameters.

Table (7.3) displays the values of the $\overline{F}_{ijk}$'s at diffracted wavelengths of 0, 200, 400 and 700 nm calculated for the astigmatism-minimized holographic gratings and a mechanically ruled grating having the same R and σ. Similar quantities for coma-corrected holographic gratings are listed in Table (7.4). In these tables, G.M. and M.M. represent holographic concave gratings whose recording parameters are determined by the general

Minimized Terms	Method Used	ρ_C	ρ_D	$\gamma°$	$\delta°$
$\overline{F}_{200}$, $\overline{F}_{020}$	General	1.522975	1.52692	-9.375113	21.56168
$\overline{F}_{300}$ (astigmatism-correction)	Modified	1.518609	1.639835	-9.54865	21.37774
$\overline{F}_{200}$, $\overline{F}_{120}$	General	1.507892	1.582646	-6.04398	25.15751
$\overline{F}_{300}$ (coma-correction)	Modified	1.48765	1.687755	-6.003934	25.20152

TABLE (7.2) Recording parameters suitable for correcting astigmatism and coma for the single holographic concave grating. It is assumed that σ = 1/1200 mm, $m\lambda$ = 0 → 700 nm and λ_o = 442 nm. For the instrumental constants used in the calculations, refer to Eqs. (7.27) and (7.28). θ_1 = o°, θ_2 = 24.83°, θ_3 = 36.87°.

λ(nm)	Grating	$\overline{F}_{200}$	$\overline{F}_{020}$	$\overline{F}_{300}$	$\overline{F}_{120}$	$\overline{F}_{400}$	$\overline{F}_{220}$	$\overline{F}_{040}$
0	MECH	0.09532	0.09532	0.00000	0.00000	-2.41849	-2.41849	-2.41849
	G.M.	-0.02791	-0.02791	0.00000	0.00000	-1.89145	-1.89145	-1.89145
	M.M.	0.09532	0.09532	0.00000	0.00000	-2.41849	-2.41849	-2.41849
200	MECH	0.07960	0.10977	0.26964	0.27722	-2.02863	-2.22820	-2.43732
	G.M.	0.00574	-0.04089	0.07019	0.02001	-1.84252	-1.93005	-1.88426
	M.M.	0.07957	0.03006	0.08097	0.02486	-2.35609	-2.42796	-2.33924
400	MECH	0.03308	0.15377	0.50482	0.56551	-0.94230	-1.64284	-2.49598
	G.M.	0.01214	-0.02432	0.11046	0.05043	-1.24577	-1.65338	-1.90565
	M.M.	0.03302	-0.00566	0.12748	0.06079	-1.59722	-2.04236	-2.29983
700	MECH	-0.08934	0.28027	0.72003	1.04530	1.41222	0.08377	-2.67593
	G.M.	-0.02425	0.06104	0.05164	0.14064	0.20493	-0.55114	-2.00601
	M.M.	-0.08946	0.00126	0.05970	0.16204	0.26611	-0.61539	-2.33207

TABLE (7.3) Values of $\overline{F}_{ijk}$'s for the mechanically ruled and the astigmatism-corrected holographic grating. The recording parameters used are listed in Table (7.2). The instrumental constants used are those described by Eqs.(7.27) and (7.28). M.M. and G.M. stand for modified method and general method respectively.

λ(nm)	Grating	$\overline{F}_{200}$	$\overline{F}_{020}$	$\overline{F}_{300}$	$\overline{F}_{120}$	$\overline{F}_{400}$	$\overline{F}_{220}$	$\overline{F}_{040}$
0	MECH	0.09532	0.09532	0.00000	0.00000	-2.41849	-2.41849	-2.41849
	G.M.	-0.02791	-0.02791	0.00000	0.00000	-1.89145	-1.89145	-1.89145
	M.M.	0.09532	0.09532	0.00000	0.00000	-2.41849	-2.41849	-2.41849
200	MECH	0.07960	0.10977	0.26964	0.27722	-2.02863	-2.22820	-2.43732
	G.M.	0.00576	-0.08769	0.07016	-0.01139	-2.01460	-2.06440	-1.83021
	M.M.	0.07956	-0.02136	0.08070	-0.01210	-2.56405	-2.58759	-2.26400
400	MECH	0.3308	0.15377	0.50482	0.56551	-0.94230	-1.64284	-2.49598
	G.M.	0.12189	-0.11793	0.11042	-0.01236	-1.58994	-1.92208	-1.79753
	M.M.	0.03301	-0.10850	0.12748	-0.01313	-2.01314	-2.36161	-2.14936
700	MECH	-0.08934	0.28027	0.72003	1.04530	1.41222	0.08377	-2.67593
	G.M.	-0.02417	-0.10278	0.05157	0.03076	-0.39738	-1.02137	-1.81681
	M.M.	-0.08947	-0.17870	0.05969	0.03268	-0.46175	-1.17408	-2.06934

TABLE (7.4) Values of $\overline{F}_{ijk}$'s for the mechanically ruled and the coma-corrected holographic grating. The recording parameters used are listed in Table (7.2). The instrumental constants used are those described by Eqs. (7.27) and (7.28). M.M. and G.M. stand for modified method and general method respectively.

method and modified method respectively. The improved spectral performance of the holographic gratings compared with the mechanically ruled gratings is evident, particularly at the longer wavelengths.

For the ray-tracing procedure the concave grating is assumed to have a radius of curvature of 508 mm and a grooved area 43.14 mm (L) × 43.14 mm (W). The rays traced are those originating at infinity and diffracted from a matrix of 121 points on the grating surface whose coordinates are described by ω = 4.31 mm and ℓ = 4.31 mm with j = 0, ±1, .. ±5 and k = 0, ±1, ... ±5.

Fig.(7.4) compares a set of spot diagrams generated from an astigmatism-corrected concave grating designed according to the general method and those for a ruled concave grating. Since Fig.(7.3) illustrates the improved behaviour of the horizontal focus for the general method grating, the instrumental constants of Eq.(7.27) are used in construction of these spot diagrams. Similar spot diagrams generated for coma-corrected holographic gratings are shown in Fig.(7.5).

The superior spectral performance of the astigmatism-minimized grating is clearly evident for all diffracted wavelengths. Not only is excellent horizontal focus achieved, but a dramatic decrease in image height occurs. This is to be expected considering the significant influence which the astigmatism coefficient has on the image height. Although good horizontal focus is exhibited by the coma-minimized grating,

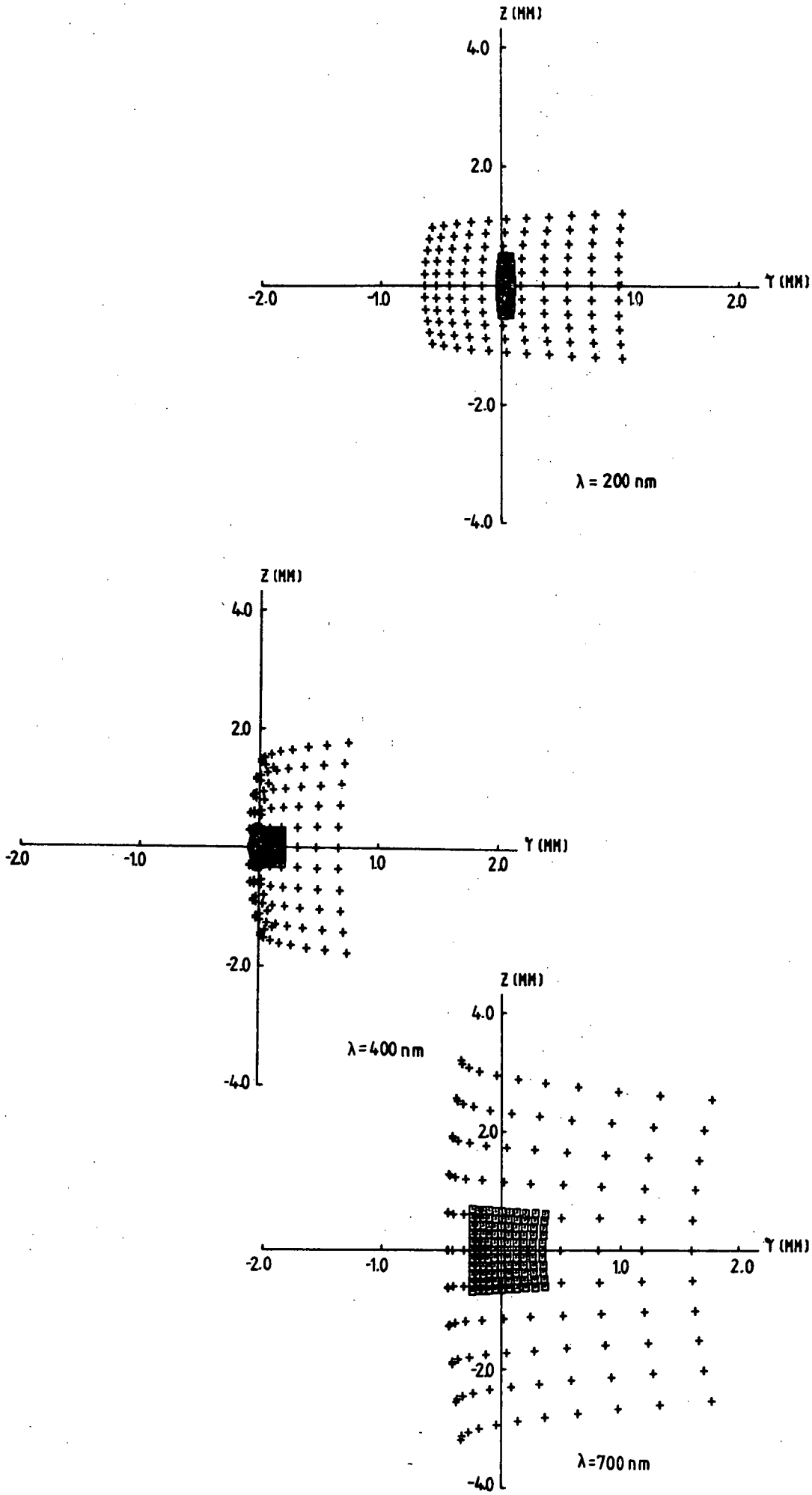

Fig. (7.4) Spot diagrams obtained by tracing rays through an astigmatism corrected holographic or mechanically ruled concave grating mounted in an auto-collimation configuration. Holographic grating □ , ruled +.

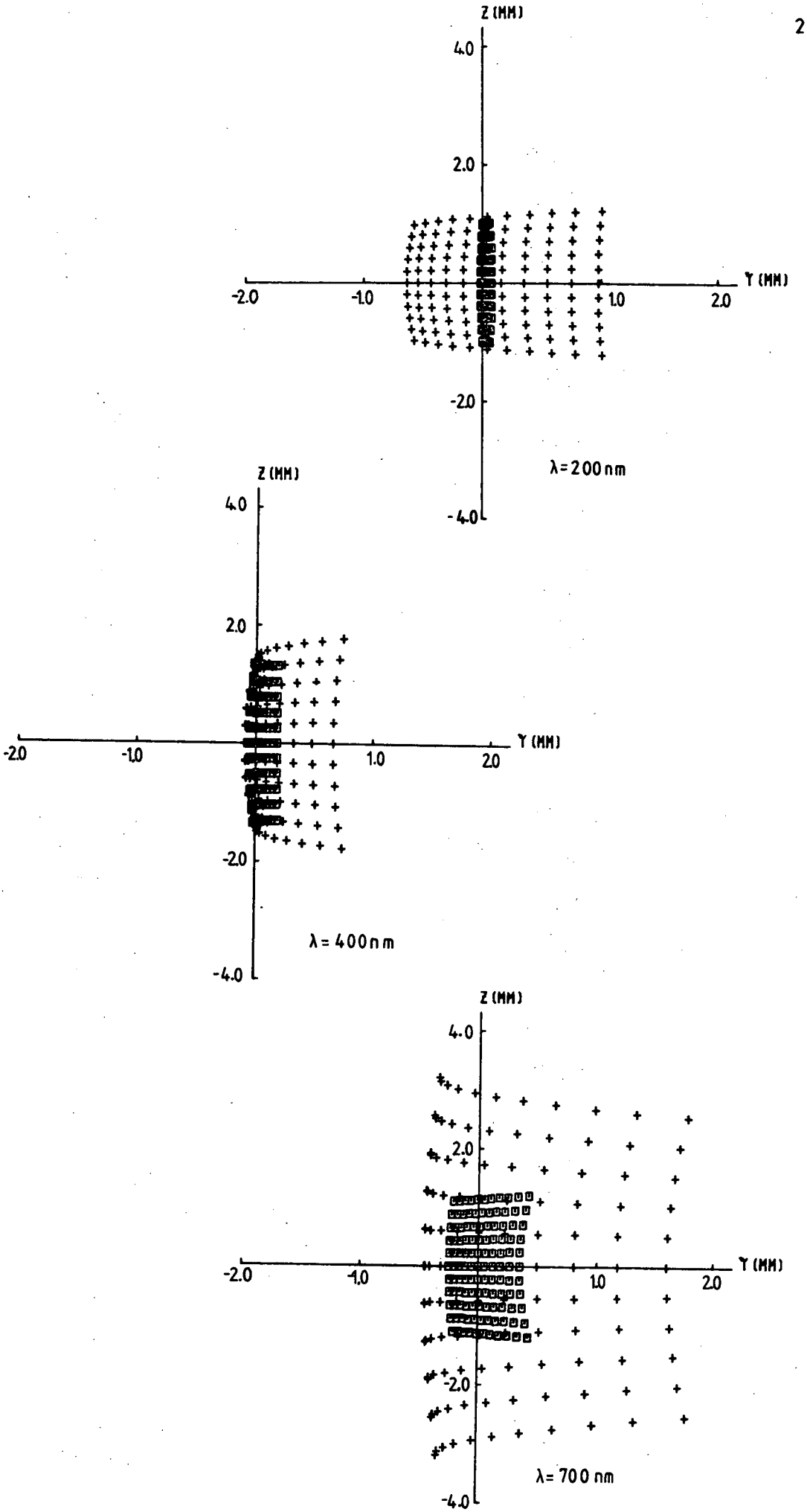

Fig.(7.5) Spot diagrams obtained by tracing rays through a coma-corrected holographic or mechanical concave grating mounted in an auto-collimation configuration. Holographic grating □ , ruled +.

no reduction in image height over that for the ruled grating is present. Obviously the choice of coma-minimization and the subsequent contraction in image width is at the sacrifice of the reduction in image height.

7.4 MIRROR AND CONCAVE GRATING MOUNTED UNI-AXIALLY

Aberration-minimized holographic gratings were designed in the previous section for use in a monochromator. The optical instrument consisted of a single concave grating mounted in an auto-collimation configuration. This configuration is now developed further by the introduction of a spherical mirror mounted uni-axially with the concave grating. Shown in Fig.(7.6) is a schematic representation of the resulting monochromator.

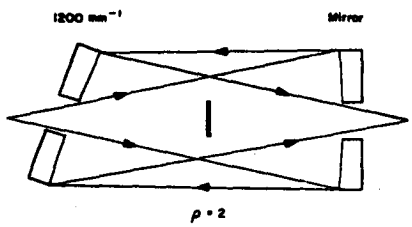

Fig.(7.6) Schematic representation of monochromator containing a concave grating mounted uni-axially with a spherical mirror.

The individual optical components satisfy the following identities:

$$\begin{aligned} &\text{(i)} \quad \text{GRATING} \qquad \bar{\rho} = 0 \\ &\text{(ii)} \quad \text{MIRROR} \qquad \bar{\rho} = 2 \qquad \bar{\rho}' = 0 \end{aligned} \tag{7.31}$$

However, the monochromator can be mathematically treated as a single entity, described by combining the instrumental constants of Eq.(7.31)with Eqs.(7.27), (7.28) and (7.29)

$$\bar{\rho} = 0 \quad \bar{\rho}' = 1.97209 \quad \text{with } A_{200} = 0.19842 \tag{7.32}$$

for the general method; and

$$\bar{\rho} = 0 \quad \bar{\rho}' = 2.09532 \quad \text{with } A_{200} = -3.91787\times10^{-6} \tag{7.33}$$

for the modified method; and

$$\bar{\rho} = 2 \quad \bar{\rho}' = 2.09532 \tag{7.34}$$

for the mechanically ruled grating.

The addition of the spherical mirror to the concave grating does not influence the determination of the instrumental constants for the minimization of the horizontal focus term. The only primary aberrations introduced into the optical system by the mirror are the components of spherical aberration. Consequently, the behaviour of the coefficient of horizontal focus with the scanning wavelength is identical to that for the single concave grating displayed in Fig.(7.3).

The recording parameters describing production of the aberration-corrected grating for this monochromator are, of course, those displayed in Table (7.2) corresponding to a single concave grating of effective grating constant 1/1200 mm.

Illustrated in Table (7.5) are the values of the $\bar{F}_{ijk}$'s at λ = 0, 200, 400 and 700 nm calculated for the instrument containing a spherical mirror and an astigmatism-corrected holographic concave grating or a mechanically ruled concave grating having the same R and σ. Table (7.6) lists similar

λ(nm)	Grating	$\overline{F}_{200}$	$\overline{F}_{020}$	$\overline{F}_{300}$	$\overline{F}_{120}$	$\overline{F}_{400}$	$\overline{F}_{220}$	$\overline{F}_{040}$
0	MECH	0.09532	0.09532	0.00000	0.00000	-4.41849	-0.41849	-4.41849
	G.M.	-0.02791	-0.02791	0.00000	0.00000	-3.89145	0.10855	-3.89145
	M.M.	0.09532	0.09532	0.00000	0.0000	-4.41849	-0.41849	-4.41849
200	MECH	0.07960	0.10977	0.26964	0.27722	-4.02863	-0.22820	-4.43732
	G.M.	0.00577	-0.04086	0.07017	0.01999	-3.84254	0.069992	-3.88428
	M.M.	0.07957	0.03006	0.08097	0.02486	-4.35609	-0.42796	-4.33924
400	MECH	0.03308	0.15377	0.50482	0.56551	-2.94230	0.35716	-4.49598
	C.M.	0.01220	-0.02427	0.11043	0.05039	-3.24581	-.34658	-3.90569
	M.M.	0.03302	-0.00566	0.12748	0.06079	-3.59722	-0.04236	-4.29983
700	MECH	-0.08934	0.28027	0.72003	1.04530	-0.58778	2.08377	-4.67593
	C.M.	-0.02416	0.06112	0.05158	0.14057	-1.79515	1.44878	-4.00608
	M.M.	-0.08946	0.00126	0.05970	0.16204	-1.73390	1.38462	-4.33267

TABLE (7.5) Values of $\overline{F}_{ijk}$'s for the monochromator containing a mirror and either a mechanically ruled or astigmatism-corrected holographic grating. The recording parameters used are listed in Table (7.2). The instrumental constants used are those described by Eqs.(7.32) and (7.33). M.M. and G.M. stand for modified method and general method respectively.

λ(nm)	Grating	$\overline{F}_{200}$	$\overline{F}_{020}$	$\overline{F}_{300}$	$\overline{F}_{120}$	$\overline{F}_{400}$	$\overline{F}_{220}$	$\overline{F}_{040}$
0	MECH	0.09532	0.09532	0.00000	0.00000	-4.41849	-0.41849	-4.41849
	G.M.	-0.02791	-0.02791	0.00000	0.00000	-3.89145	0.10855	-3.89145
	M.M.	0.09532	0.09532	0.00000	0.00000	-4.41849	-0.41849	-4.41849
200	MECH	0.07960	0.10977	0.26964	0.27722	-4.02863	-0.22820	-4.43732
	G.M.	0.00577	-0.08769	0.07017	-0.01139	-4.01460	-0.06440	-3.83021
	M.M.	0.07957	-0.02136	0.08097	-0.01200	-4.56404	-0.58759	-4.26401
400	MECH	0.03308	0.15377	0.50482	0.56551	-2.94230	0.35716	-4.49598
	G.M.	0.01219	-0.11792	0.11042	-0.01236	-3.58994	0.07793	-3.79754
	M.M.	0.03302	-0.10849	0.12749	-0.01313	-4.01313	-0.36161	-4.14937
700	MECH	-0.08934	0.28027	0.72003	1.04530	-0.58778	2.08377	-4.67593
	G.M.	-0.02416	-0.10277	0.05158	0.03076	-2.39737	0.98764	-3.81682
	M.M.	-0.08946	-0.17869	0.05970	0.03269	-2.46174	0.82593	-4.06935

TABLE (7.6) Values of $\overline{F}_{ijk}$'s for the monochromator containing a mirror and either a mechanically ruled or coma-corrected holographic grating. The recording parameters are listed in Table (7.2). The instrumental constants used are those described by Eqs.(7.32) and (7.33). M.M. and G.M. stand for modified method and general method respectively.

values for the coma-corrected holographic concave grating. Clearly evident is the insertion of the mirror into the monochromator. For the respective tables, the magnitude of the astigmatism and coma coefficients of the final spectral image are equivalent to those displayed in Tables (7.3) and (7.4) for the single grating. However, the coefficients of the spherical aberration components, $\overline{F}_{400}$, $\overline{F}_{020}$ and $\overline{F}_{040}$ differ.

Contributions to the aberrations present in the final image originating from the spherical mirror are illustrated in the spot diagrams. Figs.(7.7) and (7.8) show the results of tracing rays through the monochromator containing a mirror and an astigmatism-corrected holographic and coma-corrected holographic concave grating respectively. A comparison with a similar monochromator utilizing a mechanically ruled concave grating is also presented. The rays traced are those originating at the centre of the entrance slit, diffracted by the grating to be reflected by 121 points on the mirror surface to the image plane. This plane is considered to be the y'z' plane perpendicular to the diffracted principal ray OB_o.

Although the height of the image produced by the monochromator containing a mirror and astigmatism-corrected grating is comparable to the mechanical counterpart, the horizontal focus of the former is far superior. The addition of the mirror has had little influence on the width of the image, but it has initiated an extension in the image height. A comparison between Figs.(7.8) and (7.5) for the monochromators containing coma-corrected holographic gratings indicates at least a doubling of the image height accompanies the inclusion of the spherical mirror.

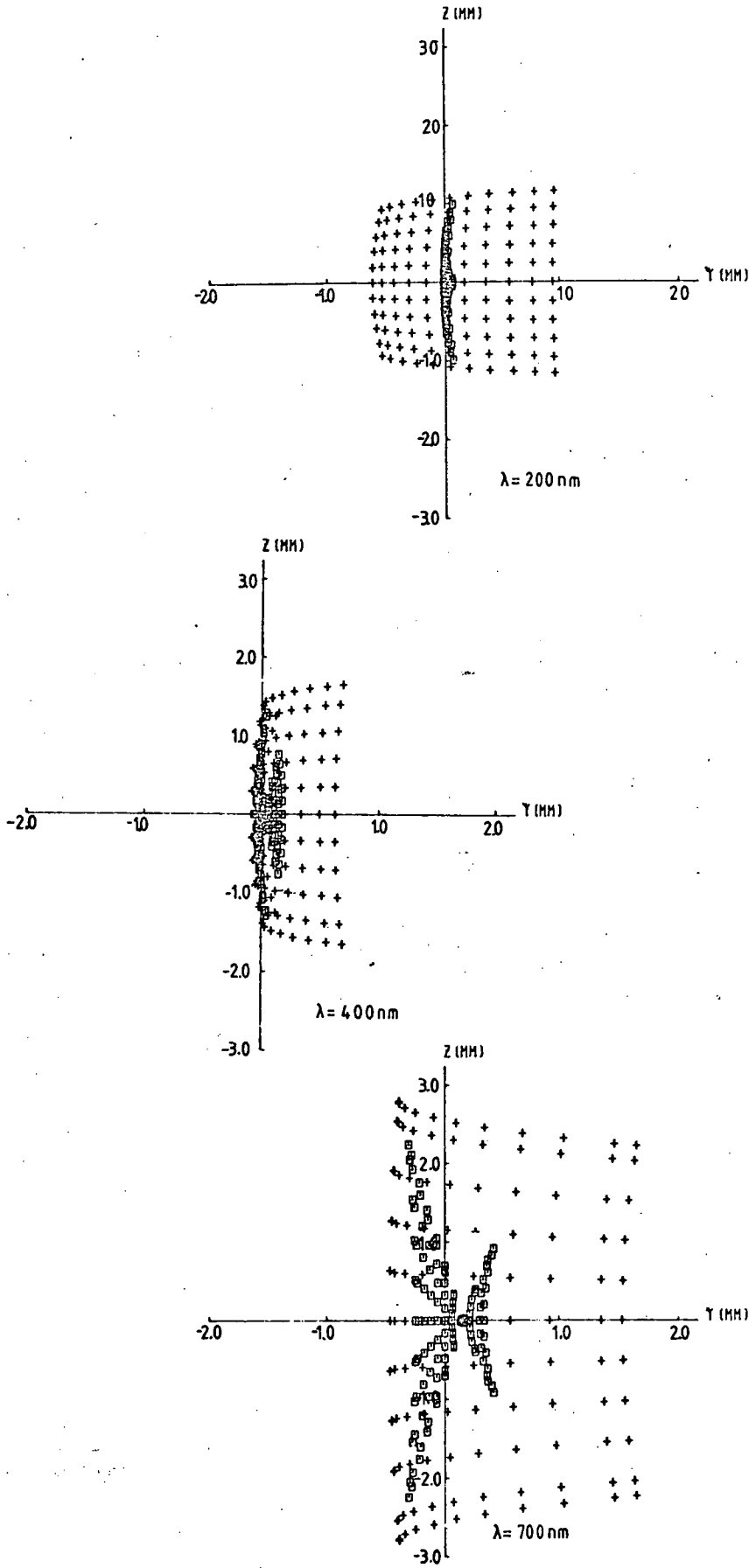

Fig.(7.7) Spot diagrams obtained by tracing rays through an astigmatism-corrected holographic or mechanically ruled grating mounted uni-axially with a spherical mirror. Holographic □ , ruled +.

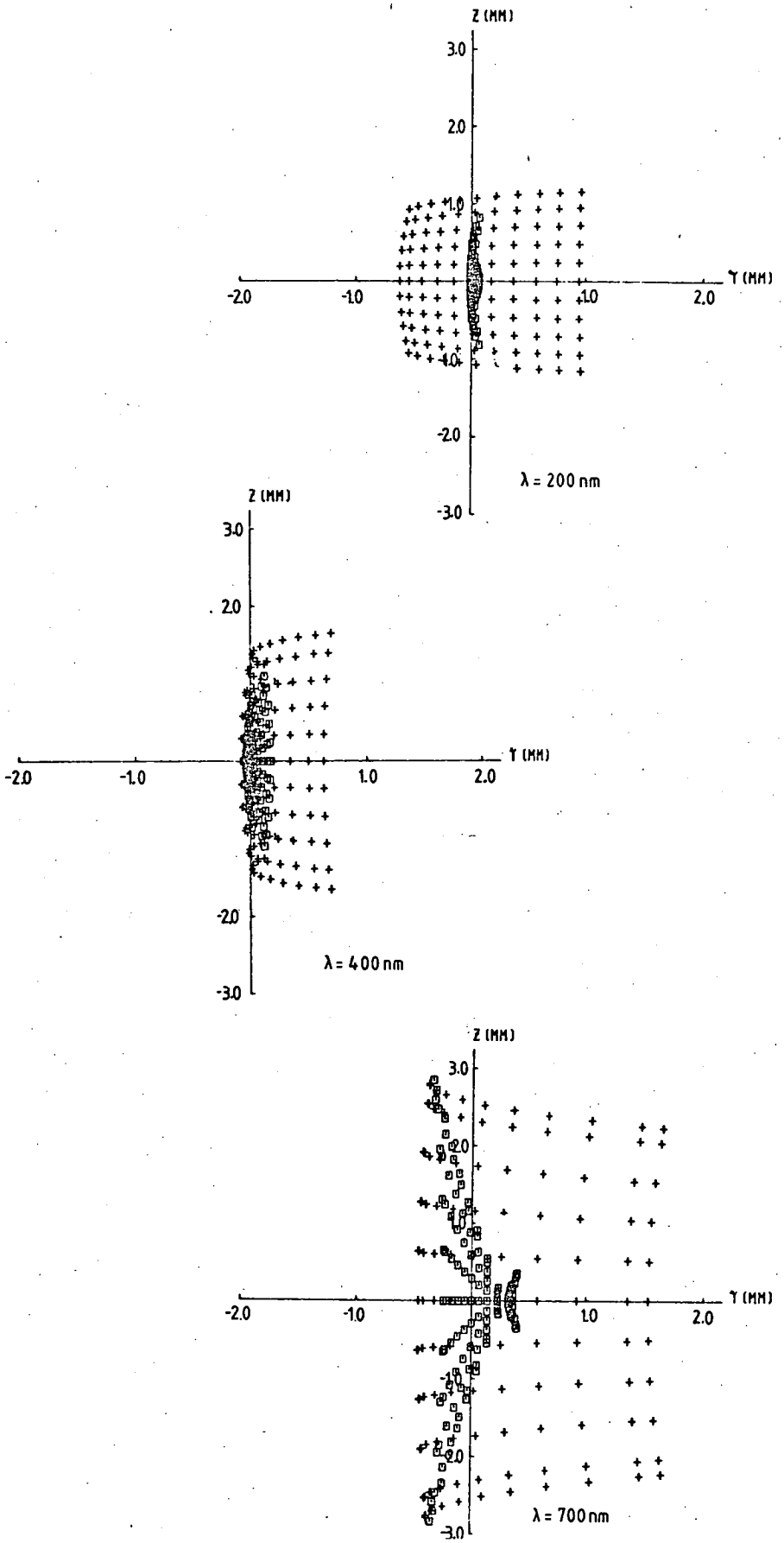

Fig.(7.8) Spot diagrams obtained by tracing rays through a coma-corrected holographic or mechanically ruled concave grating mounted uni-axially with a spherical mirror. Holographic □ , ruled +.

It is interesting to note the improved performance which could be achieved from the P.R.A. MONOCHROMATOR 030, if the presently utilized ruled gratings are replaced by astigmatism-corrected holographic concave gratings.

7.5 UNI-AXIAL DOUBLE CONCAVE GRATING MONOCHROMATOR

It is proposed to vary the monochromator discussed in the previous section by replacing the spherical mirror with a second concave grating, identical to the first. This arrangement is depicted in Fig.(7.9). The spectral performance of this

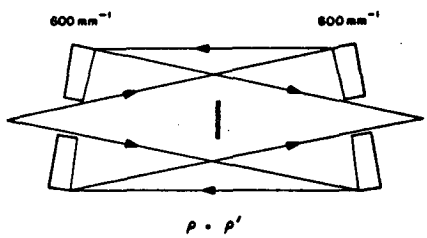

Fig.(7.9) Schematic representation of monochromator containing two identical concave gratings mounted uni-axially.

monochromator is then compared with that of the earlier instrument. However, a meaningful evaluation can only be achieved if instruments of similar dispersion are considered. Therefore, the proposed monochromator is considered to have two concave gratings of effective grating constant 1/600 mm.

The monochromator is designed for a scanning wavelength range 0 - 700 nm in the first order, while the grating constant is σ = 1/600 mm and the recording wavelength is 442 nm. Following the guidelines presented in Section (7.3) the mounting parameters for the uni-axial double concave grating instrument are calculated

to be:

$$\bar{\rho} = \bar{\rho}' = 1.99273 \qquad A_{200} = 0.10360 \tag{7.35}$$

for the general method; and

$$\bar{\rho} = \bar{\rho}' = 2.01473 \qquad A_{200} = 2.68536\times10^{-2} \tag{7.36}$$

for the modified method; and

$$\bar{\rho} = \bar{\rho}' = 2.01473 \tag{7.37}$$

for the mechanically ruled grating.

Fig.(7.10) displays the behaviour of the $\bar{F}_{200}$ curves based on the three design approaches. Clearly, the general method yields values for the mounting parameters which are more satisfactory in reducing the horizontal focus coefficient. Due to the increased size in the holographic term A_{200}, there is a slight variation between the curves for the modified procedure and the mechanically ruled grating.

An investigation into the appropriate values of θ_2 employed in the comparison of the holographic terms A_{120} and A_{300} reveals that the following limits on the angle of rotation give rise to satisfactory recording parameters:

$$\begin{aligned} &\theta_1 = 0^\circ \qquad (\lambda_1 = 0 \text{ nm}) \\ &\qquad\qquad \text{for } (ijk) = (200),(020),(300),(120) \\ &\theta_2 = 12.12^\circ \quad (\lambda_2 = 700 \text{ nm}) \\ &\qquad\qquad \text{for } (ijk) = (200),(020),(300),(210) \end{aligned} \tag{7.38}$$

From the two sets of instrumental constants given in Eqs.(7.35) and (7.36), the corresponding recording positions are

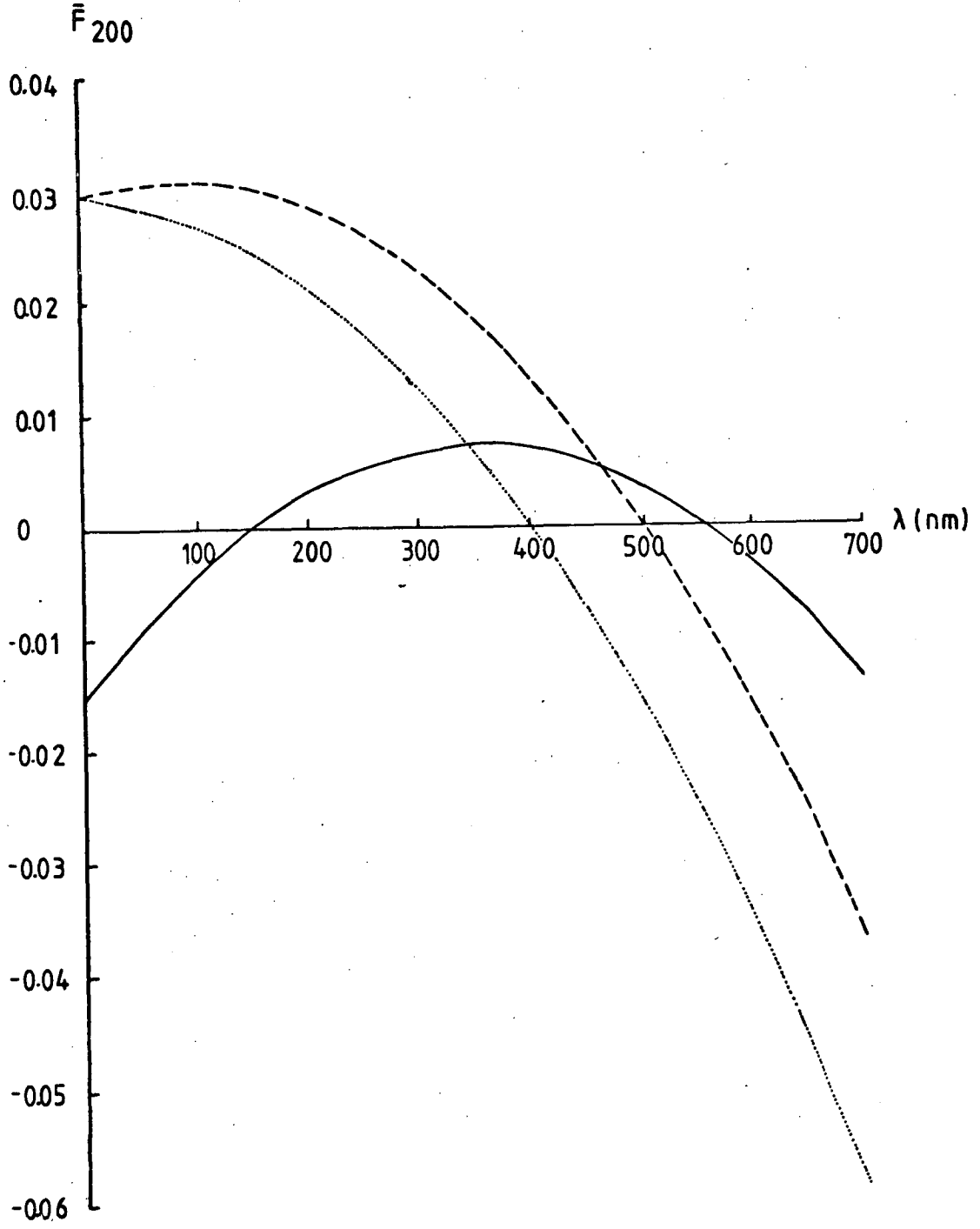

Fig.(7.10) Magnitude of $\bar{F}_{200}$ as a function of the diffracted wavelength. The solid curve and the dashed curve are calculated by the general method and the modified method respectively.

calculated for both the astigmatism and coma reduced design procedures. The results appear in Table (7.7). Inspection reveals that the recording parameters for the general approach are similar to those for the modified approach.

Tables (7.8) and (7.9) compare the behaviour of $\overline{F}_{ijk}$'s in the final spectral image as a function of the wavelength for holographic concave gratings generated according to both the general and modified design parameters with that of a mechanically ruled concave grating having the same R and σ. Table (7.8) considers astigmatism-corrected holographic gratings, while Table (7.9) corresponds to coma-corrected holographic gratings. The instrumental constants are those given in Eqs.(7.34) and (7.35) and the recording parameters are listed in Table (7.7). The two tables illustrate the improved performance of the holographically recorded gratings over that instrument containing two mechanically ruled gratings. It is interesting to note the low value of the horizontal focus coefficient for the ruled grating at λ = 400 nm. This phenomenon is clearly explained in Fig.(7.10) where the function $\overline{F}_{200}$ passes through zero at λ = 400 nm, for the ruled grating. There is very little difference between the behaviour of the holographic concave gratings, although a judgement based upon the values of $\overline{F}_{200}$ must favour the design parameters corresponding to the general method.

Figs.(7.11) and (7.12) show the results of tracing rays through the proposed monochromator to the intersection with the

Minimized Terms	Method Used	ρ_C	ρ_D	γ	δ
$\overline{F}_{200}$, $\overline{F}_{040}$	General	1.614587	1.615767	-4.817094	10.44111
$\overline{F}_{300}$ (Astigmatism correction)	Modified	1.615105	1.637145	-4.832902	10.42510
$\overline{F}_{200}$, $\overline{F}_{300}$	General	1.617817	1.607923	-5.876173	9.370683
$\overline{F}_{120}$ (Coma-type correction)	Modified	1.619792	1.630736	-5.883202	9.363597

TABLE (7.7) Recording parameters suitable for correcting astigmatism and coma-type aberrations in proposed double concave grating monochromator. It is assumed that σ = 1/600 mm, $m\lambda = 0 \rightarrow 700$ nm and λ_o = 442 nm. For the instrumental constants used in the calculations, refer to Eqs. (7.35) and (7.36).

λ(nm)	Grating	$\overline{F}_{200}$	$\overline{F}_{020}$	$\overline{F}_{300}$	$\overline{F}_{120}$	$\overline{F}_{400}$	$\overline{F}_{220}$	$\overline{F}_{040}$
0	MECH	0.02946	0.02946	0.00000	0.00000	-4.11958	-4.11958	-4.11958
	G.M.	-0.01453	-0.01453	0.0000	0.00000	-3.93503	-3.93503	3.92050
	M.M.	0.02946	0.02946	0.0000	0.00000	-4.134312	-4.13431	4.16377
200	MECH	0.02216	0.03667	0.24401	0.24576	-3.94993	-4.03800	-4.12712
	G.M.	0.00319	-0.02018	0.00816	-0.00554	-3.97565	-3.96319	3.86659
	M.M.	0.02863	0.00500	0.00837	-0.00562	-4.15529	-4.13901	4.13491
400	MECH	0.00034	0.05836	0.48012	0.49415	-3.45012	-3.89157	-4.14998
	G.M.	0.00671	-0.01134	0.00862	-0.00849	-3.70729	-3.84048	3.67630
	M.M.	0.01328	-0.00497	0.00884	-0.00861	-3.85335	-3.98612	3.96295
700	MECH	-0.05905	0.11865	0.80234	0.87752	-2.14615	-3.10092	-4.21474
	G.M.	-0.01407	0.02967	-0.02183	-0.00225	-2.78811	-3.36213	3.12433
	M.M.	0.03640	0.00782	-0.02240	-0.00231	-2.86006	-3.44964	3.42561

TABLE (7.8) Values of $\overline{F}_{ijk}$'s for the mechanically ruled and the astigmatism-corrected holographic gratings fixed in proposed monochromator. The recording parameters used are listed in Table (7.7). The instrumental constants used are those described by Eqs.(7.35) and (7.36). M.M. and G.M. stand for modified method and general method respectively.

λ(nm)	Grating	$\overline{F}_{200}$	$\overline{F}_{020}$	$\overline{F}_{300}$	$\overline{F}_{120}$	$\overline{F}_{400}$	$\overline{F}_{220}$	$\overline{F}_{040}$
0	MECH	0.02946	0.02946	0.0000	0.00000	-4.11958	-4.11958	-4.11958
	G.M.	-0.01453	-0.01453	0.0000	0.00000	-3.93503	-3.93593	3.92050
	M.M.	0.02946	0.02946	0.00000	0.00000	-4.13431	-4.13431	4.16377
200	MECH	0.02216	0.03667	0.24401	0.24576	-3.94993	-4.0380	-4.12712
	G.M.	0.00319	-0.00596	0.00816	-0.00277	-3.90978	-3.93522	3.84830
	M.M.	0.02863	0.01920	0.00837	-0.00280	-4.08827	-4.11089	4.11561
400	MECH	0.00034	0.05836	0.48012	0.49415	-3.45012	-3.79157	-4.14988
	G.M.	0.00671	0.01709	0.00862	-0.00294	-3.57556	-3.7845	3.63973
	M.M.	0.01328	0.02343	0.00884	-0.00297	-3.7193	-3.92988	3.92436
700	MECH	-0.05905	0.11865	0.80234	0.87752	-2.14615	-3.10092	-4.21474
	G.M.	-0.01407	0.02967	-0.02183	-0.00225	-2.78811	-3.36213	3.12433
	M.M.	-0.03640	0.05753	-0.02240	0.00756	-2.62552	-3.35123	3.35807

TABLE (7.9) Values of $\overline{F}_{ijk}$'s for the mechanically ruled and the coma-corrected holographic concave gratings fixed in proposed monochromator. The instrumental constants used are those described by Eqs.(7.35) and (7.36). M.M. and G.M. stand for modified method and general method respectively. The recording parameters used are listed in Table (7.7).

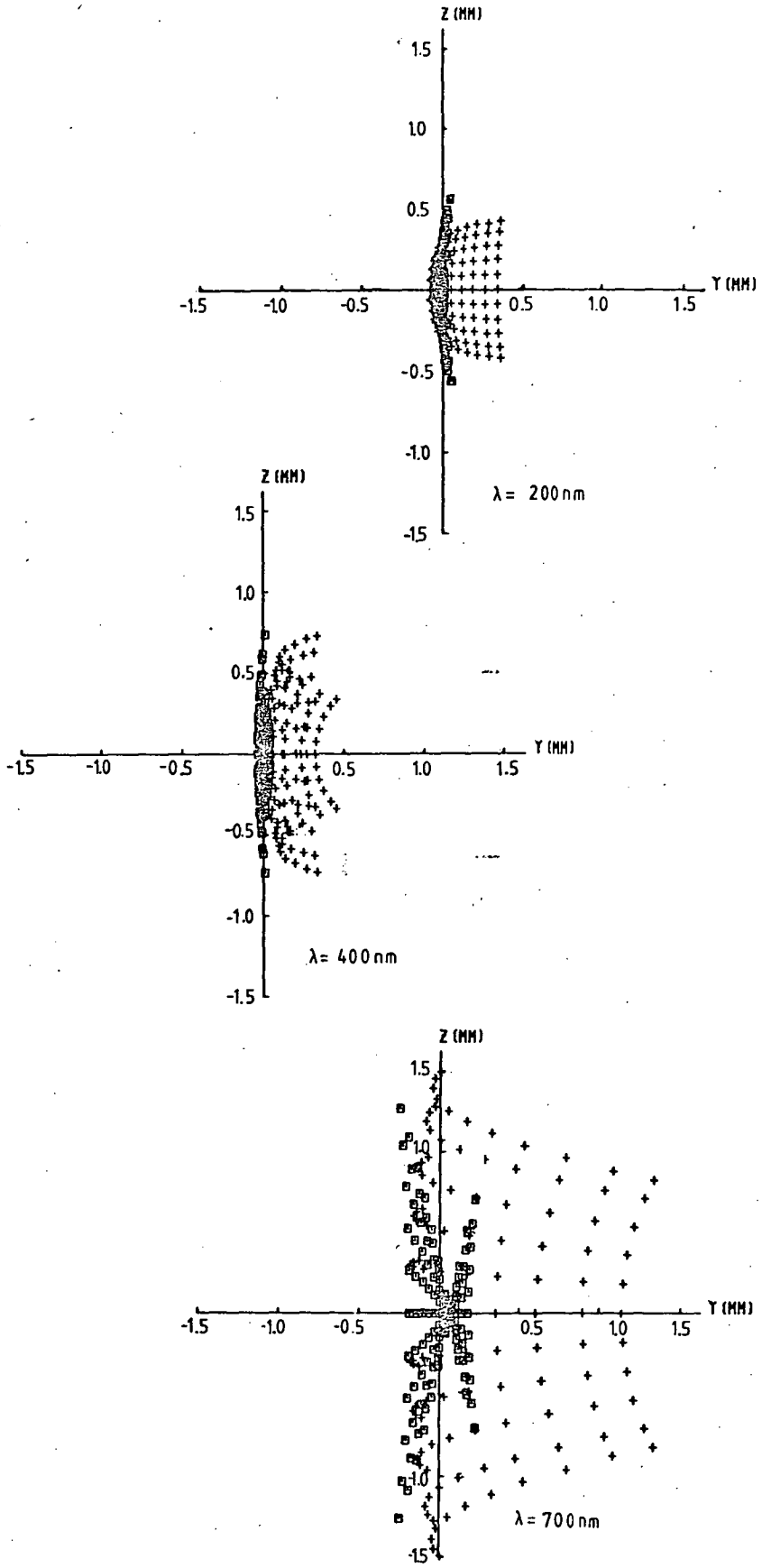

Fig.(7.11) Spot diagrams obtained by tracing rays through the proposed monochromator containing two astigmatism-corrected holographic or mechanically ruled gratings mounted uni-axially. Holographic □ , ruled +.

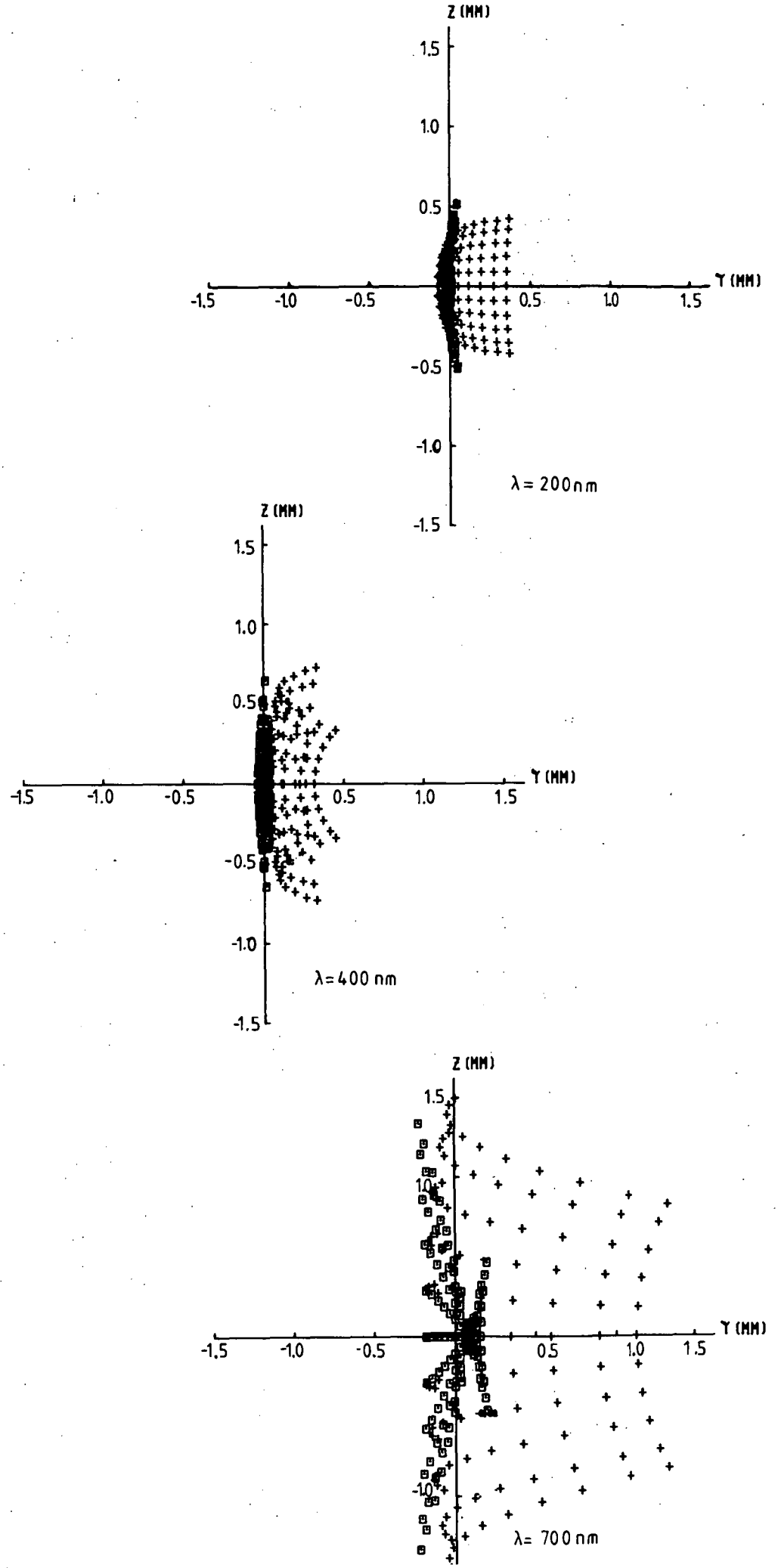

Fig.(7.12) Spot diagrams obtained by tracing rays through the proposed monochromator containing two coma-corrected holographic or mechanically ruled gratings mounted uni-axially. Holographic □,

image plane y'z'. The diagrams are for astigmatism-corrected holographic and coma-corrected holographic gratings compared with mechanically ruled gratings respectively. For the holographic gratings the instrumental parameters are those derived by the general method displayed in Eq.(7.35) due to the superior performance of the horizontal focus coefficient.

At short wavelengths, the height of the spectral image generated by a monochromator containing two mechanically ruled concave gratings mounted according to Eq.(7.37) is less than for the corresponding monochromator containing holographic gratings. However, as the wavelength increases, this advantage decreases, until at λ = 700 nm the image height for astigmatism-corrected gratings becomes coincident with that of the ruled gratings. As mentioned previously, it is most important that the final spectral line generated by any monochromator be as narrow as possible. Clearly Figs.(7.11) and (7.12) demonstrate that this requirement can only be satisfied if aberration-corrected holographic diffraction gratings are utilized for the proposed monochromator. Although both astigmatism-corrected and coma-corrected gratings yield narrow final images, the favourable image heights of the former gratings imply a more effective spectral performance.

There is a significant improvement in the size of the spectral image generated for the double holographic aberration-corrected grating monochromator over that exhibited by the mirror-holographic grating instrument. Roughly speaking, both the height and width of the spectral line formed by the

monochromator containing two holographic gratings is half that for the mirror-holographic grating combination. The improvement is particularly dramatic if the spectral performance of the proposed monochromator is compared to that produced by the ruled grating-mirror instrument.

7.6 CONCLUDING REMARKS

In the foregoing discussion, the application of aberration-minimizing techniques to the light path function has allowed the development of a novel medium resolution monochromator. The construction of this instrument is very simple, just two identical aberration-corrected holographic gratings mounted uniaxially. Operation requires only the simultaneous rotation of the two gratings. No lateral movement to trace the image focal plane is necessary.

Ray-tracing procedures clearly demonstrate the superior spectral performance of the proposed monochromator. Particularly impressive is the excellent horizontal focus leading to useful resolution.

REFERENCES

7.1 Noda,H., Namioka,T. and Seya,M. (1974) J.Opt.Soc.Am., 64, 1043.

7.2 Noda,H., Namioka,T. and Seya,M. (1974) J.Opt.Soc.Am., 64, 1037.